Mapping surface magnetism with a molecule

Alex Fetida

UNIVERSITÉ DE STRASBOURG

ÉCOLE DOCTORALE Physique et Chimie-Physique (ED 182)

Institut de Physique et Chimie des Matériaux de Strasbourg

THÈSE présentée par :

[Alex FETIDA]

soutenue le : **10 Septembre 2024**

pour obtenir le grade de : **Docteur de l'université de Strasbourg**

Discipline/ Spécialité : Physique

Mapping surface magnetism with a molecule

THÈSE dirigée par :

[M. LIMOT Laurent]	Directeur de Recherche, CNRS (IPCMS), Université de Strasbourg

RAPPORTEURS :

[M. AST Christian]	Scientifique sénior, Max Planck institute
[M. GRUBER Manuel]	Professeur, Université de Duisburg-Esssen

AUTRES MEMBRES DU JURY :

[Mme. JUHIN Amélie]	Directrice de recherche, CNRS (IMPMC), Sorbonne université
[Mme. VIART Nathalie]	Professeure, CNRS (IPCMS), Université de Strasbourg
[Mme. BAUMANN Susanne]	Scientifique sénior, Université de Stuttgart
[M. MELIN Thierry]	Directeur de recherche, CNRS (IEMN)

Acknowledgments

After more than four years with the STM team at IPCMS, I am thrilled to complete my PhD thesis. I would like to extend my gratitude to Pierre Rabu, the unit director, for welcoming me to IPCMS. I also thank the doctoral school of physics and chemistry and QUSTEC for supporting my PhD, providing opportunities to present my research at various conferences, and facilitating connections with fellow research scientists.

I am grateful to the jury members—Christian Ast, Manuel Gruber, Susanne Baumann, Amélie Juhin, Nathalie Viart, and Thierry Mélin—for being conciliant and for reviewing my manuscript over the summer.

I owe a great deal of thanks to my thesis director, Laurent Limot, for his guidance and patience throughout this journey. The beginning was not plain sails owing to the Covid pandemic and technical issues on the microscope but thank to his dedication we could finally complete this work. I would also like to thank Marie-Laure Bocquet and Guillaume Schull, the members of my monitoring committee, for ensuring my thesis stayed on track over the past four years. Their availability and advice were greatly appreciated.

Within our team, Fabrice Scheurer and Virginie Speisser were incredibly helpful and reliable, adeptly repairing equipment such as the sputtering gun and evaporators. Along with Céline Guillet, they assisted me with administrative issues. Additionally, Fabrice contributed to our publications and reviewed this manuscript. My thanks also go to Michelangelo Romeo, who collaborated with us on the mapping program and significantly contributed to the work presented here. Theoretical support from Nicolas Lorente, Roberto Robles at CFM (San Sebastian), Christine Goyhenex, and Olivier Bengone at IPCMS was crucial. I enjoyed our discussions

and learning from them.

I am thankful to former spin STM team members—Nicolas B., Benjamin V., and Léo G.—for training me on the STM and offering valuable advice about PhD studies, which facilitated my integration into the group. I enjoy collaborating with PhD students from Nicolas L. and D-J. Choi's teams. First, Cristina M. continued my STM training, and later, I had the opportunity to train Divya J., exchanging knowledge about superconductivity and assisting each other in our experiments. I also thank the light-STM team (aka the flat earthers), who don't believe in spin, for their camaraderie and for sharing their scientific experiences: Anna R., Katharina K., Song J., Kirill V., Luis P-L., Benjamin D., and Tomas N.

Other lab members also played vital roles in our experiments progress. Emmanuel Sternitzky frequently repaired power supplies and transformers and created the filters box, improving our experiments efficiency. Nicolas Beyer ensured the availability of cryogenic liquids at the institute, and the workshop team impressed with their manufacturing skills. During my PhD, I had the opportunity to complete a secondment at Basel Precision Instrument. I thank Parisa Fallahi, Dominik Zumbühl, Christian Scheller, Sergii Kokhas, and Dominik's lab group for their warm welcome. I still wish to use the filters in our STM.

Lastly, I am grateful to my parents, my sisters, my brother, and my friends for their mental support throughout this journey.

Contents

CHAPTER 1

Introduction

The ambition of this PhD thesis is to enhance the spin sensing technique pioneered by our team [1, 2], which involves attaching a nickelocene molecule to the tip of a scanning tunneling microscope (STM) to collect magnetic fingerprints of surfaces and atoms. Building upon the thesis of Benjamin Verlhac [3], who investigated Fe atoms on Cu(100) and Co bilayer nanoislands grown on Cu(111) using inelastic electron tunneling spectroscopy with a nickelocene tip, this research seeks to extend and refine these methodologies. Verlhac's measurements demonstrated that both Fe adatoms and Co atoms from the nanoisland possess a magnetization perpendicular to the surface, with the exchange field produced by the atoms or surface showing an exponential dependence on the vacuum gap of the tunneling junction. Specifically, the variation of the exchange field between the top and hollow positions of the Co lattice enables atomic network imaging without contact. Additionally, our molecular probe can measure the spin polarization at the Fermi energy of Co islands and Fe adatoms by analyzing the amplitude of the peaks and dips in the second derivative of the tunneling current with respect to bias (d^2I/dV^2).

Thus far, studied objects have exhibited only out-of-plane magnetization. During this thesis, we demonstrate that our magnetic probe can detect magnetization in different directions. Furthermore, other magnetic properties are monitored with respect to the distance between the tip and the surface. We developed a mapping technique, voxel imaging, capable of measuring with respect to lateral coordinates (x, y), the exchange energy $E_{\text{ex}}(x, y)$ between the nickelocene tip and the surface as well as the sample spin polarization $P(x, y)$. This allows us to observe the lateral

magnetic corrugation of pristine and hydrogen-contaminated Co nanoislands, as well as the nickelocene molecule itself adsorbed on cobalt.

Chapter 2 provides a state-of-the-art overview of surface magnetism. It explains techniques closely related to ours, such as spin-polarized STM, magnetic exchange force microscopy, and spin excitation spectroscopy. Additionally, it details the working principle of the nickelocene tip on magnetic objects and briefly presents other ways to sense the spin in STM like electron spin resonance (ESR-STM) or the measurement of zero-bias anomalies in the conductance of quantum magnetic impurities.

Chapter 3 begins with an explanation of the tunneling effect and covers the Bardeen, Tersoff-Hamann, and Wentzel–Kramers–Brillouin (WKB) theories, which provide a mathematical description of the current in a tunneling junction. The chapter also discusses surface imaging techniques, introduces scanning tunneling spectroscopy along with inelastic electron spectroscopy, and concludes with a detailed description of our experimental setup and data acquisition process.

Chapter 4 focuses on typical ferromagnetic cobalt (Co) islands grown on a clean copper surface, Cu(111), including monolayer-thick islands which have not been previously studied. Our findings, consistent with prior observations, show that the thickness of the ferromagnetic Co layer influences the direction of sample magnetization and spin polarization. Additionally, we illustrate that the spatial variation of the exchange energy across the surface is accurately represented by computed spin-density maps.

Chapter 5 focuses on hydrogen-contaminated Co islands. Our measurements reveal that the adsorption of hydrogen atoms rotates the magnetization from out-of-plane to in-plane. To explain this effect, we perform DFT computations of the magnetic anisotropy energy concerning the quantity of hydrogen adsorbed. Combining experimental results with theoretical computations enables us to determine the configuration of the hydrogen atoms adsorbed and estimate their quantity.

Chapter 6 investigates the nickelocene adsorbed on Co bilayer islands. We start by characterizing the adsorption and electronic properties of the molecule, identifying the molecular orbitals with a metal tip. In the second part, we use the nickelocene tip to probe the magnetism of the adsorbed nickelocene molecule on cobalt. We identify its spin orientation, and employ voxel imaging to observe lateral corrugations of the spin polarization and exchange coupling within the molecule.

Chapter 7 presents a brief overview of the thesis with some possible outlooks for future work using a nickelocene-terminated STM tip.

CHAPTER 2

Atomic scale magnetism with STM

Information storage devices like a magnetic random access memory (MRAM) are composed of different Weiss domains with finite magnetization directions. Each area defines a unit of information, either 1 or 0. These domains contain roughly millions of atoms. If we manage to reduce the size of a unit of information down to a single atom, the storage device would reach the highest memory capacity possible. However, to read information, we would have to access magnetization at the atomic scale. The scanning tunneling microscope (STM), invented in 1981, is one of the scanning probe techniques that has this ability (Fig. 2.1). Several other techniques have inspired our research: i) Spin-polarized STM (SP-STM)[4], which was invented in 1990, uses a magnetic STM tip to image magnetic surfaces taking advantage of the magneto-resistance effect. As a result, the surface image displays areas of different magnetic contrasts. ii) Spin excitation spectroscopy, developed in 2004 by A.J. Heinrich *et al.*, which uses inelastic tunnel electrons to explore the spin Hamiltonian of magnetic atoms. iii) The work by L. Gross *et al.* in 2009 [5] that showed that a molecular CO tip can image a molecule with a resolution high enough to highlight its chemical structure. Their work does not involve magnetism but inspired using an STM tip functionalized with a nickelocene molecule. As we will show monitoring the spin excitation of the nickelocene molecule through the inelastic current provides information about the magnetism of the object studied. We thus gain access to its spin polarization, magnetization direction, and magnetic exchange coupling with atomic scale resolution. In this chapter, we elaborate in more detail on the techniques mentioned above, which are used for imaging surface magnetism

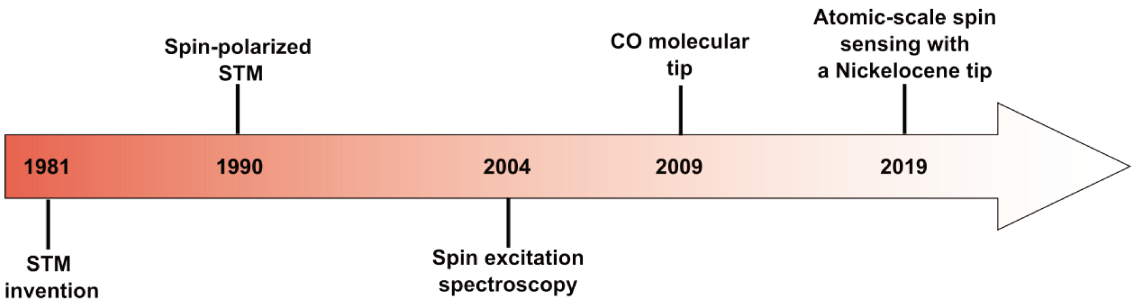

Figure 2.1: Chronology of STM techniques related to detection of magnetic properties.

and spin detection. We will illustrate these techniques by showcasing original studies that utilize them. We also provide an overview of the nickelocene-tip technique used throughout this thesis.

2.1 Magnetic surface imaging

2.1.1 Spin-polarized STM

Spin-polarized STM enables to detect the magnetization of a surface. To achieve this, the STM tip is coated with magnetic materials such as cobalt, chromium, or iron to obtain a specific magnetization orientation. Another method to create a magnetic tip is by evaporating magnetic atoms onto the surface and collecting them at the apex of the tip by a surface-to-tip transfer. Due to the magneto-resistance effect, magnetic objects with different magnetization directions exhibit different contrasts. According to Wortmann *et al.* [6], the differential conductance, dI/dV, is expressed as follows:

$$dI/dV \propto \rho_t \rho_s(eV) + m_t m_s cos\theta. \tag{2.1}$$

The first term represents the product of the local density of states (LDOS) of the tip and the sample, while the second term is the scalar product between the local magnetization direction of the tip and the local magnetization direction of the sample. Pietzsch *et al.* observed spin-polarized contrast on cobalt islands grown on Cu(111) (Fig. 2.2) [7]. They used a tungsten tip coated with a chromium film to ensure magnetization along the tip axis, that is, perpendicular to the sample surface. The dI/dV maps were acquired at a constant current, revealing islands with similar heights but varying contrasts. This difference arises from the relative angle θ between the tip magnetization and island magnetization. Without an external magnetic field, the Co islands have their magnetization parallel or anti-parallel to

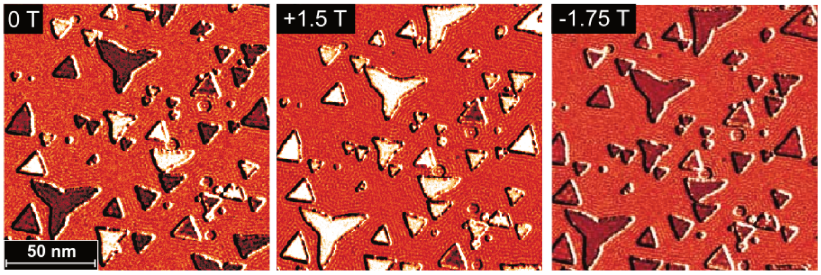

Figure 2.2: dI/dV maps of Co islands on Cu(111) acquired at $V = -0.18$ mV with different perpendicular magnetic fields. Adapted from [7].

that of the tip which leads to the different contrast. Thus, as shown in Fig. 2.2, the islands exhibit two possible contrasts. Applying a magnetic field of 1.5 T aligns the magnetization of nearly all the islands in the same direction, resulting in a bright intensity for nearly all islands. Conversely, a magnetic field of -1.75 T reverses the magnetization of the islands in the opposite direction, resulting in a darker intensity. This technique can also be used to image non-collinear spin textures such as vortex cores [8] or nano-scale skyrmions [9].

2.1.2 Magnetic exchange force microscopy

Magnetic exchange force microscopy (MexFM) utilizes a magnetic AFM tip to sense the spin or magnetization of surfaces (Fig. 2.3a). Unlike STM, AFM does not rely on a tunneling current but on the force felt by the tip. The tip is attached to a cantilever that oscillates at a resonance frequency f_0 when it is free. The interaction with the surface results in a shift of the frequency $f = f_0 + \Delta f$. While the tip scans the sample, the AFM maintains the frequency shift Δf constant by adjusting the distance z between the tip and the surface accordingly. This process yields a topographic map of the surface. Kaiser *et al.* employed an AFM iron-coated tip to image a nickel oxide (NiO) surface combined with a magnetic field of 5 T to align the spin of the tip perpendicular to the surface [10]. The (100) surface of this oxide presents neighboring rows of nickel separated by rows of oxygen atoms. Each Ni atoms of one row have the same spin direction with the spin of the closest neighboring Ni atoms row being antiferromagnetic (see Fig. 2.3a). Below the distance of 200 pm from the contact to the surface, a magnetic exchange interaction appears [11, 12],. We will see in § 2.2.3 how the contact point can be defined. The inset of Fig. 2.3b represents an average of every unit cell of the raw image and displays three different contrasts, with the brightest spots representing the oxygen atoms. Nickel atoms appear with two different contrasts, dark or lighter dark. Moreover, the corrugation next to the image confirms differences in apparent heights. This variation is explained by the

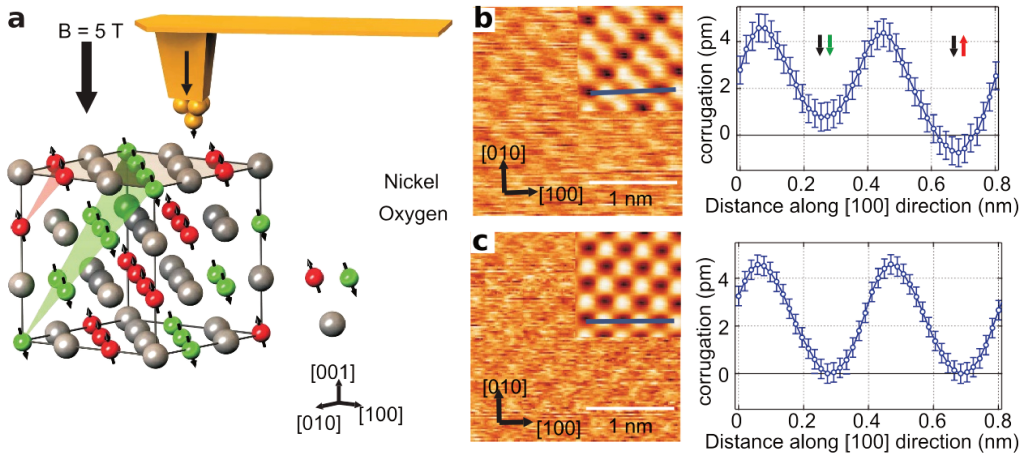

Figure 2.3: (a) Sketch of the magnetic tip scanning the NiO(001) surface in a 5 T magnetic field directed perpendicular to the surface. (b) Raw image of the NiO surface acquired at constant $\Delta f = -23.4$ Hz. The inset is an average over all the unit cells of the raw image. The right panel shows the corrugation along the blue line in the inset and shows different apparent heights for two neighboring Ni atoms. (c) Same surface imaged with the constant frequency shift $\Delta f = -22$ Hz that is scanning further away from the surface. The inset is also obtained by averaging. Adapted from [10]

orientations of the Ni spin ($\hat{S}_1$) which can be parallel or antiparallel to the tip spin ($\hat{S}_2$). Depending on the configuration, the magnetic exchange interaction is modified according to the Heisenberg model $H = -J_{12}\hat{S}_1 \cdot \hat{S}_2$. Figure 2.3c is a standard AFM image acquired at a higher distance than the image of Fig. 2.3b . No difference is observed between the Ni atoms. At this distance, the tip is only sensitive to the chemistry of the surface, not the magnetism.

2.2 Spin excitation spectroscopy

In the preceding section, we discussed scanning probe techniques developed to image the magnetism of surfaces. Other studies have also managed to access the magnetic states of single atoms or molecules by monitoring spin excitations through the inelastic tunnel current.

2.2.1 Principle

In 2004, A.J. Heinrich *et al.* [13], observed the spin excitations of Mn atoms adsorbed on Al_2O_3 islands grown on a NiAl substrate using a STM operating at 0.6 K (Fig. 2.4a). Tunneling electrons have a nonzero probability to exchange energy with the sample when they reach a certain energy threshold determined by the bias volt-

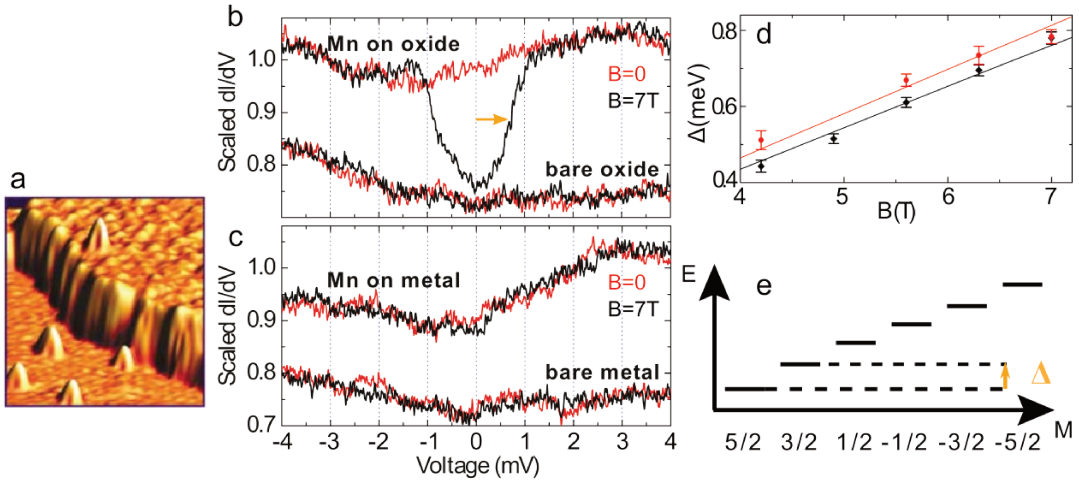

Figure 2.4: (a) STM image of the oxide Al_2O_3 grown on chNiAl(110) with adsorbed Mn atoms. (b) dI/dV spectra obtained on the Mn atom on oxide and on the bare oxide with and without the magnetic field. (c) dI/dV spectra recorded on a Mn atom adsorbed on NiAl(110) and on the bare metal with and without magnetic field. (d) Zeeman energy with respect to the magnetic field B, in red for a Mn atom near the edge of a Al_2O_3 patch, in black for an isolated Mn atom of the oxide patch . (e) Spin-state diagram and spin excitation of Mn on Al_2O_3/NiAl(110) in the presence of a magnetic field along z. Adapted from [13].

age. This phenomenon, known as inelastic electron tunneling, was first detected while exciting vibrational modes of single acetylene molecules [14]. In their study, Heinrich *et al.* measured the dI/dV on Al_2O_3 and on Mn/Al_2O_3 without and with an external magnetic field ($B = 7$ T) in the plane of the sample (Figs. 2.4b-c). When the magnetic field is applied, they observed a symmetric step in the dI/dV line shape at an energy $|\Delta| \sim 0.8$ mV whereas the signal at $B = 0$ T did not exhibit any feature. This energy increased linearly with the applied external field (Fig. 2.4d). This is explained by the Zeeman effect applied to the Mn atom energy levels. The Hamiltonian describing the system is:

$$H = -g\mu_B \hat{J} \cdot \hat{B}. \tag{2.2}$$

Here, $\hat{J}$ represents the total angular momentum and $\hat{B}$ is the applied magnetic field. The free Mn atom has an orbital momentum that can be neglected, thus the total momentum is composed only of the spin $S = 5/2$. Assuming that J is not modified when Mn is adsorbed on the surface , the magnetic states have the form $|S, M\rangle$, where M represents the projection of the spin along the z axis, taking half integer values between $+5/2, ..., -5/2$. The magnetic field lifts the degeneracy of the spin states so that the ground state $|5/2, +5/2\rangle$ and the first excited state $|5/2, +3/2\rangle$

are separated by an energy Δ. The step observed in Fig. 2.4b is the fingerprint of a spin excitation from the ground state to the first excited state (Figs. 2.4e) due to inelastic tunnel electrons. A new tunneling channel is added to the elastic current channel, leading to an increase in the dI/dV at the threshold voltage Δ (see § 3.6). During this scattering process the total angular momentum needs to be preserved (§ 2.2.2).

The spin excitation is measurable only for an Mn atom on the oxide Al_2O_3 and in the presence of a finite magnetic field. When $B = 0$ T the levels are degenerate and no spin excitation is possible. The presence of the insulating layer is essential for observing the spin excitation in the dI/dV spectrum. Nowadays, spin excitations are predominantly observed in atoms adsorbed on thin insulating layers like Cu_2N and MgO [15, 16]. In such systems, the lifetimes typically range from a few tens of nanoseconds [17, 18] to 1 millisecond [19] for 3d atoms, while reaching up to 1 hour at 2.5 K for a 4f atom of Ho deposited on MgO [20]. However, when magnetic atoms are directly adsorbed on a metal substrate, the lifetime is very low. This results in increased spectral broadening, making it challenging to resolve excitations with precision on a metal surface. Khajetoorians *et al.* estimated a lifetime of 200 fs for spin excitations of a Fe atom on Cu(111), with step heights representing only 5% of the elastic conductance [21]. This reduction in lifetime is attributed to electron, from the metal substrate, scattered by the magnetic atom.

Spin excitations serve as a means to gather magnetic information from various spin systems, such as phthalocyanine molecules on an oxide [22] and in molecular multilayers [23], or magnetic impurities on semiconductors [24]. Moreover, interactions between spins in individual atomic-scale magnetic structures can be investigated by methodically assembling linear chains with the STM tip, one magnetic atom at a time [25].

2.2.2 Spin excitations of a nickelocene molecule

Throughout this thesis, the spin excitations of nickelocene (Nc) will play a central role. As shown in Fig. 2.5a, this molecule consists of a Ni atom sandwiched between two cyclopentadienyl rings (C_5H_5 or Cp rings). The d^8 configuration of the Ni atom results in an electronic structure of $(e_2)^4(a_1)^2(e_1)^2$, providing the molecule with a spin $S = 1$ as demonstrated by several studies conducted in the gas phase [26] or on powder samples [26, 27]. As a rule of thumb, half of the magnetic moment is carried by the Ni atom, while the two Cp rings carry the other half. Figures 2.5a-b illustrate how the electronic properties determine the energetically most favorable magnetic state of Nc. The molecule's geometry leads to a crystal field of symme-

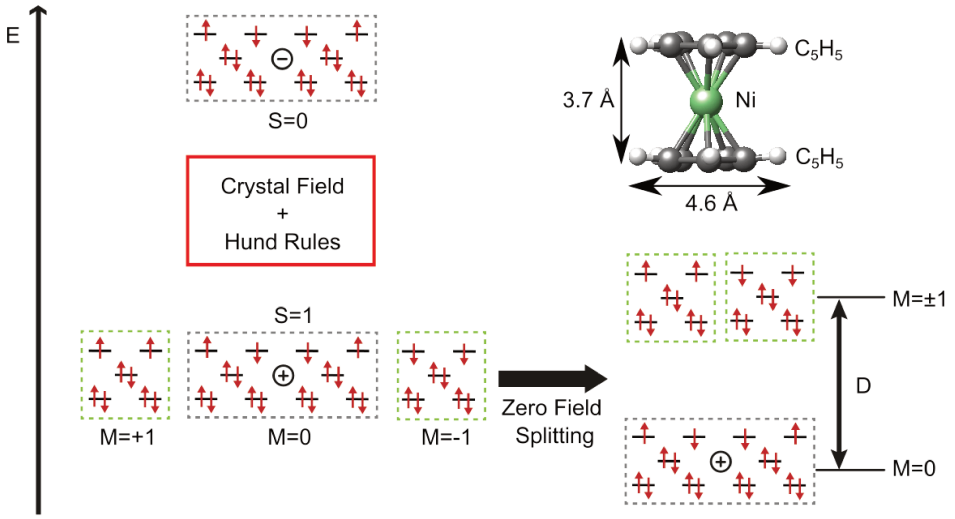

Figure 2.5: (a) Electronic d-manifold configuration of nickelocene yielding a ground state spin $S = 1$. (b) Structure of nickelocene (Ni: green, C: grey, H: white).

try D_{5h}, favoring a triplet state, specifically $|S = 1, M = 0\rangle$, $|S = 1, M = +1\rangle$, and $|S = 1, M = -1\rangle$, compared to the singlet state, which is higher in energy. Here, M represents the projection of S along the axis perpendicular to the Cp ring. Additionally, spin-orbit coupling results in a positive magneto-crystalline anisotropy D with an easy plane perpendicular to the principal molecular axis –the axis passing through the two Cp rings. This leads to a zero-field splitting of the ground state of Nc, $|S = 1, M = 0\rangle$, and the two-fold degenerate excited states $|S = 1, M = \pm 1\rangle$. In the absence of an external magnetic field, the molecule's spin Hamiltonian is:

$$\hat{H} = D\hat{S}_z^{\,2}. \tag{2.3}$$

Different studies have reported variations in D for free standing Nc. Baltzer *et al.* performed inelastic neutron scattering on Nc powder [27], either undiluted or doped into diamagnetic hosts, and found $D = 4.17$ meV. However, other groups measured $D = 3.17$ meV [26]. Figure 2.6a presents typical tunneling spectra of Nc we acquired on Cu(100). The second derivative of the current, d^2I/dV^2, recorded above Nc (solid black line) has a peak at 3.8 mV and a dip at the exact opposite bias. Similar to the spin excitation of a Mn atom, inelastic tunneling electrons exchange energy with the molecule, causing a spin excitation (Fig. 2.6b). As Nc is promoted to the two-fold degenerate excited state, the tunnel electron loses energy and must also flip its spin to preserve the total angular momentum. If the molecule is excited to $|M = 1\rangle$, the electrons flips from $m = +1/2$ to $m = -1/2$, while if the molecule is excited to $|M = -1\rangle$, the electrons flips from $m = -1/2$ to $m = +1/2$. In both cases, the electron loses an energy D. From the peak and dip positions we find a magnetic

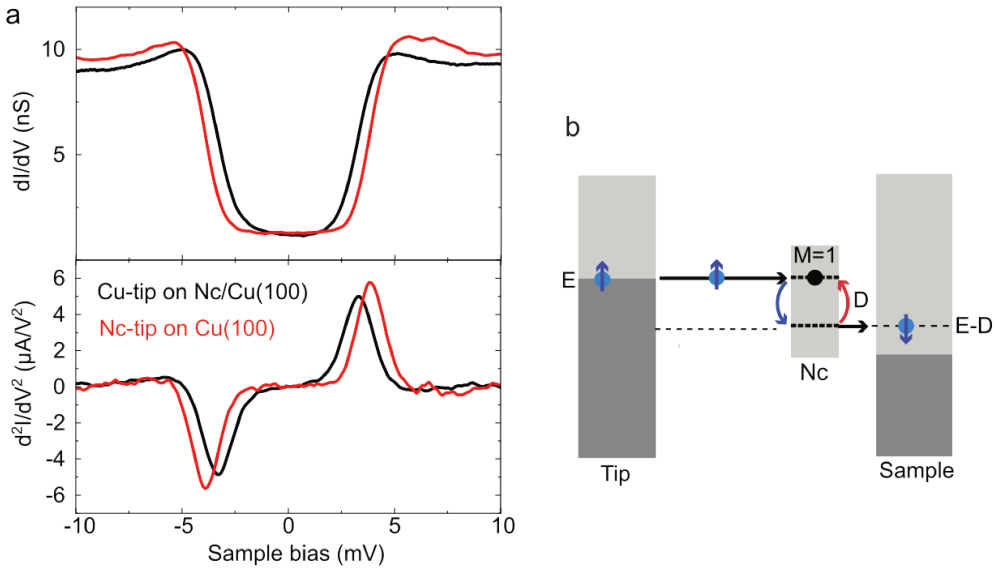

Figure 2.6: (a) dI/dV spectra and their derivative acquired with a Cu-tip over a Nc molecule (black line shape) and with a Nc-tip over the Cu(100) surface (red line shape). It's worth noting that the peak at positive bias and the dip at negative bias are features of the same event but with tunnel currents flowing in the opposite direction. (b) Sketch of a an electron tunneling inelastically in the junction tip/Nc/STM and inducing a spin excitation of Nc.

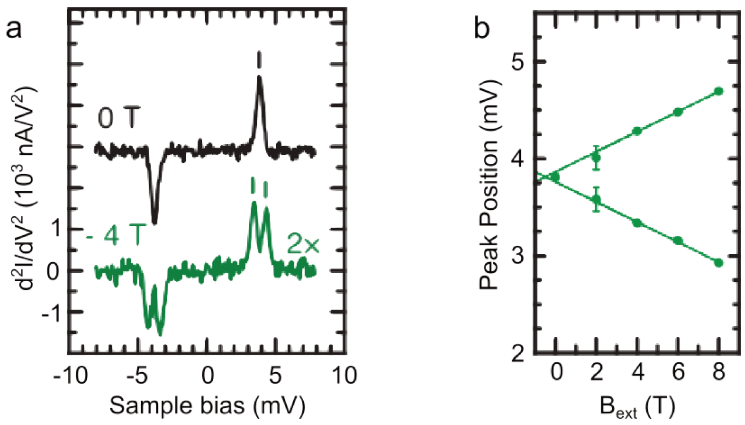

Figure 2.7: (a) Spectra d^2I/dV^2 acquired with a metal tip on Nc with and without external magnetic field B_{ext}. (b) Peak position from d^2I/dV^2 spectra with respect to B_{ext}. Adapted from [32].

anisotropy of $D = 3.3$ meV. It is important to note that unlike single atoms, Nc exhibits spin excitations while adsorbed on a metal surface, possibly owing this behavior to the cyclic π^* orbital of the Cp rings [28]. This is also the case for other molecules [29–31].

Czap *et al.* repeated the experiment with Nc adsorbed adsorbed on silver with a 4 T external magnetic field perpendicular to the surface [32], hence the new spin

Hamiltonian:

$$H = D\hat{S_z}^2 - g\mu_B \hat{S}_z B_{\text{ext}}. \tag{2.4}$$

They observed the peak/dip splitting into two new peaks/dips (solid green lines in Fig. 2.7a), corresponding to the spin excitations $|S = 1, M = 0\rangle \rightarrow |S = 1, M = +1\rangle$ and $|S = 1, M = 0\rangle \rightarrow |S = 1, M = -1\rangle$. Thanks to the energies of these spin excitations (Fig. 2.7b), they found a magnetic moment $\mu = g\mu_B = 1.89\mu_B$ for Nc on silver. A value slightly lower than for the free standing molecule where $\mu = 2\mu_B$. This difference is due to charge transfer between Nc and the surface.

2.2.3 Spin excitations of a nickelocene-terminated tip

Our group demonstrated that Nc can be attached to the apex of a STM tip [1, 33]. The process to attach the molecule is straightforward provided the tip is monoatomically sharp. On noble metal surfaces, it is sufficient to set the tunneling parameters to -1 mV and 50 pA, while carefully approaching the tip towards the molecule by a minimum of 200 pm. Once the molecule is on the tip, we then check that the molecular tip is reliable and robust. To do so, we sweep the tip toward the surface and concomitantly measure the junction conductance until it reaches the contact ($z = 0$), which is identified through a change in the slope of the trace (Fig. 2.8a) [34]. At contact, the center-to-center distance between the C atoms of the Cp ring and the Cu atoms is ≈ 250 pm [33]. The stability of the Nc-tip is assessed by recording point contact images of the copper surface [35]. This image acquisition consists of scanning at a conductance of approximately $2e^2/h$ in order to achieve a reproducible atomic resolution of the surface (Fig. 2.8b) [35]. Throughout these image acquisitions, the molecular tip remains intact, allowing the procedure to be repeated, resulting in reproducible atomic resolution of the surface.

Density functional theory (DFT) calculations were performed by modeling the molecular tip by a Nc atop a Cu atom adsorbed on a Cu(100) plane [33]. The molecular tip was placed at different distances from a Cu(100) surface and the junction was fully relaxed. The insets of Fig. 2.8a present the relaxed geometry for the tunnel (right inset) and contact (left inset) regimes. In the tunnel regime, the molecule is attached to the Cu apex-atom through two carbon atoms of the Cp ring, which results in the molecule tilting by 12° respect to the surface normal. At contact, the Cp rings are parallel to the surface and the Cu apex-atom is coordinated to five C atoms.

The tilt angle of Nc on the tip apex can be assessed experimentally by "counter imaging". This procedure consists in imaging an atom on the surface using a Nc-

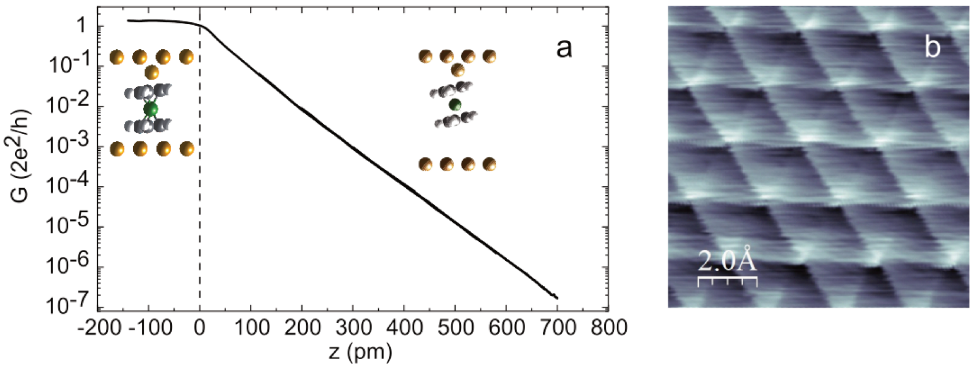

Figure 2.8: (a) Conductance versus tip-sample distance (feedback loop open at 50 pA, 50 mV). The trace was acquired atop an atom of the Cu(111) surface. The dashed black line corresponds to the contact point between the Nc-tip and the Cu surface. The insets present simulation of the adsorption of Nc on the tip in the tunneling and contact regimes. (b) Image of Cu(111) obtained by scanning with the Nc-tip in contact with the surface. The surface corrugation is visible.

tip. The resulting image is a ring (Fig. 2.9a), representing the bottom Cp ring of Nc adsorbed on the tip. This may be explained by remarking that the tunnel junction is just reverted compared to the usual tunneling conditions where a sharp metallic tip is used to image a Nc on the surface (Fig. 2.9b). From one case to the other, the current is flowing in the opposite direction. In Fig. 2.9a, the Cu atom has a brighter half which is the consequence of the tilt in the molecule adsorption on the tip mentioned previously. The appearance of nickelocene also changes when imaged with a Nc-tip. In Fig. 2.9c the molecules exhibit a bright center, indicating a protrusion rather than the typical donut shape observed with a metal tip (Fig. 2.9d). In chapter 6, we will employ STM theory to elucidate these observed differences. Most importantly, as shown in Fig. 2.6a, the spin excitations are preserved on when Nc is on the tip apex (solid red line). We find a magnetic anisotropy of $D = 3.8$ meV, which is larger than the magnetic anisotropy for Nc on the surface. We attributed this to an elongation of the molecule along its principal molecular axis [1].

We will show in this thesis that by monitoring the spin excitations of Nc it is possible to collect magnetic information from the sample such as the magnetization orientation, the spin polarization and the magnetic exchange coupling between the Nc-tip and the surface. We will extend the results from [2] to other magnetic surfaces with different spin orientations, either pristine or exposed to hydrogen, and to a magnetic molecule.

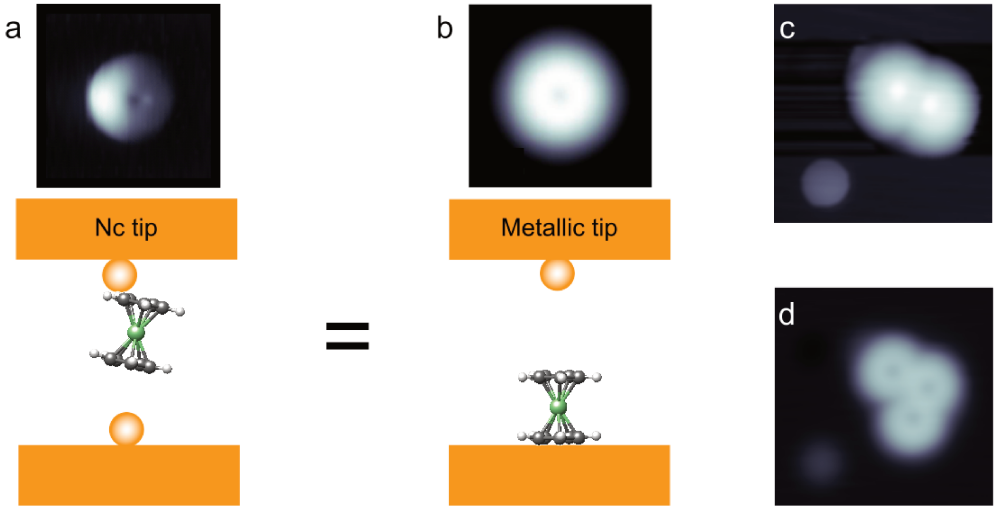

Figure 2.9: (a) Image of an adsorbed Cu atom on Cu(100) acquired with a Nc-tip (1.5×1.5 nm^2), along with a sketch of a Nc-tip scanning the Cu atom. (b) Image of a nickelocene imaged with a copper-terminated tip (2×2 nm^2), along with a sketch of a Cu-tip scanning a nickelocene adsorbed on a surface. (c) Nickelocene molecules on Cu(100) imaged with a Nc-tip. A Cu atom is present in the bottom left of the image. Same area as (d) imaged with a metallic tip, before picking up one of the Nc molecules.

2.3 Other spin-sensing techniques

Spin sensing with STM can also be achieved by taking advantage of three different phenomenons, namely electron spin resonance, Yu-Shiba-Rusinov states and the Kondo effect.

ESR-STM. To illustrate ESR-STM, we consider the pioneering study by Baumann *et al.* in 2015 [15]. A magnetic atom, Fe, is adsorbed on insulating MgO patches partially covering a silver substrate. A large magnetic field $\vec{B} = \vec{B_x} + \vec{B_z}$ is applied, where B_x is the component of B in the plane of the MgO surface, and B_z the component perpendicular to the surface such that $B_z < B_x$ (Fig. 2.10a). B_z splits the lowest energy states as $|0\rangle$ and $|1\rangle$. The role of the MgO surface is to increase the quantum coherence time of the Fe spin by preventing electrons from the substrate to scatter with the single atom. To this day, NaCl [37] and MgO are the only interstitial layers which can be used for ESR-STM experiments. To drive the spin excitation between the two states, a time-dependent radio-frequency RF electric field within the tunnel junction is employed. This is achieved by applying an RF voltage to the STM junction in addition to the DC bias voltage. When the frequency of this AC electric field matches the frequency of a spin excitation, the magnetic states become equally populated, causing the average magnetization orientation of the Fe

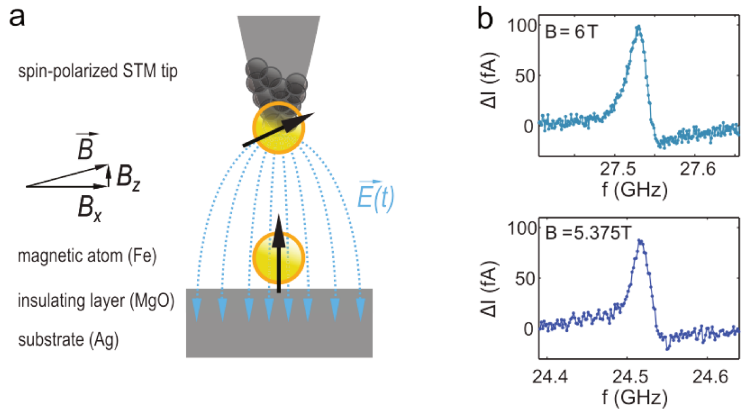

Figure 2.10: (a) Schematic model of the ESR technique: The spin polarized tip positioned on a Fe atom/MgO/Ag(001) immersed in an external field B. The black arrows represent their magnetic moments. The RF voltage within the junction creates a time-dependent electric field. (b) Two examples of ESR peaks when measuring at $B = 6$ T and $B = 5.375$ T. Adapted from [15].

atom on the surface to rotate. Another key ingredient of ESR measurement is the spin-polarized tip, which acts as a detector. Depending on the relative orientation between the magnetic moments of the tip and the Fe atom, the magneto-resistance effect modifies the tunneling current. To measure the ESR signal, the RF frequency is usually swept between 20 and 30 GHz, recently topping 60 GHz [38]. As seen in Fig. 2.10b, ΔI represents the difference between the tunneling current with and without the RF voltage at a given frequency. A peak appears at the resonant frequency with an intensity reaching 100 fA. Depending on the value of the external B, the Zeeman splitting changes, and the resonant frequency shifts.

Yang *et al.* compared the energy scales for spin excitation spectroscopy and ESR measurements on a Ti atom adsorbed on MgO/Ag(001) (Fig.2.11) [36]. ESR-STM demonstrates an impressive energy resolution of 0.1 μeV, corresponding to a millitesla field. For spin excitation spectroscopy, they evaluated a resolution of 0.28 meV, accounting for thermal broadening, given that their STM operates at 0.6 K. The ESR technique is thus capable of sensing the spin of a target atom placed laterally away from the tip [39]. At a recent conference ("Spin on Surfaces", September 2023), T. Esat *et al.* showed that a tip terminated by a nearly-freestanding molecule of PTCDA could produce an ESR resonance. Ideally, having the ESR signal on the tip rather than on the surface is a significant advantage, as it would broaden the technique's applicability to all surface-supported magnetic systems, similar to the Nc-tip but with higher energy resolution.

Yu-Shiba-Rusinov states. The STM is capable of detecting perturbations of the

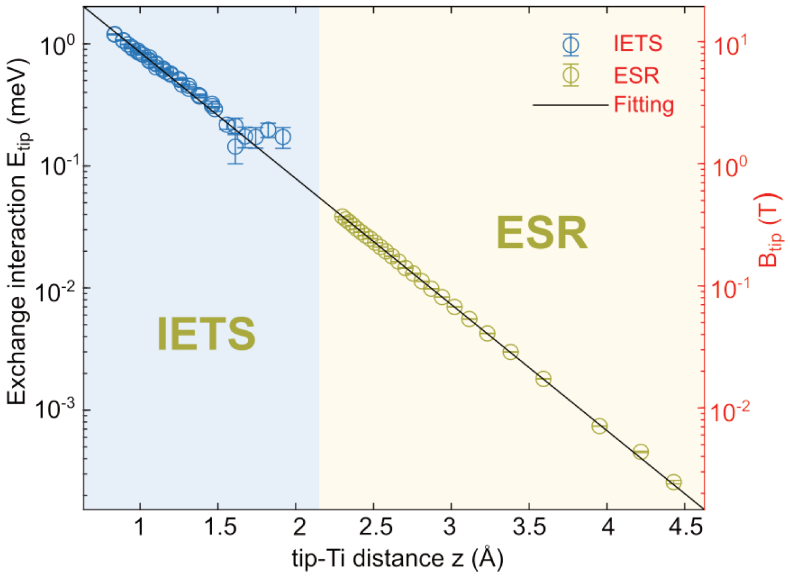

Figure 2.11: Exchange interaction, E_{tip}, and B_{tip} with respect to tip-Ti distance (log scale on y axes), measured with spin excitation spectroscopy (blue circles) and with ESR (green circles). The solid line is an exponential fit. Adapted from [36].

superconducting state at the atomic scale in the vicinity of magnetic impurities [40]. When adsorbed on the superconducting surface, or even below it, magnetic impurities locally perturb the Cooper pairs. They localize bound states also known as Yu-Shiba-Rusinov (YSR) states, which appear as peaks at opposite biases within the superconducting gap in the dI/dV measurements. These states are 100% spin-polarized subgap resonances. Interestingly, a superconducting tip can be functionalized with a magnetic impurity to yield on-tip YSR states [41] and used to perform spin-polarized measurements with increased spin sensitivity [42].

Kondo effect. Another phenomenon caused by magnetic impurities adsorbed on a metallic surface is the Kondo effect [43, 44]. The spin of the impurity is screened by the conduction electrons of the metal leading to a virtual state, which manifests in the dI/dV as a peak at zero bias. The Kondo effect can also be produced on the STM tip in a controlled way by functionalizing the tip apex with the spin $-1/2$ cobaltocene molecule ($CoCp_2$) [45]. In a similar fashion of the Nc tip, a Kondo tip can collect magnetic information of objects by monitoring the Kondo resonance.

CHAPTER 3

Scanning Tunneling Microscopy

The scanning tunneling microscope (STM), invented in 1981, marked a groundbreaking achievement in nanoscience. The key figures behind this invention, Binnig, Rohrer, Gerber, and Weibel, were honored with the Nobel Prize in 1986. The STM serves as a powerful tool for characterizing surfaces with a resolution down to the nanometer and even atomic scale in some cases. This is achieved by bringing a metallic tip within several angstroms of the sample's surface. By applying a bias voltage between the tip and the sample, a current flows across the vacuum gap, its amplitude depending on the tip-surface distance. Thanks to a feedback loop, the tip scans the surface at a constant current, and its vertical movements produce a topographic map of the surface. In addition to surface imaging, the STM enables the spectroscopic analysis of nanoscale objects. Notably, it allows accessing the surface density of states as well as the excited states of single atoms and molecules. This chapter begins by explaining the tunneling effect. Following this, we move to the Bardeen, Tersoff-Hamann and Wentzel–Kramers–Brillouin (WKB) theories, which provide a mathematical description of the current in a tunneling junction. Subsequently, we elaborate on how to image a surface and introduce scanning tunneling spectroscopy, as well as inelastic electron spectroscopy. Finally, we provide details about our experimental setup and the data acquisition process.

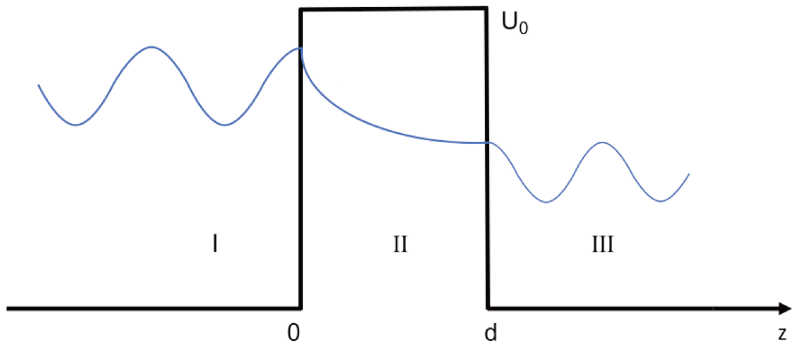

Figure 3.1: Sketch of the one dimensional tunnel barrier $U(z)$. The blue line represents the wave functions within the different areas.

3.1 The concept of tunneling

In classical physics, an electron confined within a potential energy field $U(\vec{r})$ is restricted to regions where its total energy E is greater than $U(\vec{r})$. However, in quantum mechanics, the behavior of this electron is governed by the Schrödinger equation:

$$-\frac{\hbar^2}{2m}\frac{d^2}{dz^2}\psi(z) + U(z)\psi(z) = E\psi(z), \tag{3.1}$$

where m is the mass of the electron. The eigenstates are wave functions related to the probability to find the electron at a defined position. Within this quantum framework, an electron possesses the ability to tunnel through a barrier potential even when $E < U$. To exemplify it, we considered a one dimensional potential scenario as in Fig. 3.1. In regions I ($z < 0$) and III ($z > d$) $U = 0$, and the region II ($0 < z < d$) represents the potential barrier where $U = U_0$. As detailed in [46], we solve the Schrodinger equation and derive the following solutions associated to each area:

$$\begin{aligned} \psi_{\mathrm{I}} &= A_1 e^{ik_1 z} + A_1' e^{-ik_1 z}, \\ \psi_{\mathrm{II}} &= A_2 e^{\rho_2 z} + A_2' e^{-\rho_2 z}, \\ \psi_{\mathrm{III}} &= A_3 e^{ik_1 z} + A_3' e^{-ik_1 z}, \end{aligned} \tag{3.2}$$

where $k_1 = \sqrt{2mE/\hbar^2}$ and $\rho_2 = \sqrt{2m(U_0 - E)/\hbar^2}$. First, we focus on the existence of a solution within the classically forbidden region II. This particular eigenstate manifests as an evanescent wave. Subsequently, we calculate the reflection and transmission coefficients across the barrier. In order to achieve this, we formulate the ratios of amplitudes A_1'/A_1, A_3/A_1. Given that, the incident electron originates from $z = -\infty$ and encounters no potential at the extreme right, A_3' is set to 0. The wave functions are continuous at $z = 0$ and $z = d$, thus $\psi_{\mathrm{I}}(0) = \psi_{\mathrm{II}}(0)$, $\psi_{\mathrm{I}}'(0) = \psi_{\mathrm{II}}'(0)$

as well as $\psi_{\mathrm{II}}(d) = \psi_{\mathrm{III}}(d)$, $\psi'_{\mathrm{II}}(d) = \psi'_{\mathrm{III}}(d)$. Utilizing these conditions, we express A'_1 and A_1 with respect to A_3.

$$\begin{aligned} A_1 &= \left[\cosh(\rho_2 d) - i\frac{k_1^2 - \rho_2^2}{2k_1\rho_2}\sinh(\rho_2 d)\right] e^{ik_1 d} A_3, \\ A_1^{'} &= -i\frac{\rho_2^2 + k_1^2}{k_1\rho_2}\sinh(\rho_2 d) e^{ik_1 d} A_3. \end{aligned} \tag{3.3}$$

The final expression of the transmission coefficient is :

$$T = \left|\frac{A_3}{A_1}\right|^2 = \frac{4E(U_0 - E)}{4E(U_0 - E) + U_0^2 \sinh^2\left[\sqrt{2m(U_0 - E)}d/\hbar\right]}, \tag{3.4}$$

and the reflection coefficient is $R = \left|A'_1/A_1\right|^2 = 1 - T$. The evanescent wave within area II has a penetration depth of:

$$\frac{1}{\rho_2} \simeq \frac{1.96}{\sqrt{U_0 - E}}\,\text{Å}, \tag{3.5}$$

where the energy unit is expressed in electron-volts. For a higher probability to tunnel through the barrier, the condition $d \lesssim 1/\rho_2$ should be satisfied. With typical values of $E = 100$ meV, a barrier potential $U_0 = 4$ eV, which is the typical work function of a metal, the distance d to have a decent probability to tunnel through the barrier should be of order 1 Å. On the other hand, if the barrier is wide such that $\rho_2 d \gg 1$, the transmission coefficient is exponentially decreasing with respect to d:

$$T \simeq \frac{16E(U_0 - E)}{U_0^2}\exp(-2\rho_2 d), \tag{3.6}$$

quickly dropping to zero within a few angstroms. Although this model is overly simplistic for describing realistic STM experiments, it does elucidate the high sensitivity to height changes in the sample topography. Additionally, it demonstrates that during tunneling, the atom of the tip closest to the substrate is the primary atom involved in the tunneling process.

3.2 Bardeen's theory

The Bardeen model, named after physicist J. Bardeen, is used to describe the transport of charge carriers [47], typically electrons. This model is based on the semi-classical Boltzmann transport equation, which considers both classical and quantum mechanical effects. It provides a broad understanding of carrier transport and tunneling phenomenon occurring between two electrodes brought into close proximity.

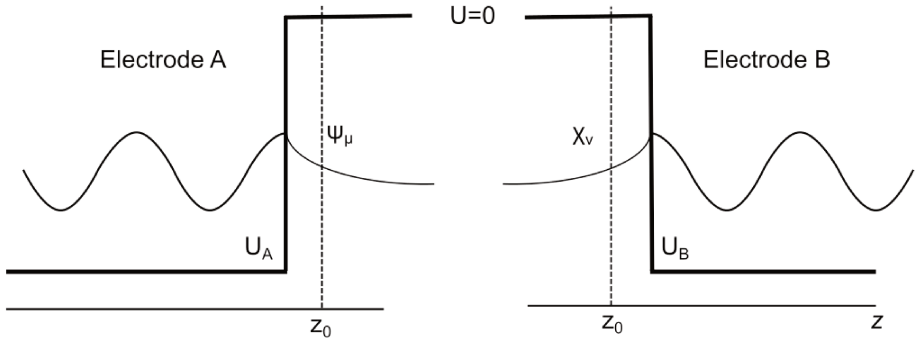

Figure 3.2: One dimensional sketch of the electrode A and B far away and their respective wave functions ψ_μ and χ_ν.

Initially we address the problem employing one dimensional electrodes. Afterwards, we generalize our results to the STM tip and a sample considering them as electrodes in three dimensions.

3.2.1 One dimensional case

We consider an electrode A characterized by a potential function U_A (Fig. 3.2). The associated wave functions is a solution to the time dependent Schrödinger's equation :

$$i\hbar\frac{\partial\Psi}{\partial t} = \left[-\frac{\hbar^2}{2m}\frac{\partial^2}{\partial z^2} + U_A\right]\Psi, \tag{3.7}$$

$\Psi(\mathbf{r},t)$ are the eigen states :

$$\Psi = \psi_\mu e^{-iE_\mu t/\hbar}, \tag{3.8}$$

where ψ_μ depends only on spatial coordinates such that :

$$\left[-\frac{\hbar^2}{2m}\frac{\partial^2}{\partial z^2} + U_A\right]\psi_\mu = E_\mu\psi_\mu. \tag{3.9}$$

For electrode B, characterized by a potential U_B, the stationary states

$$\Psi = \chi_\nu e^{-iE_\nu t/\hbar}, \tag{3.10}$$

adhere to the time dependent Schrödinger's equation :

$$i\hbar\frac{\partial\Psi}{\partial t} = \left[-\frac{\hbar^2}{2m}\frac{\partial^2}{\partial z^2} + U_B\right]\Psi, \tag{3.11}$$

with χ_ν, the spatial wave functions satisfying :

$$\left[-\frac{\hbar^2}{2m}\frac{\partial^2}{\partial z^2} + U_B\right]\chi_\nu = E_\nu\chi_\nu. \tag{3.12}$$

The wave functions ψ_μ and χ_ν decay into the vacuum region between electrodes A and B. As the two electrodes are brought together at z_0, the Schrödinger equation describing the system becomes:

$$i\hbar\frac{\partial\Psi}{\partial t} = \left[-\frac{\hbar^2}{2m}\frac{\partial^2}{\partial z^2} + U_A + U_B\right]\Psi. \tag{3.13}$$

If the two potentials U_A, U_B do not overlap with respect to the coordinate z, the solution of the new Schrödinger's equation is written as [48]:

$$\Psi = \psi_\mu e^{-iE_\mu t/\hbar} + \sum_{\nu=1}^{\infty} c_\nu(t)\chi_\nu e^{-iE_\nu t/\hbar}, \tag{3.14}$$

since $\Psi(t=0) = \psi_\mu$, $c_\nu(0) = 0$. Each set of wave functions ψ_μ and χ_ν are not solutions of the Hamiltonian in Eq. 3.13. Moreover, Bardeen's theory assumes that $\langle\psi_\mu|\chi_\nu\rangle \cong 0$. Substituting Ψ in Eq. 3.13 leads to:

$$i\hbar\sum_{\nu=1}^{\infty}\frac{dc_\nu(t)}{dt}\chi_\nu e^{-iE_\nu t/\hbar} = U_B\psi_\mu e^{-iE_\mu t/\hbar} + U_A\sum_{\lambda=1}^{\infty}c_\lambda(t)\chi_\lambda e^{-iE_\lambda t/\hbar}. \tag{3.15}$$

We neglect the second term on the right-hand side as it constitutes a second-order infinitesimal quantity and restrain the following calculation to the first order. We multiply Eq. 3.15 by the term $\chi_\nu^* e^{iE_\nu t/\hbar}$ and integrate over $z > z_0$ where U_B is non zero:

$$i\hbar\frac{dc_\nu(t)}{dt} = \int_{z>z_0}\psi_\mu U_B\chi_\nu^* d^3\mathbf{r}e^{-i(E_\mu - E_\nu)t/\hbar}. \tag{3.16}$$

From this relation it is then possible to express the tunneling current.

3.2.2 Tunneling current

To accomplish this, we begin by expressing the amplitude of the ν-th state of electrode B by integrating over time the Eq. 3.16 and substituting U_B by using Eq. 3.11 and Eq. 3.12:

$$c_\nu(t) = M_{\mu\nu}\frac{e^{-i(E_\mu - E_\nu)t/\hbar} - 1}{E_\mu - E_\nu}, \tag{3.17}$$

where:

$$M_{\mu\nu} = \frac{\hbar^2}{2m} \int_{\Omega_t} \left(\chi_\nu^* \nabla^2 \psi_\mu - \psi_\mu \nabla^2 \chi_\nu^* \right) d^3\mathbf{r}. \tag{3.18}$$

The integral is over Ω_t a subspace containing the free tip considered as electrode B. Subsequently, the square of this amplitude yields the probability of the μ-th state in the sample (electrode A) transitioning into a ν-th state in the tip at the time t:

$$P_{\mu\nu} \equiv |c_\nu(t)|^2 = |M_{\mu\nu}|^2 \, \frac{4 \sin^2 \left[(E_\mu - E_\nu) t / 2\hbar \right]}{(E_\mu - E_\nu)^2}, \tag{3.19}$$

if the time of tunneling is $t \gg 2\hbar/(E_\mu - E_\nu)$

$$\frac{2\hbar \sin^2 \left[(E_\mu - E_\nu) t / 2\hbar \right]}{\pi t (E_\mu - E_\nu)^2} = \delta(E_\mu - E_\nu). \tag{3.20}$$

Thus the probability can be written as

$$P_{\mu\nu}(t) = \frac{2\pi}{\hbar} \left| M_{\mu\nu} \right|^2 \delta(E_\mu - E_\nu) t. \tag{3.21}$$

The delta function implies that the tunneling current is elastic, meaning that $E_\mu = E_\nu$. By deriving the probability with respect to time, we obtain the transition rate:

$$\gamma_{\mu\nu} = \frac{2\pi}{\hbar} \left| M_{\mu\nu} \right|^2 \delta(E_\mu - E_\nu). \tag{3.22}$$

Naturally, an electron can only tunnel from an occupied state to an unoccupied state. At zero temperature, there is a sharp Fermi edge separating occupied and unoccupied states, while at elevated temperatures, the Fermi edge is smeared out; occupied states are then described by the Fermi-Dirac distribution:
$f(E) = (\exp\left[(E - E_F)/k_\mathrm{B}T\right] + 1)^{-1}$, while unoccupied states are described by $1 - f$. Accounting for the occupation in this manner and assuming a bias voltage V, Eq. 3.22 becomes:

$$\gamma_{\mu\nu}^{s \to t} = \frac{2\pi}{\hbar} \left| M_{\mu\nu} \right|^2 \delta(E_\mu - E_\nu - eV) f(E_\mu)[1 - f(E_\nu)], \tag{3.23}$$

while the transition rate of a tip state transferring to a sample state is:

$$\gamma_{\nu\mu}^{t \to s} = \frac{2\pi}{\hbar} \left| M_{\nu\mu} \right|^2 \delta(E_\mu - E_\nu - eV) f(E_\nu)[1 - f(E_\mu)]. \tag{3.24}$$

Up to now we have considered the tunneling process involving a single state μ to a single state ν. However the tip and sample are characterized by a continuous spectrum of states, thus we have to consider all states μ and ν. To obtain the expression of the tunneling current, we multiply the rates by e, the electron charge,

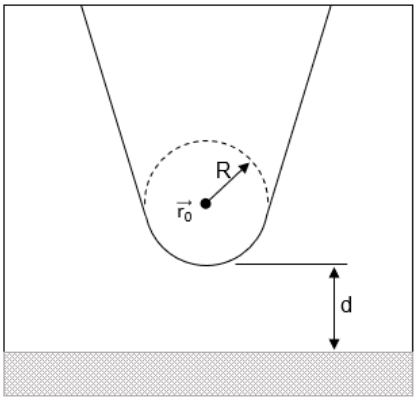

Figure 3.3: Sketch of the spherical tip apex above a flat surface. Adapted from [49].

and sum over all the tip and sample states to obtain the expression of the tunnel current:

$$\begin{aligned} I &= \sum_{\mu\nu} e(\gamma_{\mu\nu}^{s\to t} - \gamma_{\nu\mu}^{t\to s}), \\ I &= \frac{2\pi e}{\hbar} \sum_{\mu\nu} |M_{\mu\nu}|^2 \, \delta(E_\mu - E_\nu - eV)[f(E_\mu) - f(E_\nu)], \end{aligned} \tag{3.25}$$

where we assume that $M_{\nu\mu} = M_{\mu\nu}^*$. Equation 3.25 will serve as the starting point for the Tersoff-Hamann and WKB theories presented hereafter.

3.3 The Tersoff-Hamann model

In Bardeen's theory, the computation of the tunneling matrix elements can be demanding. Tersoff and Hamann facilitate this step by describing the STM tip by a spherical wave [49]. This approximation provides a relatively simple and computationally efficient method for analyzing tunneling phenomena near surfaces. It allows for quantitative analysis of STM measurements, enabling the extraction of surface properties and atomic-scale features. Due to its effectiveness and versatility, it is widely used in surface science. The tip is modeled as a spherical potential with R representing the curvature radius of center position $\vec{r_0}$ and d denoting the distance between the surface and the tip apex (Fig. 3.3). The sample wave function will be denoted as ψ_μ with μ the μ-th state, while the tip wave function is referred to as χ_ν. Taking Eq. 3.25 from Bardeen's theory, and under the experimental conditions of low voltage and low temperature, the tunneling current in the first order approximation is given by:

$$I = \frac{2\pi}{\hbar} e^2 V \sum_{\mu\nu} |M_{\mu\nu}|^2 \, \delta(E_\mu - E_F)\delta(E_\nu - E_F). \tag{3.26}$$

An important assumption in the Tersoff-Hamann theory is the local modeling of the tip as a spherical potential, thereby implying that χ_ν takes the form of a spherical wave:

$$\chi_\nu = C \frac{\exp\left(-\kappa \left|\vec{r} - \vec{r_0}\right|\right)}{\kappa \left|\vec{r} - \vec{r_0}\right|}, \tag{3.27}$$

where C represents a constant, $\kappa = \sqrt{2m\phi}/\hbar$, ϕ being the work function of the tip approximately equivalent to that of the surface. The surface and tip wave functions are expanded, as detailed in [49], and subsequently inserted into in Eq. 3.18 to calculate the tunneling matrix elements and find $M_{\mu\nu} \propto \psi_\mu(\vec{r_0})$. Finally, the tunneling current is determined as:

$$I \propto V \rho_t(E_F) \sum_{\mu} |\psi_\mu(\vec{r_0})|^2 \, \delta(E_s - E_F), \tag{3.28}$$

where ρ_t is the DOS per unit volume of the tip. The tunneling current depends on the DOS of the surface at the Fermi energy, measured at the tip position, given by:

$$\rho_s(\vec{r_0}, E) \equiv \sum_{\mu} |\psi_\mu(\vec{r_0})|^2 \, \delta(E_\mu - E). \tag{3.29}$$

This quantity is also known as the local DOS (LDOS). Furthermore, the current I exponentially diminishes with the distance d, as described by $|\psi_\mu(\vec{r_0})|^2 \propto \exp\left[-2\kappa(R+d)\right]$. These findings allowed for the computation of the corrugation of the 2×1 and 3×1 reconstruction of Au(110) resulting in an exceptional agreement with STM measurements of the same surface conducted by Binnig *et al.* [50]. In Chapter 6, we will investigate the magnetism and spin transport of an Nc molecule on a cobalt surface. We will show that the Tersoff-Hamann method can reproduce the STM images of the molecule, provided that the tip used is metallic. However, when the metallic tip is replaced by the Nc-tip, we will find that the approximation is no longer valid, and the Bardeen theory is then needed to correctly reproduce the images.

3.4 Imaging with the STM

Acquiring an STM image demands extremely precise motion control, facilitated by affixing the tip to a piezoelectric tube scanner, as depicted in Fig. 3.4. The

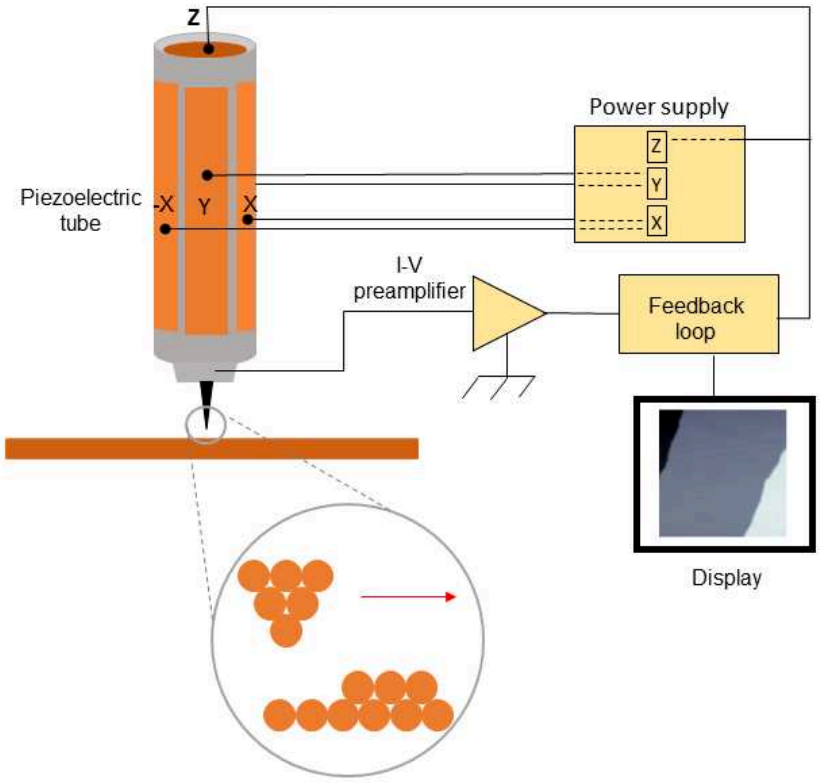

Figure 3.4: Sketch of the STM tip attached to the piezoelectric tube scanning a surface and the electronic set up.

tube, crafted from PZT, comprises four thin metal plates or quadrants on its outer surface, forming the $(\pm x)$ and $(\pm y)$ electrodes. The inner surface is similarly coated with metallic material, constituting the (z) electrode. To move in the y-direction, a voltage V is applied to the (y) electrode, while $-V$ is applied to the $(-y)$ electrodes. The voltage trigger an electric field-induced stress in opposite directions on each quadrant, resulting in the deflection of the tube in the y-direction. Alternating the voltage polarity at a finite frequency enables the tip to scan the surface. The piezoelectric tube covers distances spanning from the atomic scale to the micrometer range in the (x, y, z) directions. Additionally, it is essential to note the presence of a coarse piezoelectric mechanism that aids in moving the tip across larger distances, spanning several milimeters.

In the process of imaging, a bias voltage is applied between the sample and the tip, enabling the flow of a tunneling current. While scanning in constant current mode, the STM capitalizes on the current's sensitivity to the tip-surface distance.

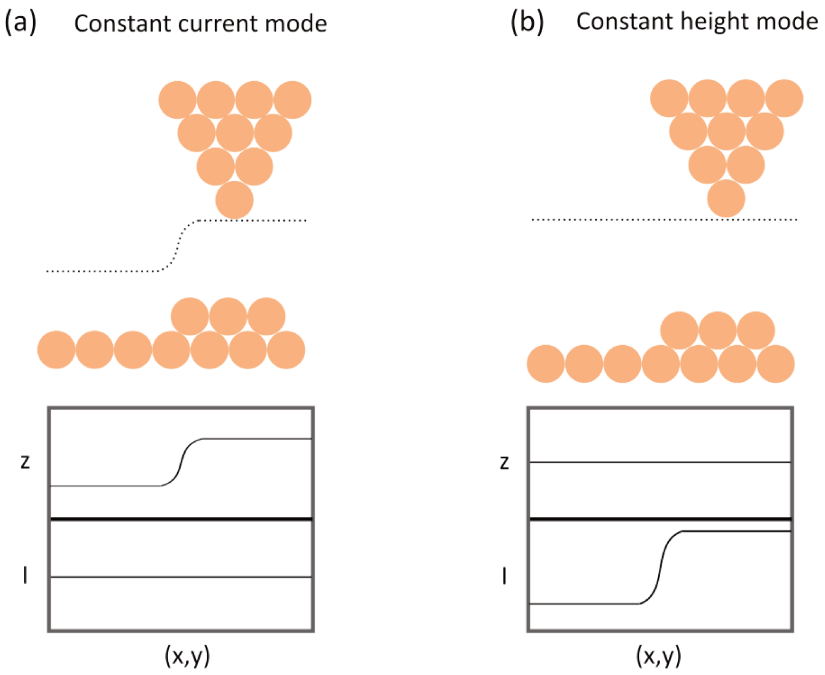

Figure 3.5: Sketch of a tip scanning an atomic step in (a) the constant current mode and (b) the constant height mode.

As shown in Fig. 3.4 a grounded pre-amplifier converts the current to a voltage at the tip location, the feedback loop compares this measurement to a previously designated current value I_0. Subsequently, the control unit (Nanonis Mimea BP4) adjusts the tip extension to maintain the tunneling current equal to I_0. As a result, the tip scans the sample while maintaining a constant vacuum gap, mirroring the surface corrugation as depicted in Fig. 3.5a. Conversely, in constant height mode (Fig. 3.5b), with the feedback loop turned off, the tip's vertical position remains unadjusted while scanning in the (x, y) plane. As illustrated in Fig. 3.5b only the current varies, yielding a so-called current image of the sample. It is important to note that the scanned surface should be flat, in the constant height mode, to prevent the tip crash. In addition, the sample should not be excessively insulating to permit electron tunneling. To obtain a clear image we make sure that the tip apex is sharp and mono-atomic by indenting the tip into a clean surface. Otherwise, the image may appear blurred, for example resulting in the imaging of a single adsorbed atom as multiple atoms.

3.5 WKB theory

The utilization of the WKB approximation aids in simplifying the expression of the tunneling current from Bardeen's theory, eliminating the need for tunneling matrix

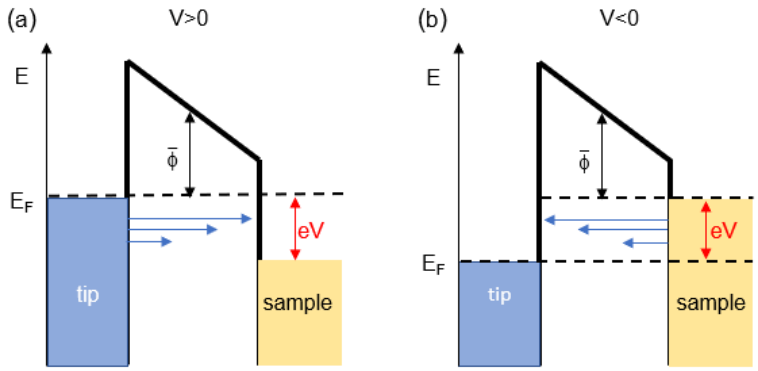

Figure 3.6: Sketch of the junction within the frame of the WKB theory for $V > 0$ (a) and $V < 0$ (b). The blue arrows show the direction of the current.

elements. This derivation, as elucidated in [51], leads to an expression particularly beneficial for a theoretical description of tunneling spectroscopy with a STM. We consider a junction composed of two planar electrodes (Fig. 3.6), namely the sample and the tip, separated by a distance z. To express the current, we replace the finite summation over the sample and tip discrete states in Eq. 3.25 by an integral over energies using the sample (ρ_s) and tip (ρ_t) DOS: $\sum \rightarrow \int \rho(E)dE$. After an appropriate change of variable we find

$$I(z,V) \propto \frac{2\pi e}{\hbar}\left(\frac{\hbar^2}{2m}\right)^2 \int_{-\infty}^{\infty} T(z,V,E)\left[f(E-eV)-f(E)\right]\rho_s(E)\rho_t(E-eV)dE. \tag{3.30}$$

The WKB approximation consists in assuming that the tunneling matrix element can be described by the transmission probability $T(z,V,E)$. For a trapezoidal barrier within the tunnel junction (Fig. 3.6), the transmission probability is approximately

$$T(z,V,E) = \exp\left[-2z\sqrt{\frac{2m}{\hbar^2}\left(\overline{\Phi}+\frac{eV}{2}-E\right)}\right], \tag{3.31}$$

where the electron momentum parallel to the electrodes surface is neglected. Here, $\overline{\Phi}$ represents the mean value of the tip and sample work functions. Under the condition where $k_BT \ll eV$ is satisfied, the Fermi-Dirac distributions can be approximated by step function and the expression of I simplifies further to:

$$I(z,V) \propto \frac{2\pi e}{\hbar}\left(\frac{\hbar^2}{2m}\right)^2 \int_{0}^{eV} T(z,V,E)\rho_s(E)\rho_t(E-eV)dE, \tag{3.32}$$

which is an expression more amenable for describing tunneling spectroscopy.

3.6 Tunneling spectroscopy

Elastic tunneling. Scanning tunneling spectroscopy experiments are aimed at probing the DOS of a sample. As the tunneling current contains information about both the sample and the tip DOS, one can calculate the derivative with respect to V to deconvolute the sample DOS as derived in [51]:

$$\begin{aligned}\frac{dI(z,V)}{dV} \cong A[&eT(z,V,E)\rho_s(E)\rho_t(E-eV)|_{E=eV} \\ &+ \int_0^{eV} T(z,V,E)\rho_s(E)\frac{d\rho_t(E-eV)}{dV}dE \\ &+ \int_0^{eV} \frac{dT(z,V,E)}{dV}\rho_s(E)\rho_t(E-eV)dE], \quad (3.33)\end{aligned}$$

where A represents a proportionality coefficient related to the effective tip-surface contact area. According to the approximation outlined in [51], only the first term remains in Eq. 3.33 since ρ_t is considered constant. Concerning the third term, at sufficiently low bias, the transmission probability shows minimal variation. Consequently, this leads to the final expression of the conductance:

$$\frac{dI}{dV}(z,V) \propto \rho_s(eV)T(z,eV,V). \quad (3.34)$$

Thus, the surface DOS can be probed through the measurement of a dI/dV. This expression, however, oversimplifies the tunneling process, as it disregards the influence of the atomic orbitals of both the tip and sample. The orbitals decay differently into vacuum, with some being less favorable to the tunneling process (*e.g.*, in-plane orbitals such as p_x, p_y, d_{x2-y2}) compared to others (s, p_z, d_z). As a result, the dI/dV signal may differ from the surface DOS at a given distance z due to the weighting of these orbitals in the tunneling process. By expanding the method to incorporate a simple orbital-dependent electron tunneling transmission, more accurate results can be obtained, showing a reasonable agreement with Bardeen-based calculations [52].

Inelastic tunneling. Up to this point, we have focused on elastic tunneling, where the energy of the tunneling electrons remains constant. However, introducing a single object (atom, molecule) into the junction can allow tunneling electrons to exchange energy with it (Fig. 3.7). Through inelastic electron spectroscopy, known as IETS, electrically induced excitations can be detected within the object, such as spin transitions [13] or vibrational modes [14, 53]. An inelastic event occurs when the tunneling electron energy surpasses an energy threshold Δ representing

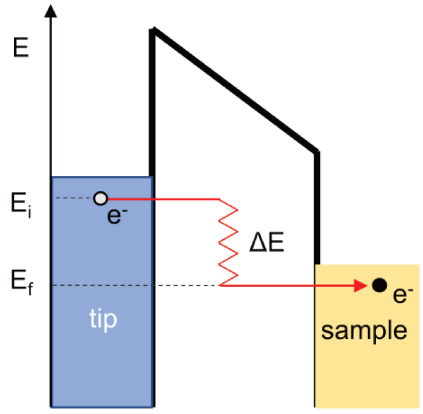

Figure 3.7: Sketch of an electron losing an energy ΔE while tunneling.

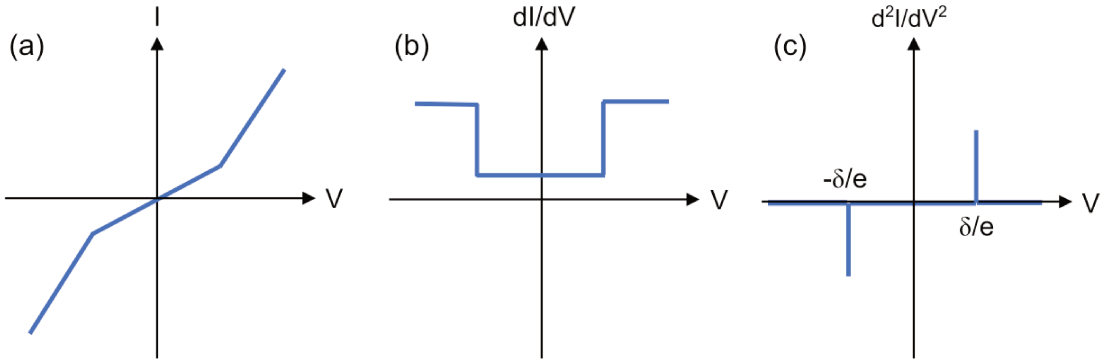

Figure 3.8: (a) Tunneling current with respect to bias voltage $I(V)$, (b) The conductance dI/dV, (c) Second derivative of the current with respect to V, d^2I/dV^2. Note that the peak (dip) are delta functions since the the steps in the conductance signal show no broadening.

the energy difference between the ground and excited states of the probed object. Figure 3.8a illustrates the signature of an inelastic event in an $I(V)$ curve obtained while sweeping the bias. As shown, a change in slope occurs at V when $eV = \pm\Delta$. This shift signifies the opening of a new tunneling channel, the inelastic tunneling channel, that enhances the junction's conductance. Consequently, the dI/dV signal exhibits steps at $\pm\Delta$ (Fig.3.8b), or a peak and a dip in d^2I/dV^2 at positive and negative bias, respectively (Fig.3.8c).

3.7 Lock-in detection

In STM, the differential conductance, dI/dV, is a key measurement. One possibility to acquire a dI/dV consists in measuring an $I(V)$ by sweeping the bias tension V and concomitantly measuring the current, and then deriving dI/dV numerically. However this leads to a low signal-to-noise ratio (Fig. 3.9). A more advantageous method

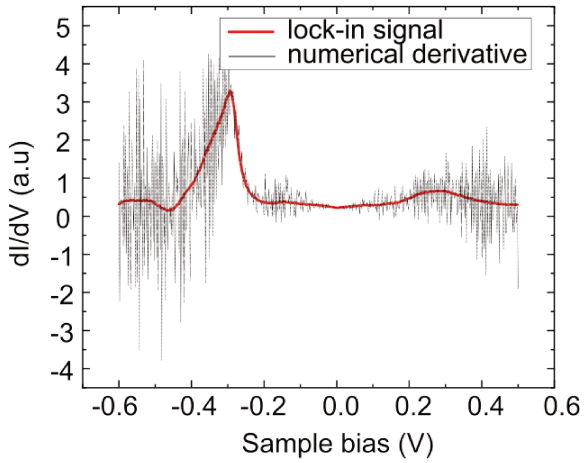

Figure 3.9: Numerical derivative of I versus dI/dV measured with a lock-in amplifier.

involves using a lock-in amplifier, which introduces a modulated signal $V_m \cos(\omega t+\theta)$ in addition to the bias voltage. The dI/dV is measured by remarking that the resulting current can be expanded using the Taylor series:

$$I[V + V_m \cos(\omega t + \theta)] = I(V) + \frac{dI(V)}{dV} V_m \cos(\omega t + \theta) + \frac{d^2I(V)}{2dV^2} V_m^2 \cos^2(\omega t + \theta) + \dots \tag{3.35}$$

where $V_m \ll V$. A phase sensitive detector multiplies the current in Eq. 3.35 by a reference signal $V' \cos(\omega_r t + \phi)$ to isolate and extract the dI/dV and the d^2I/dV^2 signals:

$$\left[\frac{dI}{dV}\right]_{\text{lock-in}} = \frac{V_m V'}{2} \frac{dI(V)}{dV} \{\cos[(\omega - \omega_r)t + \theta - \phi] + \cos[(\omega + \omega_r)t + \theta + \phi]\}, \tag{3.36}$$

and

$$\left[\frac{d^2I}{dV^2}\right]_{\text{lock-in}} = \frac{V_m^2 V'}{8} \frac{d^2I(V)}{dV^2} \{\cos[(2\omega + \omega_r)t + 2\theta + \phi] + \cos[(2\omega - \omega_r)t + 2\theta - \phi) + 2\cos(\omega_r t + \phi)]\}. \tag{3.37}$$

The discrepancy in phases θ and ϕ arises from the distinct electrical circuits through which the modulated current and reference signal pass. To extract dI/dV from Eq. 3.36, the frequency of the reference signal is set as $\omega_r = \omega$. Consequently, the first cosine function depends solely on the phases θ and ϕ, while the second cosine is frequency-dependent. By applying a low-pass filter, AC signals are eliminated,

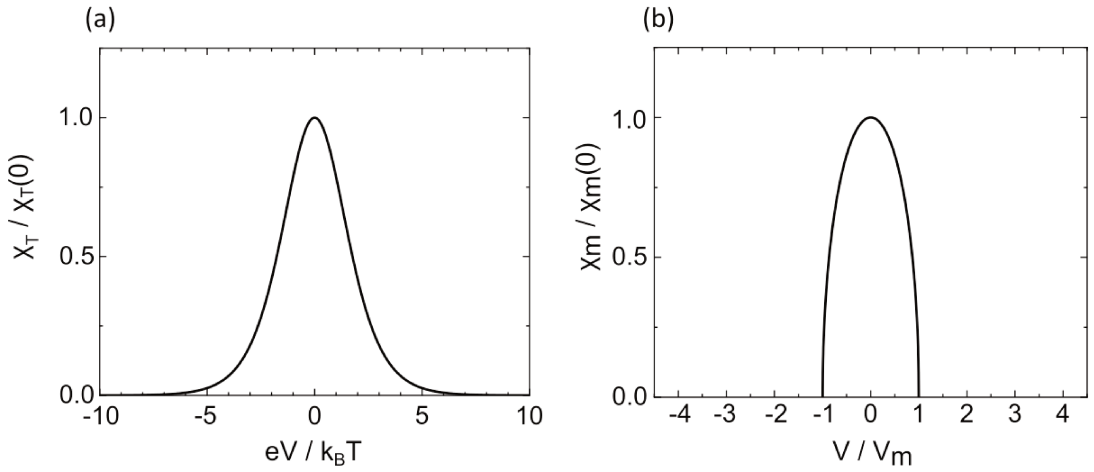

Figure 3.10: Smearing functions for elastic tunneling: (a) Thermal, (b) Lock-in.

thus yielding the dI/dV. Optimizing the phase ϕ maximizes the signal measured. Similarly, setting $\omega_r = 2\omega$ enables the retrieval of d^2I/dV^2. Notably ϕ varies with the used frequency and the pre-amplifier gain.

The selection of V_m must be done carefully. While a larger modulation amplitude enhances the signal-to-noise ratio, it also widens the line shape of our signal, as will discussed here below. Typical values we used range between $200 - 500$ μV rms for inelastic spectroscopy and $2 - 5$ mV rms for standard tunneling spectroscopy. Typical frequencies ranged between 700 Hz to 6.5 kHz. Utilizing a sufficiently large frequency modulation allows the lock-in to average more over the measured value during a given time, thereby enhancing the signal-to-noise ratio.

3.8 Line shape broadening

The line shape of the tunneling spectra is subject to broadening caused by temperature, lock-in modulation, and electromagnetic noise picked up by the cables connecting the microscope to its control unit. In the following section, we derive the line shape broadening for both elastic and inelastic tunneling spectroscopy. For a detailed description of electromagnetic-noise broadening, we refer the reader to [54]. Nonetheless, we will provide an estimate of this noise in our setup at the end of this section.

Elastic tunneling. Unlike our previous assumption, the non-zero temperature of our sample results in a smearing of the Fermi-Dirac distribution. Starting from the expression of the current derived from the WKB theory (Eq. 3.33), we can express the dI/dV by considering a constant transmission probability T and a constant tip

DOS ρ_t:

$$\frac{dI(V)}{dV} \propto \int_{-\infty}^{\infty} \rho_s(E) \frac{df(E-eV)}{dV} dE. \tag{3.38}$$

This expression can also be represented as a convolution product between ρ_s and a function χ_T:

$$\frac{dI(V)}{dV} \propto \int_{-\infty}^{\infty} \rho_s(E) \chi_T(eV - E) dE, \tag{3.39}$$

where $\chi_T(E)$ is the thermal smearing function that broadens the dI/dV signal (Fig. 3.10a):

$$\chi_T(E) = \chi_T(0)[\cosh(E/2k_\mathrm{B}T)]^{-2}, \tag{3.40}$$

where $\chi_T(0) = e/4k_\mathrm{B}T$. The thermal smearing function χ_T is responsible for broadening the dI/dV signal. The full width at half maximum (FWHM) is $\delta_T = 3.5k_\mathrm{B}T$.

The lock-in measurement, particularly the voltage modulation amplitude, introduces some smearing in spectroscopic measurements. This can be demonstrated by considering the first harmonic of the current resulting from the additional modulated bias, which is expressed as:

$$I_{1\omega}(V) = \frac{2}{\tau} \int_0^{\tau/2} I[V + V_m \cos(\omega t)] \cos(\omega t) dt. \tag{3.41}$$

$I_{1\omega}$ represents the differential conductance measured by the lock-in amplifier, $[dI/dV]_{\text{lock-in}}$, achieved by selecting the appropriate phase to maximize the signal. Upon substituting $V' = V_m \cos(\omega t)$ and integrating Eq. 3.41 by parts, we have:

$$\begin{aligned} \left[\frac{dI(V)}{dV}\right]_{\text{lock-in}} &= \int_{-\infty}^{\infty} \frac{dI}{dV}(V + V')\chi_m(V')dV', \\ &= \int_{-\infty}^{\infty} \frac{dI}{dV}(V')\chi_m(V' - V)dV', \\ &= \int_{-\infty}^{\infty} \frac{dI}{dV}(V')\chi_m(V - V')dV'. \end{aligned} \tag{3.42}$$

Consequently, the lock-in amplifier measures the convoluted differential conductance associated with a lock-in smearing function χ_m (Fig. 3.10b):

$$\begin{aligned} \chi_m(V') &= \chi_m(0) \frac{\sqrt{V_m^2 - V'^2}}{V_m}, \quad |V'| \leq V_m, \\ &= 0, \quad |V'| > V_m, \end{aligned}$$

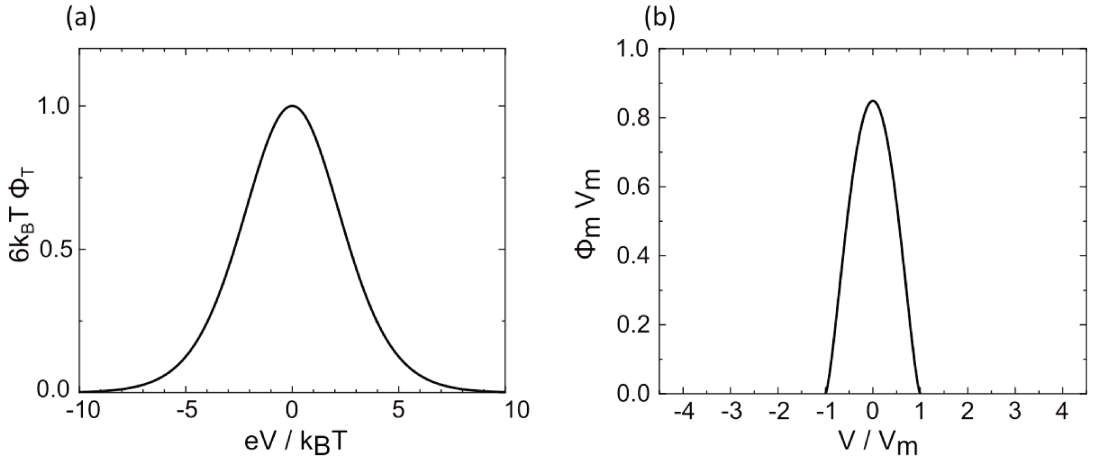

Figure 3.11: Smearing functions for inelastic tunneling: (a) Thermal, (b) Lock-in.

where $\chi_m(0) = 2/\pi$, and V_m denotes the modulation signal amplitude. The FWHM of this smearing function is $\delta_m = \sqrt{3}V_m$.

The differential conductance therefore results in a double convolution product involving the surface DOS convoluted with the thermal smearing function and the lock-in smearing function:

$$\left[\frac{dI}{dV}\right]_{\text{lock-in}} \propto (\rho_s * \chi_T) * \chi_m.$$

The energy resolution for elastic tunneling spectroscopy is then [55]:

$$\delta \approx \sqrt{\delta_T^2 + \delta_m^2}. \tag{3.43}$$

With our measurement conducted at $T = 2.4$ K and a modulation amplitude of $V_m = 200$ μV rms, our energy resolution is approximately 0.9 meV.

Inelastic tunneling. Similarly, it can be shown that the d^2I/dV^2 spectrum is convoluted by a smearing thermal function $\phi_T(E)$ [56]:

$$\phi_T(E) = \frac{1}{k_\mathrm{B}T} e^x \frac{(x-2)e^x + x + 2}{(e^x - 1)^3},$$

with $x = E/k_\mathrm{B}T$. The FWHM of ϕ_T is $\delta'_T = 5.4k_\mathrm{B}T$ (Fig. 3.11a). The smearing function resulting from V_m can also be expressed [56]. In this case, the measured second derivative becomes a convolution product between the exact value of d^2I/dV^2

and the smearing function ϕ_m (Fig. 3.11b):

$$\phi_m(V) = \frac{8e}{3\pi}\frac{(V_m^2 - V^2)^{3/2}}{V_m^4} \quad , \; |V| < V_m, \tag{3.44}$$

$$= 0 \; , \quad |V| > V_m. \tag{3.45}$$

The FWHM of ϕ_m is $\delta'_m = 1.22\ V_m$. As a result, the energy resolution for inelastic tunneling spectroscopy is approximately:

$$\delta' \approx \sqrt{\delta'^2_T + \delta'^2_m}. \tag{3.46}$$

With our measurement conducted at $T = 2.4$ K and a modulation amplitude of $V_m = 200\ \mu$V rms, our energy resolution is approximately 1.2 meV.

Estimating high-frequency noise. In Chapter 4, we will extensively use spin excitation spectroscopy to measure the magnetic properties of surfaces. These inelastic spectra can be accurately reproduced by a model calculation [57], which indicate an effective temperature $T^* = 3.4$ K for our system, whereas our working temperature is 2.4 K. The effective temperature of an experiment is always larger than its base temperature due to additional broadening effects. Along with modulation voltages and non-zero temperature as mentioned above, we may additionally include electromagnetic noise and lifetime broadening. The quantity $\delta'_{T^*} = 5.4 k_{\mathrm{B}} T^*$ therefore provides a rough estimate of the smearing for our inelastic tunneling spectra, which in our setup is 1.57 meV. We may also estimate the electromagnetic noise by inserting additional terms in Eq. 3.46:

$$\delta'_{T^*} = \sqrt{\delta'^2_T + \delta'^2_m + \delta'^2_{\mathrm{rf}} + \delta'^2_L}, \tag{3.47}$$

where δ'_{rf} quantifies the electromagnetic smearing and δ'_L quantifies the lifetime broadening. In Chapter 4, we will show that the typical lifetime for the Nc spin excitations is $\tau = 0.1$ ns, which, using the time-energy uncertainty relation, results in $\delta'_L = \hbar/(2\tau) = 3.3\ \mu$eV. Hence, a crude estimate for the electromagnetic broadening is $\delta'_{\mathrm{rf}} = 1$ meV.

3.9 Experimental setup

Our apparatus comprises two chambers, the preparation chamber where the sample is prepared and the so-called STM chamber. The two chambers are separated by a

gate valve and maintained at a pressure of approximately 10^{-10} mbar, corresponding to ultra-high vacuum (UHV) conditions. Both chambers include a turbo molecular pump connected to a scroll pump, and possess independent ion pumps. Furthermore, a load-lock chamber with its own turbomolecar pump allows for transferring tips, substrates, molecular powders from ambient air into the preparation chamber. During STM measurements, all pumps are turned off except for the ion pumps. Compressed air is utilized to suspend the chambers on dampers, isolating them from floor vibrations (< 10 Hz).

In the preparation chamber (Fig. 3.12a), the primary tasks involve sample cleaning using an Ar^+ ion sputtering gun. For cleaning the Cu surface we use an accelerating voltage of 3 kV and a gas pressure of $1.5\,10^{-6}$ mbar. Sample annealing is accomplished by passing current through a W wire beneath the sample stage (Fig. 3.12b). The emitted electrons are accelerated toward the sample via a high voltage (750 V) to bombard the sample and increase its temperature to a maximum of 700° C. Temperature monitoring occurs through a combination of a thermocouple positioned near the sample and a pyrometer placed outside of the chamber. For material deposition, the preparation chamber houses two electron beam evaporators, facilitating the deposition of materials like Fe or Co at room temperature. Sample manipulation is handled via a manipulator with storage caskets utilized for organized sample storage.

At low temperature, the STM chamber (Fig. 3.12c) operates under a pressure of $< 5 \times 10^{-11}$ mbar. A NEG pump helps limiting contamination from hydrogen. The STM system itself is a customized Omicron model designed to operate under low-temperature conditions, utilizing inner and outer cryostats. The inner one is filled with liquid helium (3.6 liters), while the outer one needs to be refilled with liquid nitrogen every 12 hours. The working temperature is maintained at 4.4 K for approximately 32 hours, after which a helium refill is necessary. Pumping the helium cryostat can temporarily lower the temperature to 2.4 K for 12 hours. The lower pressure attained compared to the preparation chamber is due to cryopumping from the cryostats. The STM sample stage, which is placed under the helium cryostat, can be suspended by three springs to dampen vertical motion. A set of radial magnets ensures, instead, lateral damping through eddy currents.

In terms of electromagnetic noise reduction strategies, efforts are made to minimize the pickup entering the STM. For this purpose, all cables used to drive the piezoelectric tube have 2 MHz low-pass filters. The bias cable is also low-pass filtered at 40 kHz. Additionally, a voltage divider, which is placed before the filters, allows for dividing the DC and AC biases by factors ranging from $N = 1$ to 500 for

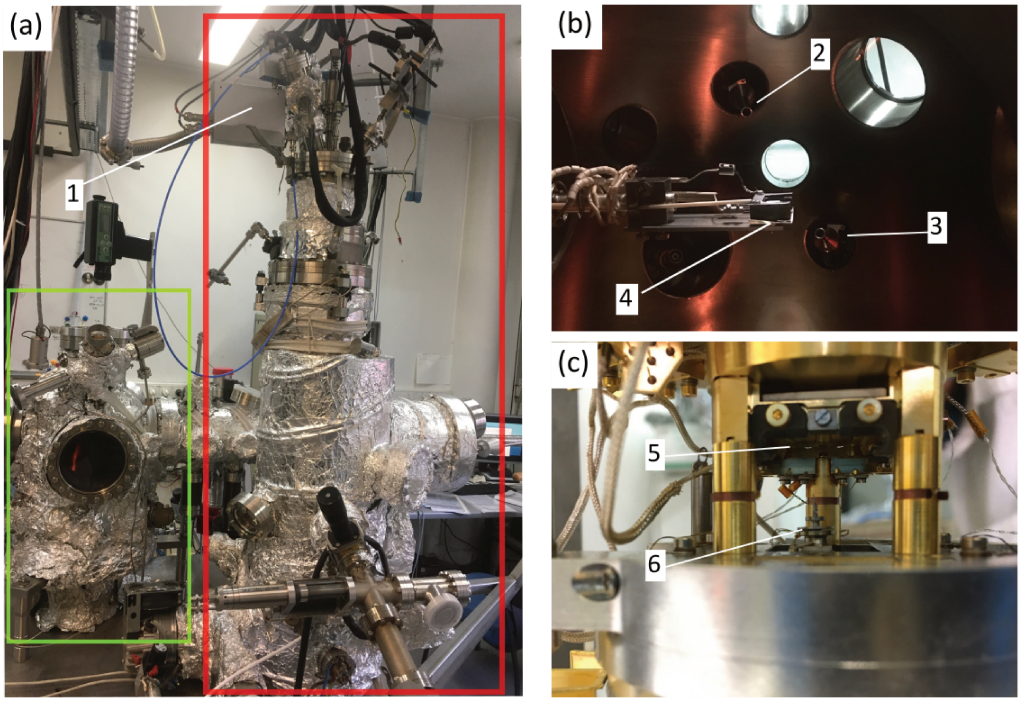

Figure 3.12: (a) The preparation chamber in green and the STM chamber in red, (1) indicates the filters and tension dividers box. (b) View inside the preparation chamber with the two evaporators of Co (2) and Fe (3). The sample is placed in (4) for the annealing and sputtering processes. (c) Photo of the STM. The sample is placed in (5) when being scanned by the tip (6).

the DC component and from $N = 100$ to 50000 for the AC component. This implies generating a signal $N \cdot S$ in the STM controller in order to anticipate the division by the divider. The idea is to improve the signal-to-noise ratio (SNR), which may be expressed as:

$$\mathrm{SNR} = \frac{N \cdot S}{\sqrt{(N \cdot B)^2 + (B')^2}}, \tag{3.48}$$

where B denotes the noise of the controller, which is also magnified by N, and B' represents the pickup noise along the cables. For inelastic measurements, we use $N = 10000$ for the AC bias; hence, the signal-to-noise ratio is governed by the STM controller as Eq. 3.48 reduces to $\mathrm{SNR} \approx S/B$. Without the voltage divider ($N = 1$), the SNR would decrease to $S/\sqrt{B^2 + B'^2}$.

3.10 Imaging with voxel (voxel imaging)

In order to probe the surface magnetism with a Nc-tip, we modified our acquisition setup in order to record voxels. The term voxel is derived from volume and pixel. In medical imaging, computer graphics, and other fields dealing with 3D data, voxels

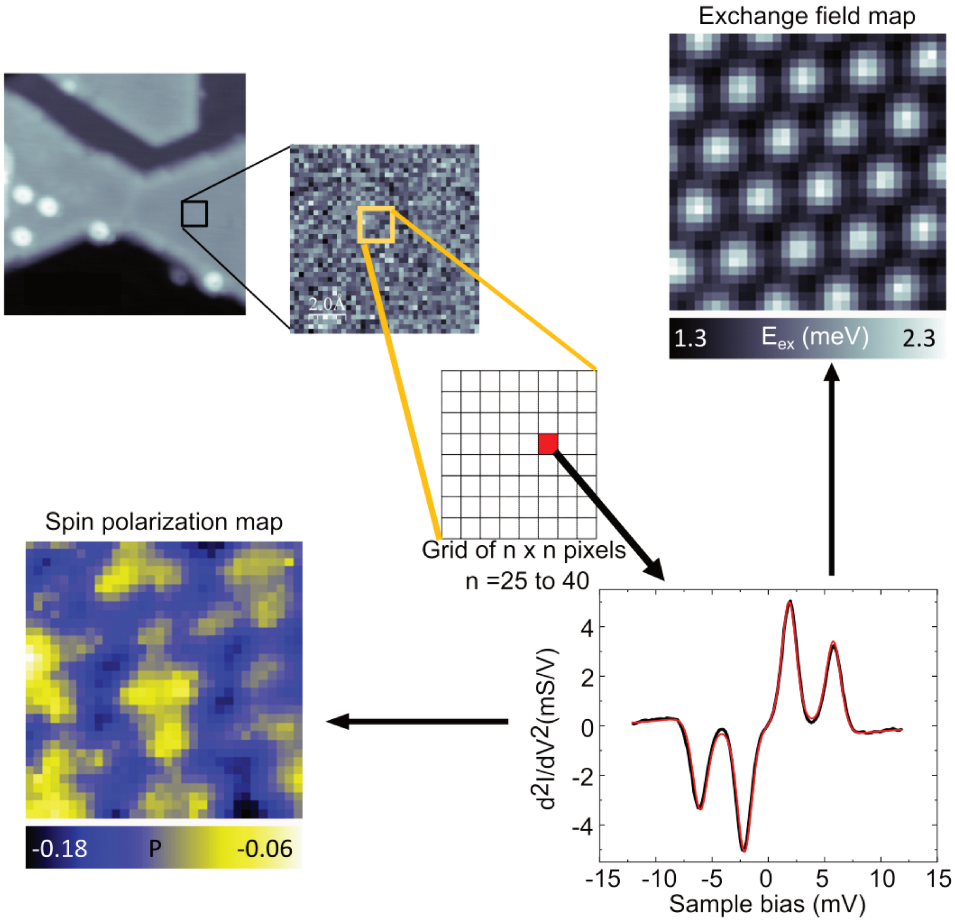

Figure 3.13: The panels sketch the acquisition of a voxel map. A grid with $n \times n$ pixels is placed on a surface. A d^2I/dV^2 spectrum is acquired at each pixel. Herein, the black line shape is the raw data and the red line shape is a fit. Magnetic information is then extracted from each spectrum resulting in distinct voxel maps.

are used to represent the value (*e.g.*, intensity or color) of a specific point in a 3D space. This data acquisition involves defining a grid, approximately 1 nm wide, comprising a maximum of 40×40 pixels, placed onto the studied surface or object as depicted in Fig. 3.13. When operating at $T = 2.4$ K, the maximum number of pixels is fixed by the liquid N_2 standing time of the microscope, that is 14 h. The tip is then scanned in constant height above each pixel, where a d^2I/dV^2 spectrum is acquired. After fitting each spectrum with a Voigt profile, that is the convolution product of a gaussian function and a lorentzian function, we extracted magnetic information, as described in Chapter 4. This information results in two distinct voxel maps: The exchange field at position (x, y) and the spin polarization at position (x, y). A third voxel map, which we will not be exploited in this Thesis, can also be defined where the magnetic anisotropy D of the Nc-tip is associated to the position (x, y).

Given the duration of the measurement, drift poses an inevitable challenge. Drift

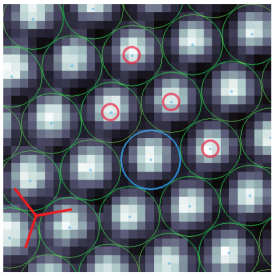

Figure 3.14: Exchange map of a cobalt surface with a simulated green lattice depicting the position of atoms. The red circles show the center of the atoms of the simulated lattice. The 3 red axis represent the compact directions

occurs due to the finite temperatures of both the surface and the tip, causing their expansion or contraction. Consequently, when the tip is directed to measure at a pixel located at $\vec{r}_0$, drift may displace the tip to $\vec{r}_0 + \Delta\vec{r}$. We suspect that due to our setup, wherein we lower the temperature to $2.4K$, the tip takes longer to thermalize compared to the sample and thus continues to contract during data acquisition. The drift accumulates over time, distorting the resulting map. To address this, we implemented an anchor point, typically the summit of an atom, serving as a reference position for the tip. After each pixel measurement, the tip returns to this anchor point and tracks its new position using the STM atom-tracking mode. Consequently, we evaluate the drift $(\delta x, \delta y, \delta z)$ and compensate by adjusting the coordinates for the subsequent pixel $(x+\delta x, y+\delta y, z+\delta z)$. Fig. 3.14 displays an exchange magnetic field map where the bright round circles represent the Co atoms. In the following analysis, we aim to quantify drift in different directions, namely (x, y) and (z). To illustrate lateral drift during map acquisition, we superimposed a simulated, thus perfect, lattice of Co atoms onto the exchange field map. We can reasonably assume that the error does not exceed two pixels in both the x and y directions, which corresponds to drift < 10 pm. By monitoring the vertical position of the tip, we measured that the drift, in the z direction, during a spectrum acquisition is lower than 2 pm.

CHAPTER 4

Single-spin sensing a cobalt island

Spin sensors can achieve sensitive magnetometry through changes in their spin states when they interact with a magnetic target. Examples include SQUID magnetometers employing nitrogen vacancy centers in diamond [58] or carbon nanotubes [59]. The inclusion of magnetic field gradients into magnetometers through scanning probe techniques has allowed for the detection of single spins with a remarkable resolution of up to 10 nm [60–62]. Nevertheless, a paradigm shift is needed to achieve the ultimate aim of atomic-scale resolution in magnetometry. A possible approach involves using a single magnetic molecule as a spin sensor. Molecules offer the advantage of a tunable electronic structure, making them well-suited for fulfilling the design requirements of a quantum sensor [63]. Notably, recent advancements in scanning tunneling microscopy (STM) techniques have enabled the detection of a molecular spin on a surface through electron spin resonance (ESR; § 2.3) [37, 64]. This breakthrough enables the detection of exchange and dipolar fields (> 10 mT) in the immediate vicinity of the molecular environment [65, 66]. To freely access all surface locations, a more advantageous strategy involves attaching the molecule to the STM tip apex. To date, this has been successfully demonstrated solely with the spin-$S = 1$ Nc molecule, albeit at the cost of limiting sensitivity to exchange fields > 1 T [2, 32].

In contrast to ESR, the spin states of a Nc-tip are in fact monitored through spin excitations arising from the inelastic component of the tunneling current (§ 2.2.3). Subangstrom precision in sample spin-sensing is made possible by the exchange interaction occurring across vacuum between the Nc-tip and the surface, which

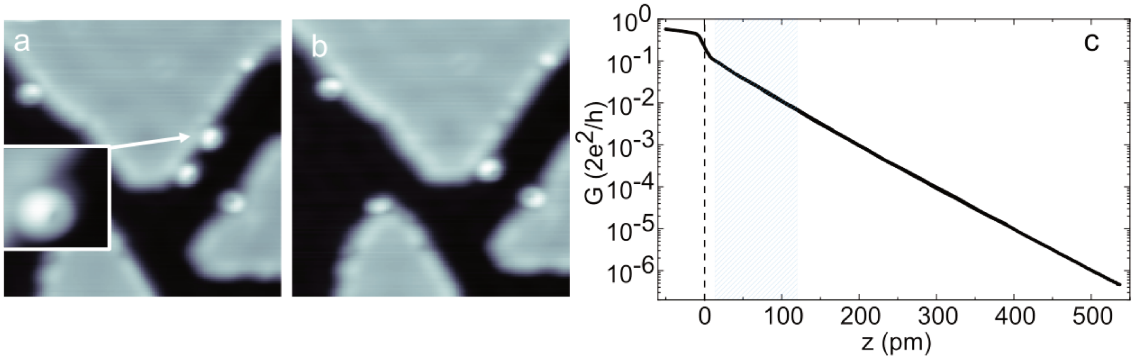

Figure 4.1: (a)-(b) Co bilayers with Nc at the step edge (12×12 nm^2, 50 mV, 50 pA), (a) before and (b) after Nc transfer to the tip apex. Inset: Close-up view of a Nc at a Co step edge (2×2 nm^2). (c) Conductance versus tip-sample distance (feedback loop open at 50 pA, 50 mV). The trace was acquired atop an atom of the Co bilayer. The dashed line corresponds to the contact point between the Nc-tip and the Co surface. The dashed area highlights the z-range where the exchange coupling can be detected in our setup.

modifies the Nc spin states [2, 32, 67]. In this chapter, we examine prototypical ferromagnetic Co islands that are grown on a pristine Cu(111) surface, including monolayer-thick islands that remain unexplored. As observed before our findings reveal that the thickness of the ferromagnetic layer exerts control over the orientation of sample magnetization and spin polarization. Our finding are supported by *ab initio* calculations performed by Roberto Robles (Centro de Física de Materiales CFM/MPC, CSIC-UPV/EHU, San Sebastián, Spain), Nicolas Lorente (CFM & Donostia International Physics Center, San Sebastián, Spain) and Olivier Bengone (IPCMS, Strasbourg, France). Furthermore, we demonstrate that the spatial dependence of the exchange energy across the surface is well captured by computed spin-density maps. Our study demonstrates the effectiveness of a Nc-tip in probing surface magnetism, even in the absence of an external magnetic field.

4.1 Sample and tip preparation

Molecular tip. To prepare a Nc-tip, we proceeded as described in § 2.2.3. Molecular attachment to the monoatomically sharp tip apex was carried with an Nc adsorbed on a cobalt or copper step edge (Fig. 4.1a), or with an Nc adsorbed on a Co island, with tunneling parameters slightly different (50 mV, 50 pA, tip excursion towards Nc: 350 pm). In order to determine the tip-sample distance, we approached the Nc-tip to a Co atom of the island surface. Contact formation was monitored through changes in the tunneling conductance $G = I/V$ as a function of tip-surface distance z (Fig. 4.1b). The contact distance ($z = 0$) was identified

through a change in the slope of the trace as in § 2.2.3. The contact conductance was $G = 0.25, (2e^2/h)$, which is lower than the contact conductance found on copper (Fig. 2.8), the transition from tunneling to contact also being more abrupt. These differences are not unusual when dealing with different surface materials [68].

Sample. The single-crystal Cu(111) substrate was cleaned by repeated cycles of Ar^+ sputtering and annealing to 520°C. The Co islands were grown at room temperature by evaporating cobalt onto Cu(111) from a thoroughly out-gassed rod at a rate of 0.3 ML min^{-1}. After a 1.1 ML deposition of cobalt, the sample was transferred in the pre-cooled STM (T $\leq$ 77 K). It results in the formation of triangular-like nanoislands, which are two atomic layers in height [7, 69, 70]. The islands, which are denoted by **2** in Fig. 4.2a, display an apparent height of approximately 325 ± 10 pm and exhibit typical sizes spanning from 10 to 30 nm. Approximately 5% of the surface area is occupied by islands that are three layers high (denoted by **3** in Fig.4.2a), characterized by an apparent height of 540 ± 10 pm. To promote the growth of one-layer high islands (referred to as **1** in Fig. 4.2b), we introduce strain relaxations in the Cu substrate by either depositing Co at sub-room temperatures or by lowering the annealing temperature of the Cu substrate [71]. The monolayer islands exhibit variable sizes within the range of $7 - 20$ nm and have an apparent height of approximately 140 ± 10 pm. Their morphology is triangular with truncated corners, which signifies that the diffusion barriers involved in their growth process differ from those of bilayer islands [71]. Nickelocene deposition was carried out by exposing the cold sample (< 100 K) to a molecular flux of 2.5×10^{-2} ML $\cdot$ min^{-1} during a few seconds. Care was taken to work in a hydrogen-free environment, as Co islands are prone to hydrogen contamination [72, 73]. We will see in Chapter 5 that this contamination can affect the magnetism of the islands.

4.2 Electronic properties (metallic tip apex)

The islands exhibit similar electronic properties. In Fig. 4.2c, we present dI/dV spectra acquired by placing a metal tip at the center of the islands. They were recorded using a lock-in amplifier operating at a frequency of 6.2 kHz and a modulation of 5 mV rms. Across all the islands, a prominent feature is observed in their dI/dV spectra, situated at energies of -0.39 eV (**1**), -0.33 eV (**2**), and -0.36 eV (**3**). Based on the *ab initio* calculations, it is assigned to minority d_{z^2} states, in agreement with previous findings [69, 70]. Figure 4.3a presents the computed local density of states (LDOS) at 300 pm over a Co atom on the surface of mono-, bi-, and trilayers, which were calculated by integrating the states in a sphere centered

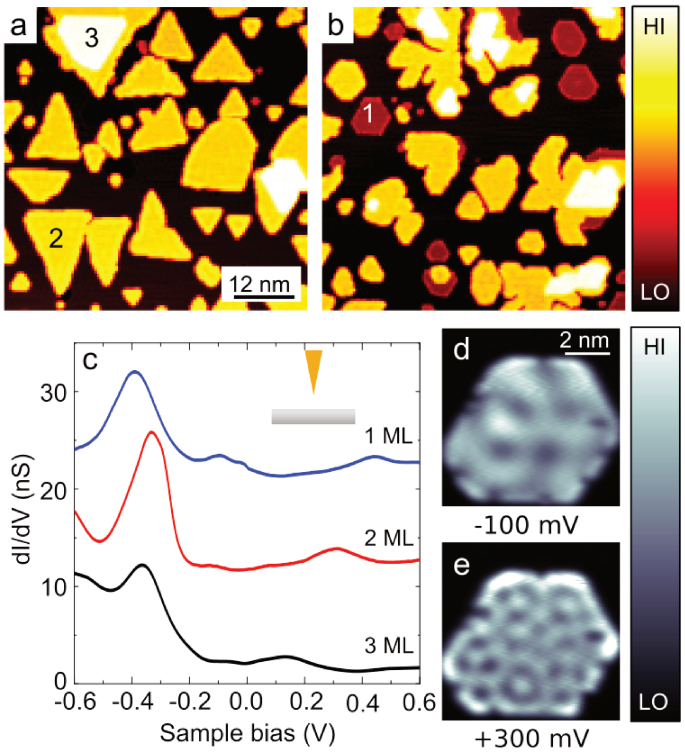

Figure 4.2: Constant-current image of Co islands grown on (a) Cu(111), (b) "strained" Cu(111) (image size: 40×40 nm^2, sample bias: 80 mV, tunnel current: 60 pA). Numbers indicate ML thickness. (c) Typical dI/dV spectra acquired in the center of **1**, **2**, and **3** ML cobalt islands. The 2- and 1-ML spectra are displaced upward by 10 and 20 nS, respectively. The feedback loop was opened at 0.5 V and 1 nA. The **2** ML spectrum was acquired on an "unfaulted" island [7]. Inset: Sketch of the tunnel junction. Constant-height dI/dV maps of a Co monolayer acquired at (d) -100 mV and (e) $+300$ mV, respectively. The feedback loop was opened in the center of Co at a distance of approximately 500 pm from tip-surface contact. The dispersive states do not have sufficient weight compared to the d states to be directly detected by tunneling spectroscopy [74, 75].

at 300 pm over the Co atom and with a radius of 50 pm. A fine grid of $200 \times 200 \times 1$ k-points was used. A Gaussian broadening of 50 meV was applied for a better comparison with the experimental dI/dV spectra shown in Fig. 1c. As expected, DFT does not precisely replicate the peak positions, but a qualitative agreement between the LDOS and dI/dV spectra is found. A prominent peak, approximately at -0.35 V, is observed in both the bi- and trilayer islands. In the monolayer, the dominant peak appears at a lower energy, accompanied by an additional peak at a higher energy. In order to get an insight on the origin of the peak at -0.35 V, we present in Fig. 4.3b the same LDOS for the bilayer but projected onto the different orbitals without broadening (see Appendix A for computational details). As visible, the peak is actually formed by two peaks of mainly s character with a

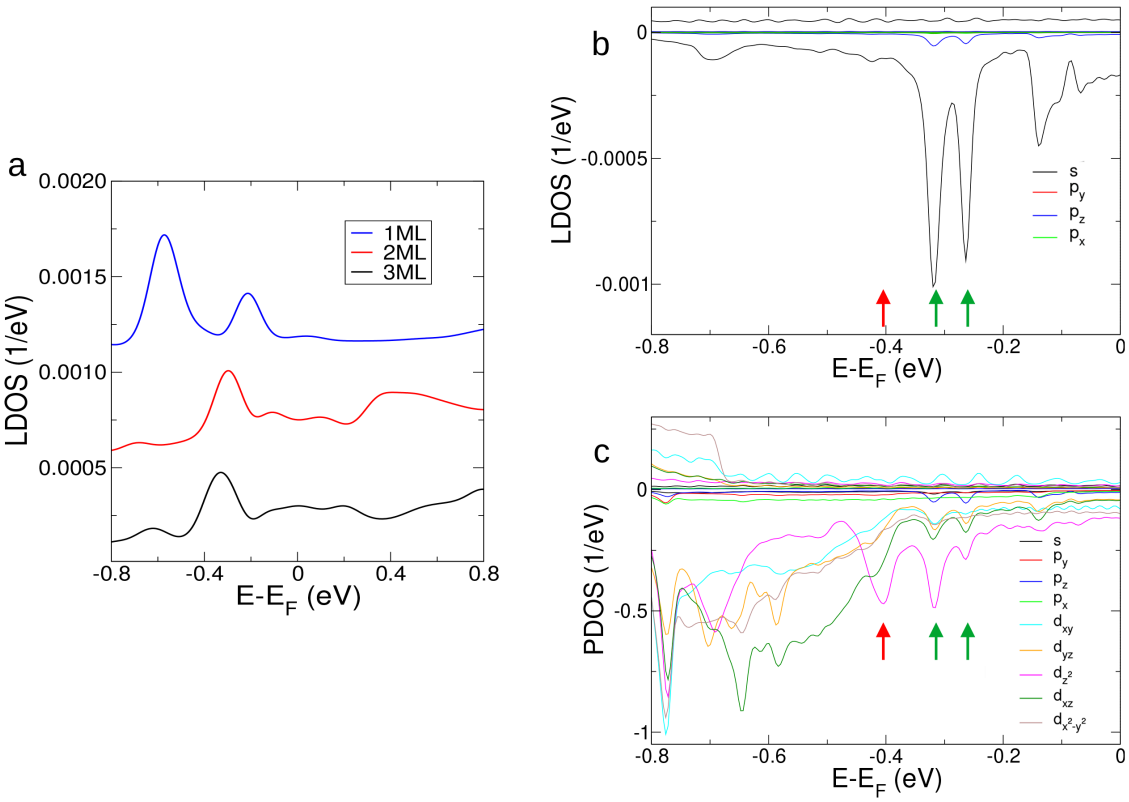

Figure 4.3: (a) Local density of states (LDOS) calculated at 300 pm over a Co atom for mono-, bi-, and trilayer plotted in blue, red, and black, respectively. A Gaussian broadening of 50 meV was applied to the data. The different curves have been displaced for clarity. (b) Detail of the LDOS at 300 pm for the bilayer plotted without broadening. (c) Projected density of states (PDOS) for the surface Co atom of a bilayer.

smaller p_z component. The origin of the peaks can be traced back to the projected density of states (PDOS) of the surface Co atom (Fig. 4.3c). This computation is a conventional DOS of a surface Co atom from a bilayer island where all the states are projected onto the orbitals of the atom. Fig. 4.3b gives an idea of how these states decay into vacuum since the calculation are done 300 pm above a Co atom of the surface –a distance comparable where we position the tip during a spectroscopy measurement. The peaks that extend into the vacuum (marked with green arrows) are formed by the hybridization of d-states (mainly d_{z^2}) with s and p_z orbitals. The hybridization with s and p_z orbitals is fundamental. For example, the d_{z^2} peak marked with a red arrow in Fig. 4.3c is not hybridized with s and p_z orbitals, and, therefore, it is not observed in the LDOS at 300 pm (Fig. 4.3b), as it decays faster into the vacuum than the hybridized peaks.

The presence of standing wave patterns on cobalt layers highlights the existence of a free-electron-like surface state [69, 74]. To analyze the dispersion of this state,

	E_0 (eV)	m^*/m
Cu(111)	-0.43	0.43
Co 1 ML	-0.28	0.44
Co 2 ML	-0.18	0.43

Table 4.1: Energy onset and effective mass extracted from Fig. 4.4g.

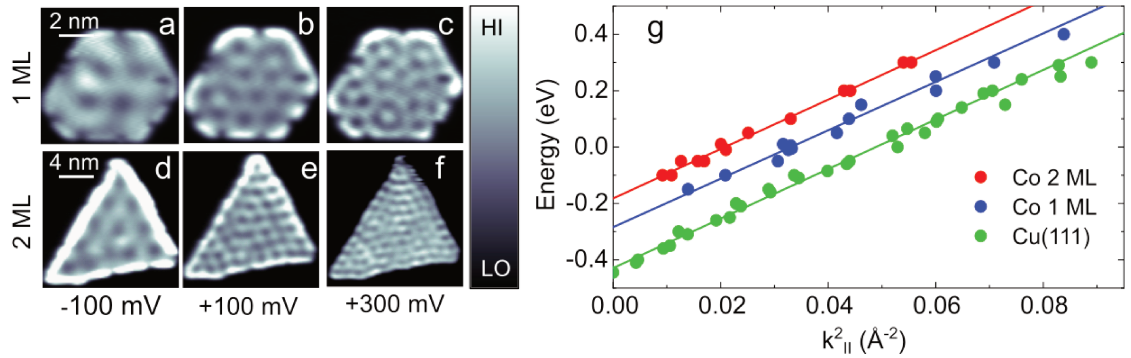

Figure 4.4: (a)-(c) Constant-height dI/dV maps of a 1 ML Co island (8×8 nm^2) acquired at (a) -100, (b) $+100$, and (c) $+300$ mV. (d)-(f) Constant-height dI/dV maps of a 2 ML Co island (18×18 nm^2, 1 nA) acquired at (d) -100, (e) $+100$, and (f) $+300$ mV. The feedback loop was opened in the center of Co at a distance of approximately 500 pm from tip-surface contact. (g) Energy versus $k_{\|}^2$ for 1 ML and 2 ML Co islands, as well as for Cu(111). The k-dispersion on Cu(111) was determined by recording the standing wave pattern at a surface step edge at various biases. Solid lines: Linear fits.

we recorded in every pixel of the image a dI/dV signal at a given bias. During image acquisition, the feedback loop was kept open (constant height measurement, see § 3.4). The constant-height dI/dV maps were recorded over a wide bias range, from -100 to $+400$ mV, for the mono- (Fig. 4.4a-c) and bilayer (Fig. 4.4d-f) islands. For reference, we also recorded the standing wave pattern of the free-electron-like surface state of Cu(111), *i.e.* the Shockley surface state. To determine the dispersion of this state, we extract the standing wave period on the Co islands at various bias voltages V (Fig. 4.4g), so a relation between energy ($E = eV$) and wave vector k can be established experimentally. The data follow a parabolic dispersion relation $E = E_0 + (\hbar k)^2/2m^*$, described by an onset E_0 below the Fermi level and an effective mass m^*. The data, which are summarized in Tab. 4.1, are consistent with previous work [69]. Note that the dispersive states do not have sufficient weight to be directly detected by tunneling spectroscopy as they are buried in the tail of the d peak (see Fig. 4.2c).

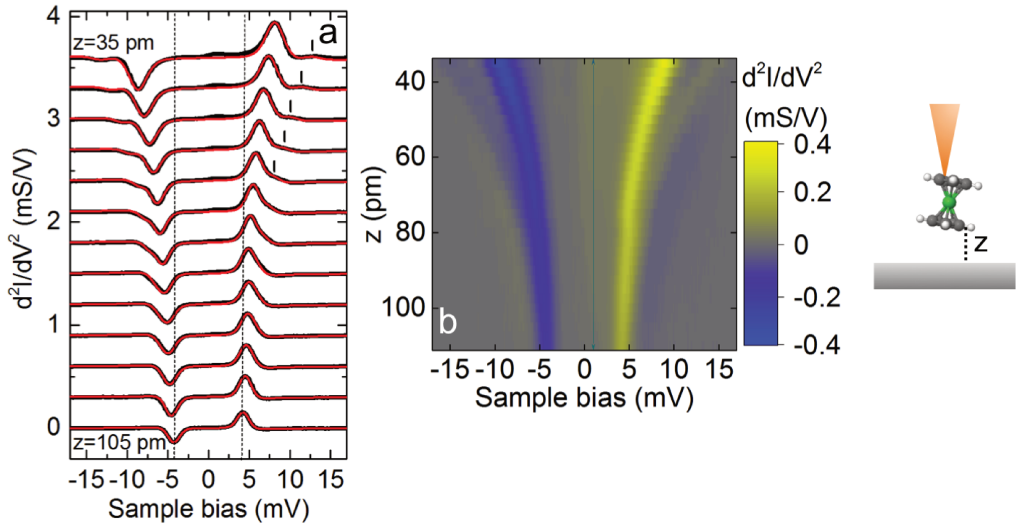

Figure 4.5: (a) d^2I/dV^2 spectra above a Co atom of a monolayer island acquired at different tip-Co distances. The spectra are displaced vertically by 0.5 ms/V from one another. The vertical solid lines in panel (a) indicate the position of excitation $|\Psi_0\rangle \rightarrow |\Psi_2\rangle$. Red lines: Simulations based on the dynamical scattering model. (b) 2D intensity plot of a series of distance-dependent d^2I/dV^2 spectra above a Co atom. Inset: Sketch of the tunnel junction.

4.3 Magnetization orientation

4.3.1 Determining the magnetization orientation

The magnetic properties differ for the different type of islands. Their magnetism is explored with a Nc-tip by recording the inelastic signal through the second derivative, d^2I/dV^2 (with a lock-in modulation of 500 μV rms). Figure 4.5a displays a series of distance-dependent d^2I/dV^2 spectra obtained above a monolayer island with the tip positioned directly above a Co atom at the island center. Figure 4.5b presents the corresponding 2D intensity plot. At a distance of $z = 105$ pm, the spectrum exhibits a peak and a dip at biases of +3.9 and −3.9 mV, respectively. These peaks and dips indicate inelastic scattering events, wherein tunneling electrons transfer momentum and energy to the spin states of Nc (§ 2.2). As the tip approaches, the peak shifts upward, and the dip shifts downward in energy by nearly 5 mV. At $z \leq 60$ pm, a second peak (dip) emerges, initially as a high-energy (low-energy) shoulder to the peak (dip), then becoming fully resolved at $z = 40$ pm due to its more pronounced energy shift. In the bilayer and a majority of trilayer islands (> 80%), we observe instead a progressive splitting of the peak and dip in the d^2I/dV^2 spectrum as the tip approaches a Co atom vertically (Fig. 4.6). However, a minority of trilayer islands (< 20%) exhibit a behavior similar to monolayer islands.

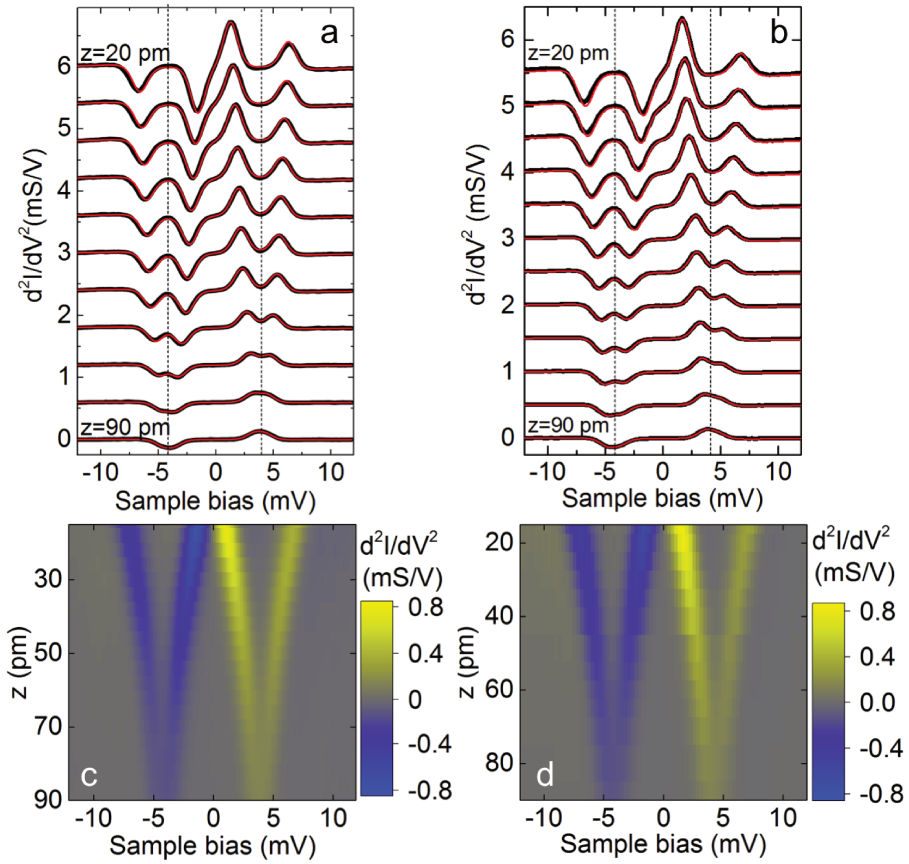

Figure 4.6: (a) d^2I/dV^2 spectra above a Co atom of a (a) bilayer, (b) trilayer island at different tip-Co distances. The spectra are displaced vertically by 0.5 ms/V from one another. The red lines are simulations based on a dynamical scattering model [57]. Panels (c) and (d) present the corresponding 2D intensity plot of a series of distance-dependent d^2I/dV^2 spectra.

To rationalize these findings, we assign the z-axis as the out-of-plane direction of the Co surface, for now assuming the molecular axis of Nc along the z-axis. We consider the Heisenberg spin Hamiltonian that describes the interaction of Nc with a single atom:

$$\hat{H} = D\hat{S}_z^2 - J\hat{S} \cdot \hat{S}_{\mathrm{Co}}. \tag{4.1}$$

In this work, the direction of the Co spin is fixed, either with in-plane orientation (monolayer island) or out-of-plane orientation (bi- and trilayer islands). Eq. 4.1 can be rewritten as:

$$\hat{H} = D\hat{S}_z^2 - g\mu_{\mathrm{B}}\hat{B}_{\mathrm{ex}} \cdot \hat{S}, \tag{4.2}$$

where $B_{\mathrm{ex}} = J\langle S_{\mathrm{Co}}\rangle/g\mu_{\mathrm{B}} = E_{\mathrm{ex}}/g\mu_{\mathrm{B}}$ represents the exchange field produced by the Co atom on the spin $\hat{S}$ of Nc, μ_{B} denotes the Bohr magneton, and $g = 1.89$

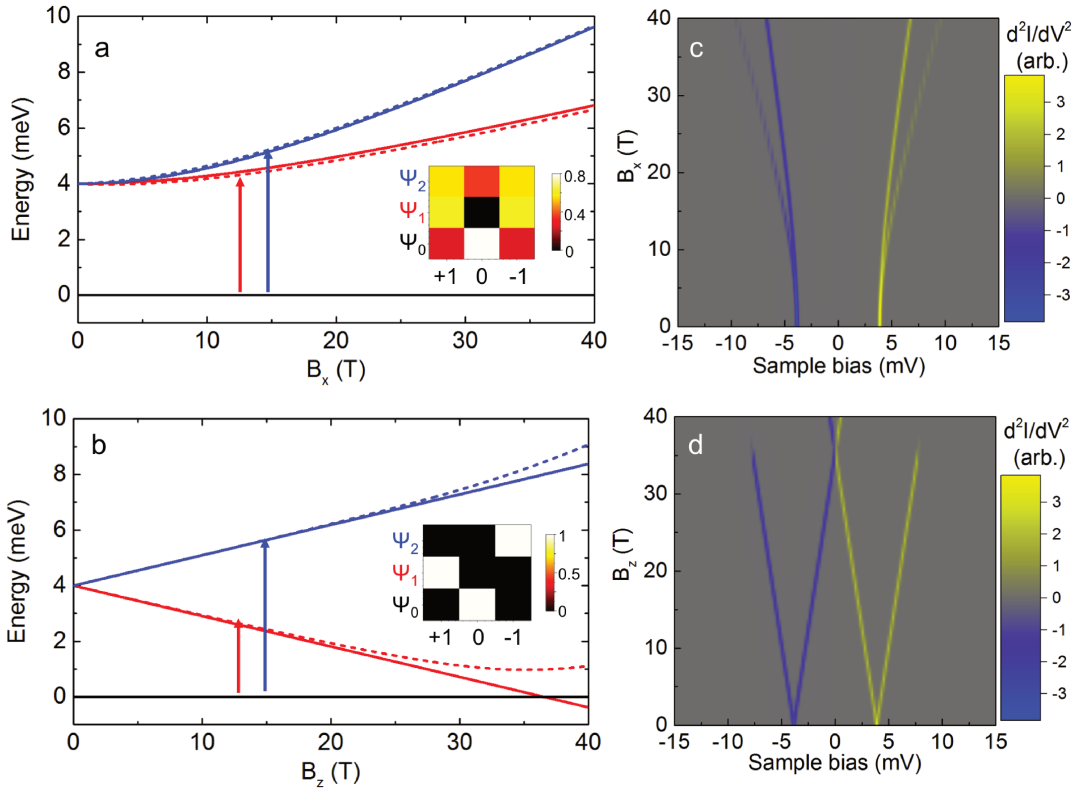

Figure 4.7: Spin-state energy as a function of the exchange field with (a) in-plane orientation ($\hat{B}_{ex} = \hat{B}_x$) and (b) out-of-plane orientation ($\hat{B}_{ex} = \hat{B}_z$). The arrows indicate the spin excitations. The dashed lines correspond to the spin states when Nc is tilted by 12° relative to the surface normal. Inset: Eigenvectors $|\Psi_0\rangle, |\Psi_1\rangle, |\Psi_2\rangle$ written as a sum of $|M\rangle$ states and obtained by diagonalizing Eq. 4.2. Simulated 2D intensity plot computed with a dynamical scattering model [57] with (c) in-plane and (d) out-of-plane exchange fields in Eq. 4.2 (tilt angle is neglected).

(§ 2.2.2). The DFT calculated magnetic moment $\langle S_{\mathrm{Co}} \rangle$ is given in Tab. 4.2 for each island type. The monolayer spectra are reproduced using a dynamical scattering model [57], provided by M. Ternes, with an in-plane exchange field (solid red lines in Fig. 4.5a), $\hat{B}_{\mathrm{ex}} = B_{\mathrm{ex}}\hat{x}$ in Eq. 4.2. In this configuration, the ground state $|\Psi_0\rangle$ and the two excited states $|\Psi_1\rangle$ and $|\Psi_2\rangle$ consist of a mixing of the $|M|$-spin states (inset of Fig. 4.7a), where M denotes the magnetic quantum number along the z-axis. The eigenvalues are $E_0 = 0$, $E_1 = (D + \sqrt{D^2 + 4E_{ex}^2})/2$, and $E_2 = \sqrt{D^2 + 4E_{ex}^2}$ where $E_{ex} = g\mu_{\mathrm{B}}B_x$ (Fig. 4.7b). As shown in Fig. 4.7c, the 2D-intensity-plot simulations of the d^2I/dV^2 spectra match well the experimental plots. The dominant peak in the d^2I/dV^2 spectrum is thus assigned to spin excitation $|\Psi_0\rangle \rightarrow |\Psi_1\rangle$. The weaker peak at higher energy is associated with spin excitation $|\Psi_0\rangle \rightarrow |\Psi_2\rangle$. It is visible relatively small tip-Co distances (Fig. 4.8a). It appears at first as a high-energy

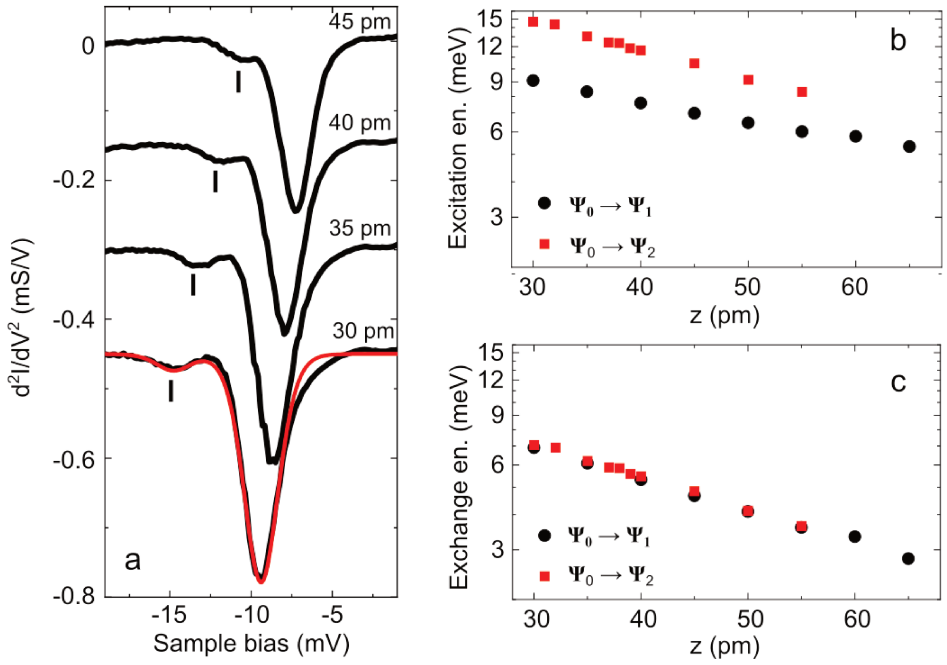

Figure 4.8: (a) d^2I/dV^2 spectra acquired above a Co atom of a monolayer island at various distances (only the negative biases are plotted for clarity). The feedback loop was opened at 100 pA and 1 mV. The spectra are displaced downward by 0.15 mS/V from one another ($z = 0$ corresponds to tip-surface contact). The vertical lines indicate the position of the $\Psi_0 \rightarrow \Psi_2$ excitation. The solid red line is a simulation based on a dynamical scattering model (without rate equations; see paragraph about spin-excitation lifetimes). (b) Excitation energies from the spectra, and (c) corresponding exchange energy determined with the analytical expressions given in the text.

shoulder to the dominant peak and then becomes resolved when $z \leq 40$ pm. This assignment can be further checked by extracting the exchange energy from their position. To do so, we first express the excitation energies as $E_{0\rightarrow1} = E_1 - E_0$ and $E_{0\rightarrow2} = E_2 - E_0$, and then express the exchange energy as $E_{ex} = \sqrt{(E_{0\rightarrow1} - D)E_{0\rightarrow1}}$ for $|\Psi_0\rangle \rightarrow |\Psi_1\rangle$, and $E_{ex} = \sqrt{(E_{0\rightarrow2}^2 - D^2)}/2$ for $|\Psi_0\rangle \rightarrow |\Psi_2\rangle$. As expected, the excitation energies of the spectra (Fig. 4.8b) yield the same exchange energy using the previous relations (Fig. 4.8c).

Conversely, the bilayer and trilayer spectra indicate instead that the exchange field has out-of-plane orientation ($\hat{B}_{\text{ex}} = B_{\text{ex}}\hat{z}$ in Eq. 4.2). In this configuration, the two excited states, $|\Psi_1\rangle = |M = +1\rangle$ and $|\Psi_2\rangle = |M = -1\rangle$, become Zeeman split (Fig. 4.6), and the eigenvalues are $E_0 = 0$, $E_1 = D - E_{ex}$, $E_2 = D + E_{ex}$. The simulated line shapes (solid red lines in Fig. 4.5c) accurately match the experimental data, but unlike the monolayer islands, a finite lifetime of $\tau \simeq 0.1$ ns is accounted for the excited states. The lifetime, which is discussed later in § 4.6, is nearly 1000 times longer than that of a magnetic atom on a metal surface [21]. The

	1 ML	2 ML	3 ML
Mag. moment (μ_B)	1.75 (I)	1.76 (I), 1.67 (II)	1.84 (I), 1.77 (II), 1.79 (III)
MCA per Co (meV)	+0.628 (in-plane)	-0.208 (out-of-plane)	+0.005
d(III,II)	–	–	−8.50%
d(II,I)	–	−10.10%	−5.70%
d(I,1)	−1.91%	−0.35%	−0.01%
d(1,2)	+0.4%	+0.08%	+1.40%
d(2,3)	+0.2%	−0.17%	+1.30%

Table 4.2: Computed structural properties and magnetism for 1, 2, and 3 ML of Co on Cu(111). These calculations correspond to 9 layers of a Cu (111) slab, with an energy cutoff of 500 eV for the plane-wave expansion and a k-point mesh of $35\times35\times1$ to evaluate the electronic contribution to the Magnetocrystalline Anisotropy Energy (MCA) using the so-called magnetic force theorem [76]. Additionally, the relative displacement of the different layers (Roman numerals for the Co layers and Arabic for the Cu ones) is expressed in terms of the unrelaxed ideal geometry.

simulated 2D-intensity-plot of the d^2I/dV^2 shows a Zeeman splitting in agreement with experiments (Fig. 4.7d). A level crossing occurs between $|\Psi_0\rangle$ and $|\Psi_1\rangle$ at an exchange field $D/g\mu_B \approx 36$ T, which is lifted when Nc has a non-zero tilt angle (dashed line in Fig. 4.7b).

4.3.2 Computed magnetization and anisotropy

To validate these observations, we conducted DFT calculations to determine the Magnetocrystalline Anisotropy Energy per Co atom (MCA) within the islands. More details concerning the MCA czn be found in § 5.4. Table. 4.2 presents the computed MCA and the magnetic moments of the Co atoms. Are also included some details of the relaxed Co/Cu structure considered. The MCA is consistent with the experimental findings, with one exception being the trilayer case, where the MCA is close to zero. Therefore, other effects not considered here play a role in the trilayer island, such as the size and shape, which influence the island strain [70], or shape anisotropy [77]. In Chapter 5, we will see that shape anisotropy stabilizes the magnetization of a Co island exposed to hydrogen. Also, the presence of Cu at the corners of the trilayer islands, as evidenced by the Nc-tip measurements (see Fig. 4.9), could also influence its magnetic properties [78]. The trilayer anisotropy reflects a delicate balance among all these effects and some variability in the orientation of magnetization for the trilayer islands can be expected, depending on the specifics of the sample preparation.

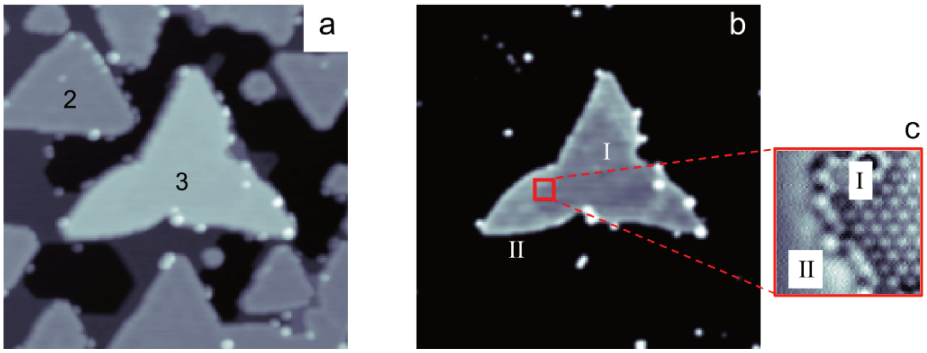

Figure 4.9: (a) Image centered on a 3 ML island (denoted **3**) acquired with a metal tip (60×60 nm^2, 50 pA, 50 mV). (b) Same image as (a), but with a change in image contrast to highlight subtle structural changes at the island corners. The area denoted **II** is 10 pm higher than the one denoted **I**. (c) Close-up view image of the island corner acquired with a Nc-tip (2×2 nm^2, 100 pA, 1 mV). In these tunneling conditions, images of the Co surface have a magnetic corrugation [2]. The absence of a magnetic signal in **II** compared to **I** indicates that Co forms the core of the island and Cu probably the corners.

4.3.3 Magnetization orientation and excitation energies

As anticipated in Fig. 4.7b, the tilt angle of Nc on the tip apex can modify its excitation energies [32]. To highlight this relationship, we use Eq. 4.1 to compute the two excitation energies: $E_{0\to1}$ (low-energy excitation) and $E_{0\to2}$ (high-energy excitation) at a given tilt angle of Nc. In particular, we focus on two angles representing two representative cases observed experimentally: A non-tilted Nc (0°) and a 12°-tilted Nc. Figure 4.10 presents the difference between the excitation energies $E_{0\to1}(12°) - E_{0\to1}(0°)$ and $E_{0\to2}(12°) - E_{0\to2}(0°)$. Figure 4.10a illustrates the difference for an out-of-plane orientation of the exchange field. The plot extends up to a value of 20 T, which is the highest exchange field observed experimentally (Fig. 4.11a). Figure 4.10b presents the difference for an in-plane orientation of the exchange field, where the highest observed exchange field is 70 T. As shown, the angular dependence causes changes of at most 0.25 meV, which is of the same order as our energy resolution. Therefore, estimates of the exchange field are robust to changes in the Nc tilt angle in the present study.

4.4 Magnetic corrugation

The simulated line shapes provide quantitative insights into the exchange energy at specific Nc-Co distances. Above all island types, the exchange energy has an exponential variation $\exp(-z/\lambda)$ with a decay length of $\lambda = 46 \pm 3$ pm (Fig. 4.11a),

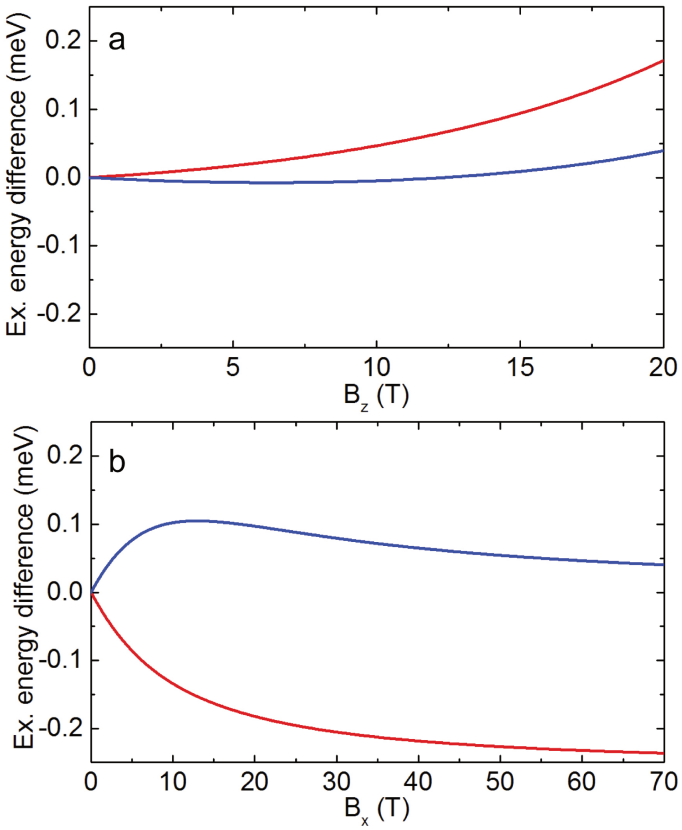

Figure 4.10: Difference between the excitation energy of a 12°-tilted and a non-tilted Nc for (a) an out-of-plane exchange field, (b) an in-plane exchange field. Magnetic anisotropy set to $D = 4$ meV. Solid red lines: $E_{0\to1}(12°) - E_{0\to1}(0°)$, solid blue lines: $E_{0\to2}(12°) - E_{0\to2}(0°)$.

consistent with other tip-induced exchange interactions [11, 32, 36, 79]. Notably, the exchange energy above the monolayer island is nearly three times stronger when compared to the bi- and trilayer islands, which exhibit identical exchange energies. The exchange coupling also changes across the surface. To visualize these variations, we acquire a voxel image (§ 3.10) consisting of a dataset in the form of $d^2I/dV^2(x, y, V)$ at a fixed distance of $z = 20$ pm above a region of interest. We then determine the exchange energy at each lateral tip position by fitting the spectra (see Fig. 3.13). The resulting image (Fig. 4.11b-c) is comparable to the magnetic interaction map obtained for a single atom using STM-ESR [80]. However, in contrast to STM-ESR, our method allows us to span over multiple surface atoms, as illustrated for monolayer and bilayer islands in Fig. 4.11b and 4.11c, respectively. These images reveal a magnetic corrugation with a periodicity of 254 ± 6 pm, corresponding to the in-plane Co-Co distance determined with a metal tip. The corrugation is approximately two times weaker in the monolayer island (Fig. 4.11d) compared to the bi- and trilayer islands (Fig. 4.11e).

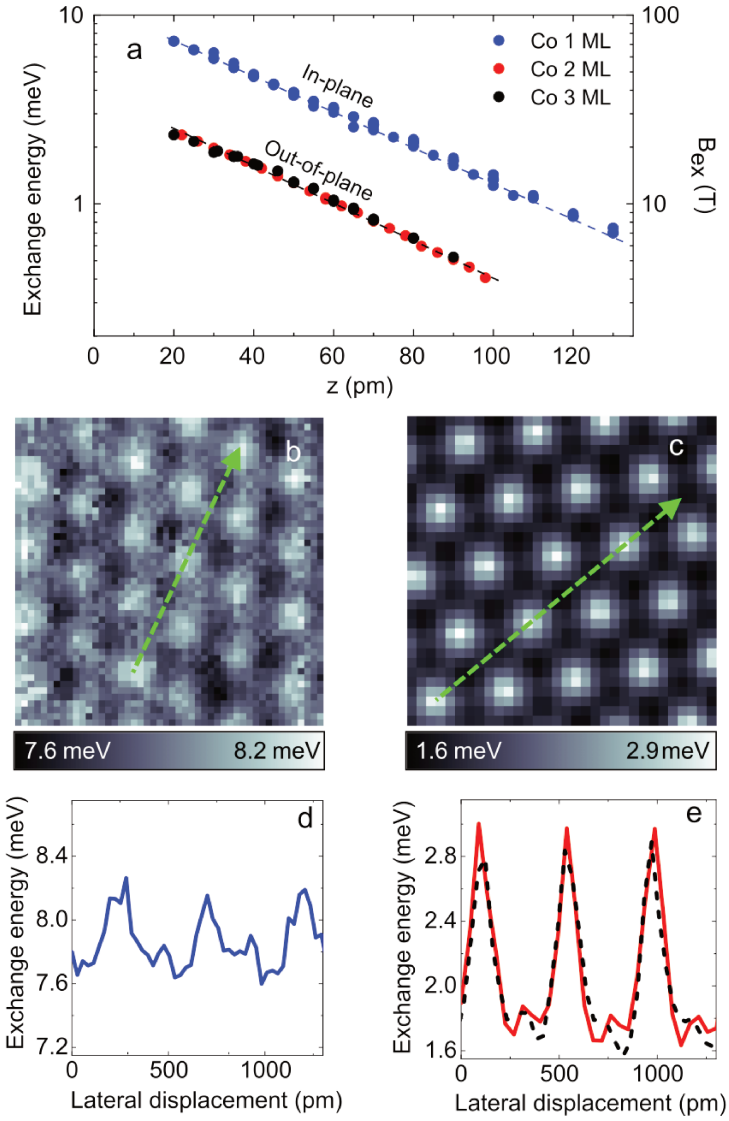

Figure 4.11: (a) Exchange energy as a function of distance z extracted from the d^2I/dV^2 spectra. The dashed lines are exponential fits described in the text. The exchange field is given on the right y-axis. (b,c) Spatial maps of the exchange energy acquired at a fixed distance of $z = 20$ pm above a monolayer and a bilayer island, respectively. (d,e) Height profiles of the layers acquired along the dashed lines indicated in (b) and (c). The dashed line in (e) is the height profile of a trilayer.

This observation is in agreement with the computed spin density maps of the Co surfaces (Fig. 4.12a and 4.12b). A spin density map is a visual representation of the distribution of electron spin density in a material (or molecule) and is expressed as:

$$m_s(\vec{r}) = \int_{-\infty}^{+\infty} [\rho_s^{\uparrow}(\vec{r}) - \rho_s^{\downarrow}(\vec{r})] f(E)\, dE, \tag{4.3}$$

where $\rho_s^{\uparrow}$ and $\rho_s^{\downarrow}$ are the surface spin-up and spin-down DOS at position $\vec{r}$, respec-

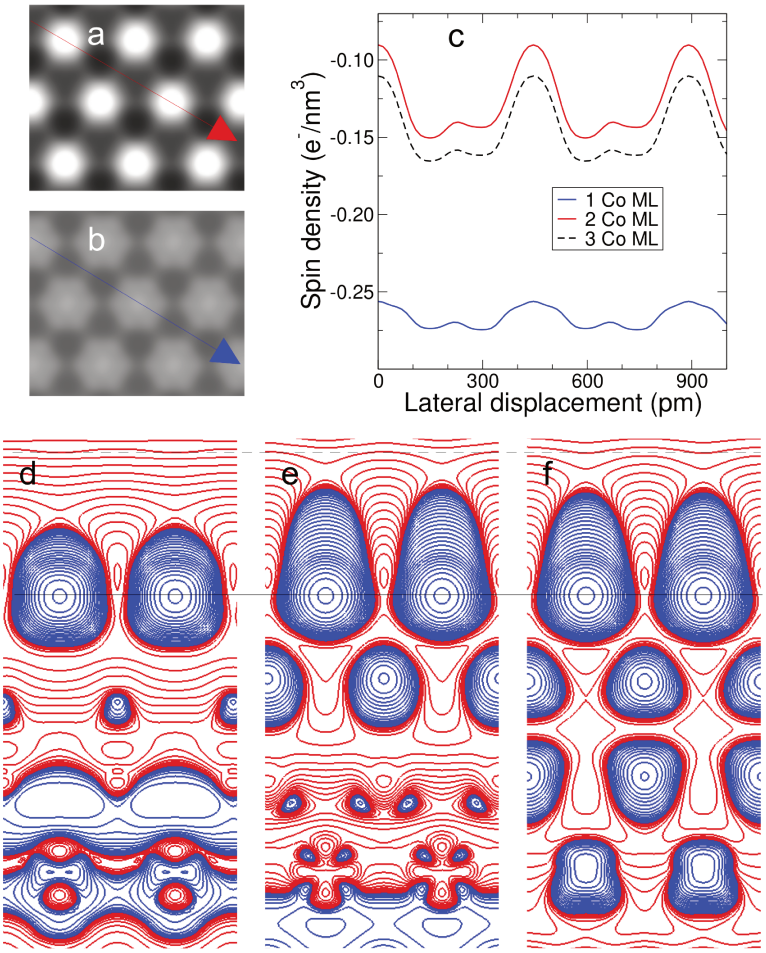

Figure 4.12: (a)-(b) Computed spin density maps at a fixed distance of 300 pm above a bilayer and a monolayer, respectively. (c) Height profiles of the layers along the lines indicated in (a) and (b). The dashed line is the height profile of a trilayer. (d)-(f) Section of the spin density in a $(11\bar{2})$ plane passing through the surface Co atom for monolayer, bilayer and trilayer, respectively. Blue (red) isolines indicate positive (negative) values. The black line indicates the position of the surface Co atoms. The height profiles in panel (c) are extracted 300 pm above the Co atoms (the position is indicated by a dashed black line).

tively, and $f(E)$ the Fermi-Dirac distribution. The maps are computed at fixed tip-surface distances and thus provide a 2D rendering of the spin density at a given height above the surface. As in the experimental exchange energy maps, the corrugation of the spin density is stronger for the bi- and the trilayer islands compared to the monolayer island. The difference can also be observed in the height profiles (Fig. 4.12c), and in the sections of the spin density in a $(11\bar{2})$ plane passing through the Co surface atoms (Fig. 4.12d-f). At 300 pm (dashed line), which corresponds to the distance probed in the experiment, the isolines show a stronger corrugation for

bi- and trilayers (Fig. 4.12e-f) than for the monolayer (Fig. 4.12d). The origin of this behavior is tracked down to the d_{z^2} orbital. While for the monolayer the orbital has a spin magnetization of 0.28 μ_B, for the bilayer it has a higher spin magnetization of 0.42 μ_B (0.43 μ_B for the trilayer). At the same time, the monolayer has a higher average absolute value for the spin density (Fig. 4.12c) in agreement with the stronger exchange energy observed experimentally. First-principle calculations would be needed for unveiling the physical rationale behind the observed values of the exchange energy [81].

4.5 Spin polarization

4.5.1 Spin-polarized measurement

The cobalt islands can also show spin polarization as their magnetization induces a spin imbalance in the tunneling current. This leads to discernible variations in the relative heights of the peaks and dips within the d^2I/dV^2 spectrum. This difference in amplitude can be viewed, for example, in (Fig. 4.13a) where the low-energy excitation of a spectrum acquired above a trilayer island exhibits a smaller dip amplitude at negative bias compared to the peak at positive bias. The explanation for this difference was given by Loth *et al.* while investigating an Mn atom on a Cu_2N surface with a magnetic tip [17]. Compared to their setup, our tunnel junction is configured in reverse (Fig. 4.13b), as the spin-excited object resides on the tip, while the surface is magnetic. The different spin-dependent amplitude is explained as follows. In the scenario of a spin excitation from the state $|M = 0\rangle$ to $|M = +1\rangle$ of Nc, the conservation of spin angular momentum dictates that the electron spin initially resides in an "up" state, denoted as $|m = +1/2\rangle$, and subsequently transitions to a "down" state, denoted as $|m = -1/2\rangle$. This change occurs after the electron undergoes scattering with Nc. Remembering that at a negative bias, the electron flows from the surface to the tip, the conservation rule implies that the inelastic signal is proportional to the spin up DOS ($\rho_\uparrow$) of the surface. Conversely, at positive bias the current flows from the tip to the surface and is sensitive to the spin down DOS ($\rho_\downarrow$) of the surface. To quantitatively assess this imbalance, we derive values from our line shape fits in the form of a spin polarization $P = (h_+ - h_-)/(h_+ + h_-)$, where h_+ and h_- represent the heights of the peak and dip of the low-energy excitation, respectively. The excitation of Nc from the ground state to its second excited state $|-1\rangle$ requires instead electrons starting in a $|\downarrow\rangle$ state and ending in a $|\uparrow\rangle$ state, resulting in a spin polarization of $-P$. The trilayer islands exhibit a spin polarization of $+0.17$ at the Fermi energy (Fig. 4.14a), while the bilayer islands remain non-polarized

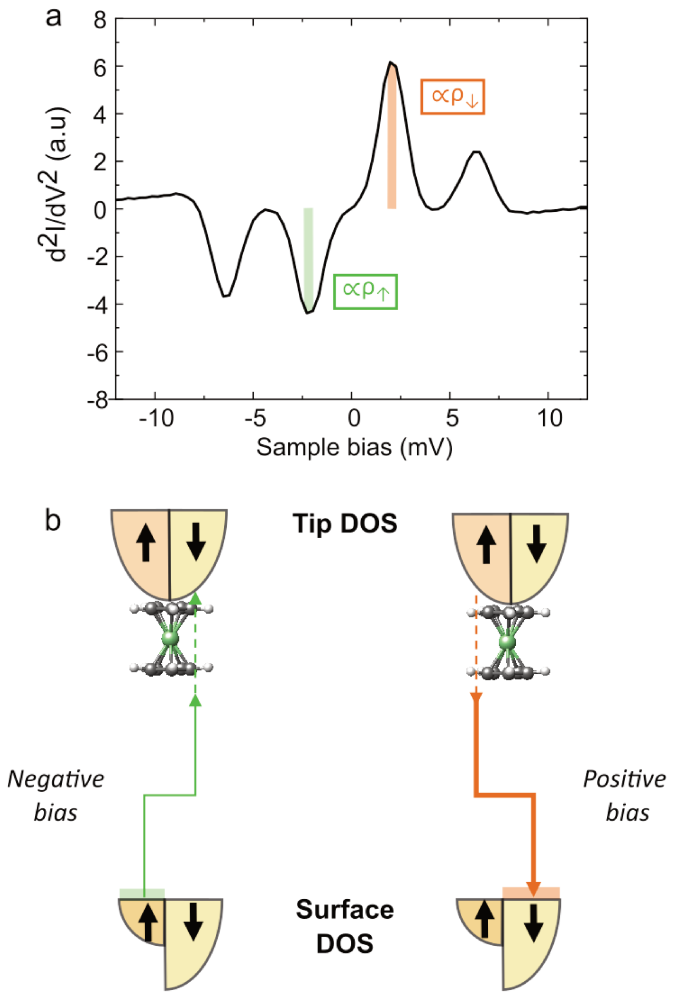

Figure 4.13: (a) d^2I/dV^2 spectrum acquired on a trilayer Co island. Here we considered the peak and dip appearing at low bias which represents the spin excitation $|M = 0\rangle \rightarrow |M = +1\rangle$. The amplitude of the first dip is proportional to the spin up DOS or $\rho_\uparrow$ while the amplitude of the first peak is proportional to the spin down DOS ($\rho_\downarrow$). (b) Inelastic tunneling of an electron between the tip DOS and the surface DOS at opposite bias voltages. The conservation of spin angular momentum obliges the electron to undergo a spin flip, transitioning from $|m = +1/2\rangle$ to $|m = -1/2\rangle$.

within the investigated z-range. Spin-polarized STM measurements acquired with a magnetic tip above Co bilayer islands also showed weak spin polarization at the Fermi energy [7, 74, 82–84].

4.5.2 Influence of the magnetization orientation

The spin polarization of the monolayer island shows instead some z-dependency (Fig. 4.14a), changing from $P = +0.2$ at $z = 100$ pm to $P = +0.05$ at $z = 20$ pm. This variation is attributed to the rotation of the molecular axis relative to

the z-axis, as predicted by DFT calculations (§ 2.2.3). In vacuum, the tilt angle is close to 10°, but approaches 0° when Nc comes into contact with the surface [1, 32]. To gain a deeper understanding of this behavior, we introduce the tip polarization (η_t) and the sample polarization (η_s), expressing the spin polarization of the tunnel junction as $P = \eta_t \eta_s$. The sample spin polarization reflects the net polarization in the sample's DOS

$$\eta_s = \frac{\rho_\uparrow - \rho_\downarrow}{\rho_\uparrow + \rho_\downarrow}. \tag{4.4}$$

The spin polarization η_t quantifies instead the spin momentum transfer during the spin excitation. Detailed calculations for this parameter are available in the work by Loth et al. [85]. In their study, they compare two distinct tunneling channels that result in the same transition from an initial state $|\Psi_i\rangle$ to a final state $|\Psi_f\rangle$. In the first channel, the inelastic electron undergoes a spin flip from $-1/2$ to $+1/2$, and the intensity associated with this transition is denoted as $T_\uparrow$. Whereas, in the second channel, the electron experiences a spin flip from $+1/2$ to $-1/2$, with an intensity labeled as $T_\downarrow$. Using these quantities, they derive η_t as follows:

$$\begin{aligned} \eta_t &= \frac{T_\uparrow - T_\downarrow}{T_\uparrow + T_\downarrow} \\ &= \frac{\left|\langle \Psi_f | \hat{S}^+ | \Psi_i \rangle\right|^2 - \left|\langle \Psi_f | \hat{S}^- | \Psi_i \rangle\right|^2}{2\left|\langle \Psi_f | \hat{\mathbf{S}} | \Psi_i \rangle\right|^2}. \end{aligned} \tag{4.5}$$

Applied specifically to our system, $\hat{S}^+$ and $\hat{S}^-$ represent the raising and lowering operators of the nickelocene spin, which is described by $|\Psi_i\rangle$ and $|\Psi_f\rangle$. In the case of a zero-tilt angle, the eigenstates are $|M = 0\rangle$, $|M = +1\rangle$ and $|M = -1\rangle$, resulting in $\eta_t = 1$, and the junction spin polarization simplifies to $P = \eta_s$. To determine how η_t changes when Nc is tilted on the tip apex, we introduce an angle θ between B_{ex} and the molecular axis and determine numerically the eigenstates $|\Psi_0\rangle$, $|\Psi_1\rangle$, and $|\Psi_2\rangle$ through Eq. 4.2, which we then insert in Eq. 4.5. The variation of η_t with respect to θ is presented in Fig. 4.14b. For small θ, the molecular axis of the Nc-tip aligns nearly parallel to the out-of-plane surface magnetization, and the measured spin polarization closely mirrors the sample polarization. This corresponds to the behavior encountered in the bi- and trilayer islands. Conversely, as θ approaches 90°, η_t exhibits a pronounced angular dependence. This behavior is characteristic of the monolayer island, where the molecular axis of the Nc-tip is almost perpendicular to the in-plane surface magnetization. For a perfect perpendicular alignment, the tip polarization becomes $\eta_t = 0$, resulting in a non-polarized tunnel junction ($P = 0$).

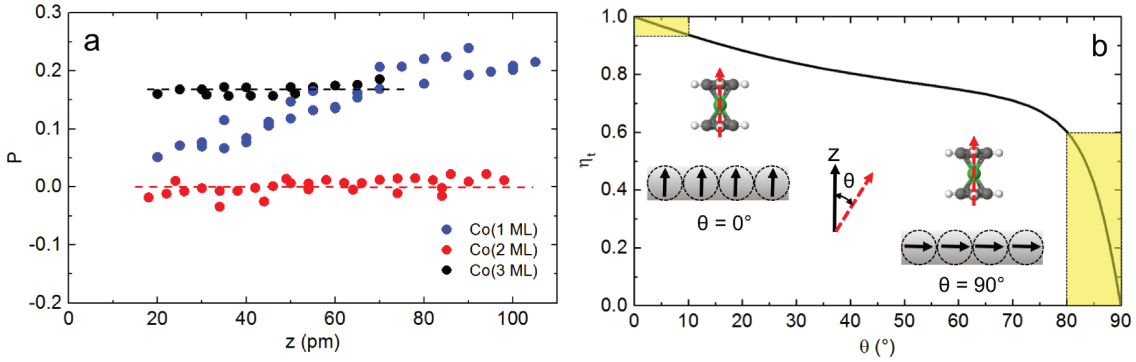

Figure 4.14: (a) Spin polarization as a function of distance z extracted from the d^2I/dV^2 spectra. The dashed lines are a guide to the eye. (b) Computed value of η_t as a function of the angle θ. The insets sketch the two extremes where $\theta = 0°$ (left) and $\theta = 90°$ (right). The light-yellow areas highlight a 10° tilt.

However, even a relatively small tilt angle of 12°, corresponding to $\theta = 78°$, is sufficient to elevate the tip spin polarization to +0.63. Assuming this tilt angle at $z = 100$ pm, we can estimate a sample in-plane polarization of $\eta_s = +0.32$ for the monolayer.

4.6 Spin-excitation lifetimes of a nickelocene tip

As mentioned in § 4.3, lifetime effects influence the line shape of the spin excitation spectra of Nc. Lifetime effects pertain to the finite duration of excited states of a spin system, which eventually decay back to the ground state through spontaneous emission or other relaxation processes. In laser rate equations, for example, lifetime effects are incorporated to describe the dynamics of population inversion and photon emission accurately. These equations account for the rates at which excited states decay and affect the temporal evolution of the laser output. A similar approach can be used to describe lifetime effects in spin systems and to connect them to the inelastic tunneling current [17]. Let us briefly recall the formalism describing this effect. The spin scattering of tunneling electrons by Nc generates spin excitations at the molecular tip, which is formally described by a transition from state $|\Psi_i\rangle$ to $|\Psi_j\rangle$. This event happens with a rate $r_{ji}^{s\leftarrow t}$ where electrons tunnel from the tip to the sample. Electrons tunneling from sample to the tip induce instead a transition with a rate $r_{ji}^{t\leftarrow s}$. A spontaneous de-excitation can also occur, which describes the spin-scattering of tip (substrate) electrons that interact with Nc and return to the tip (substrate) with a rate $r_{ji}^{t\leftarrow t}$ ($r_{ji}^{s\leftarrow s}$). The total rate is:

$$r_{ji} = r_{ji}^{s\leftarrow t} + r_{ji}^{t\leftarrow s} + r_{ji}^{s\leftarrow s} + r_{ji}^{t\leftarrow t}. \tag{4.6}$$

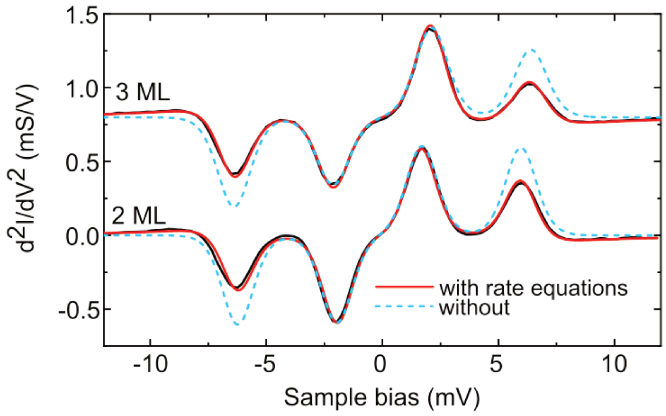

Figure 4.15: d^2I/dV^2 spectra acquired above a Co atom of a bilayer and a trilayer island at a distance of $z = 40$ and $z = 30$ pm, respectively. The feedback loop was opened at 100 pA and 1 mV. The trilayer spectrum is displaced upward by 0.8 mS/V. The solid red lines are simulations based on a dynamical scattering model that includes out-of-equilibrium spin states [57]. The dashed cyan lines are simulations at thermal equilibrium.

And depends on the barrier thickness, hence the tip-sample distance z. These scattering events determine the occupation of the spin states, which is expressed with the rate equation:

$$\frac{dn_i(t)}{dt} = \sum_j r_{ij} n_j(t) - r_{ji} n_i(t), \tag{4.7}$$

and lead to observable changes in the conductance of Nc as a function of bias [17, 85–87]:

$$I(V) = e \sum_{j,i} \left[r_{ji}^{t \leftarrow s}(V) - r_{ji}^{s \leftarrow t}(V) \right] n_i(t \to \infty, V) + b_0 G V. \tag{4.8}$$

Herein $n_i(t \to \infty)$ is the occupation of $|\Psi_i\rangle$ in the steady state regime of Eq. 4.7. The parameter b_0 is the fraction of current where electrons do not interact with Nc and G the differential conductance measured at zero bias. The lifetime of each spin state is determined by the relaxation rate in the absence of tunnel current as:

$$\tau_i = \left(\sum_j r_{ji}^{t \leftarrow t} \right)^{-1}. \tag{4.9}$$

Each spin state will in general have a different lifetime.

To simulate the d^2I/dV^2 line shape of Nc, the tunneling electrons are allowed to produce out-of-equilibrium occupations for the spin states (Eq. 4.7 and Eq. 4.8); the spin polarization of the current is also accounted for [17, 57]. Fitting this model to the measured spectra gives quantitative agreement (Fig. 4.15) and provides

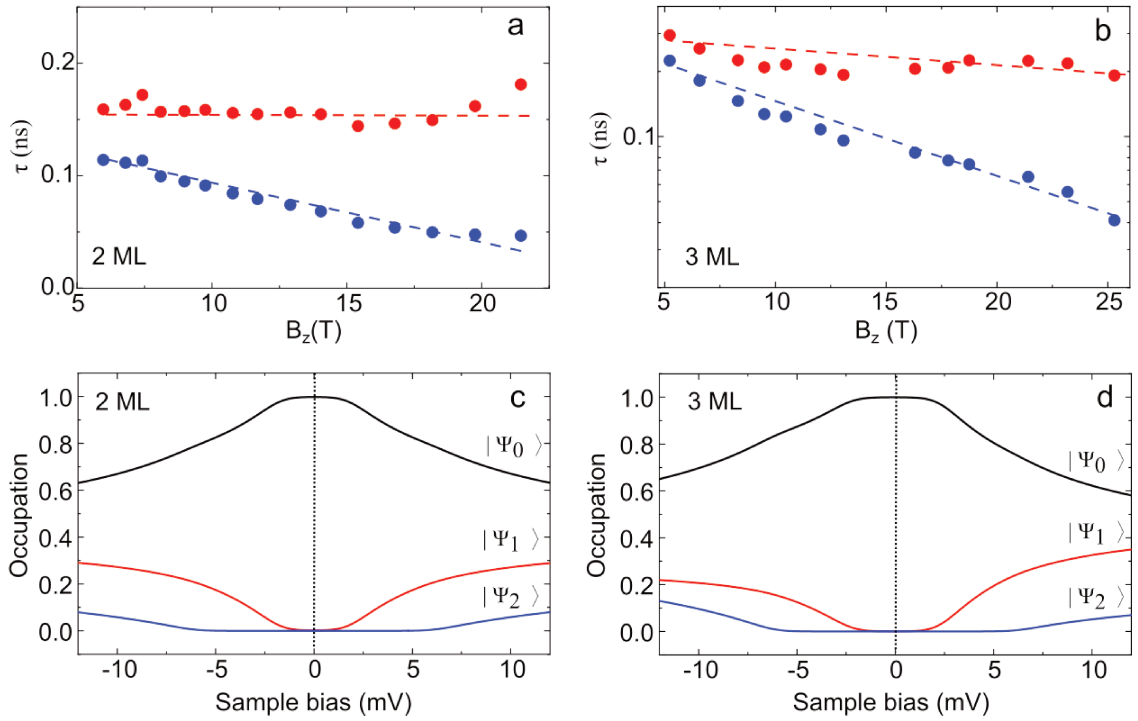

Figure 4.16: Lifetimes of the two excited states Ψ_1 (red dots) and Ψ_2 (blue dots) as a function of the exchange field above a bilayer island (a) and a 3 ML island (b). The dashed lines are a guide to the eye. Panels (c) and (d) present the spin-state occupation computed on the basis of the parameters used to fit the spectra in Fig. 4.15 for the bilayer and trilayer islands, respectively.

estimates for the lifetimes of the spin states. Figure 4.16a-b presents the evolution of the lifetime with exchange field. The data is extracted from the spectra acquired above a Co atom of a bilayer island where the exchange field is out of plane. At the lowest accessible exchange field (5 T), the two excited states $|\Psi_1\rangle$ and $|\Psi_2\rangle$ are nearly degenerate and have similar lifetimes of 0.17 ± 0.01 and 0.11 ± 0.01 ns, respectively. Measurable out-of-equilibrium effects can therefore be expected at a tunnel current of $I = e/\tau \gtrsim 1$ nA. The lifetime of $|\Psi_1\rangle$ is nearly constant with exchange field, while the lifetime of $|\Psi_2\rangle$ decreases to 0.04 ± 0.02 ns at the highest field explored. The field dependency is non-trivial and necessitates an analysis beyond the scope of this work [87]. Similar results are obtained for the trilayer island. For the lowest accessible exchange field, the lifetimes of the excited states $|\Psi_1\rangle$ and $|\Psi_2\rangle$ are 0.29 ns and 0.22 ns, respectively. When the exchange field is close to 13 T, the lifetime of $|\Psi_1\rangle$ is reduced to 0.2 ns while $|\Psi_2\rangle$ has its lifetime lowered to 0.1 ns. For the monolayer islands where the exchange field is in-plane, we did not observe any measurable difference when fitting the data with and without accounting for dynamical rate equations. This could suggest that the lifetime is shorter compared to the out-of-plane case.

For completeness, Fig. 4.16c-d present simulations of the time-averaged occupations based on our fitting parameters of Fig. 4.15. The occupations of the excited states $|\Psi_1\rangle$ and $|\Psi_2\rangle$ increase with bias at the expense of the occupation of the ground state $|\Psi_0\rangle$; the bias dependency is more pronounced for $|\Psi_1\rangle$. Unlike the bilayer island, the occupations of the trilayer island depend strongly on bias polarity due to their spin polarization [17, 86]. It is important to note that the alignment of the Nc magnetization changes as the excited states are populated. When neglecting the tilt angle of Nc, at thermal equilibrium, the Nc magnetization is in the plane of the cyclopentadienyl rings (see dashed lines at zero bias in Fig. 4.16 c-d), but based on the spin-state occupations it undergoes an out-of-plane rotation. For example, we predict a 26° rotation of the Nc magnetization when a bias of +12 mV applied above a trilayer island ($z = 30$ pm).

4.7 Concluding remarks

In summary, our investigation demonstrates the high sensitivity of an Nc-tip to surface magnetism and spin transport. A three-dimensional dataset of spin-excitation spectra allows for the construction of spatial maps of the exchange interaction, which resemble computed spin density maps. This represents a versatile and complementary option to employing force measurements in an atomic force microscope for detecting the magnetic exchange interaction between the tip and the sample [10, 12]. The maps offer atomic-level information on the spin orientation of the sample, making them valuable for magnetic imaging, particularly for intricate spin textures. Additionally, spatial maps of the surface spin polarization can be constructed by using the amplitude of the inelastic peaks—a facet we will explore in Chapter 6.

CHAPTER 5

Hydrogen-driven spin reorientation of a nanomagnet

Magnetic anisotropy plays a crucial role in determining the orientation of spins in metallic thin films and multilayers, thus constituting a critical aspect of spintronic device functionality. Among various approaches for controlling magnetic anisotropy, the incorporation of mobile ionic species in thin films through voltage-gated transport stands out as highly promising. Hydrogen, in particular, has proven superior to other ionic species, offering non-destructive and rapid toggling of magnetic anisotropy of multilayered heterostructures [88–90]. The rationale for hydrogen loading is built upon the observation that even subtle interactions, such as charge transfer between hydrogen and a metal atom, can trigger changes in the magnetic anisotropy and effective magnetic moment of the atom [91–95], while also affecting the exchange coupling among atoms [96, 97]. The magnetization orientation in ultrathin films can be modified by the adsorption and penetration of hydrogen [96–100]. This effect is observed not only in collinear magnetic films, but also in noncollinear ones [101, 102], where hydrogen has the ability to stabilize skyrmion states [103, 104]. The position and concentration of hydrogen play vital roles in this process [103, 105]. However, detailed studies at the microscopic level are still limited, in particular of model ultrathin magnets.

Single hydrogen molecules are commonly studied using STM. Hydrogen molecules assemble into coverage-dependent lattices on metal surfaces [106] and have a characteristic vibrational structure facilitating their identification [106, 107]. They can also be easily manipulated by the STM tip [108–110], adding chemical functionality to the microscope [111]. Dissociative adsorption of hydrogen molecules has also been

reported on magnetic surfaces, where hydrogen atoms then form superlattices [73, 112]. However, conducting spin-sensitive STM measurements on hydrogen-exposed magnets remains a challenging endeavor [73, 103], as it necessitates a magnetic tip, which, similar to the surface, is susceptible to hydrogen contamination [113]. Rigorous monitoring of the tip apex status is essential, preferably with an external magnetic field.

To overcome this challenge, we passivated the apex of a copper-coated W tip with a Nc molecule and focused on Co islands grown on Cu(111) and, unlike the islands in Chapter 4, exposed them to hydrogen. Magnetic exchange maps obtained with the molecular tip reveal the formation of a hydrogen superstructure on the island, as well as a 90° rotation of the magnetization compared to the pristine island. These findings are supported by *ab initio* calculations, which were performed by Roberto Robles (Centro de Física de Materiales CFM/MPC, CSIC-UPV/EHU, San Sebastián, Spain), Nicolas Lorente (CFM & Donostia International Physics Center, San Sebastián, Spain) Olivier Bengone and Christine Goyhenex (IPCMS, Strasbourg, France). The calculations suggest that hydrogen besides, adsorbing onto the Co surface must also penetrate the island in weaker quantities, primarily concentrated at the Co/Cu interface, to induce the rotation of the magnetization. These findings represent an advancement in our comprehension of how hydrogen alters the magnetism of a nanoscale system at the atomic level.

5.1 Sample exposure to hydrogen

The sample consisted of cobalt bilayer islands grown on Cu(111) and decorated with a small amount of Nc molecules. Details of sample preparation are given in § 4.1. Following the deposition of nickelocene, we initiated the hydrogenation of the sample. Hydrogen molecules constitute the predominant residual gas in the UHV chamber. In our UHV environment, where the pressure is $< 5 \times 10^{-11}$ mbar, hydrogen contaminates the Co islands over time. Achieving the desired hydrogen superstructure on the islands requires however an "efficient" hydrogenation. This consists in increasing the temperature of the cryostat to more than 17 K for less than 1 hour in order to prompt the release of H_2 from the gold-plated copper walls of the STM cryostat [114].

To investigate hydrogen exposure to cobalt, we employ two distinct operating modes of the molecular tip, as illustrated in Fig. 5.1a, which shows two conductance (G) versus tip displacement (δz) traces obtained above a pristine Co bilayer island. The first trace (solid black line) is acquired by opening the feedback loop at 50

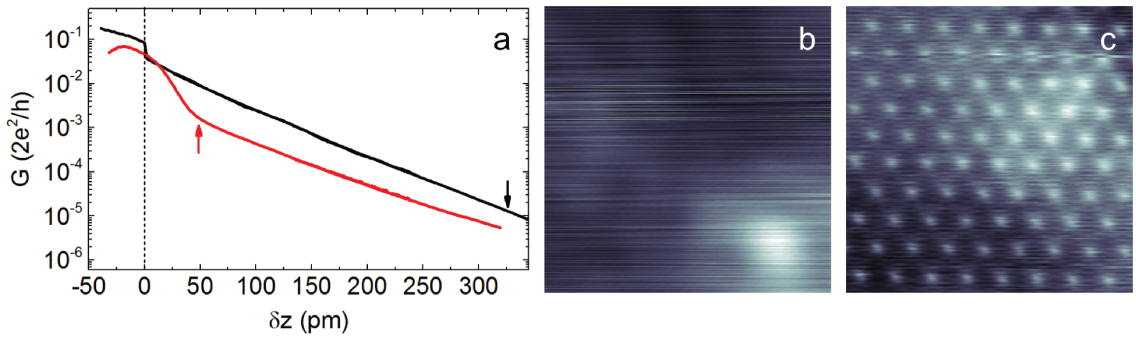

Figure 5.1: Conductance versus tip-sample distance acquired with an Nc-tip above a Co bilayer. The traces are obtained using two different feedback-loop opening parameters: 50 pA and 50 mV (solid black line) and 100 pA and 1 mV (solid red line). The opening positions are marked by arrows. The dashed line corresponds to the contact point between the Nc-tip and the Co surface. (b) Image of a Co bilayer with an Nc-tip (2×2 nm^2, 50 mV, 50 pA). (c) Image of a Co bilayer with the same Nc-tip as panel (b) but acquired with different tunneling parameters (2×2 nm^2, 1 mV, 100 pA).

pA and 50 mV. The trace is exponential, with a sharp change in slope marking the contact with the Co surface, similar to the trace presented in Fig. 4.1. From this trace, we deduce that the Nc-tip is approximately 325 pm from contact when the feedback loop is opened with these parameters (black arrow in Fig. 5.1a). The exchange interaction is absent in this case, resulting in a featureless image of the Co island (Fig. 5.1b). Thus, the Nc-tip functions as a standard STM tip. The second trace in Fig. 5.1a (solid red line) is obtained using the same Nc-tip by opening the feedback loop at 100 pA and 1 mV. This trace exhibits a faster-than-exponential behavior before reaching contact. From this trace, we deduce that the Nc-tip is 50 pm away from contact when the feedback loop is opened with this tunnel current and bias (red arrow in Fig. 5.1a). In this case, the exchange interaction is active, and when scanning the Co surface, a magnetic corrugation is observed (Fig. 5.1c). In the following sections, we use these two sets of tunneling parameters: 1 mV and 100 pA for an active exchange interaction (defined hereafter as the low-bias mode), and 50 mV and 50 pA for the absence of exchange interaction (defined as the high-bias mode). This approach allows us to visualize the electronic and magnetic properties independently.

5.2 Hydrogen superstructure on a Co island

To determine the hydrogen coverage on a nanoscale island, we employed the Nc-tip in the high-bias mode. Figure 5.2a shows a typical image of an island after hydrogen

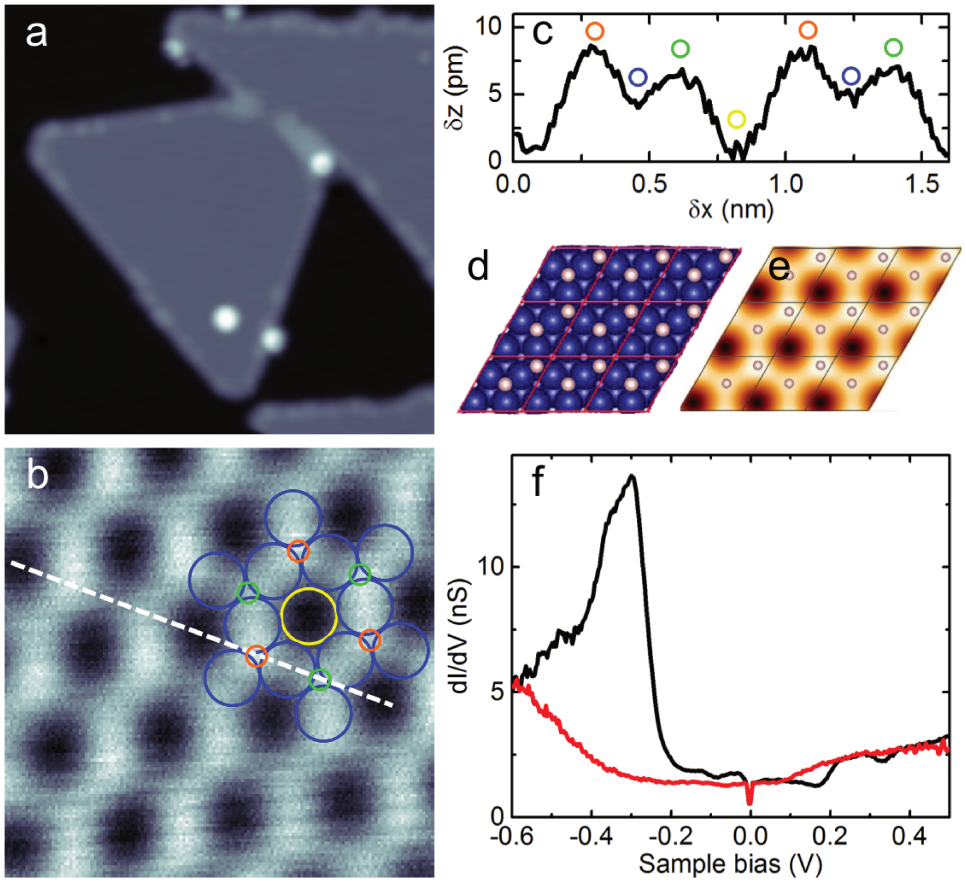

Figure 5.2: (a) Constant-current image of H-covered Co bilayer islands on Cu(111) (image size: 20×20 nm^2, sample bias: 50 mV, tunnel current: 50 pA). The bright spots are Nc molecules. (b) Close-up view of the island (1.7×1.7 nm^2, sample bias: 50 mV, tunnel current: 50 pA) with 2H-(2×2) superstructure [Co(I): yellow, Co(II): blue, H(I): green, H(II): orange]. The Co network corresponds to that of the pristine island before hydrogen exposure. (c) Height profile acquired along the dashed line indicated in (b). Coloured circles indicate the position of the H and Co atoms. (d) Model structure of 2H-(2×2) (Co: blue, H: white) and (e) corresponding DFT-computed constant-current topography (simulation done at 100 mV and 1 nA). Circles represent H atoms. (f) Typical dI/dV spectra acquired on H-contaminated (solid red line) and pristine islands (solid black line). Feedback loop opened at $G = 2.6\,10^{-5}\,G_0$ (in units of $G_0 = 2e^2/h$).

exposure, which appears similar to a pristine island. To visualize the presence of hydrogen atoms, it is necessary to zoom in on the island. A close-up view of a Co island is presented in Fig.5.2b, along with an overlaid simulation of the Co network of the pristine island. Hydrogen atoms are positioned on the hollow sites of the Co surface and alternate between two distinct hollow sites, resulting in a 2 pm difference in their apparent height (Fig.5.2c). The hydrogen coverage is 0.5 monolayers (ML), indicating that hydrogen is arranged in a 2H-(2×2) superstructure (Fig. 5.2d).

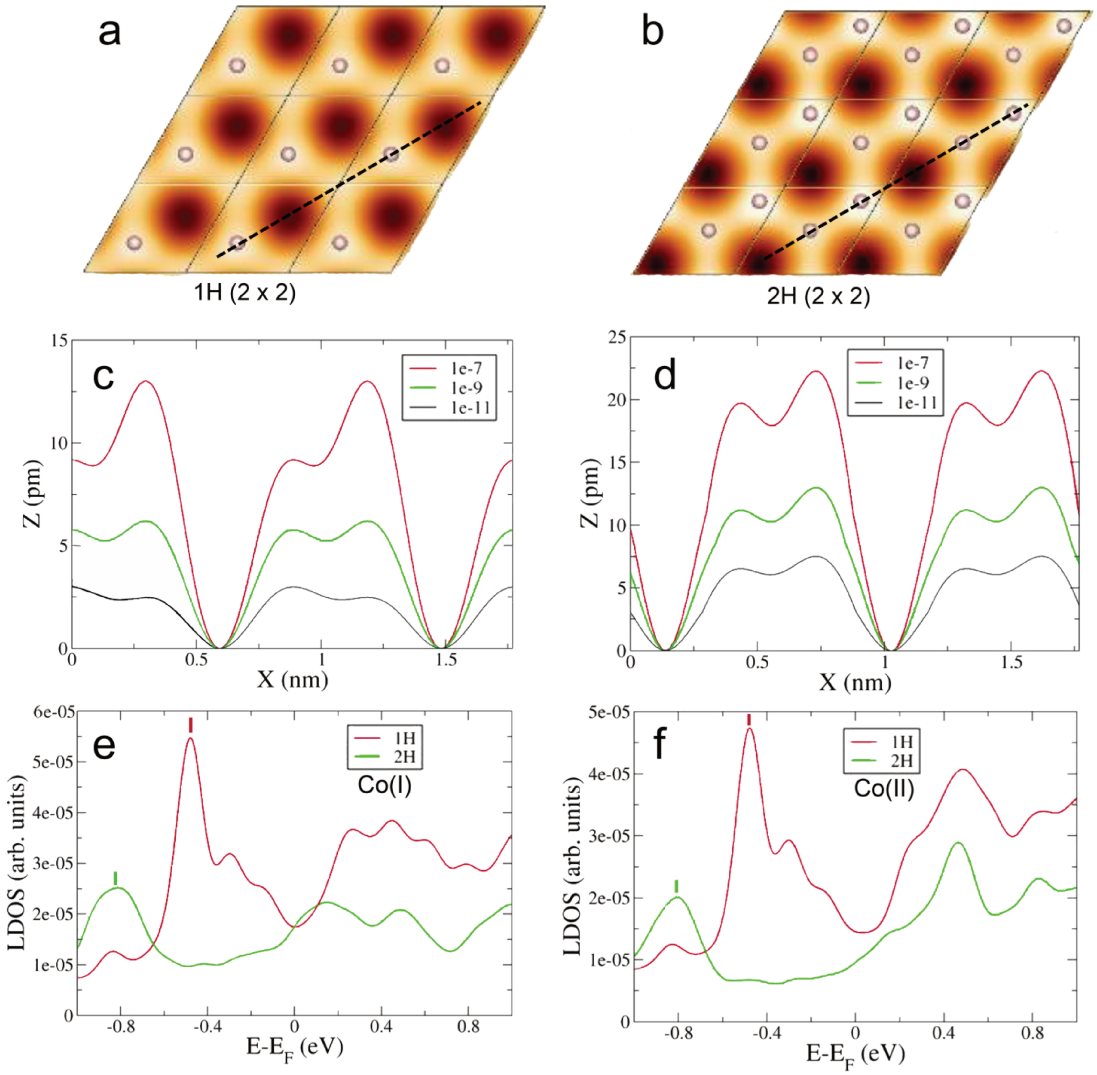

Figure 5.3: (a)-(b) Computed constant-current images of the 1H-(2 × 2) and 2H-(2 × 2) superstructures on a cobalt bilayer on Cu(111), respectively. The images were computed at 0.1 V and 1 nA. Circles represent hydrogen atoms. Panels (c) and (d) show the height profiles acquired along the dashed lines indicated in (a) and (b), respectively for various set currents. Panels (e) and (f) present the computed LDOS at 300 pm above Co(I) and Co(II), respectively. The solid red lines represent the LDOS for cobalt in the 1H-(2 × 2) superstructure, while the solid green lines represent the LDOS for cobalt in the 2H-(2 × 2) structure. The vertical tics indicate the position of dominant *d*-peak observed in tunneling spectroscopy at negative bias.

The unit cell of the superstructure contains two Co atoms: One at the center of a hexagon without neighboring H atoms [noted Co(I)], and a second, which has two neighboring H atoms [noted Co(II)]. The apparent height of Co(II) is 4 pm greater than that of Co(I). To corroborate these observations, DFT calculations were carried out, yielding good agreement with the experimental images (Fig. 5.2e). The strongest corrugation in the computed image corresponds to hydrogen in an

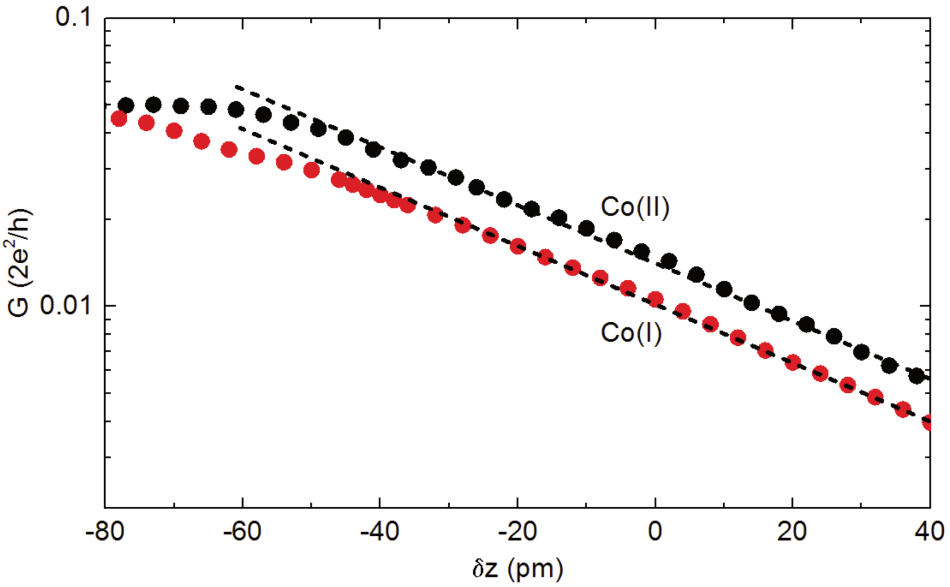

Figure 5.4: Conductance versus tip displacement traces acquired above Co(I) (red circles) and Co(II) (black circles) using an Nc-tip. The feedback loop was opened above Co(I) at 11 mV and 9 nA.

hcp site [noted H(I)], while the weaker corrugation corresponds to hydrogen in an *fcc* site [noted H(II)].

This assignment, however, is arbitrary. The 1H-(2 × 2) superstructure, where one H atom is present in a (2 × 2) Co unit cell corresponding to a 0.25 ML coverage, is in fact indistinguishable from its 2H counterpart in the computed images. This is shown in Figs.5.3a and 5.3b, where we used the Tersoff-Hamann approximation (§ 3.3) to compute the constant-current images of the 1H-(2 × 2) and 2H-(2 × 2) superstructures, respectively. The superstructures exhibit similar corrugations for currents ranging from 10 pA to 100 nA (Figs. 5.3c-d). Differentiating between the 1H-(2 × 2) and 2H-(2 × 2) superstructures requires tunneling spectroscopy as well. Figure 5.2f presents a typical dI/dV spectrum of a pristine Co island, revealing a prominent peak at −0.33 eV, arising from minority d_{z^2} states hybridized with $s - p$ states (§ 4.2). The sharp feature at zero-bias is due to the inelastic tunnel current of the Nc-tip. After H exposure, the peak shifts out of our energy window, *i.e.*, below −0.6 eV. This behavior is consistent with the computed LDOS for both Co(I) and Co(II) in the 2H-(2 × 2) superstructure (solid green lines, Fig. 5.3e and 5.3f). It contrasts with the LDOS of a 1H-(2 × 2) superstructure, which maintains instead a spin-polarized *d*-structure comparable to the pristine surface (solid red lines, Fig. 5.3e-f). Hence, the islands in this study exhibit a 2H-(2×2) superstructure after hydrogen exposure.

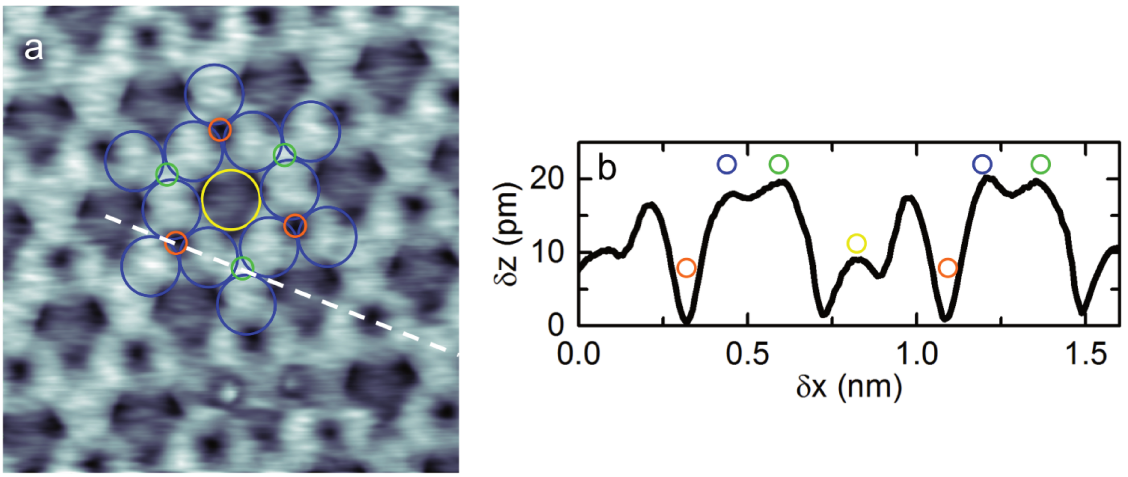

Figure 5.5: (a) Low-bias constant-current image of an H-covered Co bilayer island (1.7×1.7 nm^2, 1 mV, 100 pA) with simulated 2H-(2×2) superstructure [Co(I): yellow, Co(II): blue, H(I): green, H(II): orange]. (b) Height profile acquired along the dashed line indicated in (a). Coloured circles indicate the position of the H and Co atoms.

5.3 Magnetization in the presence of hydrogen

5.3.1 Evidence for magnetization rotation

Prior to investigating the magnetic properties, we focus on calibrating the tip-sample distance as we did for the pristine island (Fig. 4.1). Figure 5.4 presents typical traces acquired above Co(I) (red circles) and Co(II) (black circles). The traces differ from those acquired above the pristine cobalt island, where an exponential dependence on tip-Co distance is observed until a marked inflection occurs close to the quantum of conductance ($G_0 = 2e^2/h$), which signals contact formation (see § 4.1). Instead, the traces above Co(I) and Co(II) exhibit a change of the exponential decay length, λ, above $G = 0.03\,G_0$, which is more pronounced for Co(II) than Co(I). The conductance remains well below G_0 and no clear inflection is observed. This behavior resembles the conductance observed when approaching an organic molecule [111] or a CoH complex [94] with a hydrogen-functionalized tip. This results from tip-sample repulsion at small distances, which causes the vacuum gap to shorten more slowly than expected as the piezoelectric tube extends. Since the contact point cannot be clearly defined, we express the distance in terms of a tip displacement (δz). The zero displacement $\delta z = 0$ is set to a conductance of $G = 0.01\,G_0$ above a Co(I) atom.

To investigate the magnetism of the 2H-(2×2) superstructure, the surface is imaged by using the low bias mode of the Nc-tip. The low-bias image of Fig. 5.5a

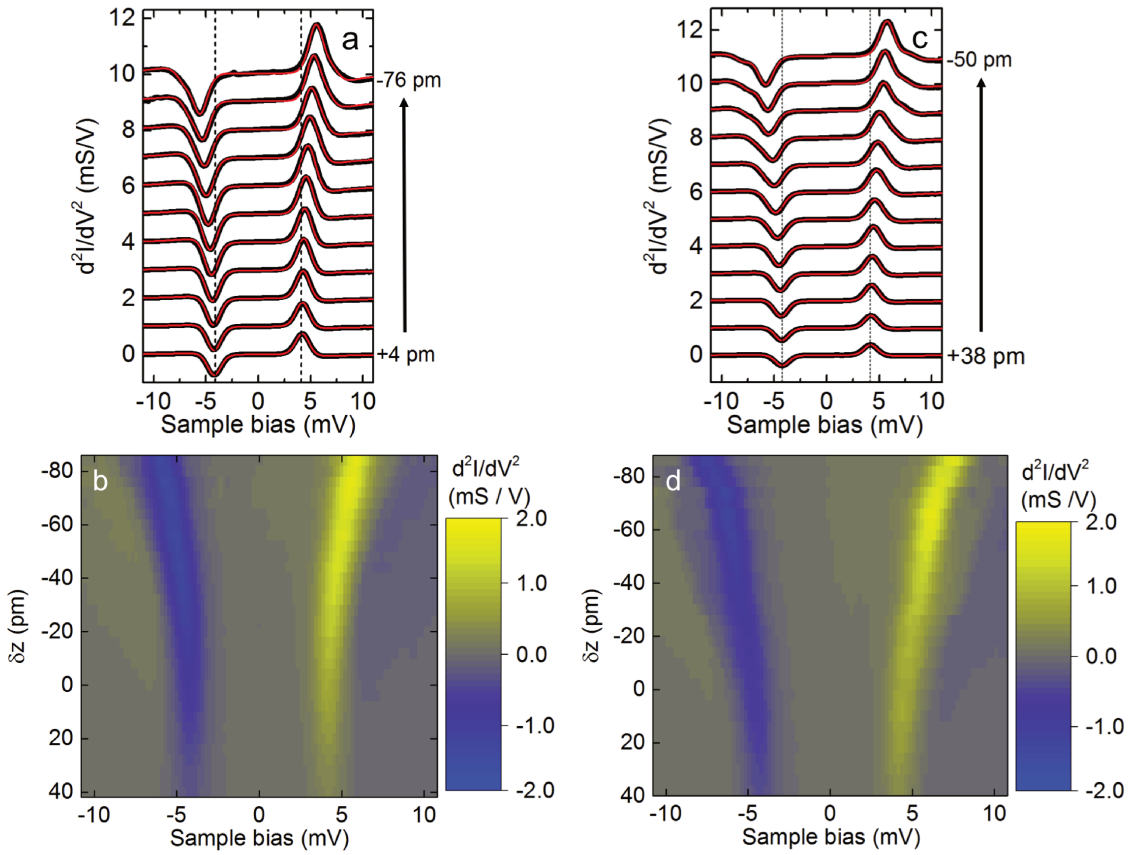

Figure 5.6: Panels (a) and (b) present the d^2I/dV^2 spectra and the 2D intensity plot acquired above Co(I) for different tip displacements. Panels (c) and (d) present the d^2I/dV^2 spectra and the 2D intensity plot acquired above Co(II). The spectra are displaced vertically by 1 ms/V from one another. Red lines: Simulations based on a dynamical scattering model [57].

differs from the one previously recorded at higher bias (Fig. 5.2). The Co(I) and Co(II) show a stronger contrast due to their distinct corrugation (Fig. 5.5b), with a measured difference of 8 pm between them. The two hydrogen atoms are also visible, but their contrast is reversed compared to the high-bias image, H(I) now exhibiting a height 20 pm larger than H(II). To determine the orientation of the island magnetization, we recorded a series of d^2I/dV^2 spectra by approaching the tip above each Co atom. As shown in Figs. 5.6a-b for Co(I) and in Figs. 5.6c-d for Co(II), at $\delta z = 0$ the spectra exhibit a peak and a dip at biases of $+4.0$ and -4.0 mV. These features are usual for Nc-tips above non-magnetic copper (§ 2.2.3) and indicate the absence of exchange interaction, or an interaction too weak to be detected. As the tip approaches the surface, the peak (dip) for both Co atoms shifts upward (downward) in energy, indicating exchange coupling between the Nc-tip and Co. The spectra can only be reproduced using a dynamical scattering model with the magnetization of the islands laying in-plane (solid red lines in Figs. 5.6b and

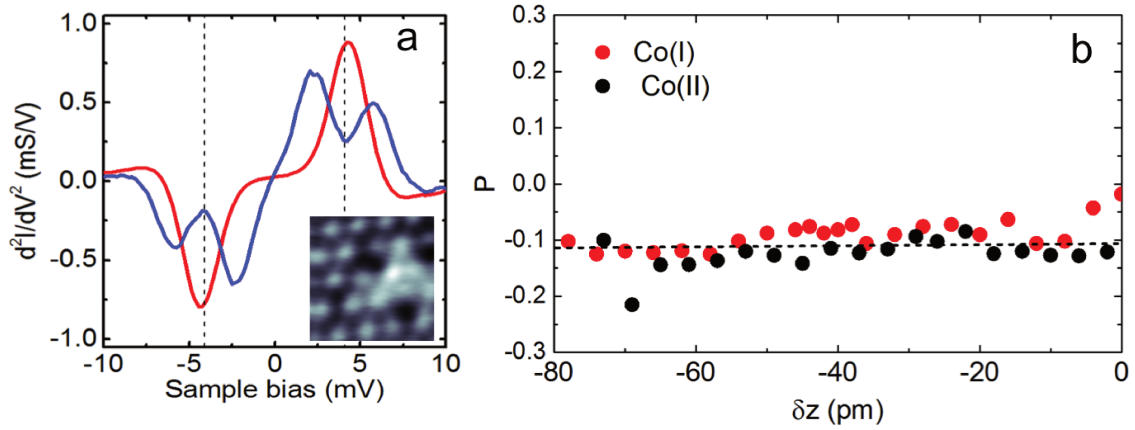

Figure 5.7: (a) d^2I/dV^2 spectra acquired before and after hydrogen removal (solid red line: before, solid blue line: after). The dashed lines indicate the non-shifted peak (dip) position. Inset: Image acquired after removal (1×1 nm^2, 1 mV, 100 pA). (b) Spin polarization versus δz from the d^2I/dV^2 spectra of Co(I) and Co(II). The dashed line is a guide to the eye.

5.6d) [57]. Peaks and dips at opposite voltage polarities exhibit different amplitudes. This is clearly visible in the spectrum of Fig.5.7a (solid red line). This disparity arises from the selection rule for spin excitation [17], and their intensity ratio provides insight into the magnitude and sign of the spin polarization of the tunnel junction (§ 4.5). The spin polarization found from our simulated spectra is constant with tip displacement with $P = \eta_s \cdot \eta_t = -0.12$ for both Co(I) and Co(II) (Fig.5.7b), where η_t is the tip spin polarization and η_s, the surface spin polarization. As we showed in Chapter 4, the spin polarization for a surface with in-plane magnetization can change when the tilt angle of Nc moves away from its equilibrium position of 12° (§ 4.5.2). The constant value for P indicates that Nc maintains this tilt angle when the tip is displaced above the Co(I) and Co(II) atoms. From Fig. 4.14b we have then $\eta_t = 0.65$, which yields an in-plane spin polarization of $\eta_s = -0.19$. The different spin polarization found compared to the pristine surface indicates that the DOS of both types of Co atoms has changed, as also anticipated by our LDOS calculations presented in Figs. 5.3e-f.

The spectra differ from those of the pristine island. This becomes evident upon removing hydrogen by locally heating the island with the STM tip [112]. Hydrogen removal is achieved through several 1 V-pulses applied for a few seconds at a tunneling current of 10 μA. It specifically targets the island beneath the tip, without perturbing neighboring islands. After the procedure, the Nc-tip is lost and must be re-prepared. Following hydrogen removal, the Co network is restored and Co atoms display a characteristic spin-split d^2I/dV^2 spectrum (solid blue line, Fig.5.7a), indicating out-of-plane magnetization and nearly-zero spin polarization as we observed

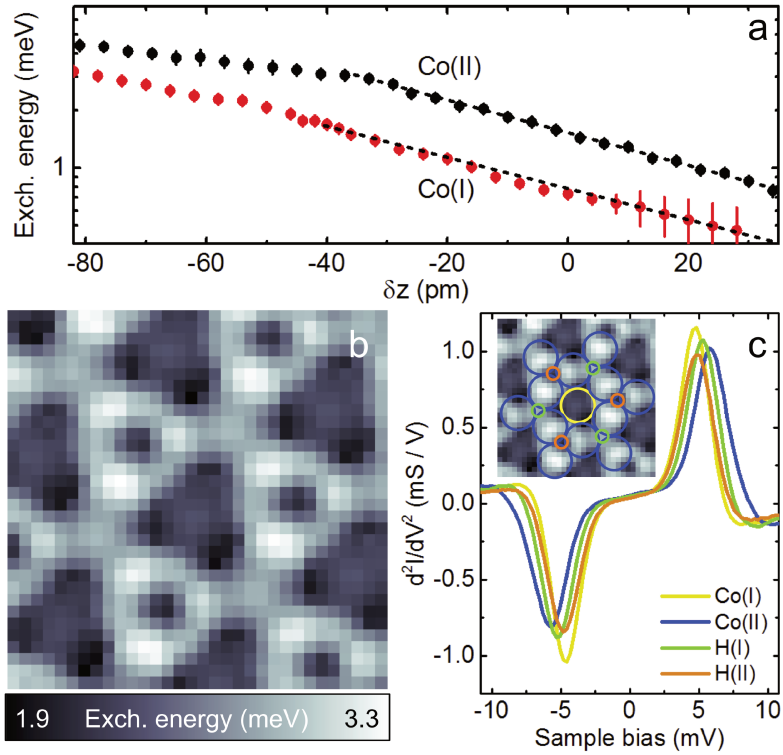

Figure 5.8: (a) Exchange energy versus δz extracted from the d^2I/dV^2 spectra of Co(I) and Co(II). The dashed lines represent the exponential fit described in the text. (b) Spatial map of the exchange energy acquired at a fixed distance above a Co island ($\delta z = -40$ pm). Lateral (vertical) tip drift between each spectrum acquisition was kept below 10 pm (5 pm) by dynamically tracking a local maximum. (c) d^2I/dV^2 spectra above Co(I), Co(II), H(I) and H(II) [Co(I): yellow, Co(II): blue, H(I): green, H(II): orange].

for the pristine islands in Chapter 4. The 2H-(2×2) superstructure can therefore be associated to a rotation of the island magnetization, from out-of-plane to in-plane.

5.3.2 Exchange maps and computed spin density

Figure 5.8a presents the distance-dependent behavior of the exchange energy derived from the spectra above Co(I) and Co(II). For $\delta z > -40$ pm, the exchange energy exhibits an exponential variation $\exp(-\delta z/\lambda)$ with a decay length of $\lambda = 46 \pm 10$ pm for both atoms, similar to a Co atom of the pristine island (§ 4.4). Notably, the exchange energy above Co(II) is nearly twice as strong as the exchange energy measured above Co(I). When the tip is approached further ($\delta z < -40$ pm), the exchange energy becomes less sensitive to tip displacement, showing a smaller decay length. As for the current-versus-displacement traces of Fig.5.4, this behavior arises from an Nc-hydrogen repulsion that is more pronounced on Co(II) than on Co(I).

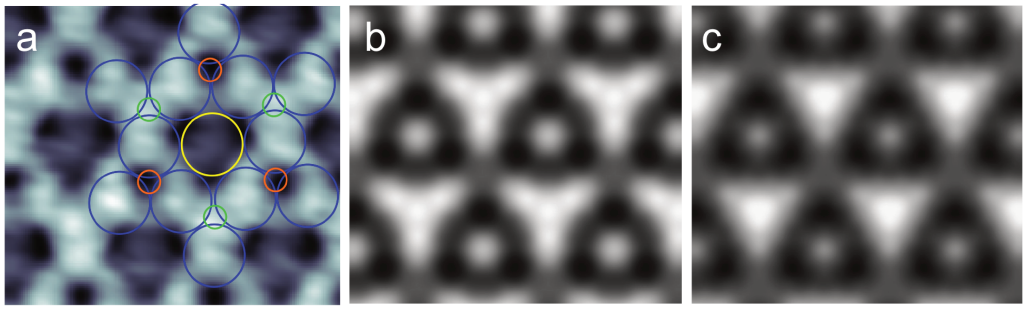

Figure 5.9: (a) Low-bias image (1 mV, 100 pA, 1.2×1.1 nm^2) above a bilayer and computed spin density map at a fixed distance of (b) 200 pm and (c) 250 pm above an H atom.

As discussed in § 5.3.1, this repulsion does not affect the tilt angle of Nc for the tip displacements used.

The exchange coupling also varies across the surface. To visualize these variations, we acquire a voxel image (§ 3.10) consisting of a dataset in the form of $d^2I/dV^2(x, y, V)$, while maintaining a fixed tip-sample distance. We then determine the exchange energy at each lateral tip position by fitting the spectra. Figure 5.8b shows the resulting magnetic exchange map, while Fig. 5.8c displays d^2I/dV^2 spectra at the Co and H atoms. The exchange map is similar to the low-bias image of Fig. 5.6a since the corrugation in both images is governed by the shift of the inelastic threshold energy. If the low-bias image allows quickly assessing the lateral dependence of the exchange coupling, it is done at the expense of a quantitative estimate of the exchange energy. The exchange map reveals a corrugation of the exchange energy over a 1.5 meV range, with clear differences among Co and H atoms. However, these differences are not reflected in their magnetic moments. The DFT computed magnetic moments are 1.9 μ_B and 1.6 μ_B for Co(I) and Co(II), respectively, while the hydrogen atoms exhibit weak magnetism, with H(I) at -0.02 μ_B and H(II) at -0.01 μ_B.

Consistent with findings on pristine Co surfaces (§ 4.4), the magnetic exchange map is satisfactorily reproduced by the DFT-computed spin density. For comparison, we present the experimental data in Fig.5.9a and the spin density map in Figs.5.9b-c. Remarkably, this agreement extends to H-covered Co islands of varying Co island thicknesses (Fig.5.10). The maps indicate that Co(II) exhibits a stronger spin density compared to Co(I) at all distances from the surface, aligning with the experimentally observed stronger exchange energy. The observed differences in the Co atoms, also visible in their computed LDOS (Fig.5.3e-f), are attributed to varying hybridization with the hydrogen atoms. Additionally, the spin density of H(II) is stronger than that of H(I), confirming the contrast reversal seen experimentally

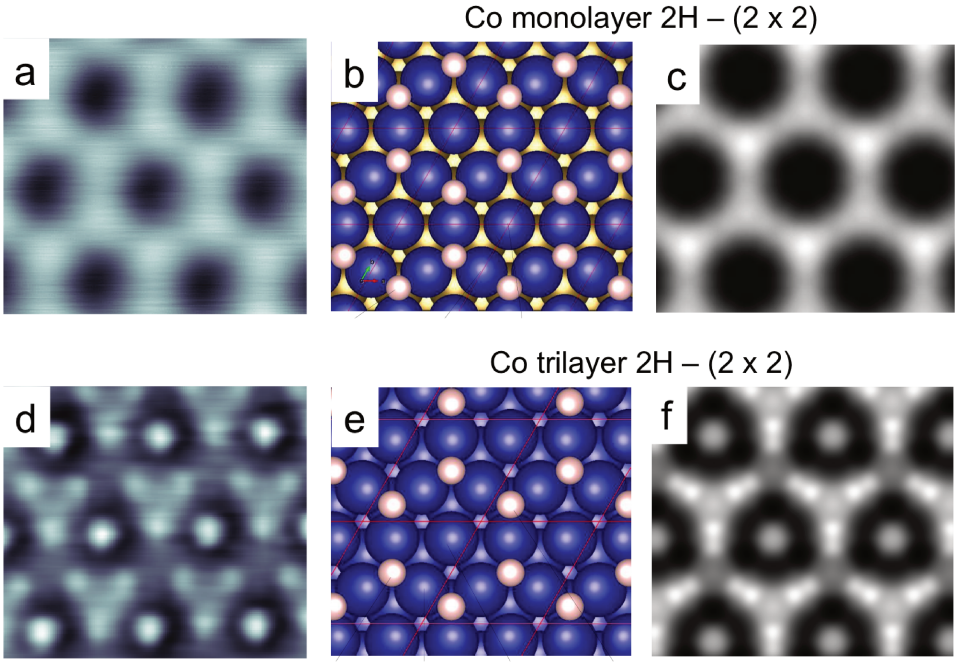

Figure 5.10: (a) Low-bias image (1.2×1.1 nm^2) acquired with a Nc-tip positioned above a Co monolayer on Cu(111) covered with hydrogen. (b) Model structure of a Co monolayer with 2H-(2×2) superstructure (Co: blue, H: white, Cu: yellow) and (c) Corresponding DFT-computed spin density map 200 pm above the H atoms. Panels (d) to (f) present same results as for panels (a) to (c) but acquired on a Co trilayer on Cu(111) covered with hydrogen. The spin density (f) is also computed 200 pm above the H atoms.

for these hydrogen atoms compared to the high-bias images.

5.4 Computed magnetic anisotropy energy

5.4.1 Magnetic anisotropy energy versus hydrogen coverage

Experimental evidence indicates that the presence of hydrogen coincides with a rotation of the Co magnetization from out-of-plane to in-plane. To gain deeper insight into this finding we have performed a computational study of hydrogen adsorption and its impact on the island's magnetization orientation. The key quantity to calculate is the Magnetic Anisotropy Energy (MAE) which is the sum of two contributions. The first contribution, known as the magnetocrystalline anisotropy energy (MCA), stems from the spin-orbit coupling (SOC). The SOC interaction is described by the Hamiltonian $H_{SOC} = \xi(\hat{L} \cdot \hat{S})$, where ξ is the SOC constant, $\hat{L}$ is the orbital angular momentum operator, and $\hat{S}$ is the spin operator. This term couples the electron spin state with its orbital state, leading to energy shifts that depend on the

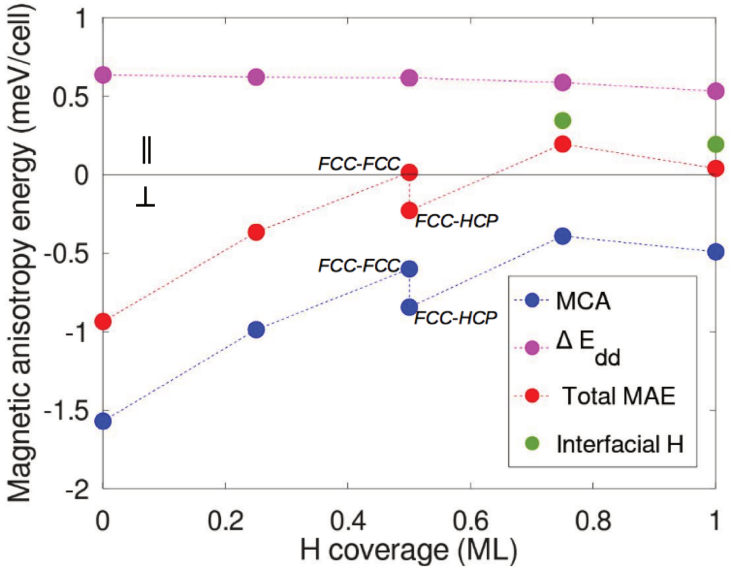

Figure 5.11: MAE versus surface hydrogen coverage (ML). Blue: MCA Energy; magenta: Shape anisotropy, ΔE_{dd}; red: Total MAE. The two additional values represented by the green circles correspond to the MAE of the configurations with 0.5 ML of H at the surface plus 0.25 ML and 0.50 ML of H at the Co/Cu interface. These values are respectively located at the equivalent 0.75 ML and 1 ML coverages. They correspond to Fig. 5.14a and Fig. 5.14b, respectively. For convenience, the energy values are given in meV/cell where the considered Co 2×2-cell contains 8 Co atoms.

relative orientation of the spin and orbital moments. It dictates the preferred alignment direction of magnetic moments within the material arising from the crystalline structure and symmetry. The second component, termed shape anisotropy, arises from the geometric shape of the magnetized object. It is driven by magnetostatic dipole-dipole interactions and manifests as a tendency for the magnetic moments to align in a specific direction dictated by the object's geometry. A negative sum of the two contributions, *i.e.* a negative MAE, corresponds to out-of-plane magnetization (denoted as $\perp$), while a positive value indicates in-plane magnetization (denoted as $\parallel$). The MCA is calculated by using the DFT. The shape anisotropy is further calculated by using as input the interatomic distances and spin magnetic moments as obtained in DFT calculations. More details can be found in Appendix B. To achieve the DFT calculations within reasonable computational times, we consider infinite bilayers of Co on a Cu(111) substrate which is a reasonable approximation considering that the triangular islands observed in experiments have sides measuring between 10 and 30 nm. Note also that for these island sizes, the shape anisotropy in a triangle is almost the same than the one of an infinite film of the same height. The configurations of interest, including hydrogen, are modeled using a 2×2-(111)

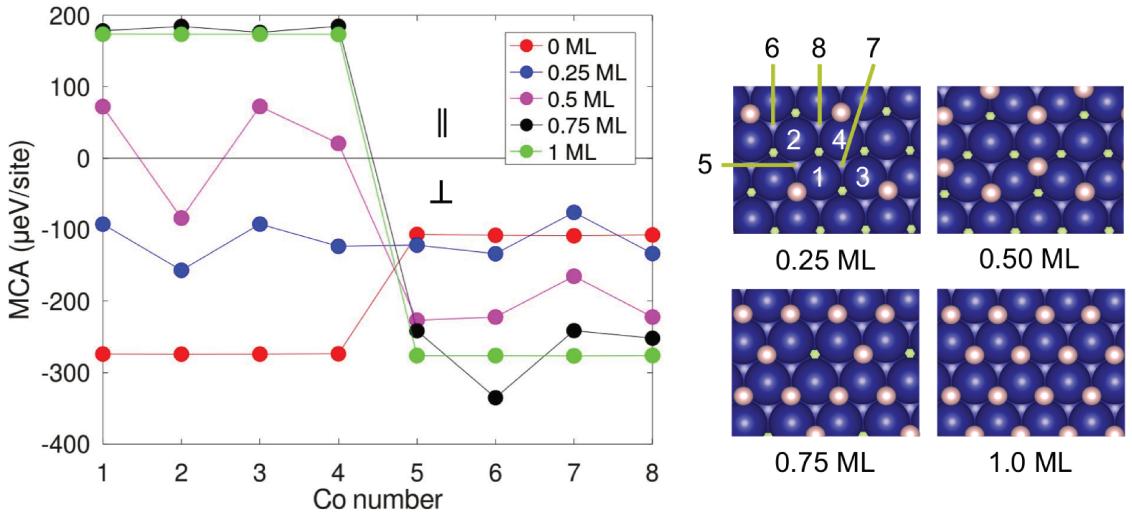

Figure 5.12: Local site analysis of the MCA. The abscissa indicate the number of the Co atom in the cell: $1-4$ for the surface layer and $5-8$ for the first Co layer.

supercell comprising 2 layers of Co (8 Co atoms) and 9 layers of underlying Cu (36 Cu atoms).

In the first step of this theoretical study, we consider only the hydrogen adsorption on top of the Co bilayer. We vary the hydrogen coverage from 0 to 1 ML and calculate the MAE for each coverage. Since these calculations are conducted using a $2 \times 2 - (111)$ cell configuration, these coverages correspond to the addition of 0 to 4 hydrogen atoms per unit cell on the (111) surface. The H atoms are positioned in hollow *fcc* sites. For the 0.5 ML coverage we also consider a superstructure alternating *fcc* and *hcp* positions as more stable, in agreement with STM experiments. The results are presented in Fig. 5.11. For pristine Co (0 ML of H), the MCA is negative and exceeds the shape anisotropy, resulting in a out-of-plane magnetization (MAE < 0). The main effect of adding hydrogen is to bring the MAE close to zero. This is driven by the MCA changing from -1.5 to -0.5 meV/cell, while the shape anisotropy remains constant at 0.6 meV/cell. At a hydrogen coverage of 0.5 ML, the two contributions compensate, resulting in an MAE that is nearly zero. Above 0.5 ML, the further growth of the MCA is slower but sufficient to favor in-plane magnetization. Thus, the MCA evolution with hydrogen coverage is the driving force behind the rotation of the magnetization toward the in-plane configuration.

A deeper understanding of the physical origin can be gained through a Co site-resolved analysis, which involves plotting the MCA for each Co site (Fig. 5.12). As the H coverage on the surface increases, the MCA increases at the Co sites on the surface (numbered 1 to 4 in Fig. 5.12). The MCA becomes large and positive above 0.5 ML, favoring an in-plane orientation of the magnetization. In contrast, the Co

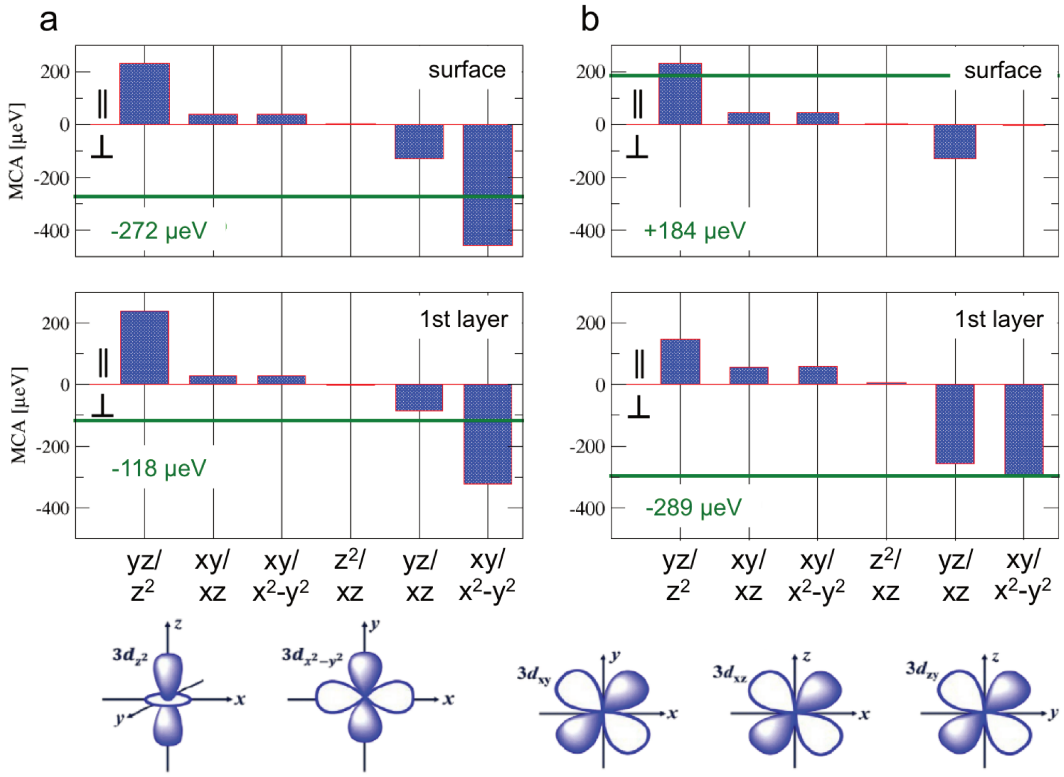

Figure 5.13: Orbital-resolved analysis of the MCA for a (a) pristine Co bilayer, (b) a Co bilayer with a 1 ML hydrogen-covered surface. The top and bottom panels correspond to the Co surface and to the Co of the first layer, respectively. The green line corresponds to the total MCA per layer. The computation uses a Co supercell-1 $\times$ 1 and 36 $\times$ 36 $\times$ 1 k-points to ensure the best possible precision.

sites of the first layer (noted 5 to 8 in Fig. 5.12), which have no hydrogen atoms as nearest neighbors, show a decrease in MCA when the H coverage is > 0.5 ML, thus favoring an out-of-plane magnetization. Adding up all the MCA per site yields a negative value, as shown in Fig. 5.11.

5.4.2 Impact of Co-H hybridization

The different MCA for surface and first-layer Co atoms can be attributed to their hybridization with H atoms. For instance, it has been shown that hydrogen absorption in Pd/Co/Pd thin films changes the relative importance of different d orbitals in their contribution to MCA [105]. To elucidate the relation between MCA and d orbitals, we use our DFT calculations including SOC to compute the matrix elements $\langle\psi_i|\hat{L}\cdot\hat{S}|\psi_j\rangle$, where $|\psi\rangle$ corresponds to a $3d$ state of Co. These matrix elements allow us to estimate the contribution to MCA from each pair (ψ_i, ψ_j) of d atomic-like orbitals. The orbital-pair contributions to the MCA are represented as bar diagrams in Fig. 5.13, where we compare a pristine and an H-covered Co bilayer.

In particular, we consider a Co bilayer with its surface fully loaded with hydrogen (1 ML coverage) to highlight the impact of Co-H hybridization on the MCA. As shown in Fig. 5.13, only three pairs of orbitals have a sizable contribution to the MCA: (yz, z^2), (yz, xz), and $(xy, x^2 - y^2)$. For the pristine Co bilayer (Fig. 5.13a), similar observations can be made for both the surface Co layer (top panel) and the first Co layer (bottom panel). The orbital pair $(xy, x^2 - y^2)$, which includes orbitals parallel to the surface, gives the strongest contribution to MCA and favors an out-of-plane orientation of the magnetization. The (yz, xz) orbital pair contributes less to MCA while also favoring an out-of-plane orientation. The (yz, z^2) orbital pair, which includes orbitals perpendicular to the surface, favors an in-plane orientation. Overall, the MCA of both the surface and the first layer is negative (green line in Fig. 5.13a). Upon adsorption of 1 ML of hydrogen and its hybridization with the Co surface atoms, drastic changes are observed (Fig. 5.13b). The out-of-plane MCA related to $(xy, x^2 - y^2)$ is suppressed in the Co surface layer (top panel), favoring in-plane magnetization for the surface. Consequently, the MCA of the surface becomes positive (green line in Fig.5.13b). This change is partly compensated in the Co first layer by the increased contribution to MCA of the (yz, xz) orbital pair (bottom panel), which favors out-of-plane magnetization. Overall, hydrogen hybridization with Co drives complex changes in the MCA of the Co bilayer but is insufficient alone to cause a rotation of the magnetization from out-of-plane to in-plane. Only when considering the contribution of shape anisotropy can a reversal of the orientation be achieved.

5.5 Considerations on hydrogen insertion

5.5.1 Effect of hydrogen loading on the magnetic anisotropy

The above considerations regarding the MCA per Co site lead us to consider the possibility of H insertion as an enhancing factor of the rotation of the island magnetization towards an in-plane orientation. We start from a coverage of 0.5 ML where the hydrogen is present only on the surface in a 2H-(2×2) superstructure, and progressively insert H atoms in octahedral sites within the island. We retain the configurations displaying in-plane anisotropy as in the experiment, and energetically most stable. We find that up to 1 ML coverage, it is more favorable to load the Co/Cu interface. The insertion of 1 or 2 H atoms (corresponding respectively to a coverage of 0.75 and 1 ML) can be carried out at different locations among the 4 available sites in the 2×2 cell. Ultimately, however, only one possibility for each coverage leads to an increase of the MCA and *a fortiori* of the total magnetic

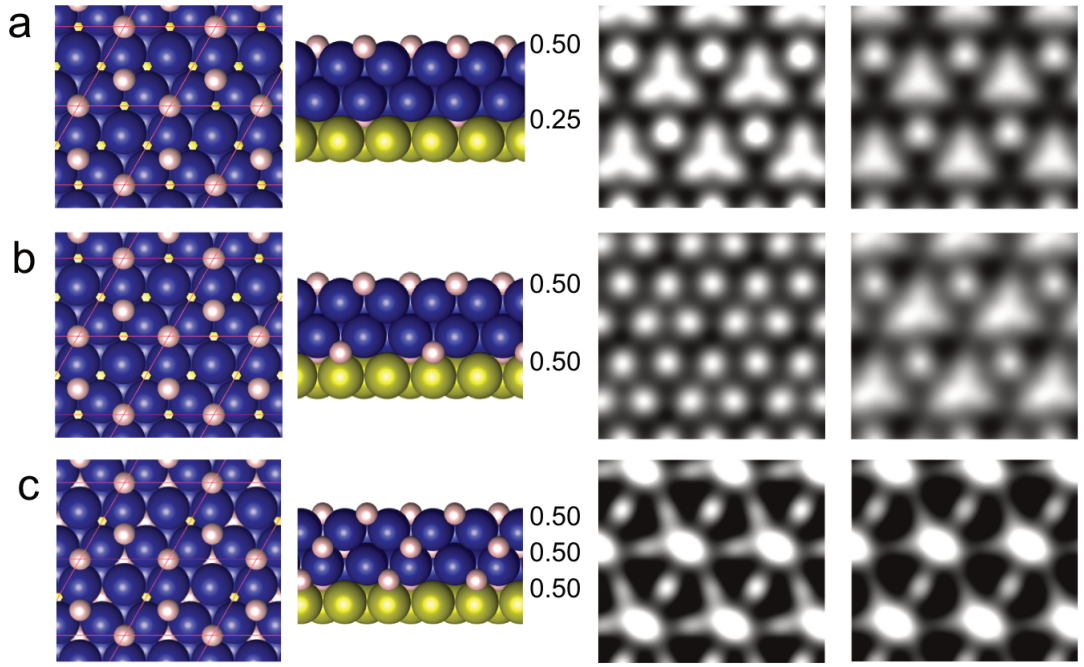

Figure 5.14: Top and side view of hydrogen loading in a Co bilayer possessing a 2H-(2×2) superstructure on its surface. Two spin density maps are presented, that are computed at two fixed distances above an H atom (left: 200, right: 250 pm). In panel (a) 0.25 ML of hydrogen was added to the Co/Cu interface, (b) 0.50 ML of hydrogen was added to the Co/Cu interface, (c) 0.50 ML of hydrogen was added to both the first Co layer and the Co/Cu interface.

anisotropy. The two corresponding values of MAE have been reported on Fig. 5.11 as green circles. Increasing the concentration above 1 ML, involves inserting H at octahedral sites in both Co/Co and Co/Cu interfaces, leading to a limited number of configurations with in-plane magnetization. For concentrations > 1.5 ML (with 0.5 ML located at the surface), the MCA energy becomes positive for all possible configurations. Having identified potential configurations, it becomes feasible to estimate the hydrogen loading in the Co bilayer by computing the corresponding spin density maps and comparing them to the exchange maps. This aspect will be further elaborated here below.

5.5.2 Determining hydrogen loading in the experiment

As demonstrated in § 5.3.2, exchange maps clearly indicate a hydrogen adsorption on top of the Co island. Extending this analysis to spin density maps that incorporate hydrogen within the island or at the Co/Cu interface allows us to determine an upper limit for hydrogen penetration into the Co island, thereby testing consistency with experimental data. Figure 5.14 presents a series of spin density maps

with increasing hydrogen loading. The configurations analyzed correspond to those identified in § 5.4, which exhibit in-plane magnetization and are energetically most favorable. Figure 5.14a shows a spin density map with an additional 0.25 ML of hydrogen at the octahedral sites of the Co/Cu interface. The computed spin densities show no substantial difference compared to the experimental map. However, increasing the hydrogen to 0.50 ML at the Co/Cu interface (Fig. 5.14b) and further hydrogen loading (Fig. 5.14c) result in spin density patterns that diverge from the experimental observations (Fig. 5.9a). Based on these findings, if hydrogen is present in the island, its coverage must be between 0.5 ML and 0.75 ML, with 0.5 ML located on the surface.

5.6 Concluding remarks

In summary, our study demonstrates that exposing a nanoscale magnet to sufficient hydrogen can induce a 90° rotation of its magnetization. Although our DFT computations are conducted on infinite Co layers, they successfully reproduce the interplay between hydrogen loading and magnetism observed in finite-size Co magnets, typically 10 nm wide or more in our measurements. This rotation is primarily driven by hydrogen adsorption on the magnet's surface and is further reinforced by the presence of hydrogen at the Co/Cu interface. While hydrogen adsorption also occurs at step edges in the experiment, our findings suggest that this effect can be neglected to first order.

CHAPTER 6

Driving spins across magnetically-coupled molecules

The precise manipulation of magnetic ordering at the atomic level, such as controlling the spin of a single object –atom or molecule– on a surface, holds significant promise for spintronics devices. The intricate interplay between the object and its environment, mediated by a supporting substrate or host, dictates the resulting spin orientation. Depending on the sign and nature of the magnetic coupling, interacting objects can align in parallel (ferromagnetic), antiparallel (antiferromagnetic), or noncollinear configurations. As we mentioned in Chapter 2, in the last decade advancements in STM have brought a variety of spin-sensitive spectroscopic techniques allowing measurement of the magnetic coupling between spins. One possibility consists in magnetically characterizing an isolated object with the STM tip and then employing it as a sensor when it is magnetically coupled to a target object. The magnetic characterization consists in probing a spin-dependent feature, for example, a zero-bias anomaly such a the Kondo effect [115–117], the magnetoresistance through SP-STM [118–120], or spin excitations [17, 25]. More recently, high-precision spin-sensitive measurements have become possible through ESR-STM –but are limited for the time being to single objects on MgO/Ag [16, 39, 121, 122], or through the Yu-Shiba-Rusinov states of magnetic objects on superconducting substrates [123–128]. Alternatively, the target object can be coupled to the magnetic tip apex of an STM. This detection scheme eliminates surface-mediated interactions and takes advantage of the vertical-displacement sensitivity of the STM, as the sensor-target distance is no longer constrained by surface corrugation. One may use a metal tip with a magnetic atom at its tip apex [36, 41, 79, 80, 129–131] or, as we showed in

previous chapters, functionalize the tip apex with a nickelocene molecule.

Yet, to date, atomic-scale studies devoted to coupled magnetic molecules, whether in a surface-to-surface [23, 64, 124, 127] or tip-to-surface [32, 67] configuration remain limited. In this chapter, we illustrate that the exchange interaction between a molecule positioned at the apex of the STM tip and a magnetic molecule on the surface can be controlled by adjusting both the distance between the tip and the surface and their lateral positioning. In particular, we investigate and visualize spin-spin interactions between a Nc molecule attached to an STM tip and a Nc molecule adsorbed on a cobalt nanoscale island. A significant difference compared to previous work with a Nc-tip [32, 67] lies in the imaging technique utilized. Here, we employ exchange imaging to chart the strength of magnetic interactions between the molecules in the lateral plane, instead of relying on conductance maps. This method enables us to pinpoint the configuration where the exchange interaction reaches its maximum. Moreover, it allows for the simultaneous probing of spatial maps of spin polarization. Interestingly, these maps reveal that spin transport is more efficient in a Nc-Nc geometry that differs from that of the maximum exchange interaction. These findings provide valuable insights into the interplay between magnetism and spin transport in exchange coupled molecules. These findings are supported by *ab initio* calculations, which were performed by Roberto Robles (Centro de Física de Materiales CFM/MPC, CSIC-UPV/EHU, San Sebastián, Spain), Nicolas Lorente (CFM & Donostia International Physics Center, San Sebastián, Spain).

6.1 Nickelocene on a Co bilayer island

6.1.1 Adsorption and electronic structure (metallic tip apex)

To investigate the adsorption and electronic properties of Nc on cobalt (noted Nc/Co), we use a metallic tip apex, *i.e.*, a W tip coated with copper by soft indentations into the surface. The sample consists of cobalt bilayer islands grown on Cu(111) that are exposed to a Nc flux of 2.5×10^{-2} monolayer/min for a few seconds at a temperature < 100 K (Fig. 6.1a). The solid white lines in Fig. 6.1a indicate the three close-packed symmetry directions, *i.e.*, the compact rows, of the Co surface: $\langle \bar{1}10 \rangle$, $\langle 10\bar{1} \rangle$ and $\langle 0\bar{1}1 \rangle$. The corrugation of the Co island is not observable under normal tunneling conditions, but can be visualized through exchange maps (§ 3.14). The sample is decorated with Nc molecules primarily adsorbed at copper and Co steps, with typically a few molecules on the islands. No molecules are present on Cu(111) terraces. To ensure a hydrogen-free surface, we use the cleaning procedure described in § 5.3.1. Figure 6.1b presents a typical image of a clean area, along

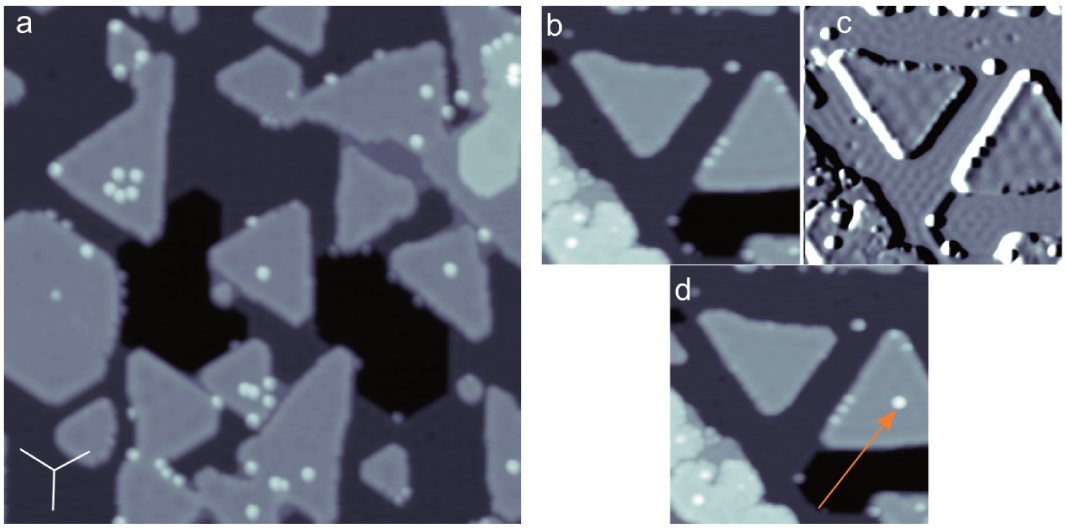

Figure 6.1: (a) STM image of Co islands and Nc molecules on Cu(111) (50 mV, 50 pA, 50×50 nm^2). Compact directions are shown by the three white axes. (b) Cobalt islands after H-removal (30×30 nm^2). (c) Derivative of the image in panel (b) to highlight the standing wave patterns of the free-electron-like surface states. (d) Nc on a Co island transferred from a Cu(111) step. The orange arrow indicates the tip trajectory.

with its spatial derivative (Fig. 6.1c). The presence of standing wave patterns on both copper and cobalt (§ 4.2) indicates that hydrogen removal was successful [112]. However, the cleaning procedure also removes Nc from the islands. To "repopulate" the island, we use the tip to first transfer a Nc molecule from a nearby copper or cobalt step to the tip apex, and subsequently from the tip apex to the center of a Co island (Fig. 6.1d). Experimental details concerning the transfer of Nc from the tip to the surface and vice versa are given in § 4.1.

Figure 6.2a presents a close-up image of two Nc molecules on cobalt. The ring-like pattern observed and the apparent height of 350 ± 10 pm (Fig. 6.2b) are typical for metallocenes [1, 45], indicating that Nc is adsorbed with one cyclopentadienyl (Cp) ring attached to the surface and the other exposed to vacuum. We find, however, that the Cp ring appears brighter on one side compared to the other (inset of Fig. 6.2b). This asymmetry occurs along a direction perpendicular to a compact row of the Co surface. Assuming this asymmetry is caused by a tilt of the molecular axis with respect to the surface normal, the tilt angle is estimated to be $2^\circ \pm 1^\circ$ from the height profile.

Typical dI/dV spectra obtained in constant-current mode at various positions above a Nc molecule adsorbed on Co are presented in Fig. 6.2c. As the tip moves laterally from the surface to the Nc molecule, the d-peak structure of the island (§ 4.2) is progressively replaced by molecular orbitals with peaks at approximately

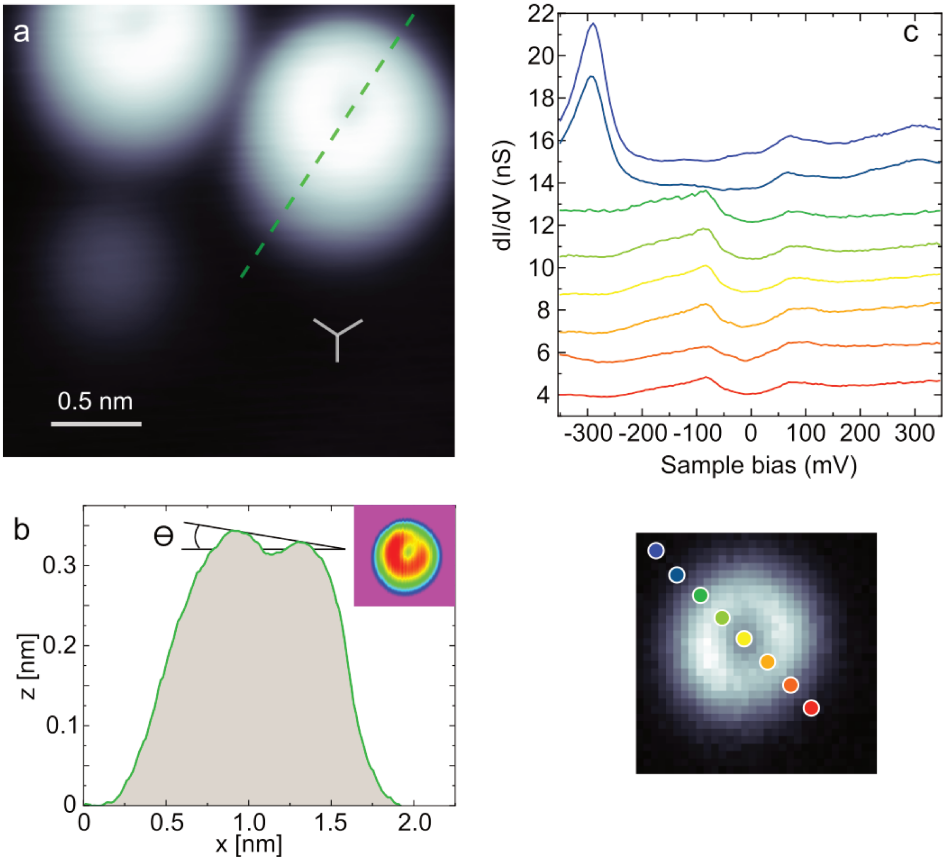

Figure 6.2: (a) Image of Nc on Co bilayer (50 mV, 40 pA, 2.5 × 2.5 nm^2). The three white axes represent the compact rows of Co. (b) Height profile of Nc along the green dashed line in (a). Inset: Image of Nc with a filtered background to highlight its asymmetry on Co (50 mV, 50 pA, 1.4 × 1.4 nm^2). (c) dI/dV spectra acquired with a metallic tip across a Nc adsorbed on a Co bilayer in constant-current mode (50 mV, 50 pA). The colored dots in the bottom panel indicate the positions where the spectra were acquired on the dI/dV map at −350 mV (Fig. 6.3)

−80 mV and 70 mV. The origin of this structure is discussed below. Unfortunately, the bias window could not extend beyond ±350 mV as the tip then causes Nc to move. The dI/dV maps in Fig. 6.3 are instead acquired at constant height. These maps exhibit an asymmetric ring pattern, with the maximum conductance, highlighted in yellow, unevenly distributed along the ring. This asymmetry is even more pronounced in the maps at the Fermi energy, where the ring appears truncated.

To complement these findings, we implemented DFT calculations on a fully relaxed system composed of an isolated Nc molecule on a Co bilayer supported by a copper slab (see Appendix C for computational details). Our DFT calculations indicate that Nc is upstanding (Fig. 6.4a) with the bottom Cp ring centered on an *fcc* hollow site of the Co surface (Fig. 6.4b). The lowest atom in Nc (C atom) is at a vertical distance of 192 pm from the surface. We examined both eclipsed (D_{5h}

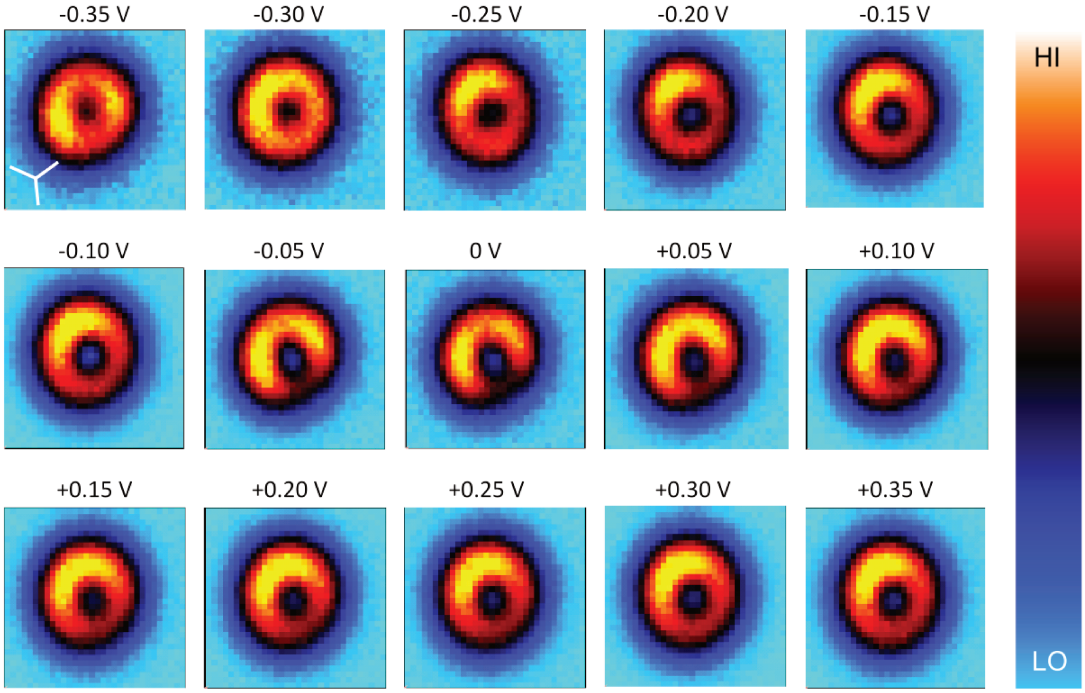

Figure 6.3: Constant-height dI/dV maps at voltage biases ranging from -350 mV to 350 mV (1.2×1.2 nm^2). The three white axes represent the compact rows of Co.

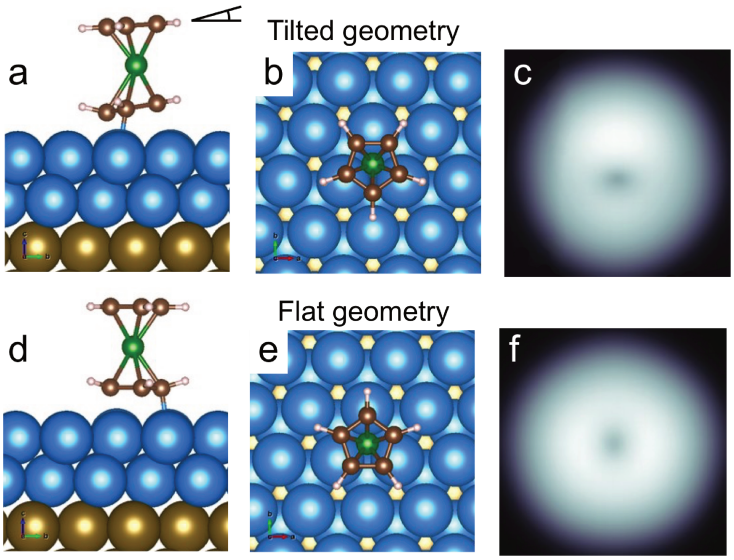

Figure 6.4: (a) Side and (b) Top view of the relaxed structure of Nc on a Co bilayer as computed by DFT ("tilted" geometry). The solid black lines in panel (b) sketch the tilt angle of Nc. (c) Tersoff-Hamann simulated image using the adsorption geometry of panels (a) and (b). (d) Side and (e) Top view of the relaxed structure of Nc on a Co bilayer as computed by DFT ("flat" geometry). (f) Tersoff-Hamann simulated image using the adsorption geometry of panels (d) and (e).

symmetry) and staggered (D_{5d} symmetry) geometries—the latter having the two Cp rings rotated by 36° with respect to each other—and found that the eclipsed

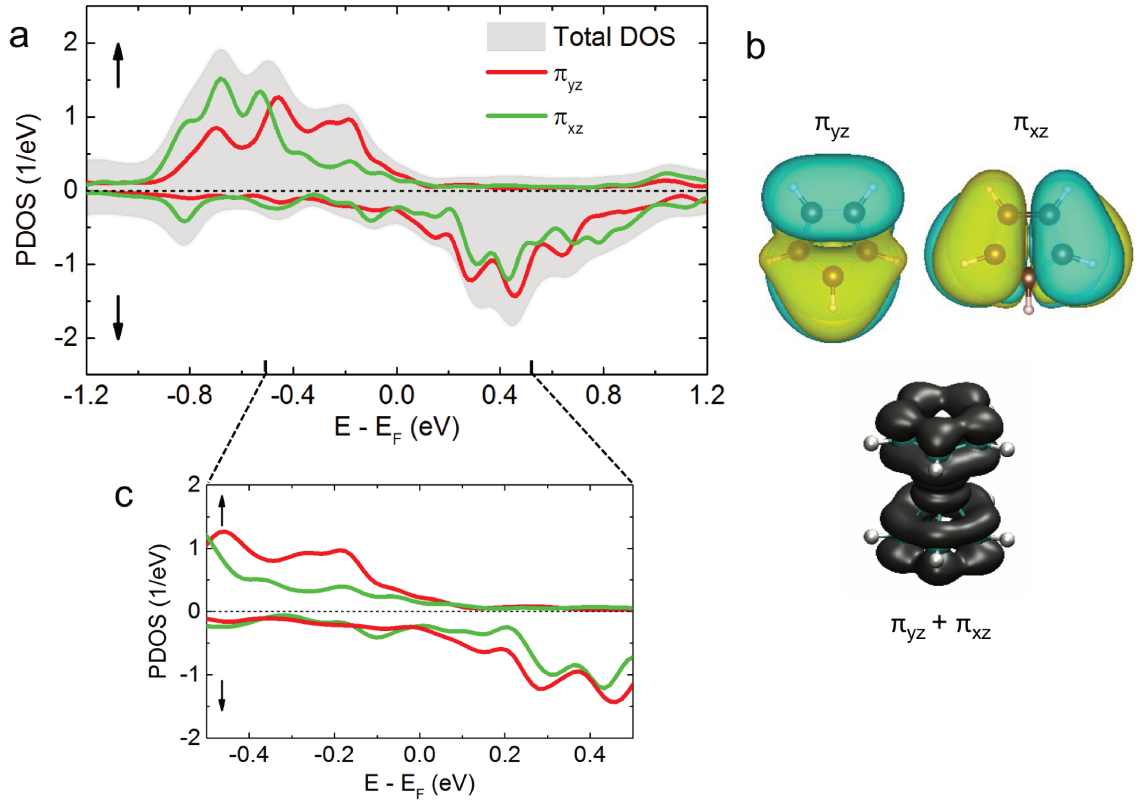

Figure 6.5: (a) Projected density of states (PDOS) for Nc when adsorbed on a cobalt bilayer in the relaxed configuration of Figs. 6.4a-b. The solid red and green lines correspond to the projection onto the π_{yz} and the π_{yz} frontier molecular orbitals, respectively, while the total PDOS is in light grey. Top panel: spin-up PDOS, bottom panel: spin-down PDOS. (b) π_{xz} and π_{yz} molecular orbitals of Nc in vacuum and their combination. (c) Close-up view of the PDOS of panel (a) in the ± 0.5 eV range.

configuration is favored. Most importantly, the Cp ring has a C atom positioned in a hollow *hcp* site (Fig. 6.4a). This causes Nc to tilt with respect to the surface normal by 4°, producing a tilted ring-like shape in the simulated Tersoff-Hamann image (Fig. 6.4c). This adsorption geometry is 5 meV more favorable than the configuration where the Cp ring is adsorbed with a C-C bond centered on an *hcp* site (Figs.6.4d-e). In this alternative geometry, the Cp rings are parallel to the surface, producing a perfect ring-like shape in the Tersoff-Hamann image (Fig. 6.4f).

The symmetry loss observed when imaging Nc is due to both a geometrical and an electronic effect. Looking at the projected density of states (PDOS, Fig. 6.5a), we observe that the mixing of C(sp), Ni(d_{xz}), and Ni(d_{yz}) orbitals results in the partially populated π_{xz} and π_{yz} frontier molecular orbitals (Fig. 6.5b). When Nc is adsorbed on a copper surface [132] or tip [33], the π orbitals are nearly degenerate and spatially add up to yield the typical ring-like shape of Nc as depicted in Fig. 6.5b. Here,

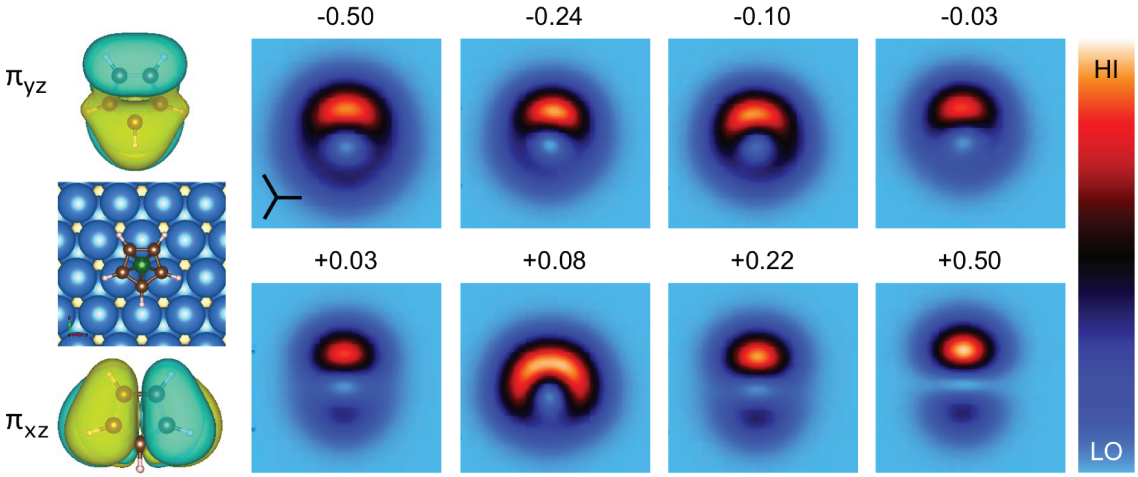

Figure 6.6: DFT-computed constant-height dI/dV maps for Nc on a Co bilayer at selected biases. The left panels show the adsorption of Nc on Co ("tilted geometry") along with the corresponding π_{xz} and π_{yz} orbitals. Tip-surface distance used for the simulated maps is 11 Å. The three black axes represent the compact rows of Co.

this degeneracy is lifted, and the corresponding PDOS differ. In an energy range around the Fermi level (Fig. 6.5c), which corresponds to the bias range explored experimentally, the π_{yz} frontier molecular orbital has the strongest contribution. This is even more striking when looking at the simulated constant-height dI/dV maps of Fig. 6.6. The two-lobe feature of π_{yz} is dominant, thereby favoring a two-lobe feature perpendicular to one of the compact directions of the Co surface. In addition, the tilt angle of Nc favors one lobe compared to the other. These simulated maps capture the behavior seen experimentally in Fig. 6.3, especially near zero-bias.

6.1.2 Magnetism

To probe the magnetic properties of Nc on cobalt, we attach a Nc molecule to the tip apex. We then conduct a comparative study between nickelocene residing on a Co bilayer island and nickelocene residing on a Co monolayer island (Fig. 6.7a). As we demonstrated in § 4.3, the bilayer island has out-of-plane magnetization, while the monolayer island has in-plane magnetization. Spin excitation spectra were acquired at different distances to the adsorbed molecules and are presented as a 2D plot in Figs. 6.7b-c. The distance is expressed in terms of a tip displacement δz and not in terms of an absolute distance as explained later in § 6.3.1. In Fig. 6.7b, a shift of the peaks is observed for Nc on the monolayer meaning that its spin is in-plane. Conversely, on a bilayer, a splitting of the peak is observed (Fig. 6.7c) thus, the spin of the molecule is out-of-plane. The exchange coupling between the adsorbed Nc and the surface is therefore larger than the nickelocene's easy-plane magnetic

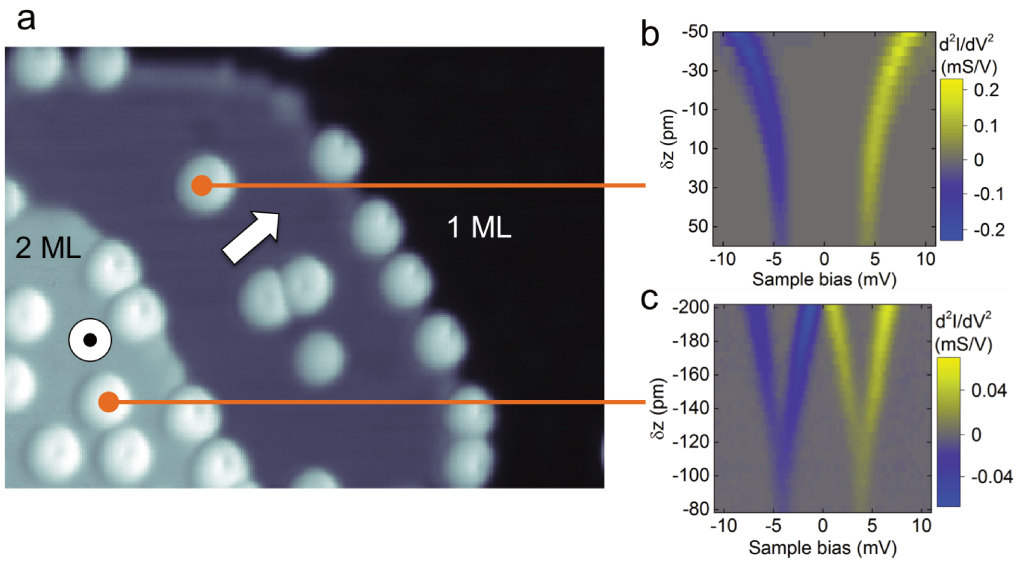

Figure 6.7: (a) Image of Nc on Co monolayer and bilayer (50 mV, 40 pA, 15 × 11 nm^2). The image was acquired with a metallic tip apex. Arrows sketch the magnetization orientation of the islands. Panels (b) and (c) show 2D intensity plots of a series of distance-dependent d^2I/dV^2 spectra acquired with a Nc-tip positioned in the center of Nc/Co for a monolayer and bilayer, respectively.

anisotropy (D) and locks the spin of the molecule to the island magnetization.

To confirm these findings, we carried out spin-polarized DFT calculations using the relaxed structure of Nc/Co(2 ML) determined above. We found a total magnetic moment of 1.28 μ_B for Nc (0.77 μ_B for Ni), which is lower than the magnetic moment of the free-standing molecule (2 μ_B). Despite this reduction in the magnetic moment, a charge transfer of only 0.02 electrons from the substrate to Nc occurs, possibly indicating weak chemisorption. Nickelocene is antiferromagnetically coupled to cobalt, as visible from the isosurface plots of the spin density in Figs. 6.8a-b. We also computed the Magnetocrystalline Anisotropy Energy (MCA) to gather information on the spin orientation of Nc and Co. The z-axis is chosen along the surface normal. In the first computation, we determine the energy of two spin configurations: one by relaxing Nc and Co with their spins along the x-axis (denoted E_x) and another where their spins are aligned along the z-axis (denoted E_z), using an antiferromagnetic configuration in both cases. We found that a collinear alignment along the z-axis is favored, as $E_z - E_x = -17.7$ meV (Fig. 6.8c). Alternatively, we checked the stability of a noncollinear spin configuration where the Nc spin is along the x-axis and the Co spin is along the z-axis. During the calculation, however, the spin of Nc rotates, resulting in the two spins becoming anti-aligned along the z axis. In a second computation, we estimated the exchange energy $E_{ex} = E_{z,P} - E_{z,AP}$, where the suffix P (AP) designates parallel (antiparallel) alignment of the Nc and

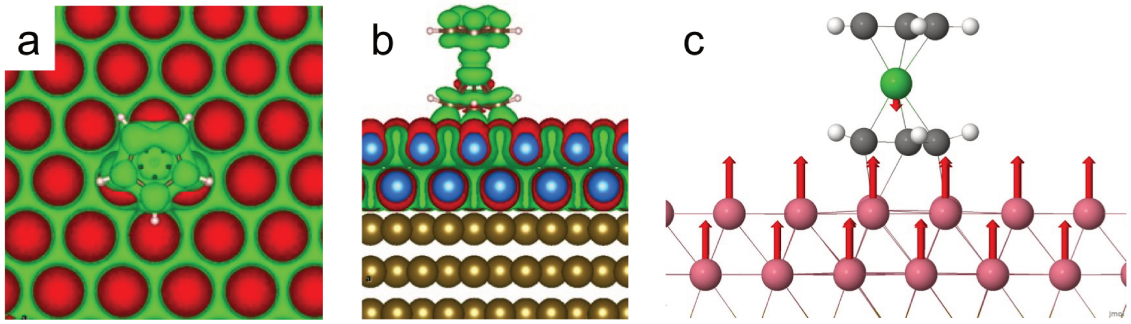

Figure 6.8: (a) Top and (b) Side-view of an isosurface plot of the spin density for the DFT-optimized structure of Nc/Co (2 ML). Red: Spin up, Green: Spin down. (c) Computed magnetization for Nc and Co. The arrows indicate the orientation of the magnetization of the various atoms.

Co spins along the z-axis. We find $E_{\mathrm{ex}} = 54$ meV, consistent with antiferromagnetic coupling. This value needs however to be handled with care, as the parallel configuration leads to a magnetic moment of Nc/Co(2 ML) of 0.28 μ_{B}, which is lower than in the antiparallel configuration, suggesting a metastable state.

The relatively high value of E_{ex} compared to the easy-plane anisotropy D of nickelocene implies that the molecules on the tip and on the surface are spin-active in distinct energy windows. The low biases used to trigger spin excitations in the Nc-tip (of the order of D) are insufficient to promote spin excitations in Nc/Co (of the order of E_{ex}). Based on these findings, we consider Nc/Co as spin inactive and model the energy landscape with the spin Hamiltonian of Chapter 4:

$$\hat{H} = D\hat{S}_z^2 - g\mu_{\mathrm{B}}\hat{B}_{\mathrm{ex,z}} \cdot \hat{S}_z, \tag{6.1}$$

where $B_{\mathrm{ex}} = J\langle S_{\mathrm{Nc/Co}}\rangle / g\mu_{\mathrm{B}}$ represents now the exchange field produced by Nc/Co and acting on the spin $\hat{S}$ of the Nc-tip through a magnetic coupling J that extends into vacuum. This system differs from the setup used by Czap *et al.* [32], where the Nc-tip was magnetically coupled to a Nc molecule on a silver surface. In their case, both nickelocenes exhibited spin excitations, complicating the data analysis.

6.2 Imaging nickelocene with a nickelocene-tip

To address the magnetic properties in detail, particularly their spatial dependence, we utilize a Nc-tip. However, this operation is not straightforward in this particular case due to the chemical interaction present between the two nickelocene molecules, which causes structural changes in the tunnel junction. These changes can be highlighted by inspecting how the nickelocene molecule on the Co surface is imaged with

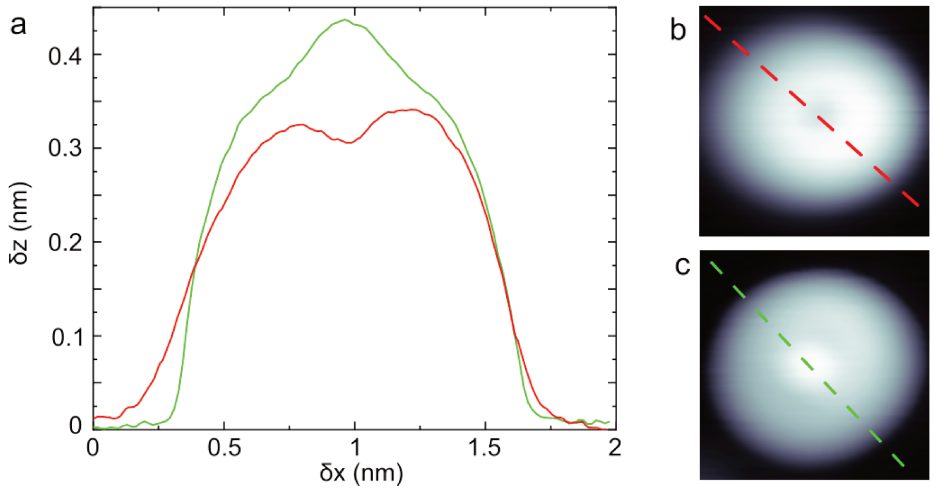

Figure 6.9: (a) Apparent-height profiles of Nc/Co (2 ML). The solid red line is the profile acquired with a metal tip along the dashed line of panel (b), while the solid green line is the profile acquired with a Nc-tip along the dashed line of panel (c). Panels (b) and (c) are images of Nc/Co acquired with (b) a metal tip (400 mV, 400 pA, 1.5×1.5 nm^2), (c) a Nc-tip (50 mV, 50 pA, 1.5×1.5 nm^2).

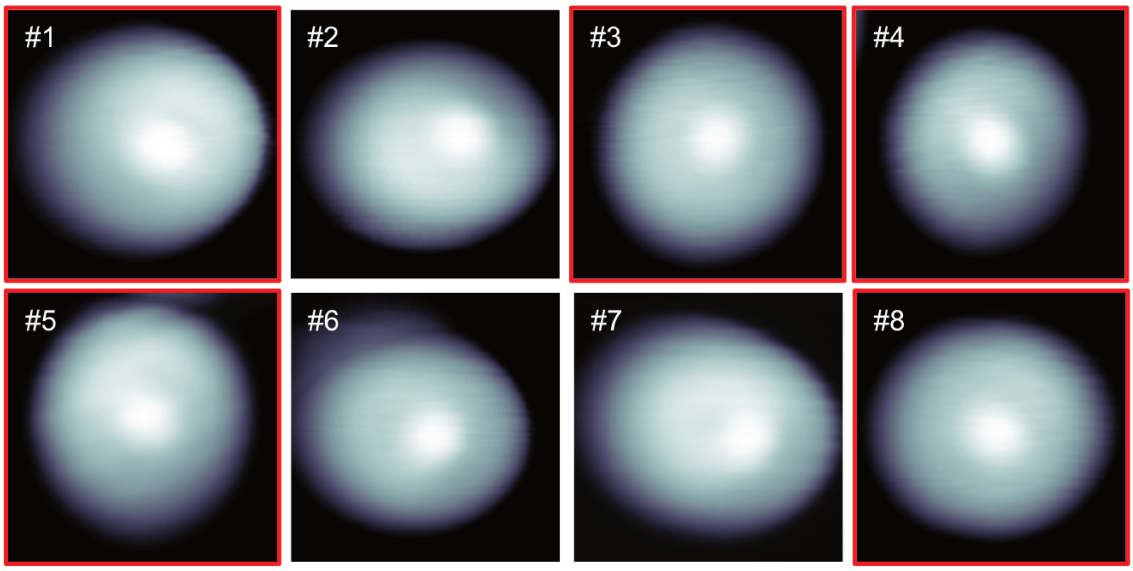

Figure 6.10: Images of Nc/Co (2 ML) acquired with different Nc-tips (50 mV, 50 pA, 1.5×1.5 nm^2).

the Nc-tip. Figure 6.9a compares the profile of a Nc/Co (2 ML) imaged with two different tips. The image taken with a metallic tip (Fig. 6.9b) shows a ring shape that is slightly tilted (solid red line in Fig. 6.9a), as mentioned in § 6.1.1. When imaged with a Nc-tip (Fig. 6.9c), the apparent width of Nc/Co is similar, with only a 0.1 nm difference. The shape of the molecule is circular, with a protrusion at the center reaching a maximum height of 435 ± 10 pm (solid green line in Fig. 6.9a). The image of Nc/Co can vary depending on the Nc-tip used (Fig. 6.10).

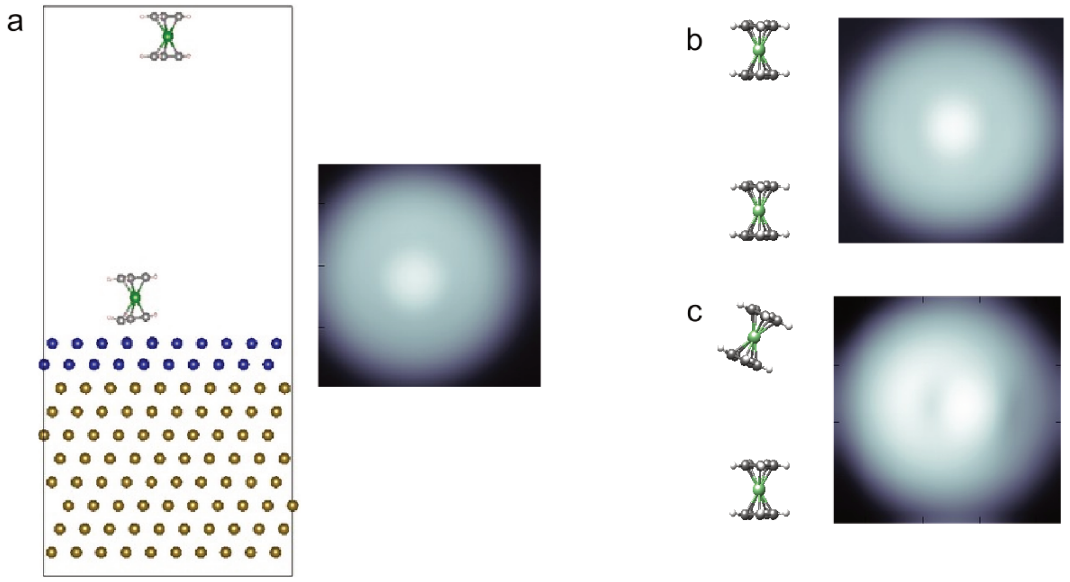

Figure 6.11: STM images simulated with Bardeen's theory (1.83×1.83 nm^2): (a) Zero-tilt angle for the Nc-tip and a "tilted" geometry for Nc/Co (2 ML), (b) Zero-tilt angle for the Nc-tip and a "flat" geometry for Nc/Co (2 ML), (c) Nc A 12° tilt angle for Nc on the tip and a "flat" geometry for Nc/Co (2 ML).

To reproduce the STM image of Nc/Co (2 ML) in presence of a Nc-tip, we go beyond the Tersoff-Hammann approximation. We simulate the image using Bardeen's theory as it accounts for the electronic structures of both the tip and the sample, considering their spatial distributions and energy levels. This approach accurately represents the tunneling process here, given the similar electronic structures of the tip and the sample. We consider Nc molecules with different adsorption configurations on the tip and the surface. As shown in Fig. 6.11a, a remarkable agreement between the experimental and the computed image is obtained when using the relaxed configuration of Nc/Co (2 ML) ("tilted" geometry, Figs. 6.4a-c) and a nickelocene with zero-tilt angle as a tip. Pushing the simulations further, we can attribute the tip-dependency observed experimentally (Fig. 6.10) to changes in the relative angles between the two nickelocene molecules. This dependence is highlighted in Figs. 6.11b-c, where we consider two different relative angles. In the first simulation (Fig.6.11b), we position Nc/Co (2 ML) in a "flat" geometry and place Nc on the tip with a zero-tilt angle. In the second simulation (Fig. 6.11c), we again use Nc/Co (2 ML) in a "flat" geometry but introduce a 12° tilt angle to Nc on the tip. When tilting Nc on the tip, the computed image tilts accordingly, resulting in an off-center spot. For subsequent experiments, we selected tips that produced images with minimal angular differences between the Nc molecules, corresponding to the images in Fig. 6.10 with a red frame.

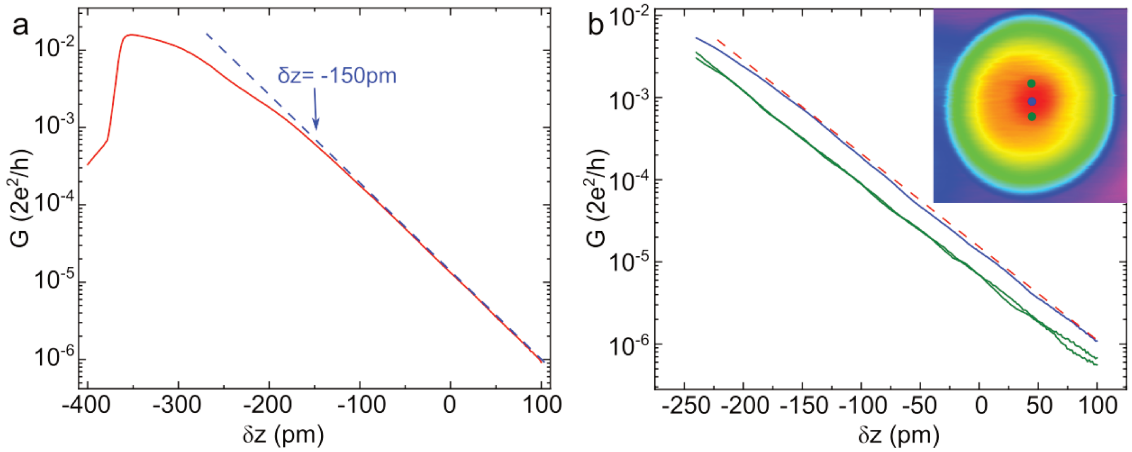

Figure 6.12: (a) Conductance versus tip displacement measured at the center of a Nc/Co (2 ML) with a Nc-tip (feedback loop opened at 50 mV, 50 pA). (b) Conductance versus tip displacement measured at three different locations (see Inset) on Nc/Co (2 ML). The feedback loop is always opened at the center before each measurement (50 mV, 50 pA). Inset: Image of Nc/Co (2 ML) (50 mV, 50 pA, 1.5×1.5 nm^2). In both panels, the dashed lines are guides for the eye. The molecular tip used in (a) and (b) are different.

6.3 Exchange map of a single nickelocene

6.3.1 Junction stability and exchange interaction

Before investigating the magnetic properties of Nc/Co (2 ML), we verify the stability of the tunnel junction by recording the conductance (G) versus tip displacement (δz) with a Nc-tip. In Fig. 6.12a, we present a typical trace that is acquired at the center of a Nc/Co with a displacement spanning 500 pm. The feedback loop is opened at a conductance of $G = 1.3 \cdot 10^{-5}\, G_0$ (where $G_0 = 2e^2/h$ is the quantum of conductance), corresponding to $\delta z = 0$. The conductance increases exponentially up to $\delta z = -150$ pm, but beyond this point, the conductance exhibits sub-exponential growth. This behavior is similar to what is observed when two C_{60} molecules, one on the tip and the other on the surface, are vertically approached to one another [133], or to what we observed on a hydrogen-contaminated Co surface (§ 5.3.1). Given the similarity to these behaviors, we attribute the sub-exponential growth to the onset of a repulsive regime between the two nickelocenes. This threshold value is however tip dependent (Fig. 6.12b), exceeding even $\delta z = -220$ pm for some tips. When $\delta z = -350$ pm, a sharp drop in G is observed, which we attribute to a junction instability possibly resulting from a lateral displacement of Nc on the tip apex. This instability does not result in an irreversible structural change, as the tip can be recovered by pulling away from Nc/Co. In Fig. 6.12b, the Nc-tip is swept toward

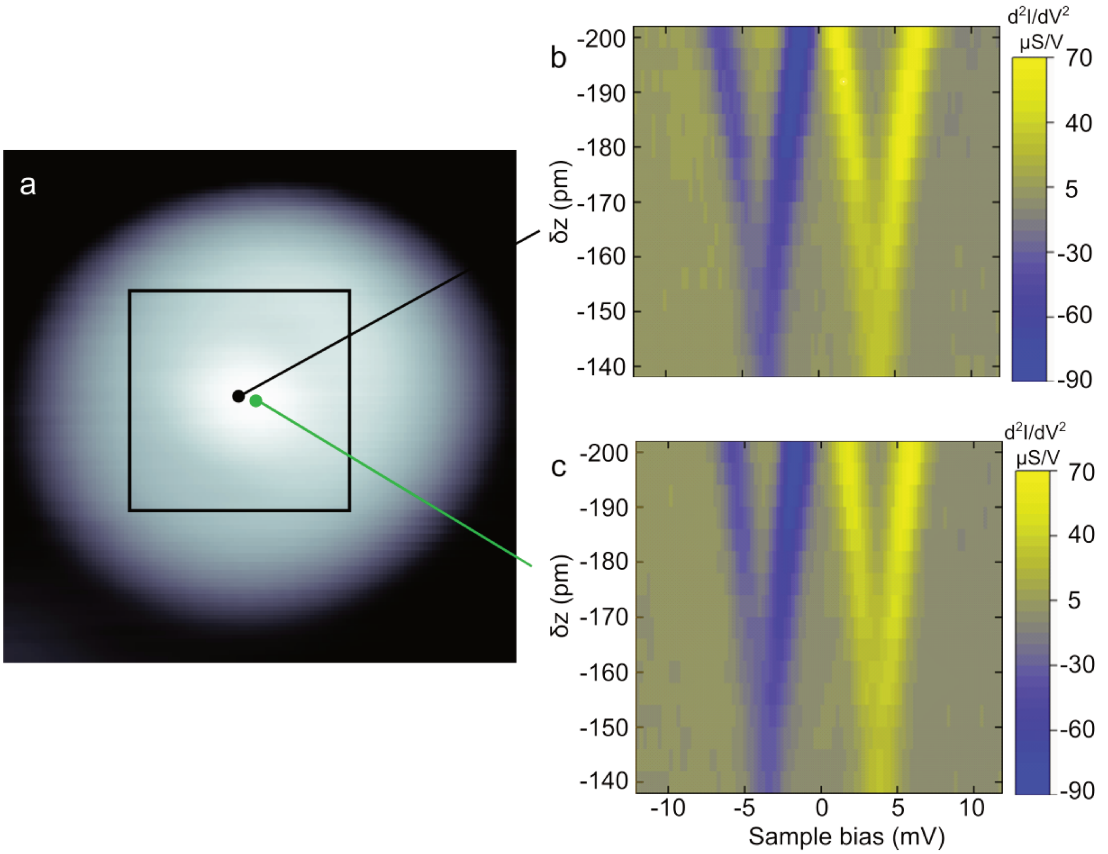

Figure 6.13: (a) STM image of Nc/Co (2 ML) (1.5 × 1.5 nm^2). The black square shows the typical size used for acquiring an exchange map. (b) 2D intensity plot of a series of distance-dependent d^2I/dV^2 spectra above the center and (c) off the center of Nc/Co (2 ML). Decreasing δz means approaching Nc/Co. The feedback loop is opened at 50 mV, 50 pA.

Nc/Co at three different lateral locations spanning the area where we perform voxel imaging (see Inset of Fig. 6.12b), with a total tip displacement of 350 pm. As the voxel imaging is done in constant height mode, the feedback loop is opened in the center of Nc/Co for all measurements. The solid blue line corresponds to the trace acquired in the center of the molecule (blue dot in Inset), and reveals a deviation from exponential behavior setting in at $\delta z = -200$ pm. The solid green lines are the traces acquired off-center (green dots in Inset), and show similar characteristics, with a repulsion regime appearing beyond $\delta z = -210$ pm. For voxel imaging in constant height, the vertical position of the tip is set according to this information. For most tips, we choose $\delta z = -200$ pm to remain in a non-repulsive tunneling regime and concomitantly optimize the detection of the exchange energy. We can therefore consider that the tunnel junction remains structurally invariant during voxel imaging.

After selecting the molecular tip and verifying the stability of the tunnel junction,

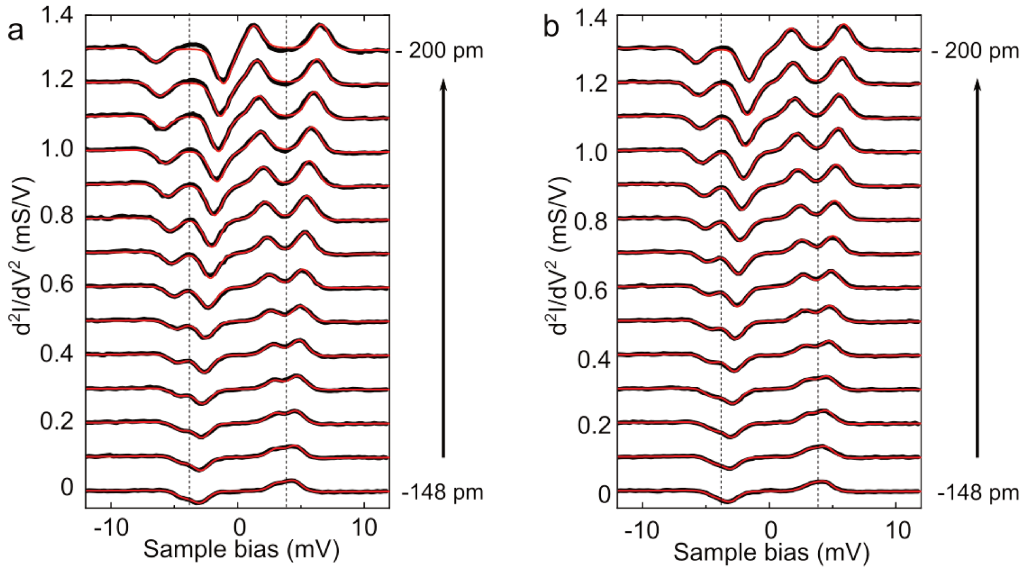

Figure 6.14: (a) d^2I/dV^2 spectra for different vertical tip displacements. The spectra were acquired on the black spot of Fig. 6.13a . (b) d^2I/dV^2 spectra for different vertical tip displacements. The spectra were acquired on the green spot of Fig. 6.13a. The solid red line are simulated line shapes using the model in [57].

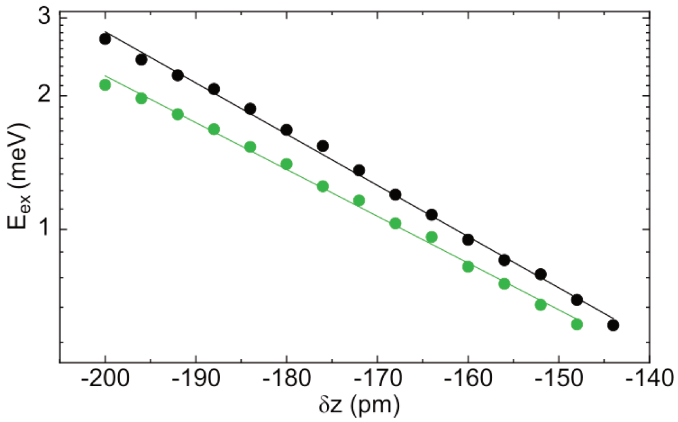

Figure 6.15: Exchange energy versus δz measured at the center (black dots) and off-center (green dots) of Nc/Co (2 ML). The exchange energies are extracted from the fits of Fig. 6.14a and Fig. 6.14b, respectively. The solid lines are exponential fits.

we monitor the evolution of the spin excitations of the Nc-tip when it is vertically moved towards Nc/Co (2 ML) (Fig. 6.13). We present two sets of d^2I/dV^2 spectra, one acquired in the center of Nc/Co (2 ML) (Fig. 6.13b), and one taken 65 pm away from the center (Fig. 6.13c). These measurements are also displayed as single d^2I/dV^2 spectra in Figs. 6.14a and 6.14b, respectively. As anticipated in § 6.1.2, a splitting is observed, which signals that Nc/Co (2 ML) has an out-of-plane magnetization. The weaker splitting observed off-center reflects a rapidly decaying exchange interaction when moving laterally. In Fig. 6.15, we plot the exchange field E_{ex} with

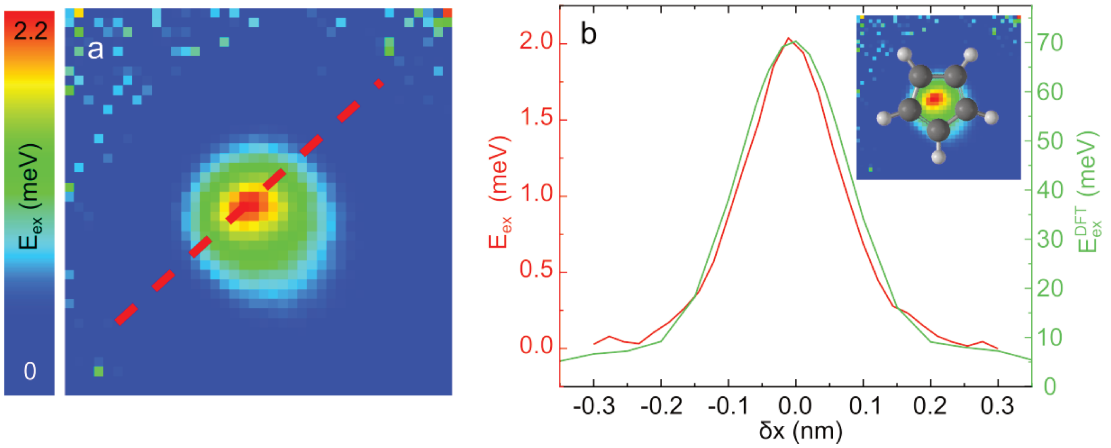

Figure 6.16: (a) The exchange energy map of Nc adsorbed on Co (2 ML) (0.65×0.65 nm^2). (b) The solid red line is the profile of E_{ex} extracted along the red dashed line of panel (a). The exchange energy is given on the left y-axis. The solid green line is the DFT-computed profile extracted along the green dashed line of Fig. 6.18c. The computed exchange energy E_{ex}^{DFT} is given on the right y-axis. Inset: Exchange map of panel (a) with Cp ring structure superimposed. The C-C bond of the Cp ring is 0.14 nm.

respect to the vertical displacement of the tip at the center (black) and off-center (green). The exponential behavior at both positions confirms the junction stability. As expected, E_{ex} is larger at the center with a decay length $\lambda = 37 \pm 2$ pm, while off-center, the decay length is $\lambda = 42 \pm 2$ pm. These values compare well to the decay lengths observed above Co islands ($\lambda = 46$ pm, § 4.4) and above single Nc on a silver surface ($\lambda = 30.4$ pm) [32].

6.3.2 Experimental and theoretical exchange map

To probe the lateral dependency of the exchange interaction, we perform voxel imaging above a single Nc adsorbed on a Co bilayer (§ 3.10). The $d^2I/dV^2(x, y, V)$ data recorded by opening the feedback loop above the center of the molecule at $\delta z = -200$ pm. The typical measurement area corresponds to a square grid of 0.65×0.65 nm^2 that is centered on the molecule (Fig. 6.13a). After fitting the spectra from each pixel of the map, we extract the exchange energy with respect to the lateral coordinates, E_{ex}(x,y) (Fig. 6.16a). The resulting exchange map has a maximum of 2.2 meV at the center of Nc/Co (2 ML); this maximum is tip dependent, some tips even displaying an exchange energy of 3.0 meV. Figure 6.16b presents a profile of the exchange map acquired along the red dashed line (Fig. 6.16a). The line profile of E_{ex} has a full width at half maximum of 190 pm, which is considerably narrower that the apparent width of Nc/Co (2 ML) (Fig. 6.9). This value is instead

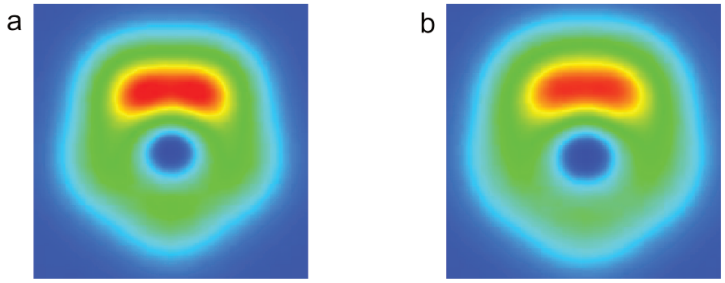

Figure 6.17: (a) Computed spin density 200 pm above Nc adsorbed on the Co bilayer. (b) Spin density computed 250 pm above Nc adsorbed on the Co bilayer (0.65×0.65 nm^2).

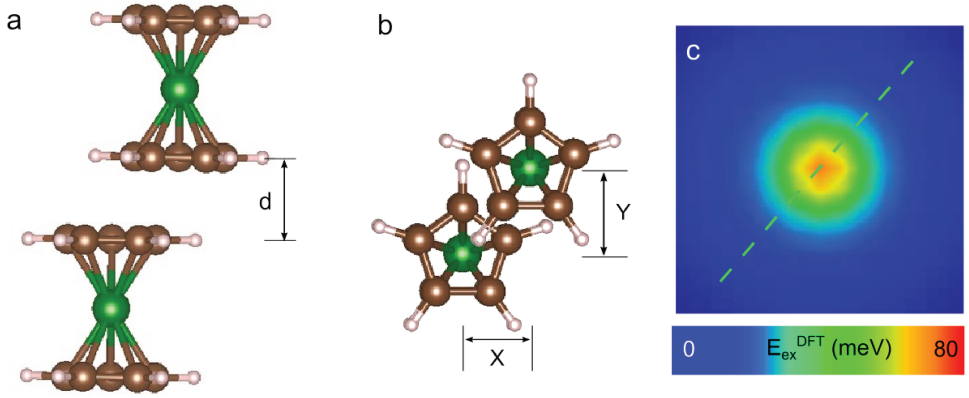

Figure 6.18: (a) Model showing a top view of the molecules in the gas phase. (b) Model showing the side view of the molecules separated by $d = 350$ pm. (c) Computed exchange coupling map as described in the text (0.65×0.65 nm^2).

of the order of the size of the Cp ring of Nc, 220 pm (Inset of Fig. 6.16b). We conclude that the exchange coupling is active only within an area equivalent to the Cp ring of Nc/Co (2 ML).

As in the previous chapters, we compute the spin density map of Nc/Co (2 ML) using the relaxed "tilted" geometry to assess our exchange energy maps (Figs. 6.17a and 6.17b). The shape of the maps is at variance with experimental findings. This discrepancy suggests that a different approach is necessary for depicting the experimental exchange maps. As we demonstrated in § 6.2, the images of Nc/Co acquired with a Nc-tip are correctly reproduced by including the Nc-tip in the calculation through a Bardeen approximation. This then suggests to also include the molecular tip for calculating the exchange maps. To do so, we adopt a simple approach where two Nc molecules in the gas phase are positioned on top of each other with their Cp rings parallel and separated by $d = 350$ pm (Figs. 6.18a and 6.18b), which corresponds to a distance from Cp-Cp contact of ≈ 100 pm. Positioning the Cp ring at $d = 450$ pm, which corresponds to a distance from Cp-Cp contact of ≈ 200 pm,

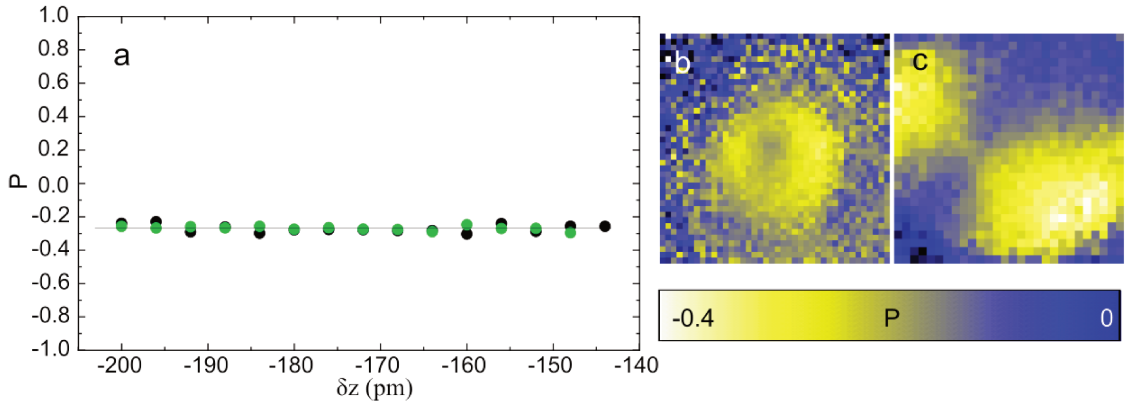

Figure 6.19: (a) Spin polarization versus tip displacement for Nc/Co (2 ML) measured at the center and 65 pm away from the center as shown in Fig. 6.13a. The spin polarization is extracted from the fits of Fig. 6.14a and Fig. 6.14b, respectively. (b), (c) the spin polarization maps of Nc/Co (2 ML) respectively 0.65×0.65 nm^2 and 0.4×0.4 nm^2 large

yielded identical results, but decreases the the exchange energy by one order of magnitude. The top molecule is moved relative to the other at coordinates (x, y), where $(0, 0)$ corresponds to perfect alignment of their Ni atoms. Note that the relative orientation of the Cp rings is in an eclipsed fashion, meaning that at (0,0), each carbon and hydrogen atom of the Cp rings are aligned. At each position (x,y), the system is relaxed and the energy difference $E_{\mathrm{ex}}^{\mathrm{DFT}} = E_{\mathrm{z,P}} - E_{\mathrm{z,AP}}$ is computed, which is indicative of the exchange coupling between the molecules. $E_{\mathrm{z,P}}$ ($E_{\mathrm{z,AP}}$) is the energy of the configuration where the spins of the molecules are parallel (antiparallel). As seen in Fig. 6.18c, this approach, which neglects both the surface and the metal tip on which Nc is attached, is already sufficient to qualitatively reproduce the experimental data. The exchange energy reaches its maximum when the molecules are aligned and drops to zero when they no longer face each other. The DFT-computed line profile matches the experimental one (Fig. 6.16b). This confirms that the exchange interaction is confined to an area equivalent to that of a Cp ring. We note, however, that the computed exchange energy has stronger values than the experimental one. This discrepancy stems from two main factors: the particular choice of the Nc-Nc distance used to compute the map, which exhibits exponential dependence, and the collinear configuration of the two spins used in the calculation. A non-collinear configuration, which would align more closely with the experimental setup, is unfortunately not feasible to calculate.

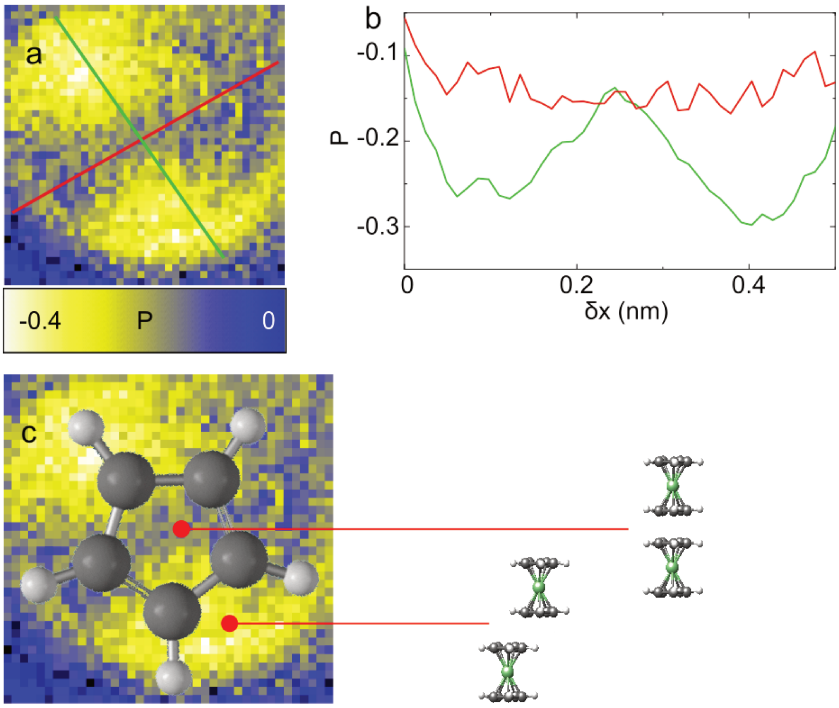

Figure 6.20: (a) Spin polarization maps acquired at the center of Nc/Co (2 ML) within an area of size 0.5×0.5 nm^2. The maps were acquired at constant height with an offset $z = -210$ pm. (b) Profile of P along the red and green directions on the map of panel. (c) Same map as (a) with Cp ring structure superimposed. The angular orientation of the model Cp ring is arbitrary. The arrows indicate Nc-Nc configurations at two different locations of the map.

6.4 Spin-polarization map of a single nickelocene

Figure 6.19 presents the spin polarization at the Fermi energy of Nc/Co(2 ML) as a function of vertical Nc-tip displacement. The spin polarization is extracted from the fits of Figs. 6.14a and Fig. 6.14b, which were acquired, respectively, at the center (black dot) and off-center (green dot) of Nc/Co (Fig. 6.13a). As explained in § 4.5.1, the amplitude of the spin excitation peaks (dips) is related to the spin polarization at the Fermi level. At both locations the value remains constant with tip displacement (Fig. 6.19a). This result is significant since the measurements presented below are conducted at constant height. Thus, the measure of $P(x, y)$ that is extracted from the voxel imaging is independent of the distance between the two nickelocenes. Several maps of $P(x, y)$ were acquired with different Nc-tips, all providing consistent results. Figure 6.19b shows a typical spin polarization map of Nc/Co(2 ML) within an area of 0.65×0.65 nm^2, where it can be seen that $P(x, y)$ is inhomogeneous within the molecule. This inhomogeneity corresponds to

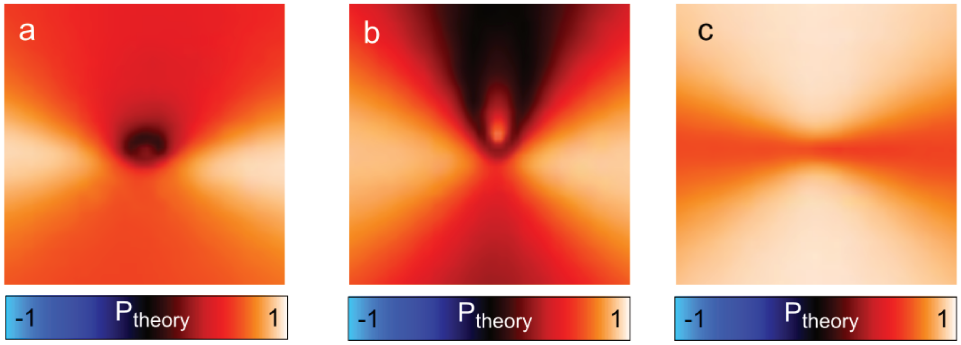

Figure 6.21: Computed spin polarization maps of Nc/Co at different voltage biases: (a) 0.03 V, (b) 0.08 V, (c) 0.22 V. The size of the three maps is 0.65×0.65 nm^2. The size is the same as the experimental map of Fig. 6.20b.

the existence of a two-lobe pattern in the spin polarization, as highlighted in the high-resolution map of Fig. 6.19c, where the spin polarization is probed in a smaller area around the center of Nc/Co (0.4×0.4 nm^2). The two-lobe pattern persists when using another Nc-tip (Fig. 6.20a). As visible in the line profiles of Fig. 6.20b, P is maximum in the lobes, ranging from -0.25 to -0.30, while in between the lobes $P = -0.13$. Contrary to the exchange interaction, the spin polarization spatially extends beyond the Cp ring of Nc/Co (Fig. 6.20c), and strong spin polarization is achieved in an off-centered configuration for the two molecules.

The presence of Nc on a Co bilayer significantly alters the junction spin polarization compared to a pristine Co bilayer island where $P = 0$ (§ 4.5.1). This observation aligns with findings from previous SP-STM studies on phthalocyanine molecules adsorbed on magnetic surfaces [82, 134]. Such changes in spin polarization are indicative of the formation of a "spinterface" [135–137], a term denoting the hybridization occurring at the interface between organic molecules and inorganic substrates. It underscores that molecular spintronics relies not only on tailoring magnetic properties of molecules but also on designing effective spin-active hybrid interfaces.

To reproduce the spin polarization maps, we consider a metallic tip and use the Tersoff-Hamann approximation (§ 3.3) to compute the differential conductance $dI/dV(x, y, V)$ by DFT, for spin-up ($\uparrow$) and spin-down ($\downarrow$) electrons. The theoretical spin polarization is calculated taking

$$P_{\text{theory}} = (dI/dV^{\uparrow} - dI/dV^{\downarrow})/(dI/dV^{\uparrow} + dI/dV^{\downarrow}). \tag{6.2}$$

The resulting maps at 0.03 V, 0.08V, and 0.22V are presented in Figs. 6.21a-c, respectively. The shape of the calculated maps presents encouraging similarities with the experimental ones. Notably, a two-lobe pattern is consistently observed. This

feature, robust across all biases, arises from the adsorption of Nc/Co (Fig. 6.8), which causes a degeneracy lift between the π_{xz} and π_{yz} molecular orbitals. We tentatively assign the experimental two-lobe pattern to these molecular orbitals. Some relevant differences are also observed. The value of the computed spin polarization differs from the experimental one, and non-spin polarized features are present in the computed maps, at variance with the experiment. The calculated maps also show a spin polarization that spreads to a larger distance compared to the experimental one (Fig. 6.20b). The reason is that in the experiment the Nc-tip must be exchange coupled to Nc/Co to yield a measurable P. Thus, the signal on the experimental map is constrained to an area close to the area of the Cp ring. These discrepancies suggest the need to account for the presence of the Nc-tip, *i.e.*, to go beyond the Tersoff-Hamann approximation. To improve the comparison, we have therefore ongoing theoretical computations using the Bardeen model with wave functions describing the nickelocene molecules on the tip and on the surface. We stress, however, that the comparison will remain qualitative, as at this stage the calculation neglects the inelastic nature of the tunneling electrons.

6.5 Concluding remarks

To summarize, our study focused on investigating the adsorption, electronic, and magnetic properties of Nc on a Co bilayer island. We utilized voxel imaging to extract spatial maps of the Nc-Nc exchange coupling across vacuum and maps of the junction spin polarization. The maps reveal that spin transport is more efficient in a Nc-Nc geometry that differs from that maximizing exchange interaction. Our findings also underscore the necessity of voxel imaging for extracting magnetic information comprehensively from measurements. Magnetic and electronic information can otherwise be intertwined, muddling the experimental message and making it less amenable to theoretical comparison. This was notably the case in the prior work by Czap *et al.* [32]. The simultaneous acquisition of both exchange and spin polarization channels offers dual insights into spin texture and spintronic properties at atomic scale resolution. This technique is particularly suitable for investigating complex spin textures, from magnetic molecules to non-collinear systems such as spin spirals, magnetic domain walls, antiferromagnets, and nano-skyrmion lattices.

CHAPTER 7

Conclusion and perspectives

Our comparative study on Co islands of varying thickness demonstrates the Nc-tip ability to sense different spin directions of the sample. We confirmed previous macroscopic studies indicating that the magnetization of Co thin films varies with thickness: a Co monolayer (1 ML) on Cu(111) exhibits in-plane magnetization, unlike a Co bilayer (2 ML), which shows out-of-plane magnetization. This difference in magnetization orientation is governed by the magnetocrystalline anisotropy of the islands. The magnetization direction of a trilayer island (3 ML) is more subtle, depending on "second order" effects such as the size and shape of the islands. We used voxel imaging to map the spatial dependence of the exchange energy between the Nc-tip and these Co islands. Exchange energy maps acquired on Co monolayers are less corrugated than those on Co bilayers, despite having an average exchange energy value that is twice as large. Remarkably, the experimental exchange maps closely correlate with spin density maps computed using density functional theory (DFT), which describe the local magnetization $m(\vec{r})$. Finally, we provided a comprehensive picture of the spin polarization measured with the Nc-tip. We found that the spin polarization of the tunnel junction depends on the magnetization orientation of the sample. For out-of-plane magnetization, the spin polarization of the tunnel junction reflects the sample spin polarization, thereby confirming findings in Ref. [2]. However, when moving away from this orientation, the tip spin polarization must be taken into account.

In our study of hydrogen-contaminated Co islands using the Nc-tip, we demonstrated that hydrogen adsorption on islands of different thicknesses (1 ML, 2 ML, and

3 ML) arranges in a 2H-(2×2) structure. Spin excitation spectroscopy and magnetic exchange maps revealed that the magnetization direction of bilayer islands rotates from out-of-plane to in-plane. The nickelocene probe is also sensitive to the quantity of hydrogen adsorbed on and within the islands. Based on DFT computations of the magnetic anisotropy energy and from the comparison between exchange maps and computed spin density maps, we concluded in fact that a minimum coverage of 0.5 ML hydrogen on the surface and 0.25 ML at the Co-Cu interface is necessary to switch the magnetization direction of the Co bilayer.

The final chapter focused on the Nc molecule adsorbed on Co bilayer islands. By combining spin excitation spectroscopy with DFT calculations, we demonstrated that the spin of the Nc molecule is locked to the island magnetization through antiferromagnetic coupling. Voxel imaging of Nc/Co (2 ML) allowed us to disentangle two spin-related pieces of information: the exchange energy and the spin polarization. Unlike the previous investigation on the pristine or H-covered Co surfaces, the exchange maps could not be reproduced with the computed spin density. By including the Nc-tip in the calculations, we were able to closely reproduce the exchange maps and show that the coupling is stronger when the Nc-tip is aligned with the surface Nc. Regarding the spin polarization maps, we observed a two-lobe pattern, which we traced back to the degeneracy lift of the frontier molecular orbitals of Nc on the cobalt island. The computed maps involved the conductance of spin-up and spin-down electrons using the Tersoff-Hamann theory. These maps showed the two-lobe pattern, but further computations also accounting the molecular tip are needed to reproduce the experimental results more accurately.

In future work, we aim at improving the spin contrast of the voxel maps. To do so, we will coat the tip apex with magnetic material in order to exploit the exchange coupling between the tip and the nickelocene attached to it. A magnetically coated tip combined with an external magnetic field could potentially control the orientation of the nickelocene spin and lock it in a specific direction. As a result, the degeneracy of the nickelocene spin states is lifted, resulting in distinct spin excitations with tunneling current which are 100% spin-polarized whether the Nc-tip is exchange-coupled or not to the sample. This approach calls for experimental and theoretical studies on how metallocenes interact with magnetic surfaces and atoms, similar to the study of Chapter 6, including their ability to preserve their quantum spin states. Such work is still scarce, and should be extended to the more straightforward case of non-magnetic surfaces, where spin preservation is already known to occur but not fully understood. Finally, we plan on extending the use of voxel imaging with a Nc-tip to investigate exotic spin textures such as cycloidal and nano-skyrmion

lattices. Further theoretical work is also needed. Our measurements show that the Nc-tip needs to be included in the calculations, suggesting to generalize the use of the Bardeen approximation for computing spin densities or spin polarization maps.

CHAPTER 8

Resume and dissemination

Education

2020-2024: PhD in physics
IPCMS (UMR 7540), University of Strasbourg, CNRS (France)
Mapping surface magnetism with a molecule
Thesis supervisor: Laurent Limot

2016-2019: Master of science in applied physics
Ecole Polytechnique Fédérale de Lausanne (Switzerland)

2012-2016: Bachelor of science in physics
Ecole Polytechnique Fédérale de Lausanne (Switzerland)

Academic internships

2018-2019: Master thesis, 4 months
Laboratory of Nanostructure at Surfaces, Lausanne (Pr. Dr.Harald Brune)
Growing a layer of BaO on Pt in-situ and characterizing the deposition with the scanning tunneling microscope

2016-2017: Practical work, 8 months
Laboratory of Physics of Living Matter, Lausanne (Pr. Dr. Giovanni Dietler)
Observe pUC DNA with the atomic force microscope to study their shape configuration with respect to the number of monomers

Internships

2022: Secondment, 2 months
Basel Precision Instruments (Basel, Switzerland)
Engineering filters to attenuate microwave parasitic signal for millikelvin measurements

2018: Master internship, 4 months
IMEC, NERF Lab (Leuven, Belgium)
Engineering a catheter that delivers drugs directly into the brain in order to treat brain diseases

Conferences

2023
DPG Meeting (Dresden, Germany), Oral
Forum Sondes Locales (Obernai, France), Oral
Science on Surfaces III (San Sebástian, Spain), Poster
ECOSS36 (Lodz, Poland), Oral

2022
GdR Nanoscience en Champ Proche sous Ultravide (online), Oral
QUSTEC summer school (Freiburg-im-Brisgau, Germany), Poster

2021
QUSTEC summer school (Engelberg, Switzerland), Poster
GdR Nanoscience en Champ Proche sous Ultravide (Toulouse, France), Poster
Colloque Louis Neel (Obernai, France), Poster

Publications

A. Fétida, O. Bengone, M. Romeo, F. Scheurer, R. Robles, N. Lorente, L. Limot
Single-spin quantum sensing: A molecule-on-tip approach
ACS Nano **18**, 13829 (2024) [138]

C. Mier, A. Fétida, R. Robles, P. Boronat, D. Jyoti, N. Lorente, L. Limot, D.-J. Choi
Two molecular devices for superconducting spintronics
arXiv:2402.00644 (2024) [139]

Appendices

APPENDIX A

Computational methods: Chapter 3

DFT calculations were performed using the Vienna Ab initio Simulation Package (VASP) code [140]. The gradient-corrected exchange-correlation functional of the Perdew-Burke-Ernzerhof (PBE) was used [141] and core electrons were treated with the projector augmented wave (PAW) method [142]. A planewave basis set was used with an energy cutoff of 400 eV. The Brillouin zone was sampled using a $30 \times 30 \times 1$ k-point mesh. The Cu (111) surface was simulated using the slab method with 15 Cu layers in a (1×1) unit cell. A vacuum layer of 20 Å was used in the direction perpendicular to the surface in order to minimize interactions between slab repetitions. Co-layers were located following pseudomorphic growth at fcc positions. The position of all atoms except the two bottom layers was relaxed until all the forces were smaller than 0.01 eV/Å. The Co layers relaxed as indicated in Table 4.2. The Magnetocrystalline Anisotropy Energy (MCA) calculations were performed by including spin-orbit coupling (SOC) in the calculations as implemented in VASP [76]. Spin density maps and sections were plotted using the VESTA code [143].

APPENDIX B

Computational methods: Chapter 4

DFT calculations were performed using the VASP code [140]. The PBE [141] form of GGA was used as an exchange and correlation functional. Core electrons were treated following the PAW method [142]. Two supercell structures were used, both representing epitaxially extended Co bilayers on a (111) oriented Cu substrate. The first one is a $2 \times 2 - (111)$ supercell including 2 layers of Co (4 Co atoms per layers) and 9 layers of underlying Cu (4 Cu atoms per layer). It enables to achieve surface hydrogen coverages between 0.25 and 1 ML by the addition of 1 to 4 hydrogen atoms in hollow sites. Possible insertion in the most stable inner octahedral sites was also considered with 4 octahedral sites available at the CoCo and CoCu interfaces, *i.e.* 8 in total or 12 including the hollow surface adsorption sites. The second used geometry is the simple $1 \times 1 - (111)$ supercell including 2 layers of Co (1 Co atom per layer) and 9 layers of underlying Cu (1 Cu atom per layer). In this case, the addition of one hydrogen atoms at the surface or at the CoCo and CoCu corresponds to full hydrogen layers. A vacuum layer of 10 Å was always added in the direction perpendicular to the surface in order to minimize interactions introduced by periodical conditions. In any case an energy cutoff of 500 eV is used. Then for the 2×2 cell a $12 \times 12 \times 1$ k-point sampling was applied while a larger $30 \times 30 \times 1$ k-point sampling was used for the smaller 1×1-cell. We checked for pristine Co and full hydrogen layers that the the magnetocrystalline anisotropy energies are the same for $30 \times 30 \times 1$ k points and $12 \times 12 \times 1$ within an error of less than 20 μeV per atom.

Calculations are performed into two main steps following the magnetic force

theorem [76], one involving spin-polarized calculations in the collinear scheme and the other including spin-orbit coupling. In the collinear case, the supercell is relaxed along the z direction while the lateral lattice constant is fixed to the one of Cu ($a = 3.635$ Å, obtained after optimization of the copper substrate alone) according to an epitaxial growth. The positions of all atoms except for those in the two bottom layers were relaxed (along z direction) until all forces were smaller than 0.01 eV/Å and the total energy converged within an accuracy of $1 \cdot 10^{-7}$ eV. At this stage, the output charge densities are used to deduce the spin-densities, whose maps are plotted with the VESTA software [143]. The same charge densities are also used in order to perform calculations including the spin-orbit interaction as implemented in VASP [76].

The magnetocrystalline anisotropy energy (MCA) was determined by rotating the spins according to different crystallographic directions. In our case, the spin-orbit coupling was taken into account non-self-consistently for the spin orientations corresponding respectively to in-plane and out-of-plane magnetizations. Site- and orbital-resolved energies are provided within the spin-orbit calculations in VASP. More precisely, we get E_{soc} on each ion which represents the accumulated energy contribution inside the augmentation sphere that is centered at each ion position.

In order to determine the total magnetic anisotropy, we add to the MCA the so-called shape anisotropy, which results from magnetostatic dipole-dipole interactions and therefore depends on the geometry of the system under study. In the case of the infinite bilayers of the present work, this contribution E_{dd} was evaluated numerically using the following summation up to an in-plane cut-off radius of 150 Å [77]:

$$E_{dd} = \frac{\mu_0}{8\pi} \sum_{i \neq j} \frac{1}{|\mathbf{r}_{ij}|^3} \left[\mathbf{m}_i \cdot \mathbf{m}_j - 3 \frac{(\mathbf{r}_{ij} \cdot \mathbf{m}_i) \cdot (\mathbf{r}_{ij} \cdot \mathbf{m}_j)}{|\mathbf{r}_{ij}|^2} \right] \tag{B.1}$$

The total MAE, between out-of-plane ($\perp$) and in-plane magnetization ($\parallel$), is therefore given by the difference of energies:

$$\begin{aligned} \text{MAE} &= \text{MCA} + \Delta E_{dd} \\ &= (E^{\text{DFT}}_{tot,\perp} - E^{\text{DFT}}_{tot,\parallel}) + (E_{dd,\perp} - E_{dd,\parallel}) \end{aligned} \tag{B.2}$$

Using this latter equation leads to positive (negative) values of MAE for in-plane (out-of-plane) orientation.

APPENDIX C

Computational methods: Chapter 5

DFT calculations were performed using the VASP code [140]. The PBE [141] form of GGA was used as exchange and correlation functional. Core electrons were treated following the PAW method [142]. A planewave basis set was used with an energy cutoff of 400 eV. The Brillouin zone was sampled using the Γ-point. The Cu(111) surface was simulated using the slab method with 5 Cu layers in a rectangular $(8 \times 5\sqrt{3})$ unit cell. A vacuum layer of 20 Å was used in the direction perpendicular to the surface in order to minimize interactions between slab repetitions. Co-layers were located following pseudomorphic growth at fcc positions. The positions of all atoms except for those in the two bottom layers were relaxed until he forces were smaller than 0.01 eV/Å. Charge transfers and magnetic moments were computed using the Bader method [144]. STM images were simulated using Tersoff-Hamann [49] and Bardeen [47] approximations following the method of Bocquet *et al.* [145] as implemented in the STMpw code [146]. Spin density maps and sections, and structural images were plotted using the VESTA code [143].

APPENDIX D

Résumé en français

Cette thèse de doctorat vise à faire progresser la technique de détection de spin développée par notre équipe de recherche, qui consiste à utiliser une molécule de nickelocène attachée à la pointe d'un microscope à effet tunnel (STM) pour collecter les empreintes magnétiques des surfaces et des atomes. En s'appuyant sur nos précédents travaux ([1],[2], [33]), cette recherche cherche à affiner ces méthodes et à explorer la magnétisation dans différentes directions. Une nouvelle technique de cartographie, l'imagerie par voxel, est introduite pour mesurer l'énergie d'échange et la polarisation de spin en fonction des coordonnées latérales, permettant une observation détaillée des propriétés magnétiques dans les nanoilots de cobalt et les molécules de nickelocène.

D.1 Etat de l'art

Le chapitre 2 offre un aperçu des techniques de pointe dans le domaine du magnétisme de surface, telles que la microscopie à effet tunnel spin-polarisé (SP-STM), la microscopie à force d'échange magnétique et la spectroscopie d'excitation de spin. Il détaille également le principe de fonctionnement de la pointe de nickelocène sur des objets magnétiques et présente brièvement d'autres méthodes de détection du spin en STM, comme la résonance de spin électronique (ESR-STM) ou la mesure des anomalies de conduction à zéro polarisation dans les impuretés magnétiques quantiques.

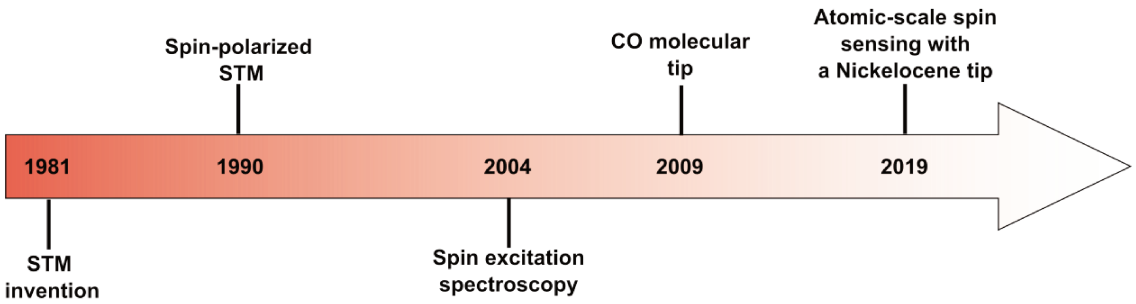

Figure D.1: Chronologie de techniques STM servant à la détection de propriétés magnétiques.

D.1.1 Imagerie magnétique

SP-STM

La STM spin-polarisée permet de détecter la magnétisation de surfaces fines. Pour cela, la pointe de la STM est recouverte de matériaux magnétiques tels que le cobalt, le chrome ou le fer pour afin de lui orientation magnétique spécifique. Une autre méthode consiste à évaporer des atomes magnétiques sur la surface et à les collecter au sommet de la pointe par un transfert de surface à pointe. En raison de l'effet de magnétorésistance, les objets magnétiques avec des directions de magnétisation différentes présentent des contrastes différents. Selon Wortmann et al. [6], la conductance différentielle, dI/dV, s'exprime comme suit :

$$dI/dV \propto \rho_t \rho_s(eV) + m_t m_s cos\theta. \tag{D.1}$$

Le premier terme représente le produit de la densité locale d'états (LDOS) de la pointe et de l'échantillon, tandis que le second terme est le produit scalaire entre la direction de magnétisation locale de la pointe et celle de l'échantillon. Pietzsch et al. [7] ont observé un contraste spin-polarisé sur des ilots de cobalt crus sur Cu(111) (Fig. D.2). Ils présentent deux contrastes possibles. En appliquant un champ magnétique de 1.5 T, la magnétisation de presque tous les ilots s'aligne dans la même direction, résultant en une intensité brillante pour presque toutes les ilots. À l'inverse, un champ magnétique de -1.75 T inverse la magnétisation des ilos dans la direction opposée, résultant en une intensité plus sombre. Cette technique peut également être utilisée pour imager des textures de spin non collinéaires telles que les vortex magnétiques [8] ou les skyrmions à l'échelle nanométrique [9].

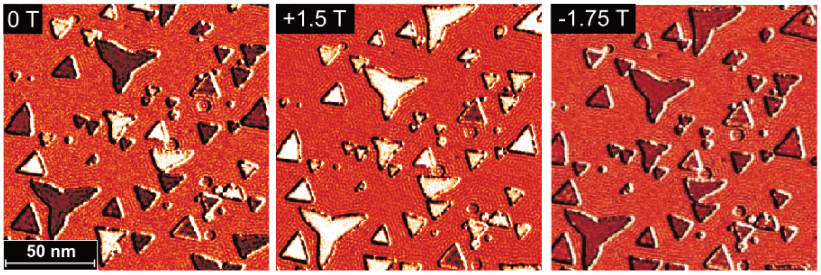

Figure D.2: Images dI/dV d'ilots de Co sur Cu (111) acquises à $V = -0.18$ mV avec différent champs magnétiques perpendiculaires à la surface. Adapté de [7].

Microscopie à force d'échange magnétique

La microscopie à force d'échange magnétique (MexFM) utilise une pointe AFM magnétique pour détecter le spin ou la magnétisation des surfaces. Contrairement au STM, l'AFM ne repose pas sur un courant de tunneling mais sur la force ressentie par la pointe. Kaiser et al. [10] ont utilisé une pointe AFM recouverte de fer pour imager une surface d'oxyde de nickel NiO combinée à un champ magnétique de 5 T pour aligner le spin de la pointe perpendiculairement à la surface (Fig. D.3a). La surface (100) de cet oxyde présente des rangées voisines de nickel séparées par des rangées d'atomes d'oxygène. Chaque atome de nickel d'une rangée a la même direction de spin. Les spins de la rangée de nickel voisine étant couplés de manière antiferromagnétique. L'encart de la Fig. D.3b représente une moyenne de chaque cellule unitaire de l'image brute acquise a une distance inférieure à 200 pm du contact de la surface, et affiche trois contrastes différents, les points les plus brillants représentant les atomes d'oxygène. Les atomes de nickel apparaissent avec deux contrastes différents, foncé ou moins foncé. Cela s'explique par les orientations de spin des atomes de Ni, $\hat{S}_1$, pouvant être parallèles ou antiparallèles au spin de la pointe $\hat{S}_2$. Selon la configuration, l'interaction d'échange magnétique est modifiée selon le modèled'Heisenberg $H = -J_{12}\hat{S}_1 \cdot \hat{S}_2$. La Fig. D.3c est une image AFM standard acquise à une distance plus grande que celle de la Fig. D.3b. Aucune différence n'est observée entre les atomes de Ni. À cette distance, la pointe est sensible uniquement à la chimie de la surface, et non au magnétisme.

D.1.2 Spectroscopie d'excitation de spin

Dans la section précédente, nous avons discuté des techniques de sonde à balayage développées pour imager le magnétisme des surfaces. D'autres études ont également réussi à accéder aux états magnétiques d'atomes isolés ou de molécules en observant les excitations de spin par le courant tunnel inélastique.

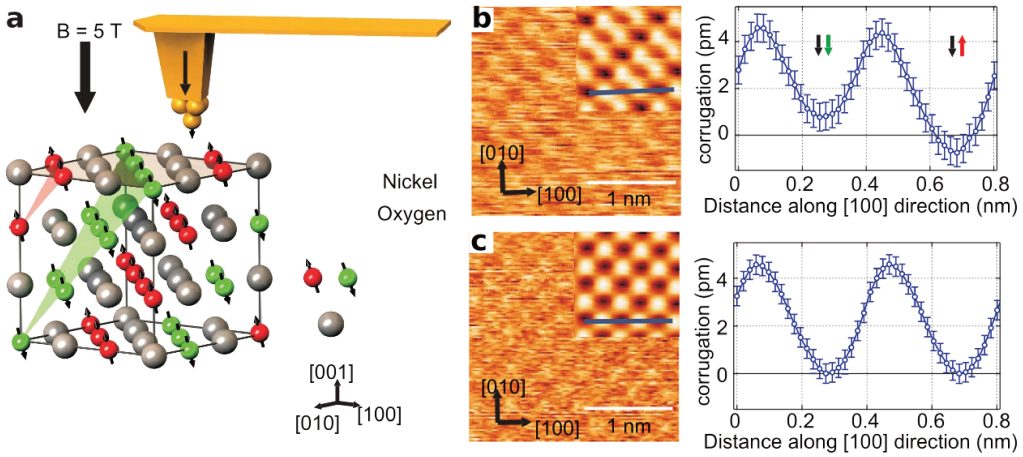

Figure D.3: (a) Dessin d'une pointe magnétique qui scanne la surface de Ni(001) dans un champ magnétique de 5 T perpendiculaire à cette surface. (b) Image brute de la surface NiO(001) acquise à décalage de fréquence $\Delta f = -23.4$ Hz constant. L'encart est une moyenne sur toutes les cellules unités de l'image brute. Le panneau droit montre la corrugation le long de la ligne bleue sur l'encart. (c) La même surface imagée avec $\Delta f = -22$ Hz constant, qui scanne plus loin de la surface. L'encart est également obtenu par moyennage. Ici, la corrugation sur le panneau de droite montre des hauteurs apparentes égales pour deux atomes de Ni voisins. Adapté de [10]

Principe

En 2004, A.J. Heinrich *et al.* [13] ont observé les excitations de spin d'atomes de Mn adsorbés sur des ilots de Al_2O_3 crus sur un substrat de NiAl en utilisant une STM opérant à 0.6 K. Les électrons tunnels ont une probabilité non nulle d'échanger de l'énergie avec l'échantillon lorsqu'ils atteignent un certain seuil d'énergie déterminé par la tension de polarisation, un phénomène connu sous le nom de évènement de tunnel inélastique [14]. Heinrich *et al.* ont mesuré le signal dI/dV sur Al_2O_3 et sur Mn/Al_2O_3 avec et sans champ magnétique externe ($B = 7$ T) dans le plan de l'échantillon (Figs. D.4b-c). En appliquant le champ magnétique, ils ont observé sur le signal dI/dV une marche symétrique aux énergies $\pm\Delta \sim \pm 0.8$ mV. Alors que le signal à $B = 0$ T ne montrait aucune caractéristique. Cette énergie augmente linéairement avec le champ externe (Fig. D.4d). Ceci s'explique par l'effet Zeeman qui lève la degénéréscence des niveaux d'énergie de l'atome de Mn. La marche observée est la signature d'une excitation de spin de l'état fonadamentale $M = -5/2$ au premier état excité $M = -3/2$, due au courant inélastique. M étant la projection du spin sur l'axe de même direction que le champs $\hat{B}$.

L'excitation de spin est mesurable uniquement pour un atome de Mn sur l'oxyde Al_2O_3 et en présence d'un champ magnétique fini. Si Mn est adsorbé sur un métal le temps de vie de l'excitation de spin serait trop faible pour pouvoir l'observer.

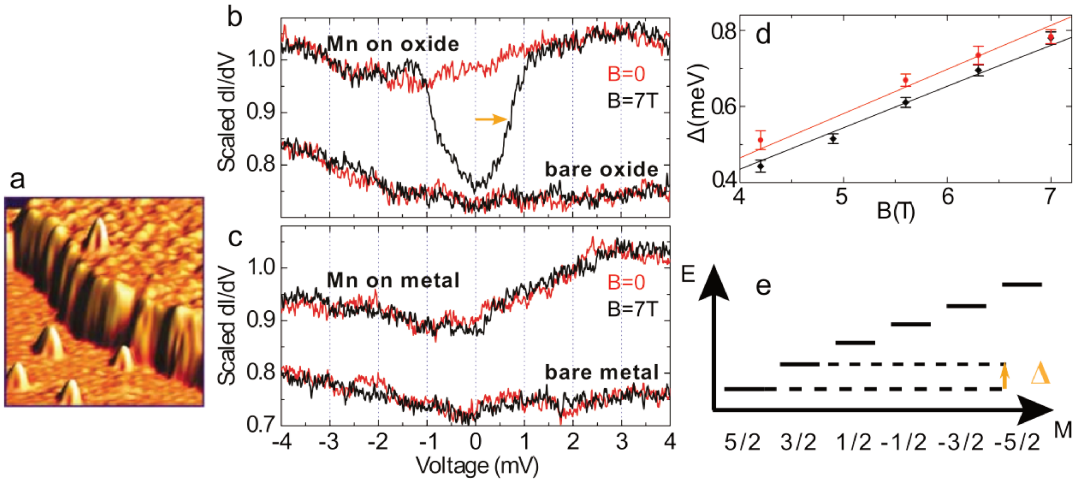

Figure D.4: (a) Image STM d'une parcelle d'oxide Al_2O_3 sur NiAl(110) avec des atomes de Mn adsorbés. (b) Spectres dI/dV acquis sur Mn/Al_2O_3 et sur Al_2O_3 avec et sans champ magnétique. (c) Spectres dI/dV acquis sur l'atome de Mn adsorbé sur NiAl(110) et sur le NiAl seul avec et sans champ magnétique. (d) Niveau d'énergie Zeeman vs. champ magnétique B, en rouge pour l'atome de Mn en bordure d'une parcelle Al_2O_3, en noir, sur un atome de Mn au centre de l'oxide. (e) Diagramme des états de spin et excitation de spin de Mn sur Al_2O_3/NiAl(110) en présence d'un champ magnétique le long de z. Adapté de [13].

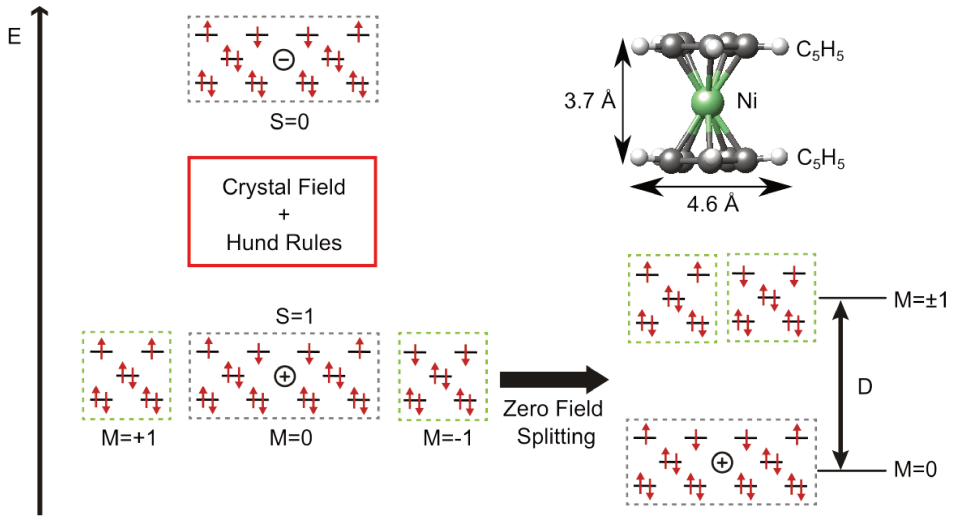

Figure D.5: Configuration électronique du nickelocène produisant un état fondamental de spin $S = 1$. En haut à droite un modèle de la structure du nickelocène (Ni : vert, C : gris, H : blanc).

Excitation de spin du nickelocene

Tout au long de cette thèse, les excitations de spin du nickelocène (Nc) joueront un rôle central. Comme illustré dans la Fig. D.5a, cette molécule consiste en un atome de Ni pris en sandwich entre deux anneaux de cyclopentadiényle (C_5H_5 ou anneaux

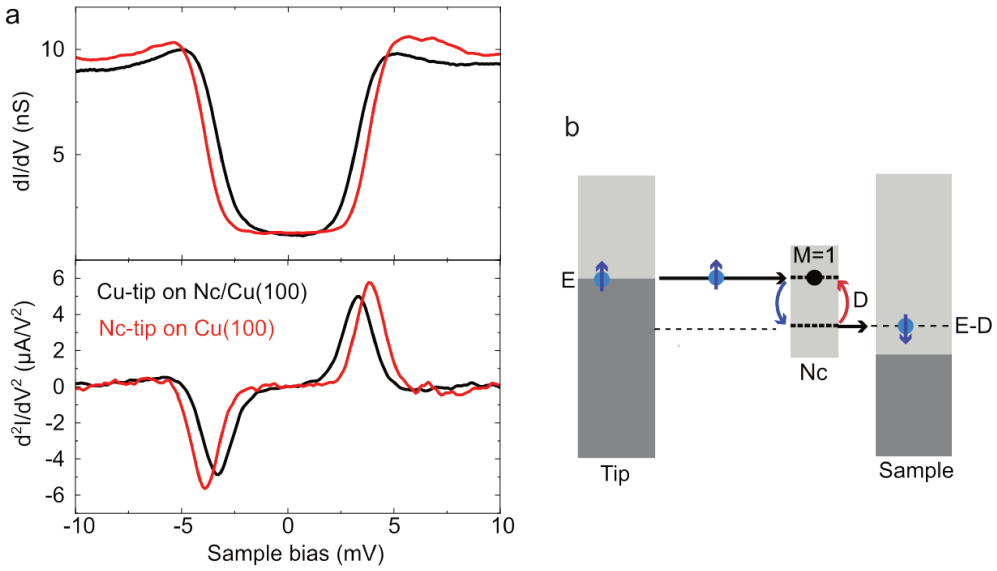

Figure D.6: (a) Spectres dI/dV et leur dérivée, d^2I/dV^2, acquis avec une pointe Cu sur une molécule de Nc (ligne noire) et avec une pointe Nc sur la surface de Cu(100) (ligne rouge). Il est à noter que le pic à polarisation positive et le creux à polarisation négative sont des caractéristiques du même événement mais avec des courants de tunnel de directions opposées. (b) Schéma d'un électron tunnellant inélastiquement dans la jonction pointe/Nc/STM et induisant une excitation de spin de Nc.

Cp). Cette molécule possède un spin $S = 1$ comme démontré par plusieurs études conduites en phase gazeuse [26] ou sur des échantillons en poudre [26, 27]. En règle générale, la moitié du moment magnétique est portée par l'atome de Ni, tandis que les deux anneaux Cp portent l'autre moitié. La figure D.5a-b illustrent comment les propriétés électroniques déterminent l'état magnétique le plus favorable de Nc. La géométrie de la molécule conduit à un champ cristallin de symétrie D_{5h} et le couplage spin-orbite résulte en une anisotropie magnétocristalline positive D avec un plan d'anisotropie facile perpendiculaire à l'axe passant par les deux anneaux Cp. Cela conduit à une séparation de l'état fondamental de Nc $|S = 1, M = 0\rangle$ et des états excités dégénérés $|S = 1, M = \pm 1\rangle$. Ici, M représente la projection de S le long de l'axe perpendiculaire à l'anneau Cp. En l'absence de champ magnétique externe, l'hamiltonien de spin de la molécule est :

$$\hat{H} = D\hat{S}_z^{\,2}. \tag{D.2}$$

L'énergie d'anisotropie est évaluée à $D = 4.17$ meV selon [27] et $D = 3.17$ meV selon [26]. La Fig. D.6a présente la dérivée seconde d^2I/dV^2 enregistrée au-dessus de Nc (ligne noire continue) montre un pic à 3.8 mV et un creux à polarisation opposée. Comme montré sur la Fig. D.6b, lorsque Nc est promu à l'état excité

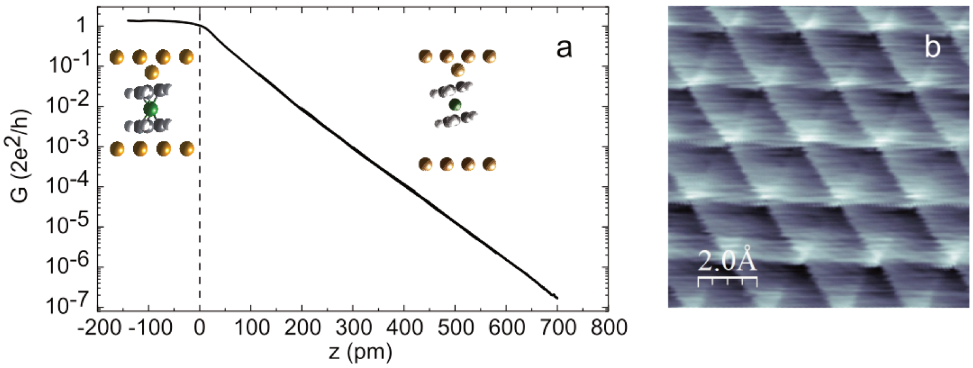

Figure D.7: (a) Conductance en fonction de la distance pointe-échantillon (boucle de rétroaction ouverte à 50 pA, 50 mV). La trace a été acquise au-dessus d'un atome de la surface de Cu(111). La ligne noire en pointillés correspond au point de contact entre la pointe Nc et la surface de Cu. Les encarts présentent une simulation de l'adsorption de Nc sur la pointe dans les régimes de tunneling et de contact. (b) Image de Cu(111) obtenue en scannant avec la pointe Nc en contact avec la surface. La corrugation de la surface est visible.

dégénéré, l'électron de tunnel perd de l'énergie et doit également inverser son spin pour préserver le moment angulaire total. Si la molécule est excitée à $|M = 1\rangle$ l'électron passe de $m = +1/2$ à $m = -1/2$ et si elle est excitée à $|M = -1\rangle$ alors l'électron passe de $m = -1/2$ à $m = +1/2$. Avec m la projection du spin de l'électron sur le même axe où est projeté M. Dans les deux cas, l'électron perd une énergie D. À partir des positions du pic et de la baisse, nous trouvons une anisotropie magnétique de $D = 3.3$ meV.

Excitations de spin d'une pointe de nickelocène

Notre groupe a démontré que le nickelocène (Nc) peut être attaché à l'extrémité d'une pointe de STM [1, 33]. Le processus d'attachement est simple, à condition que la pointe soit atomiquement aiguisée. Sur les surfaces de métaux nobles, il suffit de régler les paramètres de tunnelage à -1 mV et 50 pA, tout en approchant délicatement la pointe de la molécule d'au moins 200 pm. Une fois la molécule fixée à la pointe, nous vérifions la fiabilité et la robustesse de la pointe moléculaire en balayant la pointe vers la surface et en mesurant la conductance de la jonction jusqu'au contact(Fig. D.7a) [34]. À ce point, la distance entre les atomes de carbone de l'anneau Cp et les atomes de cuivre est d'environ 250 pm. La stabilité de la pointe Nc est évaluée en enregistrant des images de contact de la surface de cuivre, ce qui permet d'obtenir une résolution atomique reproductible de la surface (Fig. D.7b) [35].

Des calculs de la théorie de la fonctionnelle de densité (DFT) ont été réalisés en

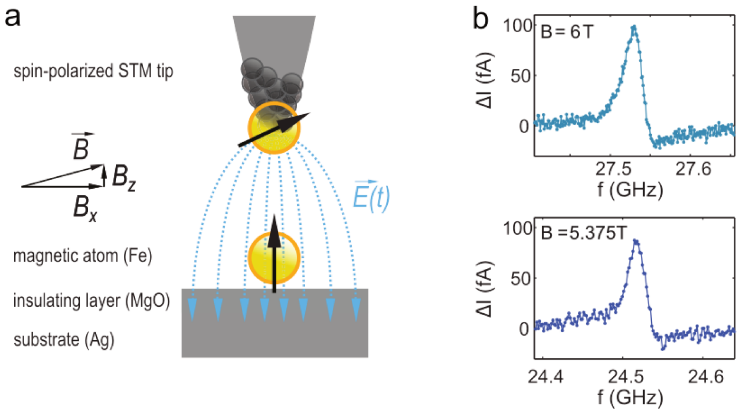

Figure D.8: (a) Modèle schématique de la technique ESR : La pointe polarisée en spin positionnée sur un atome de Fe/MgO/Ag(001) immergé dans un champ externe **B**. Les flèches noires représentent leurs moments magnétiques. La tension modulée en radio fréquence (RF) dans la jonction crée un champ électrique dépendant du temps. (b) Deux exemples de pics ESR mesurés à $B = 6$ T et $B = 5.375$ T. Adapté de [15].

modélisant la pointe moléculaire par un Nc au sommet d'un atome de Cu adsorbé sur une surface de Cu(100) [33]. Dans le régime de tunnel, la molécule est attachée à l'atome de cuivre par deux atomes de carbone de l'anneau Cp, entraînant une inclinaison de 12° par rapport à la normale de la surface. En contact, les anneaux Cp sont parallèles à la surface et l'atome de cuivre est coordonné à cinq atomes de carbone (Encartes Fig. D.7a).

Comme montré dans la Fig.D.6a, les excitations de spin sont préservées lorsque le Nc est à l'extrémité de la pointe (ligne rouge continue). Nous trouvons une anisotropie magnétique de $D = 3.8$, ce qui est plus élevé que l'anisotropie magnétique du Nc sur la surface. Nous attribuons cela à un allongement de la molécule le long de son axe moléculaire principal[1].

D.1.3 Autres techniques de détection du spin

La détection du spin avec le STM peut également être réalisée en exploitant trois phénomènes différents : la résonance de spin électronique (ESR), les états de Yu-Shiba-Rusinov et l'effet Kondo.

ESR-STM. Pour illustrer l'ESR-STM, nous considérons l'étude pionnière de Baumann et al. en 2015 [15]. Un atome magnétique, Fe, est adsorbé sur des ilots isolants de MgO couvrant partiellement un substrat en argent. Le MgO permettant d'accroite le temps de relaxation du spin. Un champ magnétique important $\vec{B}$ dont la composante perpendiculaire à la surface lève la dégénérescence des états bas en énergie (Fig. D.8a). Pour induire l'excitation de spin entre les deux états,

un champ électrique radiofréquence (RF) dépendant du temps est employé dans la jonction tunnel. Lorsque la fréquence de ce champ électrique AC correspond à celle d'une excitation de spin, les états magnétiques deviennent également peuplés, ce qui fait tourner l'orientation moyenne de la magnétisation de l'atome de Fe sur la surface. Un autre élément clé de la mesure ESR est la pointe spin-polarisée, qui agit comme détecteur. En fonction de l'orientation relative des moments magnétiques de la pointe et de l'atome de Fe, l'effet de magnétorésistance modifie le courant tunnel. Comme le montre la Fig. D.8b, ΔI représente la différence entre le courant tunnel avec et sans la tension RF à une fréquence donnée. Un pic apparaît à la fréquence de résonance avec une intensité atteignant 100 fA. En fonction de la valeur du champ externe $\vec{B}$ l'effet Zeeman change et la fréquence de résonance se déplace. L'ESR-STM possède une résolution énergétique impressionnante de 0.1 µeV, correspondant à un champ de l'ordre du millitesla.

Etats Yu-Shiba-Rusinov Le STM est capable de détecter des perturbations de l'état supraconducteur à l'échelle atomique à proximité des impuretés magnétiques [40]. Lorsqu'elles sont adsorbées sur la surface supraconductrice, ou même en dessous, les impuretés magnétiques perturbent localement les paires de Cooper. Des états liés se forment, également connus sous le nom d'états Yu-Shiba-Rusinov (YSR), qui apparaissent comme des pics à des tensions de biais opposés dans le gap supraconducteur dans les mesures de dI/dV. Ces états sont des résonances sous-gap polarisées en spin à 100%. Il est intéressant de noter qu'une pointe supraconductrice peut être fonctionnalisée avec une impureté magnétique pour produire des états YSR sur la pointe [41] et être utilisée pour effectuer des mesures spin-polarisées avec une sensibilité au spin accrue [42].

Effet Kondo. Un autre phénomène causé par des impuretés magnétiques adsorbées sur une surface métallique est l'effet Kondo [43, 44]. Le spin de l'impureté est écranté par les électrons de conduction du métal, conduisant à un état virtuel qui se manifeste dans le dI/dV comme un pic à tension de biais nulle. L'effet Kondo peut également être produit sur la pointe du STM de manière contrôlée en fonctionnalisant l'extrémité de la pointe avec la molécule de cobaltocène de spin $-1/2$ [45]. De manière similaire à la pointe Nc, une pointe Kondo peut recueillir des informations magnétiques sur des objets en surveillant la résonance Kondo.

D.2 Microscope à effet tunnel

Le **chapitre 3** commence par une explication de l'effet tunnel et couvre les théories de Bardeen, Tersoff-Hamann, et Wentzel-Kramers-Brillouin (WKB), qui fournissent

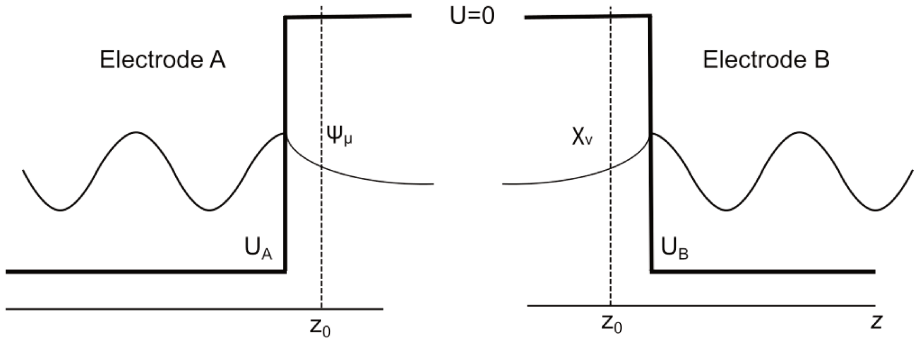

Figure D.9: Un dessin unidimensionnel des électrodes A et B éloignées et de leurs fonctions d'onde respectives ψ_μ et χ_ν.

une description mathématique du courant dans une jonction tunnel. Il aborde également les techniques d'imagerie de surface, introduit la spectroscopie à effet tunnel et la spectroscopie électronique inélastique, et conclut par une description détaillée de notre configuration expérimentale et du processus d'acquisition des données.

D.2.1 Fonctionnement

Le microscope à effet tunnel (STM), inventé en 1981, a marqué une avancée révolutionnaire dans le domaine de la nanoscience. Les figures clés derrière cette invention, Binnig, Rohrer, Gerber et Weibel, ont été honorées par le prix Nobel en 1986. Le STM sert d'outil puissant pour la caractérisation des surfaces avec une résolution allant jusqu'au nanomètre, voire à l'échelle atomique dans certains cas. Cela est réalisé en rapprochant une pointe métallique à quelques angströms de la surface de l'échantillon. En appliquant une tension de biais entre la pointe et l'échantillon, un courant traverse l'écart de vide, son amplitude dépendant de la distance pointe-surface. Grâce à une boucle de rétroaction, la pointe balaie la surface à courant constant, et ses mouvements verticaux produisent une carte topographique de la surface. En plus de l'imagerie de surface, le STM permet l'analyse spectroscopique d'objets à l'échelle nanométrique. Notamment, il permet d'accéder à la densité d'états de surface ainsi qu'aux états excités des atomes et molécules individuels.

D.2.2 La théorie de Bardeen

Le modèle de Bardeen, nommé d'après le physicien J. Bardeen, est utilisé pour décrire le transport des porteurs de charge [47], typiquement des électrons. Ce modèle est basé sur l'équation de transport de Boltzmann semi-classique, qui prend en compte à la fois les effets classiques et quantiques. Il offre une compréhension large du transport des porteurs et du phénomène tunnel se produisant entre deux

électrodes rapprochées. Ici, nous abordons le problème en utilisant des électrodes unidimensionnelles.

Nous considérons une électrode A caractérisée par une barrière de potentiel U_A (Fig. 3.2) contenant les états stationnaires ψ_μ d'énergies E_μ. Pour l'électrode B, caractérisée par un potentiel U_B, les états stationnaires sont χ_ν ayant pour énergies propres E_ν. Lorsque les deux électrodes sont rapprochées jusqu'à la coordonnée z_0 le courant de tunneling résultant est décrit par :

$$I = \frac{2\pi e}{\hbar} \sum_{\mu\nu} |M_{\mu\nu}|^2 \, \delta(E_\mu - E_\nu - eV)[f(E_\mu) - f(E_\nu)], \tag{D.3}$$

avec $M_{\mu\nu}$ le terme de la matrice tunnel.

D.2.3 Le modèle de Tersoff-Hamann

Dans la théorie de Bardeen, le calcul des éléments de matrice de tunneling peut être exigeant. Tersoff et Hamann simplifient cette étape en décrivant la pointe STM par une onde sphérique [49]. Cette approximation fournit une méthode relativement simple et efficace sur le plan computationnel pour analyser les phénomènes de tunneling à proximité des surfaces.

$$I \propto V \rho_t(E_F) \sum_{\mu} |\psi_\mu(\vec{r_0})|^2 \, \delta(E_s - E_F), \tag{D.4}$$

où ρ_t st la densité d'états (DOS) par unité de volume de la pointe. Le courant de tunneling dépend de la DOS locale de la surface à l'énergie de Fermi, mesurée à la position de la pointe,

$$\rho_s(\vec{r_0}, E) \equiv \sum_{\mu} |\psi_\mu(\vec{r_0})|^2 \, \delta(E_\mu - E). \tag{D.5}$$

Les deux théories, Bardeen et Tersfoff-Hammann ont un rôle important, dans cette thèse, afin de comparer nos résultats expérmentaux avec la théorie.

D.2.4 Spectroscopie via détection synchrone

En STM, la conductance différentielle, $dI(V)/dV$ est une mesure permettant l'accès à la densité d'état locale de la surface étudiée. En effet, en considérant une barrière potentielle trapézoïdale à l'intérieur de la jonction tunnel :

$$\frac{dI}{dV}(z, V) \propto \rho_s(eV) T(z, eV, V), \tag{D.6}$$

z étant la distance entre la pointe STM et la surface, T la probabilité de transmission de la jonction tunnel. Afin de mesurer dI/dV en maximizant le ratio signal sur bruit, nous utilisons la détection synchrone. Lors de la mesure, un signal modulé en fréquence, $V_m \cos(\omega t + \theta)$, est ajouté à la tension de biais V. θ représentant la phase du signal et ω la fréquence angulaire. Dans cette thèse nous utilisons également cette technique afin de mesurer directement d^2I/dV^2 et d'observer les évenements de tunnel inélastiques.

Les amplitudes typiques du signal modulé V_m vont de 200 à 500 μV rms pour la spectroscopie inélastique et de 2 à 5 mV rms. pour la spectroscopie de tunneling standard. Les fréquences typiques se situent entre 700 Hz et 6.5 kHz. L'utilisation d'une fréquence de modulation suffisamment élevée permet à la détection synchrone de réaliser un plus grand nombre de moyennes sur la valeur mesurée pendant un temps donné, améliorant ainsi le rapport signal sur bruit.

Dans le Chapitre 4, nous utiliserons largement la spectroscopie d'excitation de spin pour mesurer les propriétés magnétiques des surfaces. Ces spectres inélastiques peuvent être reproduits avec précision par un calcul modèle [57], qui indique une température effective $T^* = 3.4$ K pour notre système, alors que notre température de fonctionnement est de 2.4 K. La quantité $\delta'_{T^*} = 5.4 k_B T^*$ fournit donc une estimation approximative de l'élargissement de nos spectres de tunnel inélastiques, qui dans notre configuration est de 1.57 meV.

D.2.5 Imagerie par voxel

Afin d'explorer le magnétisme de surface avec une pointe Nc, nous avons modifié notre configuration d'acquisition pour enregistrer des voxels. Le terme voxel est dérivé des mots volume et pixel. En imagerie médicale, en infographie et dans d'autres domaines traitant des données 3D, les voxels sont utilisés pour représenter la valeur (par exemple, intensité ou couleur) d'un point spécifique dans un espace 3D. Cette acquisition de données implique la définition d'une grille, d'environ 1 nm de large, comprenant un maximum de 40×40 pixels, placée sur la surface ou l'objet étudié comme illustré dans la Fig. D.10. La pointe est ensuite scannée à une hauteur constante au-dessus de chaque pixel, où un spectre d^2I/dV^2 est acquis, ici avec le nickelocène attaché à la pointe du STM . Après ajustement de chaque spectre avec un profil de Voigt, nous avons extrait des informations magnétiques, comme décrit dans le Chapitre 4. Ces informations aboutissent à deux cartes de voxels distinctes : le champ d'échange $E_{\mathrm{ex}}(x, y)$ et la polarisation de spin au niveau de Fermi $P(x, y)$. Une troisième carte de voxels, qui ne sera pas exploitée dans cette thèse, peut également être définie où l'anisotropie magnétique D de la pointe Nc est

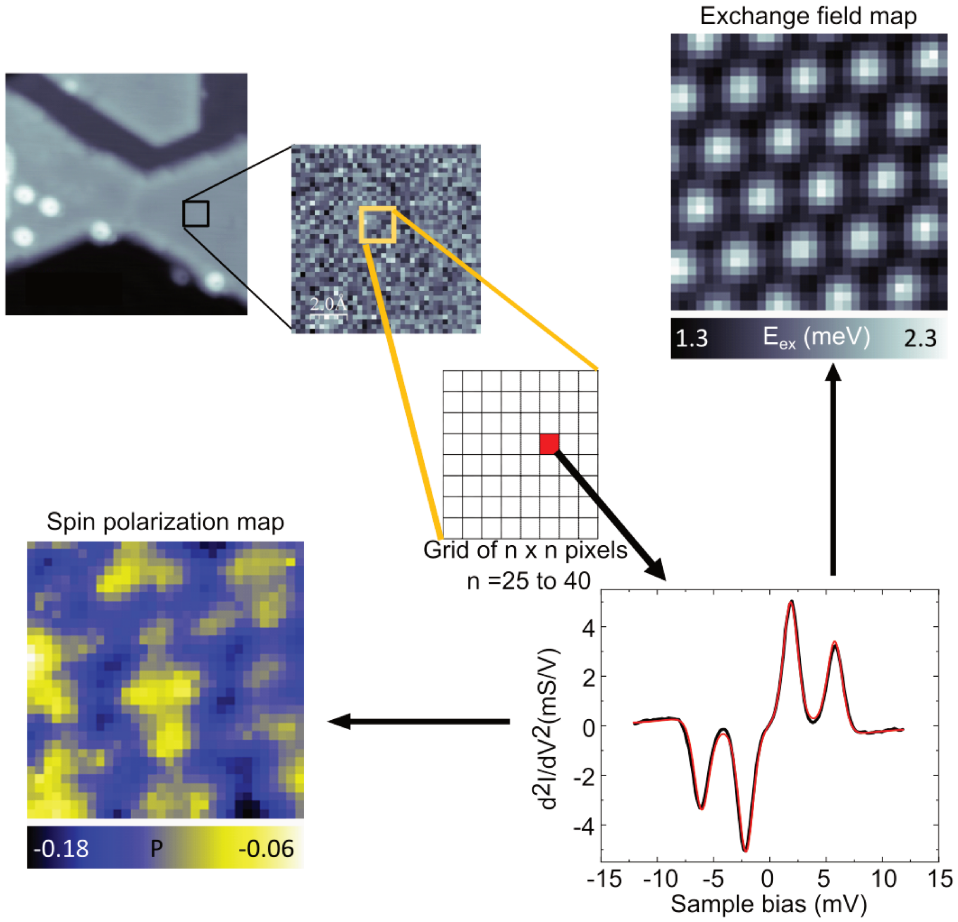

Figure D.10: Les panneaux illustrent l'acquisition d'une carte de voxels. Une grille avec $n \times n$ pixels est placée sur une surface. Un spectre de d^2I/dV^2 est acquis à chaque pixel avec une pointe de nickelocène. Ici, la ligne noire représente les données brutes et la ligne rouge représente un ajustement. Les informations magnétiques sont ensuite extraites de chaque spectre, résultant en des cartes de voxels distinctes.

associée à la position (x, y).

Étant donné la durée de la mesure, la dérive (drift) pose un défi inévitable. La dérive se produit en raison des températures finies de la surface et de la pointe, entraînant leur expansion ou contraction. Par conséquent, lorsque la pointe est dirigée pour mesurer à un pixel situé en $\vec{r_0}$, la dérive peut déplacer la pointe vers $\vec{r_0} + \Delta\vec{r}$. Nous soupçonnons que, en raison de notre configuration où nous abaissons la température à $2.4K$, la pointe prend plus de temps à se thermaliser par rapport à l'échantillon et continue ainsi de subir des contraintes pendant l'acquisition des données. La dérive s'accumule au fil du temps, déformant la carte résultante. Pour remédier à cela, nous avons mis en place un point d'ancrage, généralement le sommet d'un atome, servant de position de référence pour la pointe. Après chaque mesure de pixel, la pointe retourne à ce point d'ancrage et suit sa nouvelle position en utilisant le mode "atom tracking" du STM. Par conséquent, nous évaluons la dérive

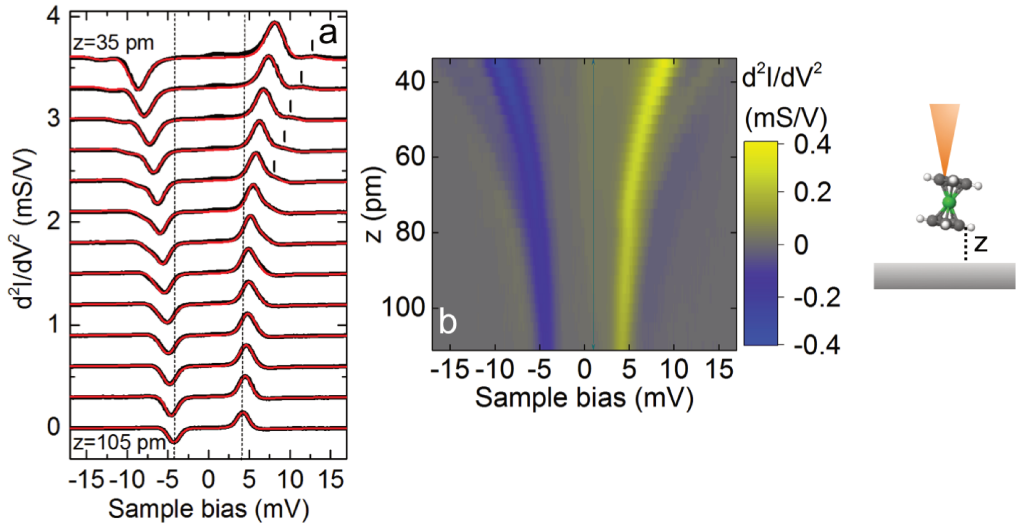

Figure D.11: (a) Les spectres de d^2I/dV^2 au-dessus d'un atome d'un ilot de Co (1 ML), acquis à différentes distances pointe-Co. Les spectres sont décalés verticalement de 0.5 ms/V les uns par rapport aux autres. Les lignes verticales pleines dans le panneau (a) indiquent la position de l'excitation $|\Psi_0\rangle \rightarrow |\Psi_2\rangle$. Lignes rouges : Simulations basées sur le modèle de diffusion dynamique. (b) Représentation en intensité 2D d'une série de spectres d^2I/dV^2 dépendants de la distance au-dessus d'un atome de Co. En encadré : Schéma de la jonction tunnel.

$(\delta x, \delta y, \delta z)$ et compensons en ajustant les coordonnées pour le pixel suivant $(x + \delta x, y + \delta y, z + \delta z)$. Cette technique nous permet de réduire la dérive en (x,y) à une valeur < 10 pm et en z à une valeur < 5 pm.

D.3 Détection de spin à l'échelle atomique sur ilot de cobalt

Contrairement à la RPE, les états de spin d'une pointe Nc sont en fait observés par le biais d'excitations de spin résultant de la composante inélastique du courant tunnel (§ 2.2.3). Une précision sub-ångström dans la détection de spin de l'échantillon est rendue possible par l'interaction d'échange se produisant à travers le vide entre la pointe Nc et la surface, ce qui modifie les états de spin de Nc [2, 32, 67]. Dans ce chapitre, nous examinons des ilots ferromagnétiques prototypes de Co sur une surface de Cu(111) propre, y compris des ilots d'épaisseur monocouche qui restent inexplorés. Nos résultats sont soutenus par des calculs ab initio effectués par Roberto Robles, Nicolas Lorente et Olivier Bengone

D.3.1 Orientation de l'aimantation

La figure D.11a montre une série de spectres d^2I/dV^2 dépendants de la distance obtenus au-dessus d'un ilot monocouche avec la pointe de Nc positionnée directement au-dessus d'un atome de Co au centre de l'ilot. La figure D.11b présente la carte d'intensité 2D correspondante. À une distance de $z = 105$ pm, le spectre présente un pic et un creux aux biais de $+3.9$ et -3.9 mV, respectivement. À mesure que la pointe se rapproche, le pic se déplace vers le haut et le creux vers le bas en énergie de près de 5 mV. À $z \leq 60$ pm, un second pic (creux) apparaît, initialement comme une épaule haute énergie (basse énergie) au pic (creux), puis devenant pleinement résolu à $z = 40$ pm en raison de son décalage énergétique plus prononcé. Dans les ilots en bicouche et la majorité des ilots en tricouche ($> 80\%$), nous observons plutôt une division progressive du pic et du creux dans le spectre d^2I/dV^2 à mesure que la pointe s'approche verticalement d'un atome de Co. Cependant, une minorité des ilots en tricouche ($< 20\%$) présentent un comportement similaire aux ilots monocouche.

Selon la direction d'aimantation des surfaces sondées, les niveaux de Zeeman de Nc, repérés à l'aide des pics (creux) sur les spectres, évoluent différemment lorsque l'on approche la pointe moléculaire de la surface. Les ajustements des spectres effectués à l'aide d'un programme de simulations [57] indiquent que les monocouches possèdent une aimantation dans le plan de la surface, alors que les bicouches et certaines tricouches possèdent une aimantation hors du plan de la surface. Les calculs des niveaux Zeeman sont effectués en utilisant l'hamiltonien : $\hat{H} = D\hat{S}_z^2 - J\hat{S} \cdot \hat{S}_{\mathrm{Co}}$. Où $\hat{S}$ est le spin de Nc. La position en énergie des pics(creux) sur les spectres permet aussi de mesurer le champ d'échange $B_{\mathrm{ex}} = J\langle S_{\mathrm{Co}}\rangle / g\mu_{\mathrm{B}}$, entre la pointe et la surface. L'orientation de l'aimantation de chaque ilots est déterminée par des calculs DFT de l'énergie d'anisotropie magnétocristalline et correspond à nos résultats.

D.3.2 Cartes du champ d'échange

L'énergie d'échange au-dessus de l'ilot monocouche est presque trois fois plus forte par rapport aux ilots bicouches et tricouches, qui présentent des énergies d'échange identiques. Le couplage d'échange varie également à travers la surface. Pour visualiser ces variations, nous acquérons une image de voxels (§ D.2.5) consistant en un ensemble de données sous la forme de $d^2I/dV^2(x, y, V)$ à une distance fixe de $z = 20$ pm au-dessus d'une région d'intérêt. Nous déterminons ensuite l'énergie d'échange à chaque position latérale de la pointe en ajustant les spectres. L'image résultante (Fig.D.12a-b) montre que la corrugation est environ deux fois plus faible dans l'ilot

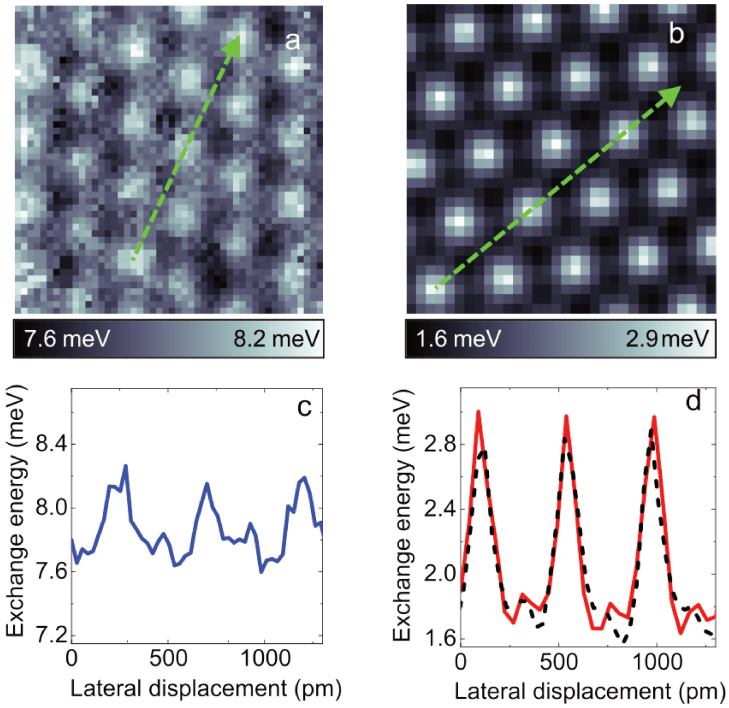

Figure D.12: (a,b) Cartes spatiales de l'énergie d'échange acquises à une distance fixe de $z = 20$ pm au-dessus d'une île en monocouche et en bicouche, respectivement. (c,d) Profils de E_{ex} des couches acquis le long des lignes pointillées indiquées dans (a) et (b). La ligne pointillée dans (d) est le profil de E_{ex} d'une tricouche.

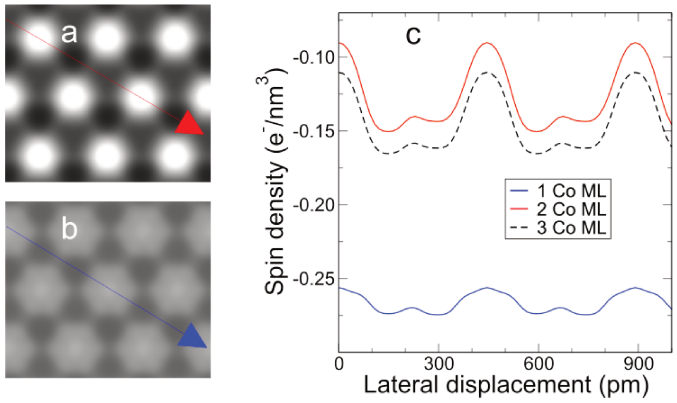

Figure D.13: (a)-(b) Cartes de densité de spin calculées à une distance fixe de 300 pm au-dessus d'une bicouche et d'une monocouche, respectivement. (c) Profils de densité de spin des couches le long des lignes indiquées dans (a) et (b). La ligne pointillée est le profil de densité de spin d'une tricouche.

monocouche (Fig.D.12c) par rapport aux ilots bicouches et tricouches (Fig. D.12d). Inversement, le champs d'échange est environ 2.8 fois plus élevé sur la monocouche. Ce comportement est bien reproduit par des cartes de densités de spins sur les 3 types d'ilots (Fig. D.13)a-b. Les profils (Fig. D.13c) montrent que la densité de spin est plus forte sur la monocouche mais la corrugation est plus faible.

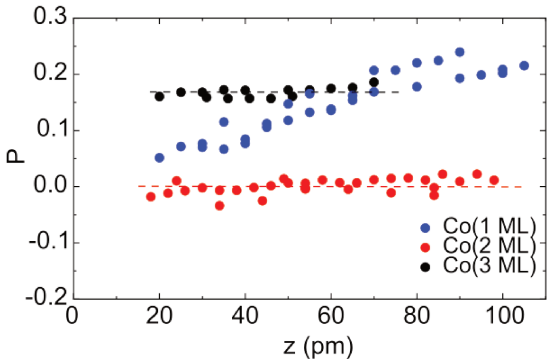

Figure D.14: Polarisation de spin en fonction de la distance pointe-surface z extraite des spectres de d^2I/dV^2. Les lignes pointillées servent de guide visuel.

D.3.3 Polarisation en spin des ilots de Co

Les ilots de cobalt peuvent également montrer une polarisation de spin, car leur aimantation induit un déséquilibre dans le courant d'électrons de spin ↑ comparé au courant d'électrons de spin ↓. Cela entraîne des variations discernables dans les hauteurs relatives des pics (h_+) et des creux (h_-) dans le spectre de d^2I/dV^2. La polarisation de la surface, au niveau de Fermi est donné par :

$$P = \frac{h_+ - h_-}{h_+ + h_-}. \tag{D.7}$$

La figure D.14 montre la polarisation de spin des 3 types d'ilots de Co (1 ML, 2 ML, 3 ML) en fonction de la distance pointe moléculaire - surface. La polarisation de spin de la monocouche n'est pas constante avec z contrairement à celle de la bicouche et de la tricouche. Pour l'expliquer, il faut revenir à la définition de P qui est le produit de la polarisation en spin de la pointe, η_t, et de la surface η_s. C'est à dire $P = \eta_s\eta_t$. Le calcul de η_t montre que dans le cas d'une surface avec aimantation dans le plan, l'angle d'adsorption de Nc sur la pointe fait varier fortement η_t en fonction de z. Or, nous savons que en approchant la surface, l'angle d'adsorbtion de Nc sur la pointe varie (Fig. D.7a), ce qui explique le caractère non monotone de P. Inversement, pour des ilots à aimantation hors du plan, $\eta_t \approx 1$ où seul η_s est sondé et P est constant.

D.4 Réorientation du spin d'un nano-aimant via adsorbtion d'hydrogène

L'adsorption dissociative des molécules d'hydrogène a également été rapportée sur des surfaces magnétiques, où les atomes d'hydrogène forment alors des supraréseaux

[73, 112]. Cependant, la réalisation de mesures STM sensibles au spin sur des aimants exposés à l'hydrogène reste une entreprise difficile [73, 103], car elle nécessite une pointe magnétique qui, similaire à la surface, est susceptible à la contamination par l'hydrogène [113]. Un contrôle rigoureux de l'état de l'apex de la pointe est essentiel, de préférence avec un champ magnétique externe.

Pour surmonter ce défi, nous avons passivé l'apex d'une pointe de W recouverte de cuivre avec une molécule de Nc et nous nous sommes concentrés sur des ilots de Co crû sur Cu(111) et, contrairement aux ilots du Chapitre 4, nous les avons exposés à l'hydrogène.

Les molécules d'hydrogène constituent le gaz résiduel prédominant dans la chambre UHV. Dans notre environnement UHV, où la pression est inférieure à $< 5\times10^{-11}$ mbar, l'hydrogène contamine les ilots de Co au fil du temps. Cependant, pour obtenir la superstructure d'hydrogène désirée sur les ilots, une hydrogénation "efficace" est nécessaire. Cela consiste à augmenter la température du cryostat à plus de 17 K pendant moins d'une heure afin de provoquer la libération de H_2 des parois en cuivre plaqué or du cryostat STM [114].

D.4.1 Superstructure d'hydrogène sur Co (2 ML)

Pour déterminer la couverture en hydrogène sur un ilot de Co (2 ML) à l'échelle nanométrique, nous avons utilisé la pointe Nc en mode haute tension. Le résultat est une image topographique affranchie de la corrugation magnétique (Fig. D.15a). Par-dessus, les cercles bleus représentent une simulation du réseau de Co de l'ilot vierge. Notre hypothèse est que l'hydrogène est arrangé en une superstructure 2H-(2×2), comme indiqué sur le modèle de la figure D.15b. La couverture est de 2 atomes d'H par cellule unité en surface, soit 0.5 ML. La simulation d'une image STM en courant constant (Fig. D.15c) de cette structure à l'aide de la théorie de Tersoff-Hamann correspond à notre image expérimentale. Cependant, la simulation de l'image STM d'un réseau 1H-(2×2), où la couverture d'hydrogène est de 0.25 ML, donne des résultats similaires. Différencier les superstructures 1H-(2×2) et 2H-(2×2) nécessite l'acquisition de spectres dI/dV sur la bicouche de Co contaminée d'hydrogène. La comparaison avec le calcul DFT de la LDOS (Fig. 5.3) indique que la superstructure de H est bien 2H-(2×2).

D.4.2 Rotation de l'aimantation

Pour déterminer l'orientation de l'aimantation de l'ilot, nous avons enregistré une série de spectres d^2I/dV^2 en approchant la pointe de Nc au-dessus de Co(I). Comme

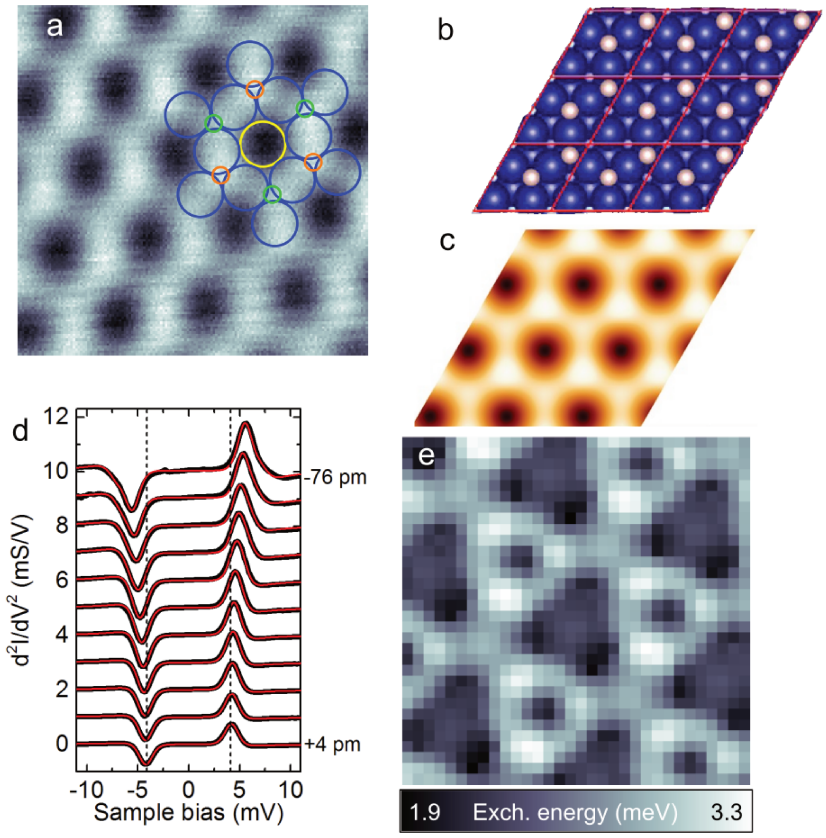

Figure D.15: (a) Image STM de l'ilot bicouche de Co (1.7×1.7 nm^2, tension : 50 mV, courant tunnel : 50 pA) avec une superstructure 2H-(2×2) [Co(I) : jaune, Co(II) : bleu, H(I) : vert, H(II) : orange]. (b) Structure modèle de 2H-(2×2) (Co : bleu, H : blanc). (c) Topographie en courant constant calculée par DFT correspondante à (b) (simulation effectuée à 100 mV et 1 nA). (d) Spectres d^2I/dV^2 acquis au-dessus de Co(I) pour différents déplacements de la pointe moléculaire (e) Carte spatiale de l'énergie d'échange acquise par imagerie voxel à une distance fixe au-dessus d'un ilot de Co ($\delta z = -40$ pm).

le montre la fig. D.15d, le pique (et le creux) se déplace vers les énergies hautes (basses), au fur et à mesure que la pointe de Nc approche l'atome. Ces spectres ne peuvent être reproduits qu'en utilisant un modèle de diffusion dynamique avec une aimantation des ilots dans le plan (lignes rouges solides dans la fig.D.15d [57]). Le résultat est similaire pour des mesures effectuées sur Co(II). L'adsorbtion d'hydrogène à donc fait tourner l'aimantation de la bicouche de Co de 90°.

D.4.3 Déterminer la quantité d'hydrogène adsorbé

La figure. D.15d est la carte spatiale de l'énergie d'échange acquise par imagerie voxel sur la bicouche de Co contaminée. Cette carte est bien reproduite par la carte de la densité de spin calculée pour une bicouche décorée d'une superstructure 2H-

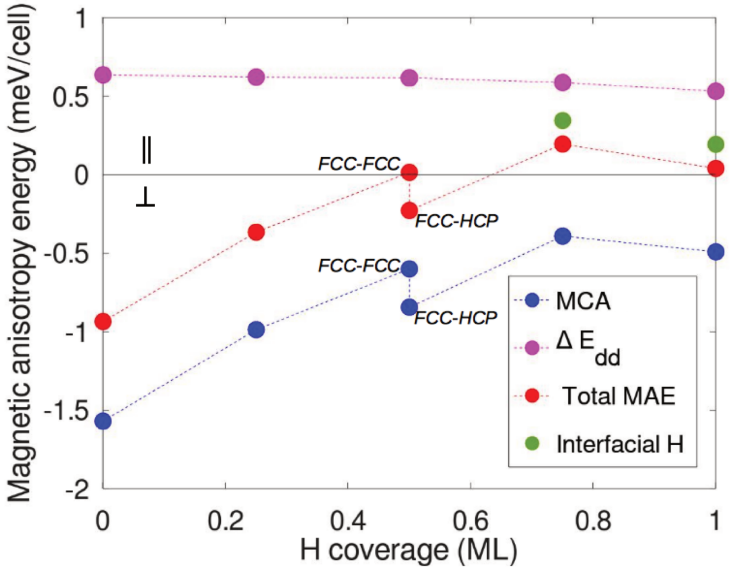

Figure D.16: MAE en fonction de la couverture en hydrogène de surface (ML). Bleu : Énergie MCA ; magenta : Anisotropie de forme, ΔE_{dd} ; rouge : MAE totale. Les deux valeurs supplémentaires représentées par les cercles verts correspondent à la MAE des configurations avec 0.5 ML de H à la surface plus 0.25 ML et 0.50 ML de H à l'interface Co/Cu. Ces valeurs sont respectivement situées aux couvertures équivalentes de 0.75 ML et 1 ML. Pour plus de commodité, les valeurs d'énergie sont données en meV/cellule où la cellule de Co considérée 2×2 contient 8 atomes de Co.

(2×2). Nous avons aussi calculée par DFT, la différence d'énergie d'anisotropie magnétique pour différentes couvertures d'hydrogène sur Co (2 ML) (fig.D.16). Si cette différence est positive, l'aimantation dans le plan est favorisée. A l'aide de nos précédentes investigations et de ce calcul, nous concluons que le taux de couverture d'atomes de H est de 0.5 ML à la surface de l'ilot ainsi que de environ 0.25 ML à l'interface cuivre-cobalt. En effet, les cartes de densités de spins où le taux de couverture d'hydrogène dépasse cette valeur ne correspondent pas à notre carte du champ d'échange de l'ilot contaminé.

D.5 Manipulation du spin à travers des molécules couplées magnétiquement

Le dernier chapitre étudie le nickelocène adsorbé sur des ilots bicouches de cobalt. Nous utilisons la pointe de nickelocene pour sonder le magnétisme de la molécule de nickelocene adsorbée sur le cobalt. Nous identifions son orientation de spin et employons l'imagerie voxel pour observer la corrugation latérales de la polarisation de spin et du couplage d'échange au sein de la molécule. Les calculs théoriques sont

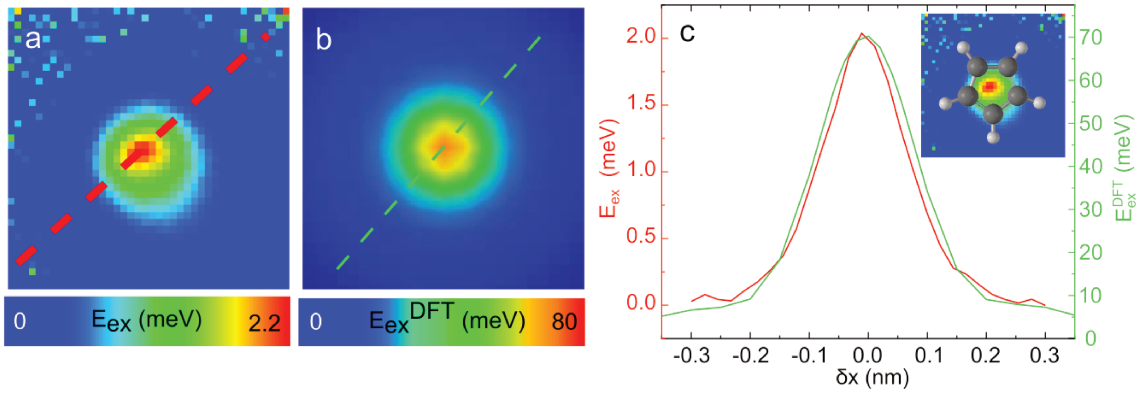

Figure D.17: (a) Carte de l'énergie d'échange $E_{\mathrm{ex}}(x, y)$ du nickelocène sur Co (2 ML) (0.65×0.65 nm^2). (b) Carte de l'énergie d'échange de Nc/Co (2 ML) calculée comme décrit dans le texte (0.65×0.65 nm^2). (c) La ligne rouge solide est le profil de E_{ex} extrait le long de la ligne rouge en pointillés du panneau (a). L'énergie d'échange est indiquée sur l'axe des ordonnées de gauche. La ligne verte solide est le profil calculé par DFT extrait le long de la ligne verte en pointillés de. L'énergie d'échange calculée par DFT est indiquée sur l'axe des ordonnés de droite. Encart : carte E_{ex} du peanneau (a) avec un modèle de l'anneau Cp superposé.

réalisés par R. Robles et N. Lorente.

D.5.1 Aimantation du nickelocene adsorbée sur ilot de co

Avec la pointe de nickelocene, des spectres inélastiques d^2I/dV^2 mesurés à différentes distances d'un nickelocène adsorbé sur Co (2 ML) montrent un pique (et un creux) qui se sépare en deux plus la pointe de Nc s'approche de la molécule en surface. Les ajustements indiquent que l'aimantation de la molécule en surface est stabilisée hors du plan. Les calculs DFT confirment que la bicouche de Co est fortement couplée au Nc adsorbée. Une estimation de l'énergie d'échange $E_{\mathrm{ex}} = E_{\mathrm{z,P}} - E_{\mathrm{z,AP}}$, où le suffixe P (AP) désigne l'alignement parallèle (antiparallèle) des spins de Nc et de Co le long de l'axe z, donne $E_{\mathrm{ex}} = 54$ meV, ce qui est cohérent avec un couplage antiferromagnétique. Cependant, cette valeur doit être manipulée avec précaution, car la configuration parallèle conduit à un moment magnétique de Nc/Co(2ML) de $0.28\mu_{\mathrm{B}}$, ce qui est inférieur à celui de la configuration antiparallèle, suggérant un état métastable.

D.5.2 Carte d'énergie d'échange du nickelocène sur Co (2 ML)

Pour sonder la dépendance latérale de l'interaction d'échange, nous effectuons une imagerie voxel au-dessus d'un Nc unique adsorbé sur une bicouche de Co (§ D.2.5).

Les données $d^2I/dV^2(x, y, V)$ sont enregistrées en ouvrant la boucle de rétroaction au-dessus du centre de la molécule à $\delta z = -200$ pm. La zone de mesure typique correspond à une grille carrée de 0.65×0.65 nm^2 centrée sur la molécule. Après ajustement des spectres de chaque pixel de la carte, nous extrayons l'énergie d'échange en fonction des coordonnées latérales, E_{ex}(x,y) (Fig.D.17a). La carte d'échange résultante a un maximum de 2.2 meV au centre de Nc/Co (2 ML); ce maximum dépend de la pointe, certaines pointes affichant même une énergie d'échange de 3.0 meV.

Comme dans les chapitres précédents, nous calculons la carte de densité de spin de Nc/Co (2 ML). La forme des cartes diffère des résultats expérimentaux. Cette divergence suggère qu'une approche différente est nécessaire pour représenter les cartes d'échange expérimentales. Pour ce faire, nous adoptons une approche simple où deux molécules de Nc en phase gazeuse sont positionnées l'une au-dessus de l'autre avec leurs anneaux Cp parallèles et séparés par $d = 350$ pm , ce qui correspond à une distance de contact Cp-Cp d'environ 100 pm. La molécule supérieure est déplacée par rapport à l'autre aux coordonnées (x, y), où $(0, 0)$ correspond à un alignement parfait de leurs atomes de Ni. À chaque position (x, y), le système est relaxé et la différence d'énergie $E_{\mathrm{ex}}^{\mathrm{DFT}} = E_{\mathrm{z,P}} - E_{\mathrm{z,AP}}$ est calculée, ce qui indique le couplage d'échange entre les molécules. $E_{\mathrm{z,P}}$ ($E_{\mathrm{z,AP}}$) est l'énergie de la configuration où les spins des molécules sont parallèles (antiparallèles). Comme on le voit dans la Fig. D.17b, cette approche, qui néglige à la fois la surface et la pointe métallique sur laquelle Nc est attaché, est déjà suffisante pour reproduire qualitativement les données expérimentales. L'énergie d'échange atteint son maximum lorsque les molécules sont alignées et tombe à zéro lorsqu'elles ne se font plus face.

La figure D.17c présente un profil de la carte d'échange acquis le long de la ligne pointillée rouge (Fig.D.17a). Le profil le long de la ligne pointillé verte sur la carte (Fig. D.17b) calculée par DFT correspond au profil expérimental . Cela confirme que l'interaction d'échange est confinée à une zone équivalente à celle d'un anneau Cp. Nous notons cependant que l'énergie d'échange calculée a des valeurs plus élevées que celle expérimentale. Cette divergence provient de deux facteurs principaux : le choix particulier de la distance Nc-Nc utilisée pour calculer la carte, qui présente une dépendance exponentielle, et la configuration colinéaire des deux spins utilisée dans le calcul. Une configuration non colinéaire, qui s'alignerait plus étroitement avec la configuration expérimentale, n'est malheureusement pas triviale à calculer. Les profil en ligne de E_{ex} on une largeur à mi-hauteur de 190 pm, ce qui est considérablement plus étroit que la largeur apparente de Nc/Co (2 ML). Cette valeur est plutôt de l'ordre de la taille de l'anneau Cp de Nc, soit 220 pm (Encart de la Fig. D.17c). Nous concluons que le couplage d'échange est actif uniquement

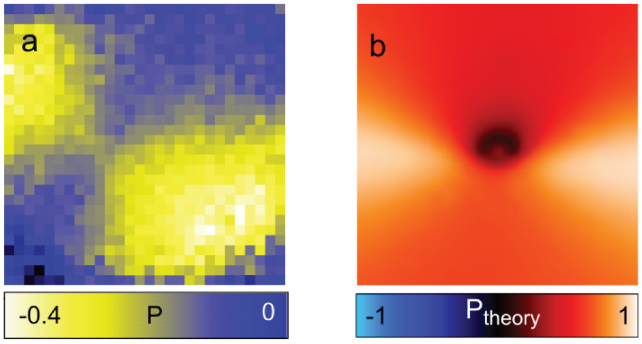

Figure D.18: (a) La carte de polarisation de spin de Nc/Co (2 ML) (0.4×0.4 nm^2) (b) Calcul de la carte de polarisation de spin de Nc/Co (2 ML) à une tension de 0.03 V (0.65×0.65 nm^2)

dans une zone équivalente à l'anneau Cp du nickelocène.

D.5.3 Carte de la polarisation de spin du nickelocène sur Co (2 ML)

La figure D.18a montre une carte typique de la polarisation de spin de Nc/Co(2ML) dans une zone de 0.4×0.4nm^2, où l'on peut voir que $P(x, y)$ est inhomogène au sein de la molécule. Cette inhomogénéité correspond à l'existence d'un motif à deux lobes dans la polarisation de spin, comme mis en évidence dans d'autres cartes (fig. 6.19, 6.20) où la polarisation de spin est sondée dans des zones plus ou moins larges autour du centre de Nc/Co (0.4×0.4 nm^2). P est maximal dans les lobes, variant de -0.25 à -0.30, tandis qu'entre les lobes $P = -0.13$. Contrairement à l'interaction d'échange, la polarisation de spin s'étend spatialement au-delà de l'anneau Cp de Nc/Co, et une forte polarisation de spin est atteinte lors que les 2 molécules sont décentrées.

Pour reproduire les cartes de polarisation de spin, nous considérons une pointe métallique et utilisons l'approximation de Tersoff-Hamann (§ 3.3) pour calculer la conductance différentielle $dI/dV(x, y, V)$ par DFT, pour les électrons de spin-up ($\uparrow$) et de spin-down ($\downarrow$). Le calcul théorique de la polarisation en spin est :

$$P_{\text{theory}} = (dI/dV^{\uparrow} - dI/dV^{\downarrow})/(dI/dV^{\uparrow} + dI/dV^{\downarrow}). \tag{D.8}$$

La carte résultante à 0.03V est présentée respectivement dans la Figure D.18b. La forme de la cartes calculée présente des similitudes encourageantes avec les cartes expérimentales. Notamment, un motif à deux lobes est constamment observé. Cette caractéristique, robuste à toutes les tensions de biais, provient de l'adsorption de Nc/Co ce qui cause une levée de dégénérescence entre les orbitales moléculaires π_{xz}

et π_{yz}. Nous attribuons provisoirement le motif à deux lobes expérimental à ces orbitales moléculaires. Certaines différences pertinentes sont également observées. La valeur de la polarisation de spin calculée diffère de celle expérimentale, et des caractéristiques non polarisées en spin sont présentes dans les cartes calculées, contrairement à l'expérience. Les cartes calculées montrent également une polarisation de spin qui s'étend sur une plus grande distance par rapport à celle expérimentale. La raison en est que, dans l'expérience, la pointe de Co doit être couplée par échange à Nc/Co pour produire une polarisation P mesurable. Ainsi, le signal sur la carte expérimentale est contraint à une zone proche de la zone de l'anneau Cp. Ces divergences suggèrent la nécessité de prendre en compte la présence de la pointe de Co, c'est-à-dire d'aller au-delà de l'approximation de Tersoff-Hamann. Pour améliorer la comparaison, nous avons donc des calculs théoriques en cours utilisant le modèle de Bardeen avec des fonctions d'onde décrivant les molécules de nickelocène sur la pointe et sur la surface. Nous soulignons toutefois que la comparaison restera qualitative, car à ce stade, le calcul néglige la nature inélastique des électrons de tunnel.

List of Figures

List of Tables

Bibliography

[1]M. Ormaza, N. Bachellier, M. N. Faraggi, B. Verlhac, P. Abufager, P. Ohresser, L. Joly, M. Romeo, F. Scheurer, M.-L. Bocquet, N. Lorente, and L. Limot, "Efficient spin-flip excitation of a nickelocene molecule", Nano Lett. **17**, 1877–1882 (2017).

[2]B. Verlhac, N. Bachellier, L. Garnier, M. Ormaza, P. Abufager, R. Robles, M.-L. Bocquet, M. Ternes, N. Lorente, and L. Limot, "Atomic-scale spin sensing with a single molecule at the apex of a scanning tunneling microscope", Science **366**, 623–627 (2019).

[3]B. Verlhac, "Atomic scale spin-sensing with a single molecule at the apex of a scanning tunneling microscope", PhD thesis (University of Strasbourg, 2019).

[4]R. Wiesendanger, H.-J. Güntherodt, G. Güntherodt, R. J. Gambino, and R. Ruf, "Observation of vacuum tunneling of spin-polarized electrons with the scanning tunneling microscope", Phys. Rev. Lett. **65**, 247–250 (1990).

[5]L. Gross, F. Mohn, N. Moll, P. Liljeroth, and G. Meyer, "The chemical structure of a molecule resolved by atomic force microscopy", Science **325**, 1110–1114 (2009).

[6]D. Wortmann, S. Heinze, P. Kurz, G. Bihlmayer, and S. Blügel, "Resolving complex atomic-scale spin structures by spin-polarized scanning tunneling microscopy", Phys. Rev. Lett. **86**, 4132–4135 (2001).

[7]O. Pietzsch, A. Kubetzka, M. Bode, and R. Wiesendanger, "Spin-polarized scanning tunneling spectroscopy of nanoscale cobalt islands on cu(111)", Phys. Rev. Lett. **92**, 057202 (2004).

[8]A. Wachowiak, J. Wiebe, M. Bode, O. Pietzsch, M. Morgenstern, and R. Wiesendanger, "Direct observation of internal spin structure of magnetic vortex cores", Science **298**, 577–580 (2002).

[9]S. Heinze, K. von Bergmann, M. Menzel, J. Brede, A. Kubetzka, R. Wiesendanger, G. Bihlmayer, and S. Blügel, "Spontaneous atomic-scale magnetic skyrmion lattice in two dimensions", Nat. Phys. **7**, 713–718 (2011).

[10]U. Kaiser, A. Schwarz, and R. Wiesendanger, "Magnetic exchange force microscopy with atomic resolution", Nature **446**, 522–525.

[11]R. Schmidt, C. Lazo, U. Kaiser, A. Schwarz, S. Heinze, and R. Wiesendanger, "Quantitative measurement of the magnetic exchange interaction across a vacuum gap", Phys. Rev. Lett. **106**, 257202 (2011).

[12]N. Hauptmann, S. Haldar, T.-C. Hung, W. Jolie, M. Gutzeit, D. Wegner, S. Heinze, and A. A. Khajetoorians, "Quantifying exchange forces of a spin spiral on the atomic scale", Nat. Commun. **11** (2020).

[13]A. J. Heinrich, J. A. Gupta, C. P. Lutz, and D. M. Eigler, "Single-atom spin-flip spectroscopy", Science **306**, 466–469 (2004).

[14]B. C. Stipe, M. A. Rezaei, and W. Ho, "Coupling of vibrational excitation to the rotational motion of a single adsorbed molecule", Phys. Rev. Lett. **81**, 1263–1266 (1998).

[15]S. Baumann, W. Paul, T. Choi, C. P. Lutz, A. Ardavan, and A. J. Heinrich, "Electron paramagnetic resonance of individual atoms on a surface", Science **350**, 417–420 (2015).

[16]F. D. Natterer, K. Yang, W. Paul, P. Willke, T. Choi, T. Greber, A. J. Heinrich, and C. P. Lutz, "Reading and writing single-atom magnets", Nature **543**, 226 (2017).

[17]S. Loth, K. von Bergmann, M. Ternes, A. F. Otte, C. P. Lutz, and A. J. Heinrich, "Controlling the state of quantum spins with electric currents", Nat. Phys. **6**, 340–344 (2010).

[18]B. W. Heinrich, L. Braun, J. I. Pascual, and K. J. Franke, "Protection of excited spin states by a superconducting energy gap", Nat. Phys. **9**, 765–768 (2013).

[19]W. Paul, K. Yang, S. Baumann, N. Romming, T. Choi, C. P. Lutz, and A. J. Heinrich, "Control of the millisecond spin lifetime of an electrically probed atom", Nat. Phys. **13**, 403–407 (2017).

[20]F. Donati, S. Rusponi, S. Stepanow, C. Wäckerlin, A. Singha, L. Persichetti, R. Baltic, K. Diller, F. Patthey, E. Fernandes, J. Dreiser, Ž. Šljivančanin, K. Kummer, C. Nistor, P. Gambardella, and H. Brune, "Magnetic remanence in single atoms", Science **352**, 318–321 (2016).

[21]A. A. Khajetoorians, S. Lounis, B. Chilian, A. T. Costa, L. Zhou, D. L. Mills, J. Wiebe, and R. Wiesendanger, "Itinerant nature of atom-magnetization excitation by tunneling electrons", Phys. Rev. Lett. **106**, 037205 (2011).

[22]N. Tsukahara, K.-I. Noto, M. Ohara, S. Shiraki, N. Takagi, Y. Takata, J. Miyawaki, M. Taguchi, A. Chainani, S. Shin, and M. Kawai, "Adsorption-induced switching of magnetic anisotropy in a single iron(II) phthalocyanine molecule on an oxidized cu(110) surface.", Phys. Rev. Lett. **102**, 167203.

[23]X. Chen, Y.-S. Fu, S.-H. Ji, T. Zhang, P. Cheng, X.-C. Ma, X.-L. Zou, W.-H. Duan, J.-F. Jia, and Q.-K. Xue, "Probing superexchange interaction in molecular magnets by spin-flip spectroscopy and microscopy", Phys. Rev. Lett. **101**, 197208 (2008).

[24]A. A. Khajetoorians, B. Chilian, J. Wiebe, S. Schuwalow, F. Lechermann, and R. Wiesendanger, "Detecting excitation and magnetization of individual dopants in a semiconductor", Nature **467**, 1084–1087 (2010).

[25]C. F. Hirjibehedin, C. P. Lutz, and A. J. Heinrich, "Spin coupling in engineered atomic structures", Science **312**, 1021–1024 (2006).

[26]R. Prins, J. van Voorst, and C. Schinkel, "Zero-field splitting in the triplet ground state of nickelocene", Chem. Phys. Lett. **1**, 54–55 (1967).

[27]P. Baltzer, A. Furrer, J. Hulliger, and A. Stebler, "Magnetic properties of nickelocene. a reinvestigation using inelastic neutron scattering and magnetic susceptibility", Inorg. Chem. **27**, 1543–1548 (1988).

[28]A. Maristella, S. Kotaru, G. Giudetti, and A. I. Krylov, "Origin of magnetic anisotropy in nickelocene molecular magnet and resilience of its magnetic behavior", J. Phys. Chem. C **127**, 3647–3659 (2023).

[29]C. Rubio-Verdú, A. Sarasola, D.-J. Choi, Z. Majzik, R. Ebeling, M. R. Calvo, M. M. Ugeda, A. Garcia-Lekue, D. Sánchez-Portal, and J. I. Pascual, "Orbital-selective spin excitation of a magnetic porphyrin", Commun. Phys. **1**, 15 (2018).

[30]S. Mishra, G. Catarina, F. Wu, R. Ortiz, D. Jacob, K. Eimre, J. Ma, C. A. Pignedoli, X. Feng, P. Ruffieux, J. Fernández-Rossier, and R. Fasel, "Observation of fractional edge excitations in nanographene spin chains", Nature **598**, 287–292 (2021).

[31]C. Li, R. Robles, N. Lorente, S. K. Mahatha, S. Rohlf, K. Rossnagel, A. Barla, B. V. Sorokin, S. Rusponi, P. Ohresser, S. Realista, P. N. Martinho, T. Jasper-Toennies, A. Weismann, R. Berndt, and M. Gruber, "Large orbital moment of two coupled spin-half co ions in a complex on gold", ACS Nano **17**, 10608–10616 (2023).

[32]G. Czap, P. J. Wagner, F. Xue, L. Gu, J. Li, J. Yao, R. Wu, and W. Ho, "Probing and imaging spin interactions with a magnetic single-molecule sensor", Science **364**, 670–673 (2019).

[33]M. Ormaza, P. Abufager, B. Verlhac, N. Bachellier, M.-L. Bocquet, N. Lorente, and L. Limot, "Controlled spin switching in a metallocene molecular junction", Nat. Commun. **8**, 1–8 (2017).

[34]L. Limot, J. Kröger, R. Berndt, A. Garcia-Lekue, and W. A. Hofer, "Atom transfer and single-adatom contacts", Phys. Rev. Lett. **94**, 126102 (2005).

[35]Y.-h. Zhang, P. Wahl, and K. Kern, "Quantum point contact microscopy", Nano Lett. **11**, 3838–3843 (2011).

[36]K. Yang, W. Paul, F. D. Natterer, J. L. Lado, Y. Bae, P. Willke, T. Choi, A. Ferrón, J. Fernández-Rossier, A. J. Heinrich, and C. P. Lutz, "Tuning the exchange bias on a single atom from 1 mT to 10 T", Phys. Rev. Lett. **122**, 227203 (2019).

[37]R. Kawaguchi, K. Hashimoto, T. Kakudate, K. Katoh, M. Yamashita, and T. Komeda, "Spatially resolving electron spin resonance of π-radical in single-molecule magnet", Nano Lett. **23**, 213–219 (2023).

[38]P. Kot, M. Ismail, R. Drost, J. Siebrecht, H. Huang, and C. R. Ast, "Electric control of spin transitions at the atomic scale", Nat. Commun. **14**, 1–4 (2023).

[39]T. Choi, W. Paul, S. Rolf-Pissarczyk, A. J. Macdonald, K. Natterer Fabian D. Yang, P. Willke, C. P. Lutz, and A. J. Heinrich, "Atomic-scale sensing of the magnetic dipolar field from single atoms", Nat. Nanotechnol. **12**, 420–424 (2017).

[40]A. Yazdani, B. A. Jones, C. P. Lutz, M. F. Crommie, and D. M. Eigler, "Probing the local effects of magnetic impurities on superconductivity", Science **275**, 1767–1770 (1997).

[41]H. Huang, C. Padurariu, J. Senkpiel, R. Drost, A. L. Yeyati, J. C. Cuevas, B. Kubala, J. Ankerhold, K. Kern, and C. R. Ast, "Tunnelling dynamics between superconducting bound states at the atomic limit", Nat. Phys. **16**, 1227–1231 (2020).

[42]L. Schneider, P. Beck, J. Wiebe, and R. Wiesendanger, "Atomic-scale spin-polarization maps using functionalized superconducting probes", Sci. Adv. **7**, eabd7302 (2021).

[43]J. Li, W.-D. Schneider, R. Berndt, and B. Delley, "Kondo scattering observed at a single magnetic impurity", Phys. Rev. Lett. **80**, 2893–2896 (1998).

[44]V. Madhavan, W. Chen, T. Jamneala, M. F. Crommie, and N. S. Wingreen, "Tunneling into a single magnetic atom: spectroscopic evidence of the kondo resonance", Science **280**, 567–569 (1998).

[45]L. Garnier, B. Verlhac, P. Abufager, N. Lorente, M. Ormaza, and L. Limot, "The Kondo effect of a molecular tip as a magnetic sensor", Nano Lett. **20**, 8193–8199 (2020).

[46]C. Cohen Tannoudji, B. Diu, and F. Laloë, *Mécanique quantique I* (Hermann, 1992).

[47]J. Bardeen, "Tunnelling from a many-particle point of view", Phys. Rev. Lett. **6**, 57–59 (1961).

[48]J. Chen, *Introduction to scanning tunneling microscopy* (Oxford university press, 2008).

[49]J. Tersoff and D. R. Hamann, "Theory of the scanning tunneling microscope", Phys. Rev. B **31**, 805–813 (1985).

[50]G. Binnig, H. Rohrer, C. Gerber, and E. Weibel, "(111) facets as the origin of reconstructed au(110) surfaces", Surface Science **131**, L379–L384 (1983).

[51]V. A. Ukraintsev, "Data evaluation technique for electron-tunneling spectroscopy", Phys. Rev. B **53**, 11176–11185 (1996).

[52]W. A. H. Krisztián Palotás Gábor Mándi, "Three-dimensional wentzel-kramers-brillouin approach for the simulation of scanning tunneling microscopy and spectroscopy", Frontiers of Physics **9**, 711, 711 (2014).

[53]J. Gaudioso, H. J. Lee, and W. Ho, "Vibrational analysis of single molecule chemistry: Ethylene dehydrogenation on Ni(110)", J. Am. Chem. Soc. **121**, 8479–8485 (1999).

[54]M. Gruber, A. Weismann, and R. Berndt, "The Kondo resonance line shape in scanning tunnelling spectroscopy: instrumental aspects", J. Phys. Condens. Matter **30**, 424001 (2018).

[55]L. Limot, personal communication, 2014.

[56]J. Klein, A. Léger, M. Belin, D. Défourneau, and M. J. L. Sangster, "Inelastic-electron-tunneling spectroscopy of metal-insulator-metal junctions", Phys. Rev. B **7**, 2336–2348 (1973).

[57]M. Ternes, "Spin excitations and correlations in scanning tunneling spectroscopy", New J. Phys. **17**, 063016 (2015).

[58]L. Thiel, D. Rohner, M. Ganzhorn, P. Appel, E. Neu, B. Müller, R. Kleiner, D. Koelle, and P. Maletinsky, "Quantitative nanoscale vortex imaging using a cryogenic quantum magnetometer", Nat. Nanotechnol. **11**, 677–681 (2016).

[59]M. Ganzhorn, S. Klyatskaya, M. Ruben, and W. Wernsdorfer, "Carbon nanotube nanoelectromechanical systems as magnetometers for single-molecule magnets", ACS Nano **7**, 6225–6236 (2013).

[60]D. Rugar, R. Budakian, H. J. Mamin, and B. W. Chui, "Single spin detection by magnetic resonance force microscopy", Nature **430**, 329–332 (2004).

[61]G. Balasubramanian, I. Y. Chan, R. Kolesov, M. Al-Hmoud, J. Tisler, C. Shin, C. Kim, A. Wojcik, P. R. Hemmer, A. Krueger, T. Hanke, A. Leitenstorfer, R. Bratschitsch, F. Jelezko, and J. Wrachtrup, "Nanoscale imaging magnetometry with diamond spins under ambient conditions", Nature **455**, 648–651 (2008).

[62]M. S. Grinolds, P. Maletinsky, S. Hong, M. D. Lukin, R. L. Walsworth, and A. Yacoby, "Quantum control of proximal spins using nanoscale magnetic resonance imaging", Nat. Phys. **7**, 687–692 (2011).

[63]C.-J. Yu, S. von Kugelgen, D. W. Laorenza, and D. E. Freedman, "A molecular approach to quantum sensing", ACS Cent. Sci. **7**, 712–723 (2021).

[64]P. Willke, T. Bilgeri, X. Zhang, Y. Wang, C. Wolf, H. Aubin, A. Heinrich, and T. Choi, "Coherent spin control of single molecules on a surface", ACS Nano **15**, 17959–17965 (2021).

[65]X. Zhang, C. Wolf, Y. Wang, H. Aubin, T. Bilgeri, P. Willke, A. J. Heinrich, and T. Choi, "Electron spin resonance of single iron phthalocyanine molecules and role of their non-localized spins in magnetic interactions", Nat. Chem. **14**, 59–65 (2022).

[66]X. Zhang, J. Reina-Gálvez, C. Wolf, Y. Wang, H. Aubin, A. J. Heinrich, and T. Choi, "Influence of the magnetic tip on heterodimers in electron spin resonance combined with scanning tunneling microscopy", ACS Nano **17**, 16935–16942 (2023).

[67]C. Wäckerlin, A. Cahlík, J. Goikoetxea, O. Stetsovych, D. Medvedeva, J. Redondo, M. Švec, B. Delley, M. Ondráček, A. Pinar, M. Blanco-Rey, J. Kolorenč, A. Arnau, and P. Jelínek, "Role of the magnetic anisotropy in atomic-spin sensing of 1D molecular chains", ACS Nano **16**, 16402–16413 (2022).

[68]J. Kröger, N. Néel, and L. Limot, "Contact to single atoms and molecules with the tip of a scanning tunnelling microscope", J. Phys. Condens. Matter **20**, 223001 (2008).

[69]L. Diekhöner, M. A. Schneider, A. N. Baranov, V. S. Stepanyuk, P. Bruno, and K. Kern, "Surface states of cobalt nanoislands on Cu(111)", Phys. Rev. Lett. **90**, 236801 (2003).

[70]M. V. Rastei, B. Heinrich, L. Limot, P. A. Ignatiev, V. S. Stepanyuk, P. Bruno, and J. P. Bucher, "Size-dependent surface states of strained cobalt nanoislands on Cu(111)", Phys. Rev. Lett. **99**, 246102 (2007).

[71]N. N. Negulyaev, V. S. Stepanyuk, P. Bruno, L. Diekhöner, P. Wahl, and K. Kern, "Bilayer growth of nanoscale co islands on cu(111)", Phys. Rev. B **77**, 125437 (2008).

[72]M. Sicot, O. Kurnosikov, H. Swagten, and B. Koopmans, "Hydrogen superstructures on co nanoislands and Cu(111)", Surf. Sci. **602**, 3667–3673 (2008).

[73]J. Park, C. Park, M. Yoon, and A.-P. Li, "Surface magnetism of cobalt nanoislands controlled by atomic hydrogen", Nano Lett. **17**, 292–298 (2017).

[74]O. Pietzsch, S. Okatov, A. Kubetzka, M. Bode, S. Heinze, A. Lichtenstein, and R. Wiesendanger, "Spin-resolved electronic structure of nanoscale cobalt islands on cu(111)", Phys. Rev. Lett. **96**, 237203 (2006).

[75]B. W. Heinrich, C. Iacovita, M. V. Rastei, L. Limot, J. P. Bucher, P. A. Ignatiev, V. S. Stepanyuk, and P. Bruno, "Spin structure of an atomic protrusion: Probing single atoms on cobalt nanoislands", Phys. Rev. B **79**, 113401 (2009).

[76]S. Steiner, S. Khmelevskyi, M. Marsmann, and G. Kresse, "Calculation of the magnetic anisotropy with projected-augmented-wave methodology and the case study of disordered $Fe_{1-x}Co_x$ alloys", Phys. Rev. B **93**, 224425 (2016).

[77]R. Hammerling, C. Uiberacker, J. Zabloudil, P. Weinberger, L. Szunyogh, and J. Kirschner, "Magnetic anisotropy of thin films of co on cu(111)", Phys. Rev. B **66**, 052402 (2002).

[78]W. Weber, C. H. Back, A. Bischof, D. Pescia, and R. Allenspach, "Magnetic switching in cobalt films by adsorption of copper", Nature **374**, 788–790 (1995).

[79]S. Yan, D.-J. Choi, J. A. J. Burgess, S. Rolf-Pissarczyk, and S. Loth, "Control of quantum magnets by atomic exchange bias", Nat. Nanotechnol. **10**, 40 (2014).

[80]P. Willke, K. Yang, Y. Bae, A. J. Heinrich, and C. P. Lutz, "Magnetic resonance imaging of single atoms on a surface", Nat. Phys. **15**, 1005–1010 (2019).

[81]M. Pajda, J. Kudrnovský, I. Turek, V. Drchal, and P. Bruno, "Ab initio calculations of exchange interactions, spin-wave stiffness constants, and Curie temperatures of Fe, Co, and Ni", Phys. Rev. B **64**, 174402 (2001).

[82]C. Iacovita, M. V. Rastei, B. W. Heinrich, T. Brumme, J. Kortus, L. Limot, and J. P. Bucher, "Visualizing the spin of individual cobalt-phthalocyanine molecules", Phys. Rev. Lett. **101**, 116602 (2008).

[83]H. Oka, P. A. Ignatiev, S. Wedekind, G. Rodary, L. Niebergall, V. S. Stepanyuk, D. Sander, and J. Kirschner, "Spin-dependent quantum interference within a single magnetic nanostructure", Science **327**, 843–846 (2010).

[84]S. Schmaus, A. Bagrets, Y. Nahas, T. K. Yamada, A. Bork, M. Bowen, E. Beaurepaire, F. Evers, and W. Wulfhekel, "Giant magnetoresistance through a single molecule", Nat.e Nanotechnol. **6**, 185–189 (2011).

[85]S. Loth, C. P. Lutz, and A. J. Heinrich, "Spin-polarized spin excitation spectroscopy", New J. Phys. **12**, 125021 (2010).

[86]F. Delgado, J. J. Palacios, and J. Fernández-Rossier, "Spin-transfer torque on a single magnetic adatom", Phys. Rev. Lett. **104**, 026601 (2010).

[87]F. D. Novaes, N. Lorente, and J.-P. Gauyacq, "Quenching of magnetic excitations in single adsorbates at surfaces: Mn on CuN/Cu(100)", Phys. Rev. B **82**, 155401 (2010).

[88]A. J. Tan, M. Huang, C. O. Avci, F. Büttner, M. Mann, W. Hu, C. Mazzoli, S. Wilkins, H. L. Tuller, and G. S. D. Beach, "Magneto-ionic control of magnetism using a solid-state proton pump", Nat. Mater. **18**, 35–41 (2019).

[89]K.-Y. Lee, S. Jo, A. J. Tan, M. Huang, D. Choi, J. H. Park, H.-I. Ji, J.-W. Son, J. Chang, G. S. D. Beach, and S. Woo, "Fast magneto-ionic switching of interface anisotropy using yttria-stabilized zirconia gate oxide", Nano Lett. **20**, 3435–3441 (2020).

[90]A. E. Kossak, M. Huang, P. Reddy, D. Wolf, and G. S. D. Beach, "Voltage control of magnetic order in RKKY coupled multilayers", Sci. Adv. **9**, eadd0548 (2023).

[91]Q. Dubout, F. Donati, C. Wäckerlin, F. Calleja, M. Etzkorn, A. Lehnert, L. Claude, P. Gambardella, and H. Brune, "Controlling the spin of Co atoms on Pt(111) by hydrogen adsorption", Phys. Rev. Lett. **114**, 106807 (2015).

[92]A. A. Khajetoorians, M. Valentyuk, M. Steinbrecher, T. Schlenk, A. Shick, J. Kolorenc, A. I. Lichtenstein, T. O. Wehling, R. Wiesendanger, and J. Wiebe, "Tuning emergent magnetism in a Hund's impurity", Nat. Nanotechnol. **10**, 958–964 (2015).

[93]P. Jacobson, T. Herden, M. Muenks, G. Laskin, O. Brovko, V. Stepanyuk, M. Ternes, and K. Kern, "Quantum engineering of spin and anisotropy in magnetic molecular junctions", Nat. Commun. **6**, 8536 (2015).

[94]P. Jacobson, M. Muenks, G. Laskin, O. Brovko, V. Stepanyuk, M. Ternes, and K. Kern, "Potential energy-driven spin manipulation via a controllable hydrogen ligand", Sci. Adv. **3**, e1602060 (2017).

[95]M. Steinbrecher, W. M. J. van Weerdenburg, E. F. Walraven, N. P. E. van Mullekom, J. W. Gerritsen, F. D. Natterer, D. I. Badrtdinov, A. N. Rudenko, V. V. Mazurenko, M. I. Katsnelson, A. van der Avoird, G. C. Groenenboom, and A. A. Khajetoorians, "Quantifying the interplay between fine structure and geometry of an individual molecule on a surface", Phys. Rev. B **103**, 155405 (2021).

[96]B. Hjörvarsson, J. A. Dura, P. Isberg, T. Watanabe, T. J. Udovic, G. Andersson, and C. F. Majkrzak, "Reversible tuning of the magnetic exchange coupling in Fe/V (001) superlattices using hydrogen", Phys. Rev. Lett. **79**, 901–904 (1997).

[97]V. Leiner, K. Westerholt, A. M. Blixt, H. Zabel, and B. Hjörvarsson, "Magnetic superlattices with variable interlayer exchange coupling: a new approach for the investigation of low-dimensional magnetism", Phys. Rev. Lett. **91**, 037202 (2003).

[98]D. Sander, W. Pan, S. Ouazi, J. Kirschner, W. Meyer, M. Krause, S. Müller, L. Hammer, and K. Heinz, "Reversible H-induced switching of the magnetic easy axis in Ni/Cu(001) thin films", Phys. Rev. Lett. **93**, 247203 (2004).

[99]K. Munbodh, F. A. Perez, C. Keenan, D. Lederman, M. Zhernenkov, and M. R. Fitzsimmons, "Effects of hydrogen/deuterium absorption on the magnetic properties of Co/Pd multilayers", Phys. Rev. B **83**, 094432 (2011).

[100]B. Santos, S. Gallego, A. Mascaraque, K. F. McCarty, A. Quesada, A. T. N'Diaye, A. K. Schmid, and J. de la Figuera, "Hydrogen-induced reversible spin-reorientation transition and magnetic stripe domain phase in bilayer Co on Ru(0001)", Phys. Rev. B **85**, 134409 (2012).

[101]G. Chen, M. Robertson, M. Hoffmann, C. Ophus, A. L. Fernandes C., R. Lo Conte, H. Ding, R. Wiesendanger, S. Blügel, A. K. Schmid, and K. Liu, "Observation of hydrogen-induced Dzyaloshinskii-Moriya interaction and reversible switching of magnetic chirality", Phys. Rev. X **11**, 021015 (2021).

[102]W.-H. Wang, C.-Y. Pan, C.-M. Liu, W.-C. Lin, and P.-h. Jiang, "Chirality-induced noncollinear magnetization and asymmetric domain-wall propagation in hydrogenated copd thin films", ACS Appl. Mater. Interfaces **14**, 20151–20158 (2022).

[103]P.-J. Hsu, L. Rózsa, A. Finco, L. Schmidt, K. Palotás, E. Vedmedenko, L. Udvardi, L. Szunyogh, A. Kubetzka, K. von Bergmann, and R. Wiesendanger, "Inducing skyrmions in ultrathin Fe films by hydrogen exposure", Nat. Commun. **9**, 1571 (2018).

[104]G. Chen, C. Ophus, A. Quintana, H. Kwon, C. Won, H. Ding, Y. Wu, A. K. Schmid, and K. Liu, "Reversible writing/deleting of magnetic skyrmions through hydrogen adsorption/desorption", Nat. Commun. **13**, 1350 (2022).

[105]K. Klyukin, G. Beach, and B. Yildiz, "Hydrogen tunes magnetic anisotropy by affecting local hybridization at the interface of a ferromagnet with nonmagnetic metals", Phys. Rev. Mater. **4**, 104416 (2020).

[106]F. D. Natterer, F. Patthey, and H. Brune, "Distinction of nuclear spin states with the scanning tunneling microscope", Phys. Rev. Lett. **111**, 175303 (2013).

[107]S. Li, A. Yu, F. Toledo, Z. Han, . Wang, H. Y. He, R. Wu, and W. Ho, "Rotational and vibrational excitations of a hydrogen molecule trapped within a nanocavity of tunable dimension", Phys. Rev. Lett. **111**, 146102 (2013).

[108]C. Lotze, M. Corso, K. J. Franke, F. von Oppen, and J. I. Pascual, "Driving a macroscopic oscillator with the stochastic motion of a hydrogen molecule", Science **338**, 779–782 (2012).

[109]P. Merino, A. Rosławska, C. C. Leon, A. Grewal, C. Große, C. González, K. Kuhnke, and K. Kern, "A single hydrogen molecule as an intensity chopper in an electrically driven plasmonic nanocavity", Nano Lett. **19**, 235–241 (2019).

[110]L. Wang, Y. Xia, and W. Ho, "Atomic-scale quantum sensing based on the ultrafast coherence of an H_2 molecule in an STM cavity", Science **376**, 401–405 (2022).

[111]C. Weiss, C. Wagner, C. Kleimann, M. Rohlfing, F. S. Tautz, and R. Temirov, "Imaging Pauli repulsion in scanning tunneling microscopy", Phys. Rev. Lett. **105**, 086103 (2010).

[112]M. Sicot, O. Kurnosikov, O. A. O. Adam, H. J. M. Swagten, and B. Koopmans, "STM-induced desorption of hydrogen from Co nanoislands", Phys. Rev. B **77**, 035417 (2008).

[113]W. A. Hofer, K. Palotás, S. Rusponi, T. Cren, and H. Brune, "Role of hydrogen in giant spin polarization observed on magnetic nanostructures", Phys. Rev. Lett. **100**, 026806 (2008).

[114]F. Natterer, F. Patthey, and H. Brune, "Quantifying residual hydrogen adsorption in low-temperature STMs", Surf. Sci. **615**, 80–87 (2013).

[115]N. Tsukahara, S. Shiraki, S. Itou, N. Ohta, N. Takagi, and M. Kawai, "Evolution of Kondo resonance from a single impurity molecule to the two-dimensional lattice", Phys. Rev. Lett. **106**, 187201 (2011).

[116]N. Néel, R. Berndt, J. Kröger, T. O. Wehling, A. I. Lichtenstein, and M. I. Katsnelson, "Two-site Kondo effect in atomic chains", Phys. Rev. Lett. **107**, 106804 (2011).

[117]Y.-S. Fu, Q.-K. Xue, and R. Wiesendanger, "Spin-resolved splitting of Kondo resonances in the presence of RKKY-type coupling", Phys. Rev. Lett. **108**, 087203 (2012).

[118]F. Meier, L. Zhou, J. Wiebe, and R. Wiesendanger, "Revealing magnetic interactions from single-atom magnetization curves", Science **320**, 82–86 (2008).

[119]A. A. Khajetoorians, J. Wiebe, B. Chilian, and R. Wiesendanger, "Realizing all-spin–based logic operations atom by atom", Science **332**, 1062–1064 (2011).

[120]A. A. Khajetoorians, J. Wiebe, B. Chilian, S. Lounis, S. Blügel, and R. Wiesendanger, "Atom-by-atom engineering and magnetometry of tailored nanomagnets", Nat. Phys. **8**, 497–503 (2012).

[121]X. Zhang, C. Wolf, Y. Wang, H. Aubin, T. Bilgeri, P. Willke, A. J. Heinrich, and T. Choi, "Electron spin resonance of single iron phthalocyanine molecules and role of their non-localized spins in magnetic interactions", Nat. Chem. **14**, 59–65 (2022).

[122]L. M. Veldman, L. Farinacci, R. Rejali, R. Broekhoven, J. Gobeil, D. Coffey, M. Ternes, and A. F. Otte, "Free coherent evolution of a coupled atomic spin system initialized by electron scattering", Science **372**, 964–968 (2021).

[123]S.-H. Ji, T. Zhang, Y.-S. Fu, X. C., X.-C. Ma, J. Li, W.-H. Duan, J.-F. Jia, and Q.-K. Xue, "High-resolution scanning tunneling spectroscopy of magnetic impurity induced bound states in the superconducting gap of Pb thin films", Phys. Rev. Lett. **100**, 226801 (2008).

[124]G. C. Ménard, S. Guissart, C. Brun, S. Pons, V. S. Stolyarov, F. Debontridder, M. V. Leclerc, E. Janod, L. Cario, D. Roditchev, P. Simon, and T. Cren, "Coherent long-range magnetic bound states in a superconductor", Nature Physics **11**, 1013–1016 (2015).

[125]M. Ruby, B. W. Heinrich, Y. Peng, F. von Oppen, and K. J. Franke, "Wavefunction hybridization in Yu-Shiba-Rusinov dimers", Phys. Rev. Lett. **120**, 156803 (2018).

[126]D.-J. Choi, C. G. Fernández, E. Herrera, C. Rubio-Verdú, M. M. Ugeda, I. Guillamón, H. Suderow, J. I. Pascual, and N. Lorente, "Influence of magnetic ordering between Cr adatoms on the Yu-Shiba-Rusinov states of the $\beta-Bi_2Pd$ superconductor", Phys. Rev. Lett. **120**, 167001 (2018).

[127]S. Kezilebieke, M. Dvorak, T. Ojanen, and P. Liljeroth, "Coupled Yu-Shiba-Rusinov states in molecular dimers on $NbSe_2$", Nano Lett. **18**, 2311–2315 (2018).

[128]P. Beck, L. Schneider, L. Rózsa, K. Palotás, A. Lászlóffy, L. Szunyogh, J. Wiebe, and R. Wiesendanger, "Spin-orbit coupling induced splitting of Yu-Shiba-Rusinov states in antiferromagnetic dimers", Nat. Commun. **12**, 2040 (2021).

[129]J. Bork, Y.-h. Zhang, L. Diekhöner, L. Borda, P. Simon, J. Kroha, P. Wahl, and K. Kern, "A tunable two-impurity Kondo system in an atomic point contact", Nat. Phys. **7**, 901 (2011).

[130]D.-J. Choi, S. Guissart, M. Ormaza, N. Bachellier, O. Bengone, P. Simon, and L. Limot, "Kondo resonance of a Co atom exchange coupled to a ferromagnetic tip", Nano Lett. **16**, 6298–6302 (2016).

[131]M. Muenks, P. Jacobson, M. Ternes, and K. Kern, "Correlation-driven transport asymmetries through coupled spins in a tunnel junction", Nat. Commun. **8**, 14119 (2017).

[132]N. Bachellier, M. Ormaza, M. Faraggi, B. Verlhac, M. Vérot, T. Le Bahers, M.-L. Bocquet, and L. Limot, "Unveiling nickelocene bonding to a noble metal surface", Phys. Rev. B **93**, 195403 (2016).

[133]G. Schull, T. Frederiksen, M. Brandbyge, and R. Berndt, "Passing current through touching molecules", Phys. Rev. Lett. **103**, 206803 (2009).

[134]J. Brede, N. Atodiresei, S. Kuck, P. Lazi ć, V. Caciuc, Y. Morikawa, G. Hoffmann, S. Blügel, and R. Wiesendanger, "Spin- and energy-dependent tunneling through a single molecule with intramolecular spatial resolution", Phys. Rev. Lett. **105**, 047204 (2010).

[135]C. Barraud, P. Seneor, R. Mattana, S. Fusil, K. Bouzehouane, C. Deranlot, P. Graziosi, L. Hueso, I. Bergenti, V. Dediu, F. Petroff, and A. Fert, "Unravelling the role of the interface for spin injection into organic semiconductors", Nat. Phys. **6**, 615–620 (2010).

[136]N. Atodiresei, J. Brede, P. Lazi ć, V. Caciuc, G. Hoffmann, R. Wiesendanger, and S. Blügel, "Design of the local spin polarization at the organic-ferromagnetic interface", Phys. Rev. Lett. **105**, 066601 (2010).

[137]S. Sanvito, "The rise of spinterface science", Nat. Phys. **6**, 562–564 (2010).

[138]A. Fétida, O. Bengone, M. Romeo, F. Scheurer, R. Robles, N. Lorente, and L. Limot, "Single-spin sensing: a molecule-on-tip approach", ACS Nano **18**, 13829–13835 (2024).

[139]C. Mier, A. Fétida, R. Robles, P. Boronat, D. Jyoti, N. Lorente, L. Limot, and D.-J. Choi, "Two molecular devices for superconducting spintronics", arXiv: 2402.00644 (2024).

[140]G. Kresse and J. Furthmüller, "Efficiency of ab-initio total energy calculations for metals and semiconductors using a plane-wave basis set", Comput. Mater. Sci. **6**, 15–50 (1996).

[141]J. P. Perdew, K. Burke, and M. Ernzerhof, "Generalized Gradient Approximation Made Simple", Phys. Rev. Lett. **77**, 3865 (1996).

[142]G. Kresse and D. Joubert, "From ultrasoft pseudopotentials to the projector augmented-wave method", Phys. Rev. B **59**, 1758 (1999).

[143]K. Momma and F. Izumi, "VESTA 3 for three-dimensional visualization of crystal, volumetric and morphology data", . Appl. Crystallogr **44**, 1272–1276 (2011).

[144]W. Tang, E. Sanville, and G. Henkelman, "A grid-based Bader analysis algorithm without lattice bias", J. Phys. Condens. Matter **21**, 084204 (2009).

[145]M.-L. Bocquet, H. Lesnard, S. Monturet, and N. Lorente, "Theory of Elastic and Inelastic Electron Tunneling", in *Computational Methods in Catalysis and Materials Science*, edited by R. A. v. Santen and P. Sautet (Wiley-VCH Verlag GmbH & Co. KGaA, 2009), pp. 199–219.

[146]N. Lorente and R. Robles, *STMpw v1.0b2 (Zenodo)*, version v1.0b2, 2019.

Alex FETIDA

Mapping surface magnetism with a molecule

Résumé

Pendant mon doctorat, j'ai exploité une molécule de nickelocène (Nc) fixée à la pointe d'un microscope à effet tunnel pour examiner le magnétisme de surface. Dans cette démarche, il est crucial de placer le nickelocène à une distance suffisamment proche de la surface (<100 pm) pour que le champ d'échange de celle-ci provoque des altérations dans les niveaux Zeeman du nickelocène. Ces altérations sont ensuite détectées électriquement grâce aux excitations entre niveaux Zeeman induites par les électrons tunnel inélastiques, soit ceux qui échangent de l'énergie avec le nickelocène. En spectroscopie tunnel, ces modifications se traduisent par des pics dans la conductance d^2I/dV^2. La localisation en énergie de ces pics permet de déterminer le champ d'échange, tandis que leur amplitude fournit un accès à la polarisation en spin au niveau de Fermi. Au cours de ma thèse, j'ai démontré que l'acquisition de spectres d^2I/dV^2 à chaque coordonnée (x, y) de la surface permet de cartographier les variations spatiales du champ d'échange et de la polarisation de spin avec une résolution atomique. Il est apparu que les images du champ d'échange révèlent l'orientation de l'aimantation de la surface (ou d'une molécule en surface), et que ces images présentent une corrugation magnétique qui est bien reproduite par des calculs DFT de la densité de spin. Cette technique d'imagerie a également permis d'analyser l'impact de l'hydrogène sur le magnétisme des nanoaimants, ainsi que la manière dont les molécules peuvent altérer localement le magnétisme de ces nanostructures.

Mots clés : STM, spectroscopie tunnel, surfaces, molécules, spintronique, nanomagnétisme

Résumé en anglais

During my doctorate, I used a nickelocene molecule (Nc) attached to the tip of a scanning tunneling microscope to study surface magnetism. To do this, it is necessary to position the nickelocene close enough to the surface (<100 pm) so that the exchange field of the latter induces changes in the Zeeman levels of the nickelocene. These changes are detected electrically through excitations between Zeeman levels induced by inelastic tunneling electrons, i.e., electrons that exchange energy with the nickelocene. They manifest in tunneling spectroscopy as peaks in the conductance d^2I/dV^2. The energy position of these peaks allows determination of the exchange field, while their amplitude provides access to spin polarization at the Fermi level. During the thesis, we showed that acquiring d^2I/dV^2 spectra at each coordinate (x, y) of the surface allows visualization of spatial variations in the exchange field and spin polarization with atomic spatial resolution. We demonstrated that exchange field images provide access to the orientation of surface magnetization (or of a molecule on the surface), and notably, these images exhibit a magnetic corrugation that is well reproduced by DFT calculations of spin density. This imagery has also allowed visualization of the impact of hydrogen on the magnetism of nano-magnets, or how molecules can locally alter the magnetism of nano-magnets.

Keywords: STM, tunneling spectroscopy, surfaces, molecules, spintronics, nanomagnetism